Energy-efficient oxide-confined VCSELs for optical interconnects in data centers and supercomputers

vorgelegt von
Diplom-Physiker
Philip Moser
geb. in Berlin

Von der Fakultät II - Mathematik und
Naturwissenschaften
der Technischen Universität Berlin
zur Erlangung des akademischen Grades
– Dr. rer. nat. –

genehmigte Dissertation

Promotionsausschuss:
Vorsitzende: Prof. Dr. Janina Maultzsch
Berichter/Gutachter: Prof. Dr. Dieter Bimberg
Berichter/Gutachter: Prof. Dr. Anders Larsson

Tag der wissenschaftlichen Aussprache: 13. April 2015

Berlin 2015

To my family Yongling, Jan, Kilian, and Jutta.

Abstract

This dissertation provides the first systematic analysis of the dynamic energy efficiency of vertical-cavity surface-emitting lasers (VCSELs) for optical interconnects. Energy-efficient VCSELs are the key component to address the pressing ecological and economic issues of the exponentially growing energy consumption in data centers via energy-efficient optical interconnects. Energy-efficient data communication is one of the most important fields in "*Green Photonics*" enabling higher bit rates at significantly reduced energy consumption per bit.

General rules of how to achieve energy-efficient data transmission with VCSELs are derived by the systematic investigation of the static and dynamic VCSEL properties of different oxide-confined VCSEL designs emitting at 850-nm and 980-nm. These rules are applicable to all oxide-confined VCSELs of any wavelength. The derived rules are verified via data transmission experiments leading to record energy-efficient error-free data transmission at room temperature of 56 fJ/bit at 25 Gb/s. It is demonstrated that energy-efficient operation can also be achieved at high bit rates up to 40 Gb/s and across long multimode fiber transmission distances of up to 1000 m at 25 Gb/s, and over distances of 5 m at 46 Gb/s at 85°C and 50 Gb/s at 25°C with record VCSEL modulation bandwidths of 24.7 and 23.0 GHz at 25 and 85°C, respectively.

One main conclusion of this work is that the future required performance goals in terms of energy efficiency, bit rate, and temperature stability can be achieved with oxide-confined VCSELs. In order to achieve these goals simultaneously, the VCSELs must have small oxide-aperture diameters of 3-5 µm and must be operated at low current densities.

Prior to this dissertation work the main focus of oxide-confined VCSEL research was on VCSELs with larger oxide-aperture diameters of 7-10 µm as these devices are currently employed in commercial optical interconnects, because these oxide-aperture diameters typically yield the largest modulation bandwidths. It has been the conventional wisdom that in order to meet the future bandwidth demands such large oxide-aperture diameter VCSELs will be used in future optical interconnects. In this dissertation it is demonstrated that such large oxide-aperture diameter VCSELs are not suited for energy-efficient operation especially not at the required high bit rates and at high ambient temperatures and low current densities. For those VCSELs trade-offs between energy efficiency and all other performance goals exist. This dissertation work demonstrates that VCSELs with smaller oxide-aperture diameters are more energy-efficient than similar VCSELs with larger oxide-aperture diameters. At the required low current densities for reliable commercial application small oxide-aperture diameter VCSELs are simultaneously faster and significantly more energy-efficient than similar VCSELs with larger oxide-aperture diameters and the modulation bandwidth and energy efficiency are more temperature stable as well. This paradigm change has stimulated the work of other

groups on the energy efficiency of VCSELs with smaller oxide-aperture diameters.

In order to investigate the suitability and potential for different VCSELs and VCSEL designs in different optical interconnect technologies, the modulation factor M is introduced. M is the equivalent to the spectral efficiency from Information Theory, relating the maximum channel capacity or bit rate of the system to the modulation bandwidth of the VCSEL. M is as a free parameter representing different optical interconnect systems technologies. By assuming certain M-factor values, the energy consumption per bit can be calculated from the measured intrinsic VCSEL properties for different VCSELs at given bit rates employed in different optical interconnect technologies. This new method allows optical interconnect designers on the systems level to include VCSELs into their models and predict the optimum optical interconnect technology operating at maximum energy efficiency and simultaneously fulfilling the performance goals required by the specific application.

Curriculum Vitae

Philip Moser

Personal Data

Date of birth:	28 November 1983
Place of birth:	Berlin, Germany
Marital status:	married, one child

Dissertation

October 2008 - December 2014	PhD student in the group of Prof. Dr. D. Bimberg at the Technical University of Berlin, Berlin, Germany.

Academic Education

September 2008	Diploma in Physics
October 2007 - October 2008	Diploma student in the group of Prof. Dr. D. Bimberg
October 2005	Vordiplom in Physics
October 2003 - September 2008	Study of Physics at the Technical University of Berlin, Berlin, Germany

Awards

February 2015	Corecipient of the *SPIE Green Photonics Award in Communications 2015*, received at the Photonics West 2015, San Francisco, USA
March 2014	*Photonics21 Student Innovation Award 2014*, received at the Photonics21 Annual Meeting, Brussels, Belgium
February 2014	*SPIE Green Photonics Award in Communications 2014*, received at the Photonics West 2014, San Francisco, USA
November 2012	*Chorafas Prize*, received at the Technical University of Berlin, Berlin, Germany
January 2012	*SPIE Green Photonics Award in Communications 2012*, received at the Photonics West 2012, San Francisco, USA
August 2010	iNow 2010 Best Poster Award, received at the International Nano-Optoelectronic Workshop 2010 (iNow 2010) in Beijing, PR China

Own Publications

Parts of this thesis were published in the following journal papers and conference proceedings.

1. Journal Papers

1. **P. Moser**, J. A. Lott, G. Larisch, and D. Bimberg, "Impact of the Oxide-Aperture Diameter on the Energy-effciency, Bandwidth, and Temperature-Stability of 980-nm VCSELs", *IEEE Journal of Lightwave Technology*, vol. 33, no. 4, pp. 825831, Feb. 2015.

2. **P. Moser**, J. A. Lott, P. Wolf, G. Larisch, H. Li, and D. Bimberg, "Error-free 46 Gb/s operation of oxide-confined 980 nm VCSELs at 85°C", *Electronics Letters*, vol. 50, no. 19, pp. 1369-1371, Sep. 2014.

3. **P. Moser**, J. A. Lott, P. Wolf, G. Larisch, H. Li, and D. Bimberg, "85 fJ dissipated Energy per bit at 30 Gb/s across 500 m Multimode Fiber using 850 nm VCSELs", *IEEE Photonics Technology Letters*, vol. 25, no. 16, pp. 1638-1641, Jul. 2013.

4. P. Wolf, **P. Moser**, G. Larisch, H. Li, J. A. Lott, and D. Bimberg, "Energy efficient 40 Gb/s transmission with 850 nm VCSELs at 108 fJ/bit dissipated heat energy", *Electronics Letters*, vol. 19, no. 4, pp. 666-667, May 2013.

5. **P. Moser**, J. A. Lott, and D. Bimberg, "Energy-Efficiency of directly modulated oxide-confined high bit rate 850-nm VCSELs for Optical Interconnects," *IEEE Journal of Selected Topics in Quantum Electronics*, vol. 19, no. 4, p. 1702212-1-, Jul./Aug. 2013.

6. **P. Moser**, J. A. Lott, P. Wolf, G. Larisch, H. Li, N. Ledentsov, and D. Bimberg, "56 fJ dissipated energy per bit of oxide-confined 850 nm VCSELs operating at 25 Gbit/s," *Electronics Letters*, vol. 48, no. 20, p. 1292-1293, Sep. 2012.

7. **P. Moser**, J. A. Lott, P. Wolf, G. Larisch, A. Payusov, N. Ledentsov, and D. Bimberg, "Energy-Efficient Oxide-Confined 850 nm VCSELs for

Long Distance Multimode Fiber Optical Interconnects," *IEEE Journal of Selected Topics in Quantum Electronics*, vol. 19, no. 2, p. 7900406, Sep. 2012.

8. **P. Moser**, J. A. Lott, P. Wolf, G. Larisch, A. Payusov, N. N. Ledentsov, W. Hofmann, and D. Bimberg, "99 fJ/(bit · km) Energy to Data-Distance Ratio at 17 Gb/s Across 1 km of Multimode Optical Fiber With 850-nm Single-Mode VCSELs," *IEEE Photonics Technology Letters*, vol. 24, no. 1, pp. 19-21, Jan. 2012.

9. **P. Moser**, W. Hofmann, P. Wolf, J. A. Lott, G. Larisch, A. Payusov, N. N. Ledentsov, and D. Bimberg, "81 fJ/bit energy-to-data ratio of 850 nm vertical-cavity surface-emitting lasers for optical interconnects," *Applied Physics Letters*, vol. 98, no. 23, pp. 231106-1-3, Jun. 2011.

2. Conference Proceedings

1. **P. Moser**, M. Volwahsen, G. Larisch, J. A. Lott, and D. Bimberg, "Maximizing temperature insensitivity and energy-efficiency of 25-50 Gbs 980 nm VCSELs via small oxide-aperture diameters and photon lifetime tuning", *Proceedings of SPIE 9381, 93810T, Vertical-Cavity Surface-Emitting Lasers XIX*, San Francisco, CA, USA, 7-12 Feb. 2015.

2. **P. Moser**, J. A. Lott, P. Wolf, G. Larisch, N. Li, and D. Bimberg, "Temperature-stable oxide-confined 980 nm VCSELs operating error-free at 46 Gb/s and 85°C," in *24th IEEE International Semiconductor Laser Conference (ISLC)*, Palma de Mallorca, Spain, 7-10 Sep. 2014, paper TA7.

3. **P. Moser**, P. Wolf, G. Larisch, H. Li, J. A. Lott, and D. Bimberg, "Energy-efficient oxide-confined high-speed VCSELs for optical interconnects", *Proceedings SPIE, 9001-2, Vertical-Cavity Surface-Emitting Lasers XVIII*, San Francisco, CA, USA, 5-6 Feb. 2014.

4. **P. Moser**, G. Larisch, P. Wolf, H. Li, J. A. Lott, and D. Bimberg, "Green Photonics for Data and Computer Communication", in *2013 IEEEPhotonics Society Summer Topical Meeting Series*, Waikaloa, HI, USA, 8-10 Jun. 2013, pp. 5-6.

5. P. Wolf, **P. Moser**, G. Larisch, H. Li, J. A. Lott, and D. Bimberg, "119 fJ of Dissipated Energy per Bit for Error-free 40 Gbit/s Transmission Across 50 m of Multimode Optical Fiber Using Energy Efficient 850 nm VCSELs", in *2013 Conference on Lasers and Electro-Optics (CLEO)*, San Jose, CA, USA, 9-14 Jun. 2013, paper CTu3L.4.

6. **P. Moser**, P. Wolf, G. Larisch, H. Li, J. A. Lott, and D. Bimberg, "Energy Efficient 850 nm VCSELs for Error-free 30 Gb/s Operation across 500 m of Multimode Optical Fiber with 85 fJ of Dissipated Energy per Bit", in *Proceedings of the 2103 IEEE Optical Interconnect Conference*, Santa Fe, NM, USA, 5-8 May 2013, pp.13-14.

7. **P. Moser**, J. A. Lott, P. Wolf, G. Larisch, H. Li, N. N. Ledentsov, and D. Bimberg, "Impact of the aperture diameter on the energy-efficiency of oxide-confined 850-nm high-speed VCSELs", in *Vertical-Cavity Surface-Emitting Lasers XVII*, San Francisco, California, USA, 2-7 Feb. 2013, pp. 8639-30.

8. **P. Moser**, J. A. Lott, P. Wolf, G. Larisch, N. N. Ledentsov, and D. Bimberg, "25 Gb/s operation of oxide-confined 850-nm VCSELs with ultralow 56 fJ dissipated power per bit," in *23nd IEEE International Semiconductor Laser Conference (ISLC)*, San Diego, CA, USA, 7-10 October 2012, pp. 157-158.

9. **P. Moser**, P. Wolf, J. A. Lott, G. Larisch, A. Payusov, A. Mutig, W. Unrau, N. N. Ledentsov, W. Hofmann, and D. Bimberg, "High-speed VCSELs for energy efficient computer interconnects," in *Semiconductor Lasers and Laser Dynamics V*, Brussels, Belgium, 16-19 Apr. 2012, pp. 843202.

10. **P. Moser**, J. A. Lott, P. Wolf, G. Larisch, A. Payusov, G. Fiol, N. N. Ledentsov, W. Hofmann, and D. Bimberg, "Energy-efficient vertical-cavity surface-emitting lasers (VCSELs) for "green" data and computer communication," in *Vertical-Cavity Surface-Emitting Lasers XVI*, San Francisco, California, USA, 21-26 Jan. 2012, pp. 82760J-8.

11. **P. Moser**, W. Hofmann, P. Wolf, G. Fiol, J. A. Lott, N. N. Ledentsov, and D. Bimberg, "83 fJ/bit energy-to-data ratio of 850-nm VCSEL at 17 Gb/s," in *37th European Conference and Exhibition on Optical Communication (ECOC)*, Geneva, Switzerland, 18-22 Sep. 2011, pp. 1-3.

3. Other Journal Papers

1. H. Li, J. A. Lott, P. Wolf, P. Moser, G. Larisch, and D. Bimberg, "Temperature-Dependent Impedance Characteristics of Temperature-Stable High-Speed 980 nm VCSELs," *IEEE Photonics Technology Letters*, vol.PP, no.99, pp.1, Jan. 2015. doi: 10.1109/LPT.2015.2393863

2. H. Li, P. Wolf, **P. Moser**, G. Larisch, J. A. Lott, and D. Bimberg, "Temperature-Stable, Energy-Efficient, and High-Bit Rate Oxide-Confined 980 nm VCSELs for Optical Interconnects," *IEEE Journal of Selected Topics in Quantum Electronics*, vol.21, no.6, pp.1700409, Nov./Dec. 2015.

3. N. A. Maleev, S. A. Blokhin, M. A. Bobrov, A. G. Kuzmenkov, A. A. Blokhin, **P. Moser**, J. A. Lott, D. Bimberg, and V. M. Ustinov, "Study of high-speed semiconductor VCSELs based on AlInGaAs heterostructures with large gain-cavity detuning," *Semiconductors*, vol. 49, no. 1, pp. 88-91, Jan. 2015.

4. S. A. Blokhin, M. A. Bobrov, N. A. Maleev, A. G. Kuzmenkov, A. V. Sakharov, A. A. Blokhin, **P. Moser**, J. A. Lott, D. Bimberg, and V. M. Ustinov, "Anomalous lasing of high-speed 850 nm InGaAlAs oxide-confined vertical-cavity surface-emitting lasers with a large negative gain-to-cavity wavelength detuning," *Applied Physics Letters*, vol. 105, no. 6, pp. 061104, Aug. 2014.

5. H. Li, P. Wolf, **P. Moser**, G. Larisch, J. A. Lott, and D. Bimberg,"Temperature-Stable 980 nm VCSELs for 35 Gbs operation at 85°C with 139 fJ/bit Dissipated Heat", *IEEE Photonics Technology Letters*, vol. 26, no. 23, pp. 2349-2352, Dec. 2014.

6. H. Li, P. Wolf, **P. Moser**, G. Larisch, A. Mutig, J. A. Lott, and D. Bimberg,"Impact of the quantum well gain-to-cavity etalon wavelength offset on the high temperature performance of high bit rate 980 nm VCSELs", *IEEE Journal of Quantum Electronics*, vol. 50, no. 8, pp. 613-621, Jun. 2014.

7. H. Li, P. Wolf, **P. Moser**, G. Larisch, A. Mutig, J. A. Lott, and D. Bimberg, "Energy-Efficient and Temperature-Stable Oxide-Confined 980-nm VCSELs Operating Error-Free at 38 Gb/s at 85°C", *Electronics Letters*, vol. 50, no. 2, pp. 103-105, Jan. 2014.

8. P. Wolf, **P. Moser**, G. Larisch, W. Hofmann, and D. Bimberg, "High-Speed and Temperature-Stable oxide-confined 980-nm VCSELs for Op-

tical Interconnects", *IEEE Journal of Selected Topics in Quantum Electronics*, vol. 19, no. 4, p. 1701207, Jul./Aug. 2013.

9. W. Hofmann, **P. Moser**, and D. Bimberg, "Energy-Efficient VCSELs for Interconnects," *IEEE Photonics Journal*, vol. 4, no. 2, pp. 652656, Apr. 2012.

10. P. Wolf, **P. Moser**, G. Larisch, M. Kroh, A. Mutig, W. Unrau, W. Hofmann, and D. Bimberg, "High-performance 980 nm VCSELs for 12.5 Gbit/s data transmission at 155°C and 49 Gbit/s at -14°C C," *Electronics Letters*, vol. 48, no. 7, pp. 389390, Mar. 2012.

11. **P. Moser**, P. Wolf, A. Mutig, G. Larisch, W. Unrau, W. Hofmann, and D. Bimberg, "85°C error-free operation at 38 Gb/s of oxide-confined 980-nm vertical-cavity surface-emitting lasers," *Applied Physics Letters*, vol. 100, no. 8, pp. 081103-1-3, Feb. 2012..

12. A. Mutig, J. A. Lott, S. A. Blokhin, **P. Moser**, P. Wolf, W. Hofmann, A. A. Nadtochiy, and D. Bimberg, "Modulation Characteristics of High-Speed and High-Temperature Stable 980 nm Range VCSELs Operating Error Free at 25 Gbit/s up to 85°C," *IEEE Journal of Selected Topics in Quantum Electronics*, vol. 17, no. 6, pp. 1568-1575, Nov./Dec. 2011.

13. J. A. Lott, A. S. Payusov, S. A. Blokhin, **P. Moser**, N. N. Ledentsov, and D. Bimberg, "Arrays of 850 nm photodiodes and vertical cavity surface emitting lasers for 25 to 40 Gbit/s optical interconnects," *physica status solidi (c)*, vol. 9, pp. 290-293, Nov. 2011.

14. A. Mutig, J. A. Lott, S. A. Blokhin, P. Wolf, **P. Moser**, W. Hofmann, A. M. Nadtochiy, A. Payusov, and D. Bimberg, "Highly temperature-stable modulation characteristics of multioxide-aperture high-speed 980 nm vertical cavity surface emitting lasers," *Applied Physics Letters*, vol. 97, no. 15 pp. 151101-151101-3, Oct. 2010.

15. A. Mutig, G. Fiol, K. Potschke, **P. Moser**, D. Arsenijevic, V. A. Shchukin, N. N. Ledentsov, S. S. Mikhrin, I. L. Krestnikov, D. A. Livshits, A. R. Kovsh, F. Hopfer, and D. Bimberg, "Temperature-Dependent Small-Signal Analysis of High-Speed High-Temperature Stable 980-nm VCSELs," *IEEE Journal of Selected Topics in Quantum Electronics*, vol.

15, no. 3, pp. 679-686, May/Jun. 2009.

16. A. Mutig, G. Fiol, **P. Moser**, D. Arsenijevic, V. A. Shchukin, N. N. Ledentsov, S. S. Mikhrin, I. L. Krestnikov, D. A. Livshits, A. R. Kovsh, F. Hopfer, and D. Bimberg, "120°C 20 Gbit/s operation of 980 nm VCSEL," *Electronics Letters*, vol. 44, no. 22, pp. 1305-1306, Oct. 2008.

4. Other Conference Proceedings and Presentations

1. P. Spiewak, T. Czyszanowski, J. Walczak, R. P. Sarzala, **P. Moser**, D. Bimberg, J. A. Lott, and M. Wasiak, "Single and double oxidations in a 980 nm VCSEL 980 impact on certain electrical and optical properties", *Proceedings SPIE, 93810N, Vertical-Cavity Surface-Emitting Lasers XIX*, San Francisco, CA, USA, 7-12 Feb. 2015.

2. S. A. Blokhin, M. A. Bobrov, N. A. Maleev, A. G. Kuzmenkov, A. V. Sakharov, A. A. Blokhin, **P. Moser**, J. A. Lott, D. Bimberg, V. M. Ustinov, "Impact of a negative gain-to-cavity wavelength detuning on the performance of InGaAlAs oxide-confined vertical-cavity surface-emitting lasers", *Proceedings SPIE, 93810W, Vertical-Cavity Surface-Emitting Lasers XIX*, San Francisco, CA, USA, 7-12 Feb. 2015.

3. P. Wolf, H. Li, **P. Moser**, G. Larisch, J. A. Lott, and D. Bimberg, "Extraction and analysis of high frequency response and impedance of 980 nm VCSELs as a function of temperature and oxide aperture diameter", *Proceedings SPIE, 93810H, Vertical-Cavity Surface-Emitting Lasers XIX*, San Francisco, CA, USA, 7-12 Feb. 2015.

4. H. Li, P. Wolf, **P. Moser**, G. Larisch, J. A. Lott, and D. Bimberg, "Temperature-Stable Energy-Efficient High-Bit-Rate Oxide-Confined 980 nm VCSELs for Optical Interconnects", *Asia Communications and Photonics Conference, ACP 2014*, Shanghai, PR China, 11-14 Nov. 2014, paper ATh1A.

5. J. A. Lott, **P. Moser**, and D. Bimberg, "Energy Efficient Emitters for Computer Interconnects", *Asia Communications and Photonics Conference, ACP 2014*, Shanghai, PR China, 11-14 Nov. 2014, Tutorial, paper AW4B.1.

6. D. Bimberg, G. Larisch, **P. Moser**, P. Wolf, Hui Li, and J.A. Lott, "Energy-efficient, temperature stable, high data rate VCSELs for optical interconnects," *Transparent Optical Networks (ICTON), 2014 16th*

International Conference on, Graz, Austria, 6-10 Jul., 2014.

7. D. Bimberg, D. Arsenijevic, G. Larisch, H. Li, J. A. Lott, **P. Moser**, H. Schmeckebier, and P. Wolf , "Green nanophotonics for future datacom and Ethernet networks", Proceedings of SPIE 9134, *Semiconductor Lasers and Laser Dynamics VI*, 9134-02, Brussels, Belgium, 14-17 Apr. 2014.

8. H. Li, **P. Moser**, P. Wolf, G. Larisch, L. Frasunkiewicz, M. Dems, T. Czyszanowski, J. A. Lott, and D. Bimberg, "Energy efficiency, bit rate, and modal properties of 980 nm VCSELs for very-short-reach optical interconnects", *Proc. SPIE, 9001-10, Vertical-Cavity Surface-Emitting Lasers XVIII*, San Francisco, CA, USA, 5-6 Feb. 2014.

9. J. A. Lott, **P. Moser**, V. P. Kalosha, P. Wolf, A. S. Payusov, G. Larisch, H. Li, and D. Bimberg, "Progress Toward Optimizing 850-nm and 980-nm Vertical Cavity Surface Emitting Lasers (VCSELs) for Optical Interconnects", *5th Workshop on Physics and Technology of Semiconductor Lasers*, Krakow, Poland, 17-20 Nov. 2013.

10. H. Li, **P. Moser**, P. Wolf, G. Larisch, J. A. Lott, and D. Bimberg, "Energy efficient 850 nm VCSELs for multimode fiber based optical interconnects," *Proceedings International Nano-Optoelectronics Workshop (iNOW)*, Cargèse, France, 19-30 Aug. 2013.

11. P. Wolf, **P. Moser**, G. Larisch, H. Li, J. A. Lott, and D. Bimberg, "Energy Efficient 40 Gb/s Data Transmission with 850 nm VCSELs at 108 fJ/bit of Dissipated Heat," *Proceedings International Nano-Optoelectronics Workshop (iNOW)*, Cargèse, France, 19-30 Aug. 2013.

12. P. Wolf, **P. Moser**, G. Larisch, W. Hofmann, H. Li, J. A. Lott, C.-Y. Lu, S. L. Chuang, and D. Bimberg, " Energy-Efficient and Temperature-Stable High-Speed VCSELs for Optical Interconnects," in *Proceedings of the 3rd Workshop on Green Optical Communications, in conjunction with the 15th International Conference on Transparent Optical Networks (ICTON)*, Cartagena, Spain, 23-27 Jun. 2013.

13. J. A. Lott, **P. Moser**, G. Larisch, V. P. Kalosha, H. Li, P. Wolf, and D. Bimberg, "Infrared VCSELs for Short Distance High Bit Rate Free

Space Optical Interconnects," *Proceedings VCSEL Day 2013*, Lausanne, Switzerland, 31 May - 01 June 2013.

14. **P. Moser**, P. Wolf, G. Larisch, H. Li, J. A. Lott, and D. Bimberg, "Energy efficient 850 nm VCSELs for Data and Computer Communication," in *Proceedings of the VCSEL Day 2013*, Lausanne, Switzerland, 31 May 01 Jun. 2013.

15. J. A. Lott, **P. Moser**, and D. Bimberg, "Breaking the 50 fJ/bit Energy Efficiency Barrier with Nano-Engineered 50 Gb/s Vertical Cavity Surface Emitting Lasers," *Proceedings Nanoelectronics and Nanophotonics Workshop*, Clear Water Bay, Kowloon, Hong Kong, China, 27-29 May 2013.

16. J. A. Lott, **P. Moser**, and D. Bimberg, "Progress on efficient VCSELs for near-zero to kilometer-length optical interconnects," in *Optoelectronic Interconnects XIII*, San Francisco, CA, USA, 2-7 Feb. 2013, pp. 8630-27.

17. W. Hofmann, **P. Moser**, P. Wolf, G. Larisch, H. Li, W. Li, J.A. Lott, and D. Bimberg, "VCSELs for exascale computing, computer farms, and green photonics," in *Semiconductor Lasers and Applications V*, Beijing, China, 5-6 Nov. 2012, pp. 855205.

18. W. Hofmann, P. Wolf, **P. Moser**, G. Larisch, W. Unrau, A. Mutig, M. Kroh, and D. Bimberg, "High-speed temperature-stable 980-nm VCSELs," in *23nd IEEE International Semiconductor Laser Conference 2012 (ISLC 2012)*, San Diego, CA, USA, 7-10 October 2012, pp. 161-162.

19. N. N. Ledentsov, J. A. Lott, P. Wolf, **P. Moser**, J. R. Kropp, and D. Bimberg, "High speed VCSELs for energy-efficient data transmission," in *23nd IEEE International Semiconductor Laser Conference (ISLC)*, San Diego, CA, USA, 7-10 October 2012, pp. 151-152.

20. P. Wolf, **P. Moser**, J. A. Lott, G. Larisch, N. N. Ledentsov, W. Hofmann, and D. Bimberg, "VCSEL: green photonics for optical interconnects," *Proceedings International Nano-Optoelectronics Workshop (iNOW)*, Berkeley and Stanford, CA, USA, 7-15 Aug. 2012.

21. G. Larisch, P. Wolf, **P. Moser**, A. Mutig, M. Kroh, W. Hofmann, and D. Bimberg, "Temperature-stable high-speed 980-nm VCSELs," *Proceedings International Nano-Optoelectronics Workshop (iNOW)*, Berkeley and Stanford, CA, USA, 7-15 Aug. 2012.

22. N. N. Ledentsov, J. A. Lott, J.-R. Kropp, V. A. Shchukin, D. Bimberg, **P. Moser**, G. Fiol, A. S. Payusov, D. Molin, G. Kuyt, A. Amezcua, L. Y. Karachinsky, S. A. Blokhin, I. I. Novikov, N. A. Maleev, C. Caspar, and R. Freund, "Progress on single mode VCSELs for data- and telecommunications," in *Vertical-Cavity Surface-Emitting Lasers XVI*, San Francisco, CA, USA, 21-26 Jan. 2012, pp. 82760K-11.

23. W. Hofmann, **P. Moser**, P. Wolf, G. Larisch, W. Unrau, and D. Bimberg, "980-nm VCSELs for optical interconnects at bandwidths beyond 40 Gb/s," in *Vertical-Cavity Surface-Emitting Lasers XVI*, San Francisco, CA, USA, 21-26 Jan. 2012, pp. 827605-9.

24. A. Mutig, **P. Moser**, J. A. Lott, P. Wolf, W. Hofmann, N. N. Ledentsov, and D. Bimberg, "High-speed 850 and 980 nm VCSELs for high-performance computing applications," in *Optoelectronic Materials and Devices VI*, Shanghai, China, 13-16 Nov. 2011, pp. 830818-7.

25. A. Mutig, W. Hofmann, S. A. Blokhin, P. Wolf, **P. Moser**, A. M. Nadtochiy, D. Bimberg, and J. A. Lott, "High speed high temperature stable 980 nm VCSELs operating error-free at 25 Gbit/s up to 85°C for short reach optical interconnects," in *Optical Fiber Communication Conference and Exposition (OFC/NFOEC), 2011 and the National Fiber Optic Engineers Conference*, Los Angeles, CA, USA, 6-10 Mar. 2011, pp. 1-3.

26. A. Mutig, J. A. Lott, S. A. Blokhin, **P. Moser**, P. Wolf, W. Hofmann, A. M. Nadtochiy, and D. Bimberg, "High-speed highly temperature stable 980 nm VCSELs operating at 25 Gb/s at up to 85°C for short reach optical interconnects," in *Vertical-Cavity Surface-Emitting Lasers XV*, San Francisco, CA, USA, 22-27 Jan. 2011, pp. 79520H-11.

27. W. Hofmann, **P. Moser**, P. Wolf, A. Mutig, M. Kroh, and D. Bimberg, "44 Gb/s VCSEL for optical interconnects," in *Optical Fiber Communication Conference and Exposition (OFC/NFOEC), 2011 and the National Fiber Optic Engineers Conference*, Los Angeles, CA, USA, 6-10 Mar. 2011, pp. 1-3.

28. A. Mutig, J. A. Lott, S. A. Blokhin, **P. Moser**, P. Wolf, W. Hofmann, A. Nadtochiy, and D. Bimberg, "High speed 980 nm VCSELs for short reach optical interconnects operating error-free at 25 Gbit/s up to 85°C," in *Conference on Lasers and Electro-Optics 2011 (CLEO 2011)*, Baltimore, 1-6 May 2011, pp. 1-2.

29. W. Hofmann, **P. Moser**, A. Mutig, P. Wolf, W. Unrau, and D. Bimberg, "980-nm VCSELs for optical interconnects at 25 Gb/s up to 120°C and 12.5 Gb/s up to 155°C," in *Conference on Lasers and Electro-Optics 2011 (CLEO 2011)*, Baltimore, 1-6 May 2011, pp. 1-2.

30. A. Mutig, J. A. Lott, S. A. Blokhin, **P. Moser**, P. Wolf, W. Hofmann, A. M. Nadtochiy, A. Payusov, and D. Bimberg, "High-speed 980-nm VCSELs for very short reach optical interconnects," in *22nd IEEE International Semiconductor Laser Conference 2010 (ISLC 2010)*, Kyoto, Japan, 26-30 Sep. 2010, pp. 158-159.

31. J. A. Lott, N. N. Ledentsov, V. A. Shchukin, J-R. Kropp, S. A. Blokhin, A. M. Nadtochiy, A. Mutig, P. Wolf, **P. Moser**, G. Fiol, and D. Bimberg, "High-Speed VCSELs and Subassemblies for Short Range Optical Communications," *Proceedings ECOC 2010*, Torino, Italy, 19-23 Sep. 2010.

32. **P. Moser**, A. Mutig, J. A. Lott, S. A. Blokhin, P. Wolf, N. N. Ledentsov, and D. Bimberg, "Oxide-confined 850 and 980 nm VCSELs for optical interconnects," *Proceedings International Nano-Optoelectronics Workshop (iNOW)*, Beijing and Changchun, PR China, 1-15 Aug. 2010.

33. N. N. Ledentsov, J. A. Lott, V. A. Shchukin, A. Mutig , G. Fiol, T. Germann, **P. Moser**, P. Wolf, D. Bimberg, S. A. Blokhin, L. Y. Karachinsky, and A. M. Nadtochiy, "Prospects of MBE for Optoelectronic Devices," *Proceedings MBE Taiwan 2010*, Taipei, Taiwan, 24-25 May 2010.

34. J. A. Lott, V. A. Shchukin, N. N. Ledentsov, T. D. Germann, J.-H. Schulze, A. Mutig, **P. Moser**, P. Wolf, G. Fiol, D. Bimberg, "Directly and electrooptically-modulated Bragg reflector vertical cavity surface emitting lasers for high-speed and short-reach optical links," Invited, *Proceedings SPIE 7720-2, Semiconductor Lasers and Laser Dynamics IV*, Brussels, Belgium, 12-16 Apr. 2010.

35. **P. Moser**, A. Mutig, J. A. Lott, S. Blokhin, G. Fiol, A. M. Nadtochiy, N. N. Ledentsov, and D. Bimberg, "Oxide confined 850-nm VCSELs for high-speed datacom applications," in *Semiconductor Lasers and Laser Dynamics IV*, Brussels, Belgium, 12-16 Apr. 2010, pp. 77201W-7.

36. **P. Moser**, A. Mutig, G. Fiol, D. Arsenijevic, V. A. Shchukin, N. N. Ledentsov, F. Hopfer, and D. Bimberg, "High temperature stable 980 nm VCSEL: 20 Gb/s Operation at 120°C," *Proceedings International Nano-Optoelectronics Workshop (iNOW)*, Stockholm, Sweden and Berlin, Germany, 2-15 Aug. 2009.

37. A. Mutig, G. Fiol, K. Potschke, **P. Moser**, D. Arsenijevic, V. A. Shchukin, N. N. Ledentsov, S. S. Mikhrin, I. L. Krestnikov, D. A. Livshits, A. R. Kovsh, F. Hopfer, and D. Bimberg, "Small signal analysis of high temperature stable 980 nm VCSELs," *Proceedings International Nano-Optoelectronics Workshop (iNOW)*, Stockholm, Sweden and Berlin, Germany, 2-15 Aug. 2009.

38. D. Bimberg, S. A. Blokhin, A. Mutig, A. M. Nadtochiy, G. Fiol, **P. Moser**, D. Arsenijevi, F. Hopfer, V. A. Shchukin, J. A. Lott, and N. N. Ledentsov, "Nano-VCSELs for the Terabus," in *Proceedings 17th International Symposium Nanostructures: Physics and Technology*, Minsk, Belarus, 22-27 Jun. 2009.

39. N. N. Ledentsov, J. A. Lott, V. A. Shchukin, H. Quast, F. Hopfer, G. Fiol, A. Mutig, **P. Moser**, T. Germann, A. Strittmatter, L. Y. Karachinsky, S. A. Blokhin, I. I. Novikov, A. M. Nadtochi, N. D. Zakharov, P. Werner, and D. Bimberg, "Quantum dot insertions in VCSELs from 840 to 1300 nm: growth, characterization, and device performance," in *Quantum Dots, Particles, and Nanoclusters VI*, San Jose, CA, USA, 24-29 Jan. 2009, pp. 72240P-72240P-12.

40. F. Hopfer, A. Mutig, G. Fiol, **P. Moser**, D. Arsenijevic, V. A. Shchukin, N. N. Ledentsov, S. S. S. Mikhrin, I. L. Krestnikov, D. A. Livshits, A. R. Kovsh, M. Kuntz, and D. Bimberg, "120°C 20 Gbit/s operation of 980 nm VCSEL based on sub-monolayer growth," in *Vertical-Cavity Surface-Emitting Lasers XIII*, San Jose, CA, USA, 24-29 Jan. 2009, pp. 72290C-8.

41. V. A. Shchukin, N. N. Ledentsov, J. A. Lott, H. Quast, F. Hopfer, L. Y. Karachinsky, M. Kuntz, **P. Moser**, A. Mutig, A. Strittmatter, V.

P. Kalosha, and D. Bimberg, "Ultra high-speed electro-optically modulated VCSELs: modeling and experimental results," in *Physics and Simulation of Optoelectronic Devices XVI*, San Jose, CA, USA, 19-24 Jan. 2008, pp. 68890H-15.

42. A. Mutig, G. Fiol, **P. Moser**, F. Hopfer, M. Kuntz, V. A. Shchukin, N. N. Ledentsov, D. Bimberg, S. S. Mikhrin, I. L. Krestnikov, D. A. Livshits, and A. R. Kovsh, "120°C 20 Gbit/s operation of 980 nm single mode VCSEL," in *Proceedings of the IEEE International Semiconductor Laser Conference 2008 (ISLC 2008)*, Sorrento, Spain, 14-18 Sep. 2008, pp. 9-10.

43. F. Hopfer, A. Mutig, A. Strittmatter, G. Fiol, **P. Moser**, D. Bimberg, V. A. Shchukin, N. N. Ledentsov, J. A. Lott, H. Quast, M. Kuntz, S. S. Mikhrin, I. L. Krestnikov, D. A. Livshits, A. R. Kovsh, and C. Bornholdt, "High-speed directly and indirectly modulated VCSELs," in *20th International Conference on Indium Phosphide and Related Materials, (IPRM 2008)*, Versailles, France, 25-29 May 2008, pp. 1-6.

Contents

Own Publications **vi**
1. Journal Papers . . . vi
2. Conference Proceedings . . . vii
3. Other Journal Papers . . . ix
4. Other Conference Proceedings and Presentations . . . xi

List of Figures **xxi**

List of Tables **xxvi**

List of acronyms **xxvii**

1. Introduction **1**
1.1. Internet and energy consumption . . . 1
1.2. Optical Interconnects . . . 3
1.3. State-of-the-art of vertical-cavity surface-emitting lasers for optical interconnects . . . 4
1.4. Future Requirements . . . 7
1.5. Dissertation contribution . . . 8
1.6. Organization of the Dissertation . . . 8

2. VCSEL Fundamentals **10**
2.1. Laser principle . . . 10
2.1.1. Creation of light . . . 10
2.1.2. Population inversion . . . 12
2.1.3. Population inversion in semiconductor laser diodes . . . 13
2.1.4. Laser cavity . . . 15
2.2. Confinement of light and current in VCSELs . . . 17
2.2.1. Distributed Bragg reflectors . . . 17
2.2.2. Oxide-apertures in VCSELs . . . 34

3. Dynamic properties of oxide-confined VCSELs **40**
3.1. Rate equations . . . 40
3.2. Small-signal modulation . . . 42

4. Dynamic energy efficiency **46**
4.1. Dissipated heat-to-bit rate ratio (HBR) and energy-to-data ratio (EDR) . . . 46
4.2. Modulation factor M . . . 48

4.3. Impact of the oxide-aperture diameter on the energy efficiency 53

5. Fabrication of high-speed VCSELs 57
5.1. Process flow overview 57
5.2. *In situ*-controlled selective wet oxidation 60
5.3. High-frequency mask layout 63

6. VCSEL Design 68
6.1. Oxide-confined 850-nm VCSELs for optical interconnects . . . 68
6.2. Oxide-confined 980 nm VCSELs for optical interconnects . . . 69

7. 850-nm VCSEL results 78
7.1. Static properties 78
7.1.1. *LIV*-characteristics at room temperature 79
7.2. Small-signal modulation response 84
7.2.1. D-factor and MCEF versus oxide-aperture diameter . . 84
7.2.2. Power-to-bandwidth ratio and energy per bit for a 3 µm oxide-aperture diameter VCSEL 86
7.2.3. Impact of the oxide-aperture diameter on the energy efficiency: comparison of 3 µm and 5 µm oxide-aperture diameter VCSELs 90
7.2.4. Determination of the optimum oxide-aperture diameter for energy-efficient operation 95
7.3. Energy-efficient data transmission 104
7.3.1. Impact of the oxide-aperture diameter on the energy efficiency of the data transmission 105
7.4. Energy-efficient data transmission up to 40 Gb/s and across up to 1 km of MMF 108

8. 980-nm VCSEL results 115
8.1. Static properties 116
8.1.1. Temperature dependence of the *LIV*-characteristics of a 4.5 µm oxide-aperture diameter VCSEL 116
8.1.2. Impact of the oxide-aperture diameter on the static temperature-stability of the 980-nm VCSELs 119
8.2. Small-signal modulation 121
8.2.1. Temperature stability of the modulation bandwidth of a 5 µm oxide-aperture diameter VCSEL 121
8.2.2. Temperature stability of the energy efficiency of an 5 µm oxide-aperture diameter 980-nm VCSEL 122
8.2.3. Impact of the oxide-aperture diameter on the temperature stability of the modulation bandwidth 127
8.2.4. Impact of the oxide-aperture diameter on the temperature stability of the energy efficiency 129

8.3. Impact of the photon lifetime on the temperature stability of the modulation bandwidth and energy efficiency 134
8.3.1. Impact of the photon lifetime on static properties and their temperature stability 135
8.3.2. Impact of the photon lifetime on the modulation bandwidth and its temperature stability 135
8.3.3. Impact of the photon lifetime on the energy efficiency and its temperature stability 139
8.3.4. Trade-offs between bit rate, energy efficiency, and current density at 85°C 143
8.4. Data transmission 146

9. Conclusions and Outlook **148**
9.1. Summary and Conclusions 148
9.2. Outlook 150

Appendix **xxix**

A. Process flow **xxix**

Bibliography **xxxv**

Index **xlvii**

List of Figures

2.1. Fundamental electron photon interactions. 11
2.2. Populatin inversion. 13
2.3. Reflectian and transmission on interfaces. 19
2.4. Constructive and destructive interefence of light reflected by a $\lambda/4$ layer. 20
2.5. Schematics of DBR structures with different refractive indices and optical thicknesses. 22
2.6. Refractive index and e-field intensity of a 8-period DBR. 23
2.7. Refractive index and e-field intensity of a 8-period DBR with varying refractive index contrast. 24
2.8. Refractive index and e-field intensity of a 8-period DBR with an optically inactive $\lambda/2$ layer. 25
2.9. Calculated power reflectance versus wavelength for three $Al_xGa_{1-x}As$-DBRs 26
2.10. Calculated power reflectance versus wavelength for different number of $\lambda/2$-layers 26
2.11. Calculated power reflectance versus wavelength at normal incidence for different thicknesses of absentee layers 27
2.12. Reflectance spectrum for an AlAs/GaAs DBR with different numbers of mirror pairs. 29
2.13. Power reflectance and reflectivity phase spectrum at normal incidence for an AlAs/GaAs DBR with 25.5 mirror pairs. . . . 29
2.14. Calculated power reflectance R at 980-nm versus the etch depth of an AlAs-DBR with 25.5 mirror pairs. 30
2.15. Power reflectance versus number of DBR pairs for different refractive index contrasts. 31
2.16. Power reflectance spectra for a DBR with 25.5 pairs of different refractive index contrasts. 31
2.17. Refractive index profile and electric field intensity for an etalon with $\lambda/2$-cavity. 32
2.18. Refractive index profile and electric field intensity for an etalon with $\lambda/2$-cavity. 33
2.19. SEM of 980-nm VCSEL structure with three absentee layers. . 34
2.20. Topview of oxidation test structures. 35
2.21. Schematic cross section of a VCSEL with and without oxide-aperture. 37
2.22. SEM image of oxide-aperture and deep oxidation layers. 39

3.1. Simulated S21-response for different currents 44

4.1. Calculated M-factor versus signal-to-noise ratio 51
4.2. Measured and calculated electrical power versus resonance frequency. 54
4.3. Calculated bandwidth-power ratio versus modulation bandwidth and EDR versus bit rate. 55
4.4. Calculated EDR versus the bit rate for VCSELs with two different oxide-aperture diameters. 56

5.1. Process flow for the fabrication of high-speed VCSELs 59
5.2. *In situ*-image of the oxidation process. 61
5.3. *In situ*-image of the oxidation process. 62
5.4. *In situ*-image of the oxidation process. 63
5.5. Unit cell of the TUB mask set TUB_SE2010 64
5.6. Schematic of the high-frequency GSG pad layout 65
5.7. Optical micrograph of a GSG-layout 66
5.8. Optical micrograph of an unit cell 66
5.9. CW map a processed wafer piece. 67

6.1. Real refractive index and e-field intensity for the top DBR and active region of a 850-nm VCSEL. 69
6.2. Real refractive index and e-field intensity for a complete 980-nm VCSEL. 70
6.3. Zoom-in of the real refractive index and e-field intensity for the top DBR of a 980-nm VCSEL. 72
6.4. Zoom-in of the real refractive index and e-field intensity on the active region of a 980-nm VCSEL. 73
6.5. Power reflectance versus wavelength for the 980-nm VCSEL. . . 73
6.6. SEM image of a cleaved 980-nm VCSEL epitaxial structure showing oxidized aperture layers. 74
6.7. Electric field intensity profile and mirror penetration depths for a 980-nm VCSEL. 76
6.8. Calculated photon lifetime versus etch depth for a 980-nm VCSEL. 77
6.9. Calculated power reflectance versus etch depth for a 980-nm VCSEL. 77

7.1. Static *LIV*-characteristics of 850-nm VCSELs with different oxide-aperture diameters 80
7.2. Selected CW parameters for 850-nm VCSEL 81
7.3. Optical output power versus current density and P_{el} versus bias current and current density 83
7.4. Optical emission spectra for VCSELs with oxide-aperture diameters of 3.5, 4, and 5 µm. 83

7.5. Determination of the D-factor of 850 nm VCSELs with different oxide-aperture diameters . . . 85
7.6. Electrical, dissipated, and optical power versus f_r and f_{3dB} . . 87
7.7. Photons per bit versus bit rate for a 3 µm oxide-aperture diameter 850 nm VCSEL . . . 88
7.8. EDR for different M-factors . . . 89
7.9. Modulation response of 3 and µm oxide-aperture diameter VCSEL. . . . 91
7.10. Modulation bandwidth and electrical power versus the current density. . . . 92
7.11. M-factor evaluation for VCSELs with oxide-aperture diameters of 3 and 5 µm. . . . 94
7.12. EDR versus M-factor for VCSELs with oxide-aperture diameters of 3 and 5 µm. . . . 95
7.13. Electrical power versus f_r and f_{3dB} . . . 97
7.14. Dissipated and optical power versus f_{3dB} . . . 97
7.15. Electrical and dissipated power over f_{3dB} versus f_{3dB} . . . 98
7.16. Bandwidth-to-power ratio versus aperture diameter. . . . 99
7.17. Bandwidth power ratio versus J for all 9 VCSELs . . . 100
7.18. Calculated EDR and HBR versus J for all 9 VCSELs . . . 101
7.19. Calculated EDR and HBR versus J for all 9 VCSELs . . . 101
7.20. Bit rate at EDR = 100 fJ/bit versus the M-factor . . . 102
7.21. Bit rate of 850 nm VCSELs at EDR = 100 fJ/bit versus the oxide-aperture diameter. . . . 103
7.22. Bit rate of 850 nm VCSELs at different EDR values versus the oxide-aperture diameter. . . . 104
7.23. BER at 25 Gb/s for VCSELs with oxide-aperture diameters of 3.5, 4.0, and 5.0 µm. . . . 107
7.24. BER at 25 Gb/s across up to 100 m of MMF and 17 Gb/s across 1000 m of MMF. . . . 109
7.25. Optical eye diagrams of 850-nm VCSELs operated at 17 and 25 Gb/s at 25°C. . . . 110
7.26. BER measurements up to 40 Gb/s. . . . 111
7.27. BER measurement at 12.5 Gb/s across 2000 m of MMF. . . . 112
7.28. BER versus received optial power at 30 Gb/s up to 400 of MMF. 113

8.1. StaticLIV of a 980-nm VCSEL with an oxide-aperture diameter of 4.5 µm from at 25 and 85°C . . . 117
8.2. Static parameters versus heat-sink temperature of a 980-nm VCSEL. . . . 117
8.3. WPE and output power change for different temperatures. . . . 118
8.4. LIV at 25 and 85°C for 980-nm VCSELs with differen oxide-aperture diameters. . . . 120

8.5. Output power change versus current and current density for VCSELs with different oxide-aperture diameters. 121
8.6. f_{3dB} and MCEF of a 5 µm oxide-aperture diameter 980-nm VCSEL at 25 and 85°C 122
8.7. Change of f_{3dB} versus current of a 5 µm oxide-aperture diameter 980-nm VCSEL due to an temperature increase from 25 to 85°C 123
8.8. Change of the electrical bandwidth-to electrical power ratio versus current of a 5 µm oxide-aperture diameter 980-nm VCSEL due to an temperature increase from 25 to 85°C 123
8.9. Change of the bandwidth-to electrical power ratio versus f_{3dB} and *EDR* vs. bit rate of a 5 µm oxide-aperture diameter 980-nm VCSEL due to an temperature increase from 25 to 85°C 124
8.10. *EDR* versus bit rate for a 5 µm oxide-aperture diameter 980-nm VCSEL at 25 and 85°C. 125
8.11. Bit rates at 80, 100, and 120 fJ/bit versus M-factor for a 5 µm oxide-aperture diameter 980-nm VCSEL at 25 and 85°C. 125
8.12. MCEF for 980-nm VCSELs with oxide-aperture diameters of 5, 6, and 7 µm. 128
8.13. Temperature-induced change of f_{3dB} versus oxide-aperture diameter of 980-nm VCSELs. 128
8.14. f_{3dB}/P_{el} ratio versus f_{3dB} for 980-nm VCSELs with different oxide-aperture diameters at 25 and 85°C. 130
8.15. *EDR* versus bit rate for 5, 6, and 7 µm 980-nm oxide-aperture diameter VCSELs at 25 and 85°C. 131
8.16. Temperature-induced *EDR* change versus bit rate for 980-nm VCSELs with different oxide-aperture diameters. 132
8.17. Bit rate at different *EDRs* for 980-nm VCSELs with different oxide-aperture diameters at 25 and 85°C. 133
8.18. Temperature-induced bit rate change versus M-factor for different *EDRs* and oxide-aperture diameters. 133
8.19. LI-characteristic at 25 and 85°C and output power change for a 5 µm oxide-aperture diameter 980-nm VCSEL with calculated photon lifetimes of 3.7 and 1.8 ps 136
8.20. Modulation bandwidth versus current for a 5 µm oxide-aperture diameter 980-nm VCSEL with different photo lifetimes. 137
8.21. Relative change of f_{3dB} due to a photon lifetime and temperature change for a 5 µm oxide-aperture diameter 980-nm VCSEL. 137
8.22. f_{3dB}/P_{el} ratio of a 980-nm 5 µm oxide-aperture diameter VCSEL at 85°C for different photon lifetimes. 140
8.23. *EDR* versus bit rate for different photon lifetimes and temperatures 141
8.24. Temperature-induced *EDR* change versus bit rate for different photon lifetimes. 142

8.25. Bit rate at an *EDR* of 100 fJ/bit for different temperatures and photon lifetimes. 142
8.26. Temperature-induced bit rate change versus the M-factor for different photon lifetimes. 143
8.27. *EDR* and *HBR* versus oxide-aperture diameter at 10 kA/cm^2 . 145
8.28. *EDR* and *HBR* versus photon lifetime at 10 kA/cm^2 146

List of Tables

4.1. M-factors for error-free data transmission with 850-nm and 980-nm VCSELs 49

7.1. Side-mode suppression ratio and spectral width of 850-nm VCSELs with oxide-aperture diameters of 3.5, 4.0 and 5.0 µm. 84
7.2. S21-parameters of 850-nm VCSELs with oxide-aperture diameters of 3 and 5 µm. 91
7.3. Data transmission at 25 Gb/s of VCSELs with three different oxide-aperture diameters. The parameters are at the bias currents of the data transmission. . . 107
7.4. State-of-the-art of energy-efficient 850-nm VCSELs across MMF 114
7.5. State-of-the-art of energy-efficient 850-nm VCSELs across MMF (continued) 114

8.1. Static and dynamic VCSEL properties at the current of $\mathrm{d}f_{3\mathrm{dB}} = 0\%$ for a temperature increase from 25 to 85°C for 980-nm VCSELs with different oxide-aperture diameters. 129
8.2. Impact of the photon lifetime on important VCSEL properties for a 5 µm oxide-aperture diameter 980-nm VCSEL with $\mathrm{d}f_{3\mathrm{dB}}$ =0% and $\mathrm{M} = 2.0\,(\mathrm{b/s})/\mathrm{Hz}$. 138
8.3. Static and dynamic VCSEL properties at $10\,\mathrm{kA/cm^2}$ and 85°C for $\mathrm{M} = 2.0\,(\mathrm{b/s})/\mathrm{Hz}$. 146

List of acronyms

BCB	bisbenzocyclobutene
BER	bit-error ratio
BR	bit rate
DBR	distributed Bragg reflector
DQE	differential quantum efficiency
EDR	energy-to-data ratio
GSG	ground-signal-ground
HBR	heat-to-bit rate ratio
HF	high frequency
MMF	multimode optical fiber
MOVPE	metal organic chemical vapor phase epitaxy
NMP	N-methylpyrrolidinone
NRZ	non-return to zero
OI	optical interconnect
PRBS	pseudo-random bit sequenze
SMF	single-mode optical fiber
S/N	signal-to-noise ratio
VCSEL	vertical-cavity surface-emitting laser
WPE	wallplug efficiency

Chapter 1.

Introduction

This Chapter provides a short introduction into the problem of the exponentially increasing energy consumption in data centers and supercomputers mainly caused by the growth of the global Internet traffic and computational bandwidth demand. The resulting need for energy-efficient optical interconnects, in particular optical interconnects based on vertical-cavity surface-emitting lasers (VCSELs), is briefly explained, followed by a detailed overview of the state-of-the-art of VCSELs for data communication and VCSEL-based optical interconnects. Then the future performance requirements of VCSELs and the contribution of this dissertation to the field of energy-efficient VCSELs for optical interconnects are explained, before the Chapter ends with a Section about the organization of this dissertation.

1.1. Internet and energy consumption

The global Internet traffic has been increasing exponentially in the past decades and its growth is predicted to continue to increase exponentially in the next decades as well [1, 2, 3]. The number of Internet users is growing due to social and economic development in developed and in developing countries. But not only the number of people with access to the Internet is increasing, also new Internet-based services and devices that require access to the Internet are evolving and leading to an additional increase of Internet traffic in addition to the conventional Internet use via desktop computers.

One characteristic of the global bandwidth demand is, that each increase of the upload or download capacity for a single Internet user, group of users, companies, or research institutes stimulates innovative new applications which in turn further increases the bandwidth demand.

About 80% of the data transferred via the Internet in 2018 will be videos files [3]. While Internet video platforms like YouTube and others are well established and have been used for several years, videos on demand or Internet television (TV) via for instance Netflix and Amazon Video are comparably new in Europe. The provided quality of such videos on demand has become already very high enabled by fast streaming or download speeds, resulting in large volumes of transferred data. With high resolution computer screens and smart TVs even three dimensional (3D) high definition videos with high quality sound are expected from many Internet users to be accessible online.

Mobile Internet traffic growths faster than the average Internet traffic [3].

For many people in the industrial nations and the newly industrialized countries, permanent Internet access via mobile devices such as smart phones or tablets has become a basic necessity. Seamless access to the Internet via wifi networks at airports, in train stations, throughout airports and during flights, at universities, in libraries, administration buildings, in shopping malls and department stores, in restaurants, in hotels, and many other public places enables immediate and nearly instantaneous information transfer for many simultaneous users. For example ubiquitous connectivity enables one to send and receive email and tweets, document or track every moment of one's life, gain access to cloud services and other stored content, and use a smart phone for navigation. Smart phones, tablet computers, and other new product families that enable and require access to the Internet lead therefore to a seemingly limitless growth of the Internet traffic.

It is predicted that more than 50% of the global Internet traffic in 2018 will be due to devices other than personal computers such as smart TVs, smart phones, tablet computers, and other portable devices with Internet access [3]. It has already become common that Internet users are simultaneously connected to the Internet with several devices, such as a desktop computer, a smart phone, and a smart TV or Internet radio. Further development and innovation of devices with Internet access, will increase this trend of multiple Internet access. *Smart homes* are envisioned where air conditioning, heating, surveillance technology, windows, lighting, and other features of a home are automatically or remotely controlled. Also many items in the home may be *smart* and connected including toasters, refrigerators (that automatically order food when supplies run low) and stores will deliver goods via mobile vehicles or drones. Although an automatic control of many devices without the need for Internet access is possible, in reality many features such as video surveillance will be controlled via web browsers or smart phones when the home owner is not at home. Then people even may generate Internet traffic at their homes while being somewhere else.

The growing Internet traffic has led to a corresponding dramatic growth of the energy consumption, especially in data centers and supercomputers. While in 2010 most of the energy consumption of the Internet can be attributed to the access networks, it is predicted that data centers will require the largest fraction of the Internet energy consumption in 2020 [2]. The enormous energy consumption of data centers is already today a pressing ecological and economical problem. New massive data centers are built in sub-polar regions or similar higher northern and southern latitudes where the electricity cost is low and and *free* cooling is available via access to naturally cold water in close proximity to the data center facilities from rivers, lakes, or the sea. This has led to the construction of new data centers in northern Europe, for example a Facebook datacenter in Luleå in Sweden. Other examples include data centers in Norway [4] where hydroelectricity is abundant, and in Iceland where hydrothermal energy may serve a large fraction of the data center energy needs.

Because the energy consumption caused by the Internet is growing faster than the global electricity production [2], new technologies are required that enable data transmission at larger data rates and simultaneously significantly lower energy consumption per bit. Most of the energy in a data center is consumed by inter or intra-rack data transfer and for cooling the hardware. About 80% of the traffic in a data center stays in the data center, 5% goes to other data centers, and only 15% of the traffic actually goes to the users.

Depending on the assumed annual improvement of the energy efficiency of the hardware the energy consumption for transferring one single bit of information via the Internet is predicted be 1 to 4 μJ per bit in 2020 [2]. The largest fraction of this energy will be consumed in the interconnects inside the data centers. Thus fast (high bit rate) *and* energy-efficient optical interconnects are a *key-enabling technology* for an ecological, economical, and sustainable Internet.

1.2. Optical Interconnects

Optical interconnects have already partly replaced electrical interconnects in data centers and supercomputers due to their larger maximum bandwidth-distance product.

Optical interconnects consist of the transmitter optical subassembly (TOSA), a lightguiding medium such as single or multimode optical fiber that transports the information, and the receiver optical subassembly (ROSA). In general the TOSA consists of an electrical interface, an integrated driver circuit that provides the electrical power to the light source, an optical interface that couples the light into the light guiding medium, then again an optical interface that couples the light to the detector or photo receiver of the ROSA. The electrical signal may then be modified by electrical amplifiers followed by an electrical interface again.

Electrical interconnects are running into intrinsic limitations once the bandwidth-distance product is increased beyond a certain value. Therefore 850-nm VCSEL-based optical interconnects have already replaced electrical interconnects for short-reach (SR) data transmission at 10-14 Gb/s from several meters of multimode optical fiber (MMF) up to 300 m of MMF. At longer transmission distances typically distributed feedback (DFB) edge-emitting laser diodes and single-mode fiber (SMF) are used. Because the energy consumption of an edge-emitting laser is at least one order of magnitude larger than that of a VCSEL it is desired to extend the MMF transmission distance of the VCSEL-based optical interconnects in order to replace the SMF-based DFB-laser optical interconnects.

The performance of the complete optical interconnect such as the maximum error-free bit rate and the total energy consumption depend on the combined performance of the individual optical, electronic, and optoelectronic components of the optical interconnect. Thus different optical interconnect designs

that are optimized to fullfil different performance requirements will consist of different combinations of the electronic and optoelectronic components. In order to optimize an optical interconnect for a specific performance goal the impact of each component in a given different optical interconnect configuration, e.g. different combinations of the electronic and optoelectronic components, has to be known or predicted by systems-level modeling or testing. Since in the past the main focus of the development of optical interconnects was primarily on increasing the bit rate, good experience exists here. For future optical interconnects, performance goals such as high bit rates, long MMF transmission distance, and temperature-stable operation, all at low current densities, have to be achieved at simultaneously high energy efficiencies.

Prior to the work in this dissertation very little systematic analysis of the dynamic energy efficiency of VCSELs for optical interconnects had been accomplished. Therefore it has not been possible to predict the optimal optical interconnect design for future energy-effiecient optical interconnects. The main purpose of this dissertation is to provide a systematic investigation of the dynamic energy efficiency of VCSELs in terms of consumed and dissipated energy per bit. Via the proposed and demonstrated evaluation methods and the revealed intrinsic trade-offs between different performance goals, the dynamic energy efficiency performance of VCSELs shall be made accessible for systems designers in order to optimize the overall energy efficiency of complete optical interconnects.

The state-of-the-art of VCSELs for optical interconnects and VCSEL-based optical interconnects as well as future optical interconnect performance goals are summarized in the next two Sections.

1.3. State-of-the-art of vertical-cavity surface-emitting lasers for optical interconnects

Optical interconnects based on vertical-cavity surface-emitting lasers (VCSELs) are especially well-suited for data transmission at large bit rates and low consumed energy per bit, because of the VCSELs' small mode-volume compared to edge-emitting semiconductor lasers. In addition VCSELs can be fabricated cost-efficiently with yields of 10,000s or 100,000s of devices per wafer which can be automatically characterized prior to dicing and cleaving. Wafer-scaling to wafers with 4 or 6-inch diameters and shrinking the footprint of the VCSEL to $150 \times 150\,\mu$m is predicted to result in 250,000 and more than 500,000 VCSELs per 4-inch and 6-inch diameter wafer [5], respectively. The vertical light emission allows the fabrication of VCSEL arrays with a small geometric footprint for parallel optical interconnects with high aggregated bit rates [6].

Depending on the required emission wavelength, VCSELs have been realized in different material systems each with its own advantages and difficulties. This dissertation focuses on shorter wavelength infrared VCSELs that operate

in the wavelength range of 850 to 1060-nm.

For application in short-reach (SR)(several meters up to approximately 300 m) optical interconnects based on multimode optical fiber (MMF) to ultrashort-reach (USR) (a few centimeters to millimeters) optical interconnects VCSELs emitting in the wavelength range of approximately 850-nm to 1060-nm are most important. While the wavelength of 850-nm is the current standard wavelength for SR optical interconnects across MMF and will most likely remain the standard wavelength for this application, no standards exist yet for future very short-reach (VSR) (up to a few meters), USR, and on-chip optical interconnects. The VCSELs for these new optical interconnects must accommodate additional performance requirements as compared to the attributes of current SR optical interconnects. This includes extremely energy-efficient operation with low energy per transmitted bit at simultaneously high bit rates at high ambient temperatures.

Wavelengths longer than 850-nm might have advantages for high temperature operation due to the deeper quantum wells. This has led to intense research of VCSELs emitting at 980-nm. In addition GaAs is transparent at this wavelength, enabling the easy fabrication of bottom-emitting VCSELs with a small device footprint without the need to remove the substrate. Also GaAs-layers with large carrier mobility and high thermal conductance can be used in the VCSEL mirrors which is advantageous for the general overall VCSEL performance.

Commercial state-of-the-art oxide-confined VCSELs for optical interconnects are developed and produced by Finisar Incorporated (Sunnyvale, California, USA) [7] and Philips Technologie GmbH U-L-M Photonics [5]. The fastest VCSELs with the largest modulation bandwidths and error-free bit rates to date have been developed at Chalmers University in the group of Prof. Anders Larsson. These oxide-confined 850-nm VCSELs demonstrate record-large modulation bandwidths of 28 GHz and 21 GHz at 25 and 85°C [8, 9], respectively. The error-free bit rate for on-wafer measurements could be increased up to 57 Gb/s at 25°C [10] and 40 Gb/s at 85°C [9]. These record-bandwidth VCSELs have enabled even larger error-free bit rates in packaged modules in cooperation with IBM Incorporated as is described in a following paragraph. By employing small surface relief modifications of the outcoupling mirror that reduce the spectral width of the optical emission, error-free operation could be achieved at 20 and 25 Gb/s across 2000 and 1300 m of MMF [11] at low current densities.

Using VCSELs with proton implantation and a photonic crystal structure, error-free 25 Gb/s operation across 1000 m of MMF could be demonstrated at a low current-density of 5.4 kA/cm^2 [12] by the group of Prof. Kent Choquette of the University of Illinois. Recently a large modulation bandwidth of 37 GHz has been demonstrated by the same group with transversely coupled coherent VCSEL arrays [13], but large-signal modulation results have not been published yet to verify whether this large bandwidth also translates

into large error-free bit rates. Transversely coupled cavity 980-nm VCSELs developed in the group of Prof. Fumio Koyama at the Institute of Technology Tokyio demonstrated 25 Gb/s operation [14]. Thus at present, optically coupled VCSELs have not yet been demonstrated to achieve bit rates superior to conventional directly current-modulated VCSELs. At a lower bit rate of 14 Gb/s error-free 2000 m MMF transmission is achieved using 850-nm VCSELs with zinc diffusion and oxide-relief apertures [15] developed in the group of Prof. Jin-Wei Shi at the National Central University of Taiwan, where oxidized layers are removed leaving an air gap for current-confinement.

Oxide-confined 980-nm VCSELs developed at the University of California at Santa Barbara in the group of Prof. Larry Coldren have for a long time been considered to be the most energy-efficient VCSELs showing error-free operation up to 35 Gb/s with 286 fJ of dissipated energy per bit [16, 17, 18]. Large error-free bit rates of up to 38 Gb/s at up to 85°C have been demonstrated with oxide-confined 980-nm VCSELs developed by our group led by Prof. Dieter Bimberg at the Technische Universität Berlin [19, 20, 21, 22]. While increasing the bit rate at 85°C reflects considerable progress, these devices had to be operated at comparably large current densities and with large energy dissipations in excess of 25 kA/cm^2 and 600 fJ/bit, respectively. Large progress has been made, as presented in this dissertation, in improving the energy efficiency while simultaneously increasing the bit rate and the temperature stability.

At 1060-nm error-free operation was demonstrated up to 40 Gb/s at 25°C [23] with tunnel junction VCSELs and at 25 Gb/s up to 100°C [24] with oxide-confined VCSELs by the NEC Corporation. While it is nearly impossible for university groups to test the reliability of VCSELs without a large commercial partner, reliability studies were published for the oxide-confined 1060-nm VCSEL technology [25]. With a focus on energy efficiency and reliability Furukawa Electric Co., Ltd. demonstrated error-free VCSEL operation at 10 Gb/s VCSEL with 140 fJ/bit of dissipated energy per bit [26, 27]. These VCSELs are oxide-confined, have intra-cavity contacts, and a dielectric top DBR. In recent work by IBM and Furukawa such 1060-nm VCSELs with small oxide-aperture diameters of 4.1 µm are employed in a prototype optical interconnect TOSA for energy-efficient operation [28] as discussed in the following paragraph.

The dynamic performance of a VCSEL typically improves in a packaged module due to for example the use of a matched driver circuit. Recently, the error-free bit rate of packaged 850-nm VCSELs has been increased by IBM to a record-large 71 Gb/s at 25°C and 50 Gb/s at 90°C using a matched SiGe integrated driver circuit [29] and a Chalmers University VCSEL. This is presently the largest single-channel data rate ever demonstrated for a VCSEL. The system uses nonreturn-to-zero coding and feed forward equalization. With packaged 1060-nm VCSELs from Furukawa Electric Co., Ltd., IBM demonstrated energy-efficient operation at 26 Gb/s with a total energy consumption

of 1.1 pJ/bit for a complete optical interconnect consisting of a transmitter and receiver. The most energy-efficient VCSEL-based optical interconnect reported to date was demonstrated by IBM and operates at a slightly smaller bit rate of 25 Gb/s with a total energy consumption of 0.96 pJ/bit [30] using VCSELs from Emcore Inc. (acquired by Sumitomo Electric Device Innovations USA, Inc. in 2012) and a low-power silicon-on-insulator CMOS-based VCSEL driver integrated circuit.

1.4. Future Requirements

Depending on the application, different desired performance goals such as large bit rate, low energy per bit operation, or long mulimode optical fiber (MMF) transmission distance can be identified. Some of these goals have not yet been achieved simultaneously. In general the error-free bit rate and thus the modulation bandwidth is desired to be as large as possible. In addition the current density is desired to be as low as possible, because for oxide-confined VCSELs it is directly related to the reliability of the VCSEL. In commercial applications current densities of below 10 kA/cm^2 have typically been demonstrated to enable reliable oxide-confined VCSEL operation [31].

For future ultrashort-reach (USR) and on-chip optical interconnects large bit rates in excess of 40 Gb/s have to be achieved at high ambient temperatures up to 85°C, preferably without cooling of the VCSEL devices. Thus VCSELs for such optical interconnects need to show their best performance at the given high ambient temperature or need to be very insensitive to a temperature increase. Because the number of employed optical interconnects inside the racks of the data centers increases with decreasing transmission distance, the energy efficiency is extremely important for such USR optical interconnects. Due to the high level of integration of such VCSELs, especially for a future integrated on-chip architecture, extremely high reliability has to be guaranteed. Thus oxide-confined VCSELs for future VSR, USR, and on-chip interconnects need to achieve $\geq$40 Gb/s operation at $\leq$10 kA/cm^2 at temperatures up to 85°C or higher without active cooling. Based on estimates and predictions using extrapolations of the International Technology Roadmap for Semiconductors, light-sources for on-chip optical interconnects need to operate with 10s of femtojoules of dissipated energy per transmitted bit [32] in addition to the above-mentioned requirements of bit rate, current density, and temperature stability.

The presently used 850-nm VCSEL-based short-reach (SR) optical interconnect technology will remain important in future data centers and supercomputers, but trends show that the single channel data rate must be increased to 100 Gb/s and larger [33]. The massive challenge here will be the optimization of the energy efficiency of the optical interconnect in addition to issues of packaging, VCSEL integration with silicon-based systems, bandwidth density, and more.

In addition to the SR 850-nm VCSEL-based optical interconnects, the maximum MMF distance in data centers must be increased to 2000 m or even longer (i.e. medium-reach distances) at an error-free bit rate of at least 25 Gb/s [34, 35]. The state-of-the art results given in the previous Section 1.3 show that this will certainly be possible with further VCSEL design optimization, but most likely with larger energy consumption per bit than for the shorter transmission distances. Large single-mode powers are required at low current densities for these VCSEL-based medium-reach optical interconnects, which will most likely require the introduction of additional mode-selective losses leading to a less energy-efficient operation of the VCSELs.

The contribution of this dissertation in advancing the field of energy-efficient VCSELs for optical interconnects and to the evaluation of the intrinsic trade-offs between the above-mentioned performance goals will be described in the following Section.

1.5. Dissertation contribution

This work presents the first systematic analysis of the dynamic energy efficiency of VCSELs. The dependence of the dynamic energy efficiency on various device parameters such as the oxide-aperture diameter, the bias current, the ambient temperature, the bit rate, and the photon lifetime is demonstrated for the first time. General principles that apply for all oxide-confined VCSELs are derived and verified by measurements of 850 and 980-nm VCSELs. Applying these principles led to record energy-efficient data transmission with 850-nm VCSELs with 56 femtojoule (fJ) of dissipated energy per bit at 25 Gb/s and 108 fJ/bit at 40 Gb/s. With 980-nm VCSELs record-large modulation bandwidths up to 23.0 GHz at 85°C could be demonstrated, resulting in a record-large error-free bit rate of 46 Gb/s at 85°C. Substantial progress has been achieved by this dissertation work in the understanding of the dynamic energy efficiency of oxide-confined VCSELs for optical interconnects which has stimulated similar work of other groups on increasing the energy efficiency of VCSELs by using smaller oxide-aperture diameters.

1.6. Organization of the Dissertation

This dissertation is organized as follows. The fundamental laser principles are explained and discussed in Chapter 2, followed by a detailed introduction of the concept of distributed Bragg reflectors (DBRs) and oxide-apertures for light and current-confinement in VCSELs.

The standard rate-equation theory and the small-signal modulation characteristics of laser diodes are explained in Chapter 3. Then the energy-to-data ratio and the heat-to-bit rate ratio are introduced in Chapter 4 as figures-of-merit for comparing the energy efficiency in terms of the consumed and dissipated energy per bit of VCSELs. The modulation factor M is introduced

to calcuate the energy per bit from the intrinsic bandwidth-to electrical power ratio of the VCSEL and to compare the suitability of VCSELs for applications in different optical interconnect system designs.

The fabrication and geometric design variations of oxide-confined VCSELs for optical data transmission are explained in detail in Chapter 5, followed by the epitaxial VCSEL design of the 850-nm and 980-nm VCSELs in Chapter 6.

The impact of the oxide-aperture diameter on the static and dynamic VCSEL properties and the energy efficiency is discussed in detail in Chapter 7. General rules for achieving energy-efficient data transmission with VCSELs are derived from systematic small-signal modulation analysis and verified via data transmission experiments. Finally, record energy-efficient data transmission results at various bit rates and across different multimode optical fiber distances is demonstrated.

The impact of the oxide-aperture diameter on the temperature stability of the static and dynamic VCSEL properties including the energy efficiency is demonstrated with oxide-confined 980-nm VCSELs in Chapter 8. A record-large modulation bandwidth and error-free bit rate at 85°C is demonstrated.

The key findings and achievements of this thesis are summarized in Chapter 9 and an outlook on future work based on the results of this dissertation is given.

Chapter 2.

VCSEL Fundamentals

The fundamentals of semiconductor lasers in general and vertical-cavity surface-emitting lasers (VCSELs) in particular are explained in this Chapter. Basic design principles that are especially important for VCSELs and that enabled the development of present high-speed VCSELs, such as distributed Bragg reflectors and oxide-apertures are explained in detail with many examples. A broad range of different VCSEL applications exist, resulting in many different VCSEL designs and the use of different material systems to build the VCSELs. The intention of this Chapter is not to provide a complete introduction of VCSELs for all possible emission wavelengths or applications, but rather to present those design principles that directly apply to the GaAs-based VCSELs presented in this dissertation for optical data transmission with peak emission wavelengths in the range of approximately 850 to 1060-nm.

2.1. Laser principle

The well-known acronym "laser" stands for "**L**ight **A**mplification by the **S**timulated **E**mission of **R**adiation". Albert Einstein first postulated *stimulated emission* of radiation in 1916 [36]. A vast number of different lasers exist that all differ in the design and properties, but that are all based on the same principles: creation and amplification of light via stimulated emission in a cavity. In the following these basic laser principles that apply for all different lasers are explained.

2.1.1. Creation of light

In a radiative equilibrium of a quantum mechanical system, for example a single atom, three types of photon electron interaction exist. First an excited electron with the Energy E_1 can spontaneously relax to a lower energy level E_2 under emission of a photon with the energy $E_{21} = E_1 - E_2 = h\nu$, where h is the Planck constant and ν is the frequency of the photon. This process is called spontaneous emission. Second, an electron at the energy level E_2 can absorb a photon with the energy E_{21} and move to the higher energy state E_1. Finally there is the phenomena of *stimulated emission* postulated by Albert Einstein. A photon with the energy E_{21} stimulates an electron at the energy level E_1 to move to the lower energy level E_2 by emitting an photon of the exact same energy, wavelength, direction, impulse, polarization and phase as the initial photon. Thus the incident and the emitted photon are coherent. A laser makes

use of the stimulated emission in order to create emission of coherent photons. Each of these processes has its own rate, which are R_{sp}, R_{abs}, and R_{st} for the spontaneous emission, absorption, and stimulated emission, respectively. The three fundamental electron photon interactions are illustrated in Figure 2.1.

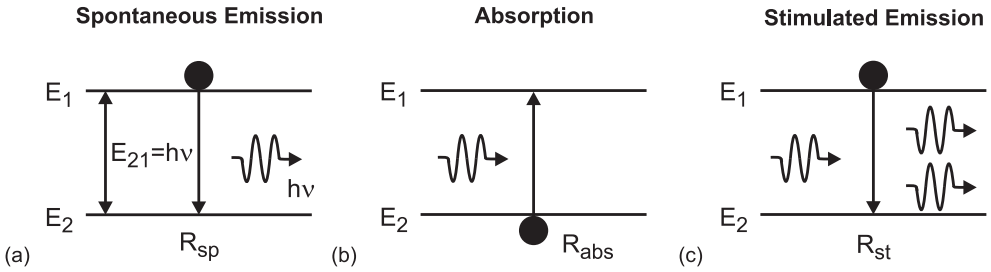

Figure 2.1.: Three fundamental electron-photon interactions in a radiative equilibrium. (a) An electron relaxates from the higher energy level resulting in the spontaneous emission of a photon with the energy of hν; (b) absorption; and (c) stimulated emission.

Spontaneous emission can only occur if electrons populate the higher energy level E_1. Thus R_{sp} is proportional to the electron concentration N_1 at the energy level E_1. Thus one can write:

$$R_{sp} = A_{sp} \cdot N_1 \tag{2.1}$$

where A_{sp} is the proportionality factor of the spontaneous emission. At least one photon is required in order to enable absorption and stimulated emission. Since absorption requires electrons in the lower energy level E_2 and stimulated emission requires electrones at the higher energy-level E_1, the rates for the absorption R_{abs} and for the stimulated emission R_{st} are proportional to the electron concentrations N_2 and N_1, respectively. Since both processes require incident photons, both rates are also proportional to the light intensity Φ. Thus the rates for the absorption and the stimulated emission can be written as :

$$R_{abs} = B_{abs} \cdot N_2 \cdot \Phi, \tag{2.2}$$
$$R_{st} = B_{st} \cdot N_1 \cdot \Phi, \tag{2.3}$$

where B_{abs} and B_{st} are the proportionality factors of the absorption and the stimulated emission, respectively. A_{sp}, B_{abs}, and B_{st} are called the Einstein coefficients for the spontaneous emission, absorption, and the stimulated emission, respectively. Absorption means annihilation of photons whereas the effects of spontaneous and stimulated emission create photons. In a radiative equilibrium the number of photons remains constant, thus the annihilation

and creation processes balance each other and thus:

$$R_{abs} = R_{sp} + R_{st}. \tag{2.4}$$

2.1.2. Population inversion

In a semiconductor laser the effect of stimulated emission is employed to create coherent light emission with a large optical power. Thus the stimulated emission is desired to be as large as possible for efficient light amplification. In other words the goal is a positive net optical gain. The derivation of the condition for a positive net optical gain is explained in Ref. [37] and only the conclusions are given here. In an equilibrium the ratio of the electron concentration at the higher energy level to that of the lower energy level, thus N_1/N_2 can be expressed by Boltzmann statistics. Inserting the blackbody radiation intensity spectrum and making use of equation 2.4 yields the conclusion that for all temperatures:

$$B_{abs} = B_{st}. \tag{2.5}$$

Because of Equation 2.5 the Einstein coefficients B_{abs} and B_{st} will in the following simply be called B. When the semiconductor laser diode is operated in the laser mode the contribution of the spontaneous emission to the coherent light emission is very small and can therefore be neglected, as is also done in several assumptions in Chapter 3.1. Then the stimulated emission is considered to be the only photon creation process and the absorption remains the only photon annihilation process and the net stimulated emission rate is simply the difference between the rate of these two processes and is given by:

$$R_{st} - R_{abs} = (N_1 - N_2) \cdot B \cdot \Phi. \tag{2.6}$$

Net light amplification is realized when R_{st} is larger than R_{abs}, thus when $N_1 > N_2$. In an equilibrium more electrons will be in the lower energy level E_2 than at the level of E_1 and therefore $N_1 < N_2$. The case of $N_1 > N_2$ is called *population inversion* and is one prerequisite for lasing. A schematic of a population inversion and the principle of light amplification via stimulated emission is shown in Figure 2.2. As shown in [37], population inversion can not be achieved in an equilibrium. Thus the system needs to be pumped with energy from outside of the system. This pumping can be realized optically by photons of the energy $E_{21} = h\nu$. One big advantage of semiconductor lasers is the ability to use electrical pumping that allows a very small device footprint on the order of micrometers. Then the population inversion can be realized by forward biasing a pn-junction laser diode structure. The basic operation principles of semiconductor laser diodes is discussed in the following Section.

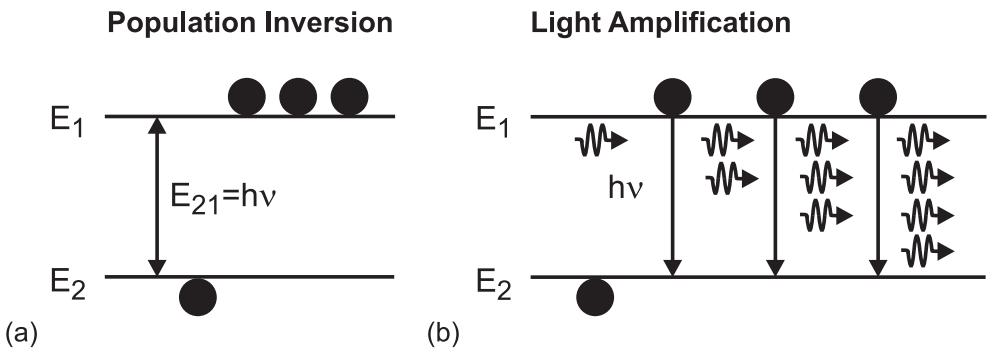

Figure 2.2.: (a) In a population inversion, more electrons are in the energy-level E_1 than in the energy-level E_2, thus $N_1 > N_2$. (b) An incident photon of the energy $h\nu$ enables light amplification by stimulated emission.

2.1.3. Population inversion in semiconductor laser diodes

Semiconductor lasers are a key enabling technology for many applications that impact our daily life. A detailed review of the development of semiconductor lasers can be found in Ref. [38]. In semiconductor lasers the population inversion is more complex than explained in the previous Section. In principle the upper and lower energy levels E_1 and E_2 are the lowest conduction and and highest valence bands of the semiconductor material that serves as the active material. Thus in a semiconductor laser diode E_1 and E_2 can then be named as E_{CB} and E_{VB}, respectively. At room temperature or elevated ambient temperatures not all electrons are in the lowest energy levels and the closely spaced energy levels form a continuum of energy levels called an energy band. In a bulk 3D semiconductor interband transitions from upper band to lower band energy levels must also be considered. Thus energy bands exist in bulk semiconductors and not single discrete energy levels, and as a result a range of energy transitions corresponding to different absorption and emission energies are possible.

The energy-difference of the lowest conduction band and the highest valence band is the band gap energy E_g. Thus the energy $E_{21} = h\nu$ must be E_g and the wavelength of the stimulated emission is determined by the E_g of the active semiconductor material.

An electron-hole pair, instead of a single electron, interacts in a semiconductor laser with the photon(s). Thus in a semiconductor laser the stimulated emission rate R_{st} is not only proportional to the probability (f_1) of electrons in the conduction band, but also to the probability of unoccupied states in the valence band ($1 - f_2$), the probability of existing holes. In other words an electron and a corresponding hole have to exist in order to enable stimulated emission. The same is true for spontaneous emission. For the absorption of a photon with an energy of $h\nu = E_g$ empty states at the energy level E_1 have to exist, which is given by $(1 - f_1)$. Thus the rates of the spontaneous emission,

absorption, and stimulated emission in a semiconductor material change to:

$$R_{sp} = A_{sp} \cdot f_1(1 - f_2), \tag{2.7}$$
$$R_{abs} = B \cdot f_2(1 - f_1) \cdot \Phi, \tag{2.8}$$
$$R_{st} = B \cdot f_1(1 - f_2) \cdot \Phi. \tag{2.9}$$

The condition for population inversion in a semiconductor material is derived in the same way as previously in the general case and is explained in detail in Refs. [39] and [40]. Using Equation 2.5 and again neglecting spontaneous emission, the expression for the net photon generation rate in the semiconductor is similar to Equation 2.6 derived for the general case:

$$R_{st} - R_{abs} = (f_1 - f_2) \cdot B \cdot \Phi. \tag{2.10}$$

In semiconductor material the occupation probabilities f_1 and f_2 are described using the Fermi-Dirac statistics. Thus f_1 and f_2 become for nondegenerately-doped semiconductors [39]:

$$f_1 = \frac{1}{e^{(E_{CB} - E_{\mathrm{F,CB}})/k_B T} + 1}, \tag{2.11}$$
$$f_2 = \frac{1}{e^{(E_{VB} - E_{\mathrm{F,VB}})/k_B T} + 1} \tag{2.12}$$

where $E_{\mathrm{F,CB}}$ and $E_{\mathrm{F,VB}}$ are the conduction and valence band quasi-Fermi levels, k_B is the Boltzmann constant and T is the temperature. Assuming that the spontaneous emission can be neglected, a net stimulated emission occurs when the stimulated emission rate $\mathrm{R_{st}}$ is larger than the rate $\mathrm{R_{abs}}$ of the absorption. Thus for a net stimulated emission the ratio of $\mathrm{R_{st}}$ to $\mathrm{R_{abs}}$ must be larger than 1:

$$\frac{R_{st}}{R_{abs}} > 1. \tag{2.13}$$

The ratio of $\mathrm{R_{st}}$ and $\mathrm{R_{abs}}$ as given in Equations 2.9 and 2.8 is:

$$\frac{R_{st}}{R_{abs}} = \frac{B \cdot f_1(1 - f_2) \cdot \Phi}{B \cdot f_2(1 - f_1) \cdot \Phi}. \tag{2.14}$$

The Einstein coefficient B and Φ cancel each other out and writing $(E_{CB} - E_{VB})$ as $\mathrm{E_g}$ and $(E_{F,CB} - E_{F,VB})$ as ΔE_F yields:

$$\frac{R_{st}}{R_{abs}} = \frac{f_1(1 - f_2)}{f_2(1 - f_1)} = e^{(\Delta E_F - E_g)/k_B T}. \tag{2.15}$$

Thus the condition 2.13 is true and a net stimulated emission can be achieved when:

$$(\Delta E_F - E_g) > 0 \;\Rightarrow\; \Delta E_F > E_g. \tag{2.16}$$

According to Equation 2.16 the quasi-Fermi level separation must be larger than the bandgap energy E_g. This can be achieved for a doped semiconductor pn-junction diode when a forward voltage is applied. The quasi-Fermi level separation is proportional to the applied forward voltage. Thus there exists a minimum voltage that needs to be applied to create the population inversion that is necessary for net stimulated emission, e.g. net optical gain. This minimum voltage depends on the doping concentration of the semiconductor material and the band gap E_g.

2.1.4. Laser cavity

To increase the stimulated emission rate, mirrors are used to confine the photons in a cavity such that they pass several times through the active region before leaving the laser. High mirror power reflectances eventually lead to high light intensities Φ inside the cavity which according to Equation 2.9 gives rise to the stimulated emission rate R_{st}. Each photon that is created via stimulated emission increases the light intensity Φ.

In general mirror cavities define resonant laser modes via the condition for standing waves. For planar cavities such as a "Fabry-Perot" cavity only those wavelengths can lase which fulfill the following condition for constructive interference:

$$L = \frac{\lambda}{2} m \tag{2.17}$$

where L is the cavity length, e.g. the distance between the two mirrors, and m is an integer. Thus if L is large compared to λ, many laser modes will be allowed. As can also be seen in Equation 2.17 when setting, $m = 1$ the shortest possible cavity length L is half the wavelength. For most lasers, even most semiconductor laser diodes, L is much larger than the wavelength λ leading to hundreds or thousands of possible lasing wavelengths, e.g. longitudinal modes.

Electrically pumped semiconductor laser diodes are the smallest practical lasers. The length of edge emitting laser diodes is on the order of 100s of micrometers. Still this length allows many modes. Since in vertical-cavity surface-emittig lasers the cavity lengths are defined by the epitaxial growth instead of by cleaving waferpieces it is relatively simple to realize lasers with the shortest possible optical cavity length of $L = \lambda/2$. As will be discussed later such a short cavity length has several advantages among which a smaller mode volume is one of the most important, leading to potentially higher modulation bandwidth and more energy-efficient operation. The epitaxial design of 980-nm VCSELs with a short $\lambda/2$-cavity and measurement results of these VCSELs are presented later in this dissertation in Section 6.2 and Chapter 8, respectively.

In a real semiconductor laser diode additional effects such as the nonradiative recombination of electron-hole pairs need to be taken into account. These

effects result from electrons that interact with other electrons or phonons and experience an energy transfer without the creation of photons. The two main nonradiative recombination effects in semiconductor lasers are Auger-effects and recombination at defects, interfaces, and surfaces, and can be represented by a common nonradiative recombination lifetime τ_{nr} and rate $\mathrm{R_{nr}}$. One main prerequisite for minimizing nonradiative recombination is a high crystalline quality with low defect densities. But also the quality of the semiconductor processing can have an impact on $\mathrm{R_{nr}}$, for instance rough semiconductor sidewalls. Because nonradiative recombination is a loss that increases the required minimum pump energy to achieve lasing, $\mathrm{R_{nr}}$ should be as small as possible. The goal of minimizing $\mathrm{R_{nr}}$ is accounted for in the epitaxtial design of the laser and to a great extent is determined by the epitaxial material used in the active region of the laser diode.

Photons that are created via stimulated emission can stimulate the creation of further photons as well as increase the light intensity Φ. Thus the emission of one stimulated photon will eventually result in the stimulated emission of many equal photons. In a real semiconductor the abovementioned losses exist. While stimulated emission (no matter whether population inversion is reached or not) is an optical gain free carrier absorption and optical scattering are potential loss terms. In general the gain and loss is not homogenous in the laser cavity, thus both vary with the position in the cavity. Because light amplification is desired the light intensity Φ should increase with each roundtrip of the photons within the cavity. Assuming that the gain and loss are distributed homogeneously whithin a one-dimensional (1D) cavity the dependence of Φ on the distance z (counted from the position of the initial photon creation) can be expressed as [37, 39]:

$$\Phi(z) \propto e^{(g-\alpha)z} \tag{2.18}$$

where g is the optical gain and α is the optical loss of the cavity. Thus α includes absorption as well as scattering losses, and other losses of the cavity. Considering a complete roundtrip in a cavity between two mirrors with power reflectance values of R_1 and R_2, the intensity Φ has been increased if the following condition is fulfilled [37, 39]:

$$R_1 R_2 e^{(g-\alpha)2L} > 1 \tag{2.19}$$

where L is again the 1D cavity length. After a complete roundtrip $2 \cdot L$ all losses and gains have been experienced twice. At each mirror a fraction (1-R_1) or (1-R_2) of the light is transmitted through the respective mirror, leaves the cavity and thus can also be considered to be a loss that must be compensated by the gain. Thus in order to amplify the light intensity the condition 2.19 can be rewritten in the following form where the gain equals the losses [37, 39]:

$$g_{th} = \alpha + \frac{1}{2L} ln\left(\frac{1}{R_1 R_2}\right) = \alpha + \alpha_m \tag{2.20}$$

where g_{th} is the threshold gain for lasing and α_m is the mirror loss. In case the gain inside the cavity is smaller than g_{th} no lasing can be achieved. In order to achieve lasing a maximum allowed mirror loss α_m is given by Equation 2.20 leading to minimal required values of R_1 and R_2, respectively.

In general semiconductor lasers do not always have gain along the entire cavity length, e.g. the light travels in regions inside the cavity where it may experience losses but not gain. Typically edge-emitting laser diodes have gain in larger fractions of the cavity length L. While in edge-emitting semiconductor lasers the light travels in parallel to the active layers with gain, the light propagates perpendicular to these layers in VCSELs. Thus while edge-emitting laser diode designs exist where the light can experience gain in the complete length L of the cavity, this is not possible for VCSELs. Therefore VCSELs have typically a much shorter gain length as compared to edge-emitting laser diodes. The gain length in VCSELs is simply the accumulated thickness of the quantum wells (QWs). As is shown in Chapter 6.2 the accumulated thickness of five QWs of the 980-nm VCSELs presented in this dissertation is 20 nm. For simple edge-emitting semiconductor lasers the gain length can be as long as the cavity and is thus on the order of several 100s of µm. Due to the very short gain length in VCSELs its mirror loss has to be very small in order to achieve lasing. Thus the power reflectance of a simple semiconductor/air interface of ~30% is by far not large enough for VCSELs which require mirrors with a power reflectance approaching 100%. Such high power reflectances can be achieved with distributed Bragg reflectors (DBRs) as explained in the next Section.

2.2. Confinement of light and current in VCSELs

The present state-of-the-art VCSEL designs incorporate many different design features in order to enable error-free operation at large bit rates. Two of the most important *building blocks* that are used by the presently fastest and most efficient VCSELs are all semiconductor distributed Bragg reflectors (DBRs) that confine the light in the longitudinal direction and oxide-apertures for transverse optical and current confinement. Although there exists a great degree of freedom in designing different DBRs and oxide-apertures, the basic principle and functionality of these two important VCSEL building blocks remain the same and are explained in the following Sections.

2.2.1. Distributed Bragg reflectors

Due to the small length of material with gain inside the cavity of typically only tens of nanometers, the mirror loss α_m has to be very small for VCSELs in order to reach threshold gain g_{th} as given by Equation 2.20. This is usually realized by using distributed Bragg reflectors (DBRs) which can easily achieve power reflectance values close to 100%.

In present VCSELs typically semiconductor and dielectric DBRs are used for confining the light in the longitudinal direction. These mirrors can be modified in different ways by using extra layers, varying the layer thicknesses or material compositions, or etching parts of the layers and thus creating symmetric or nonsymmetric lateral patterns such as for example rings, circles [41, 42, 43, 44], or photonic crystals. High-contrast gratings (HCGs) [45, 46, 47] can theoretically completely or partly replace DBRs, but to date the dynamic performance of HCG VCSELs is not comparable to that of modern VCSELs with semiconductor DBR mirrors. Also the processing of HCGs is very challenging and requires electron beam lithography and an extremely good control of all process parameters. Thus wafer-scale fabrication of thousands or millions of HCG VCSELs with is neither practical nor cost-efficient. Therefore epitaxially-grown high crystalline quality semiconductor DBRs remain the preferred choice for cost-efficient large wafer-scale VCSEL fabrication.

DBR mirrors are based on the fundamental principal of reflection and transmission of light at interfaces of two different materials having two different refractive indices. At any interface part of the light is transmitted and part of it is reflected. In the following analysis absorption of light and scattering losses are neglected, thus the intensity Φ of the transmitted and of the reflected light add up to the initial intensity of the incident light. Then the fraction of the reflected light is given by the power reflectance R (a value between 0 and 1) and the fraction of the transmitted light is given by the transmittance T=(1-R). If n_0 is the real refractive index of the first material and n_1 the real refractive material of the second material, then the reflectance for normal incidence as shown in Figure 2.3 (a) is given by:

$$R_0 = \left(\frac{n_0 - n_1}{n_0 + n_1}\right)^2. \tag{2.21}$$

Adding a third material significantly increases the complexity of reflection and transmission of the light, because multiple transmitted and reflected light rays exist. Incident light of the intensity Φ gets reflected at the interface of the materials with refractive indices n_0 and n_1. Light with the intensity of $R_0 \cdot \Phi$ is reflected and the fraction $T_0 \cdot \Phi$ is transmitted and hits the second interface of the materials characterized by the refractive indices n_1 and n_2, respectively. Again reflection and transmission occur. The transmittance is T_1, thus the transmitted intensity is $T_1 \cdot T_0 \cdot \Phi$. The reflected intensity is $R_1 \cdot T_0 \cdot \Phi$ and experiences transmission and reflection at the interface between the materials with refractive indices n_1 and n_0, respectively. The intensity $\Phi \cdot T_0 \cdot R_1 \cdot T_1'$ is transmitted to the material with the refractive index n_0 and can now interfere with the first reflected light. The different reflected and transmitted light intensities in a system with three layers of different refractive index is schematically shown for normal incidence in Figure 2.3 (b).

Multiple reflections occur in a multilayer system as shown in Figure 2.3 (b), and thus a large number of light rays exist that all interfere with each

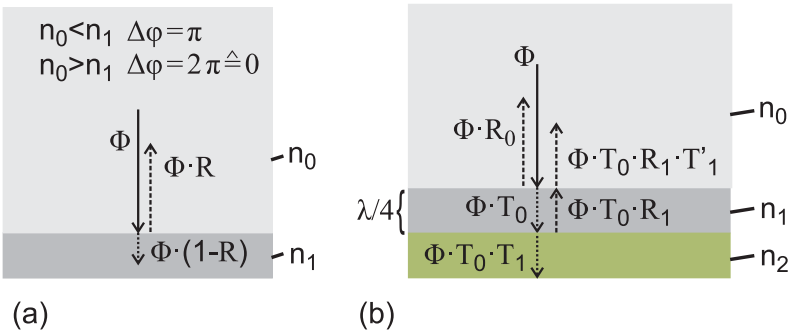

Figure 2.3.: (a) Reflection and transmission of the light intensity Φ at the interface of two materials with different real refractive indices n_0 and n_1 for normal incidence. (b) Reflection and transmission for light intensity at a three-layer system for normal incidence. Not all possible light rays are shown.

other. In general the interference will increase or decrease the intensity of the resulting light ray, depending on the phase values of the interfering rays. The two extreme cases are constructive and destructive interference, where the light intensities add up, or the light intensity becomes 0. Constructive interference occurs between two rays when their phase difference $\Delta\varphi$ is 0 (or 2π) and destructive interference occurs for a phase difference of π. Two different effects lead to a phase-change $\Delta\varphi$. The phase-change $\Delta\varphi$ due to propagation along the geometric distance d of light with the wavelength λ through a medium with the real refractive index n is:

$$\Delta\varphi = \frac{2\pi}{\lambda} d \cdot n. \tag{2.22}$$

The product $d \cdot n$ of the geometrical distance d and the real refractive index n is called the *optical thickness*. For a phase-change of 2π, equivalent to 0, thus no change of the phase, the optical thickness must equal the wavelength λ. For an optical thickness of $\lambda/2$ the phase difference $\Delta\varphi$ becomes π. The phase of the light can also experience a change when it is reflected at an interface of materials with two different refractive indices as depicted in Figure 2.3 (a). When the incident light gets reflected at the interface of the two materials with refractive indices of n_0 and n_1 a phase shift of π occurs when $n_0 < n_1$ and there is no phase shift for $n_0 > n_1$. Taking into account the two effects causing the phase of the light to shift, one can derive the conditions for constructive and destructive interference of the reflection at an optically-thick $\lambda/4$ layer depicted in Figure 2.3 (b). Two reflections at different interfaces resulting in two different reflected beams need to be considered. Because the layer with the refractive index of n_1 has an optical thickness of $\lambda/4$, the phase change of the beam that is reflected at the second interface between materials with refractive indices of n_1 and n_2 experiences a phase shift of π for propagating through the $\lambda/4$-layer twice. Thus for $n_0 > n_1 > n_2$ the phase difference

of the two beams will be π leading to destructive interference. The case of $n_0 < n_1 < n_2$ leads to destructive interference as well, because both reflected beams experience a phase shift of π due to the reflection. The phase-shift of π caused by the round trip through the $\lambda/4$-thick layer has to be added to the second beam, resulting in a phase difference $\Delta\varphi = \pi$ between the two beams. In case the refractive index of the $\lambda/4$-layer is larger than those of the other two layers, a phase change of π occurs at the first reflection at the interface of the first medium and the $\lambda/4$-layer and the light that is reflected at the second interface of the materials with n_1 and n_2 experiences a phase change of π for propagating through the $\lambda/4$-layer. Thus the resulting phase difference is $\Delta\varphi = 2\pi = 0$. If the refractive index of the $\lambda/4$-layer is smaller than the other two, there will be a phase change of π due to reflection at the interface n_1/n_2 and in addition there is the same phase change due to propagating the optical distance of $\lambda/2$. Thus the resulting phase difference $\Delta\varphi$ will be 0 leading to constructive interference. The resulting phase differences $\Delta\varphi$ for the four different combinations of the n_0, n_1, and n_2 values are shown in Figure 2.4 (a)-(d).

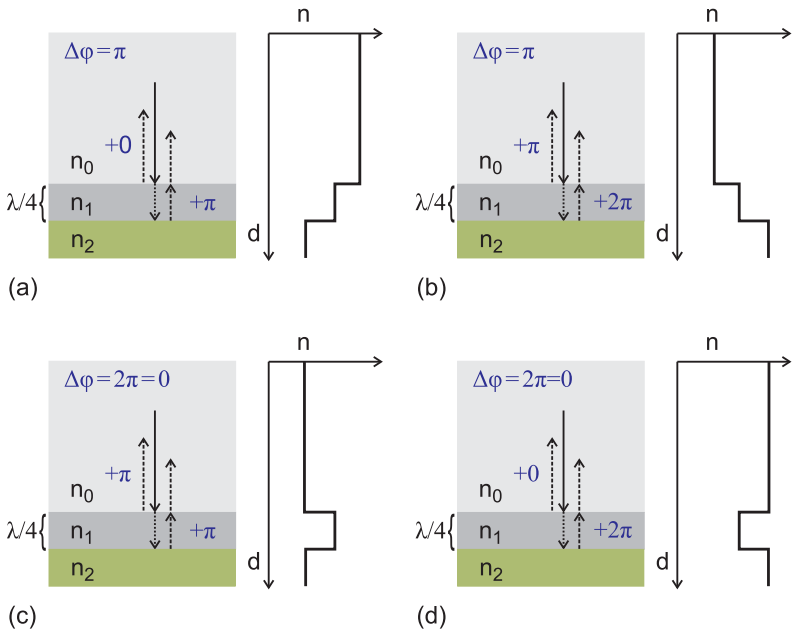

Figure 2.4.: Phase difference $\Delta\varphi$ between incident and reflected light for reflection at a $\lambda/4$-layer and different combinations of the refractive indices n_0, n_1, and n_2. In the case of (a) $n_0 > n_1 > n_2$ and (b) $n_0 < n_1 < n_2$, the resulting phase difference caused by propagation and reflection is π leading to destructive interference. For (c) $n_1 > n_0, n_2$ and (d) $n_1 < n_0, n_2$ the phase difference $\Delta\varphi$ is 2π which is equivalent to zero and thus the light will experience constructive interference.

The simplest DBR consists of a stack of alternating layers of two different materials with different real refractive indices n_1 and n_2. Thus relative to

each other one material has a higher refractive index and the other has a lower refractive index. The difference between these two refractive indices is the refractive index contrast Δn. In most cases it is desirable to have a large refractive index contrast Δn in case this does not cause other drawbacks such as an increased electrical resistance or a low heat conductance. The optical thickness of each layer is $n \cdot d = \lambda_0/4$, where n is the real refractive index, d the geometric layer thickness, and λ_0 is the wavelength in freespace or vacuum. Because the refractive index varies with the wavelength λ_0, the mirror layer has an optical thickness $\lambda/4$ for only one design target wavelength λ_0. In the following examples absorption and other losses such as scattering are neglected and all calculations are performed for the case of normal incidence.

A schematic of a simple DBR with eight DBR pairs of materials with real refractive index values of n_1 and n_2 placed onto a substrate taken to be infinitely thick with a real refractive index of n_{sub} is shown in Figure 2.5 (a). The incident medium above the DBR mirror is assumed to be air taken to be infinitely thick with a real refractive index of $n_{air} = 1$. More complex DBR structures can exist of more than two different materials as indicated in Figure 2.5 (b) showing an example with six different materials all having an optical thickness of $\lambda/4$. In general a DBR can also contain layers with an optical thickness that is different from $\lambda/4$. For example optically inactive layers with an optical thickness that is an integer multiple of $\lambda/2$ can be inserted into any DBR mirror without changing the power reflectance at the design wavelength λ_0 of the DBR as shown in Figure 2.5 (c). Assuming that no losses like absorption occur in the optically inactive additional $\lambda/2$-thick ("absentee") layer the power reflectance at the design wavelength λ_0 of the structures shown in 2.5 (a) and (c) is therefore the same. The top and bottom DBRs of the 980-nm VCSEL designs presented in this dissertation employ optically inactive GaAs-layers in order to facilitate current spreading and heat dissipation as discussed in Section 6.2.

For simple DBR structures as shown in Figure 2.5 (a) consisting only of alternating $\lambda/4$ layers the power reflectance value at normal incidence for the Bragg design wavelength can easily be calculated using the following equations. The power reflectance R_{2N} of a simple DBR for alternating $\lambda/4$ layers with the refractive indices n_1 and n_2 placed onto a substrate with the refractive index n_{sub} and having air on the other side of the DBR is given for normal incidence by the following equation for an even number 2N of DBR pairs:

$$R_{2N} = \left| \frac{n_{sub} \left(n_2/n_1\right)^{(2N)} - 1}{n_{sub} \left(n_2/n_1\right)^{(2N)} + 1} \right|^2 \tag{2.23}$$

where N is the integer number of DBR pairs (periods). For an uneven

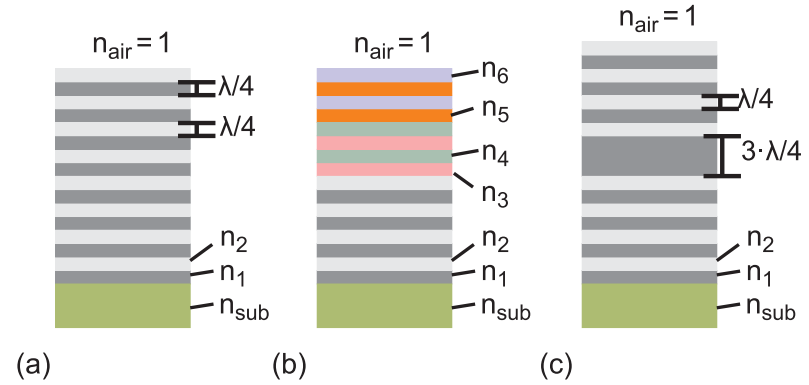

Figure 2.5.: Schematics of distributed Bragg reflector (DBR) structures placed onto a substrate and having air on the top. (a) All DBR mirror pairs are the same, (b) more than two different refractive indices are used in the DBR stack, and (c) one additional $\lambda/2$-thick optically inactive layer is inserted.

number (2N+1) of DBR pairs the reflectivity $|r_{2N+1}|^2$ is given by:

$$R_{2N+1} = \left| \frac{{n_1}^2 \left(n_1/n_2\right)^{(2N)} - n_{sub}}{{n_1}^2 \left(n_1/n_2\right)^{(2N)} + n_{sub}} \right|^2 . \tag{2.24}$$

For more general and complex DBR structures or complete VCSEL designs the power reflectance values and spectra and electric field intensity profiles are calculated using the software POLYMORPH [48]. All of the following DBR examples are designed for a wavelength of 980-nm. The refractive index profile and the electric field intensity of the simple DBR structure of Figure 2.5 (a) are plotted in Figure 2.6. The plotted real refractive indices of n_{sub} and n_2 correspond to GaAs and n_1 corresponds to AlAs, all at a wavelength of 980-nm. The electric field intensity is calculated for incident light from the GaAs-substrate. The amplitude of the electric field intensity slowly decays in the 8 DBR pairs having a local maximum at each interface between the high refractive index GaAs and the low refractive index AlAs. A certain amplitude of the electric-field intensity leaves the mirror on the right side into the air with a refractive index of 1. The power reflectance R at 980-nm calculated with POLYMORPH is 94.51% (R = 0.9451).

The electric field intensity profile in the DBR structure shown in Figure 2.5 (b) looks similar to that of the structure in Figure 2.5 (a). In contrast to the DBR stack in Figure 2.6, the first top DBR pairs have been replaced with DBR pairs with a smaller refractive index contrast Δn as compared to the first case where binary AlAs/GaAs-DBR pairs are used. As an example the top two DBR pairs are formed by $Al_{0.8}Ga_{0.2}As/Al_{0.2}Ga_{0.8}As$ and the third and fourth DBR pairs are formed by $Al_{0.9}Ga_{0.1}As/Al_{0.1}Ga_{0.9}As$. Thus the refractive index contrast Δn differs for different pairs of the DBR as do the geometric layer thicknesses in order to keep the optical thicknesses equal to $\lambda/4$. The

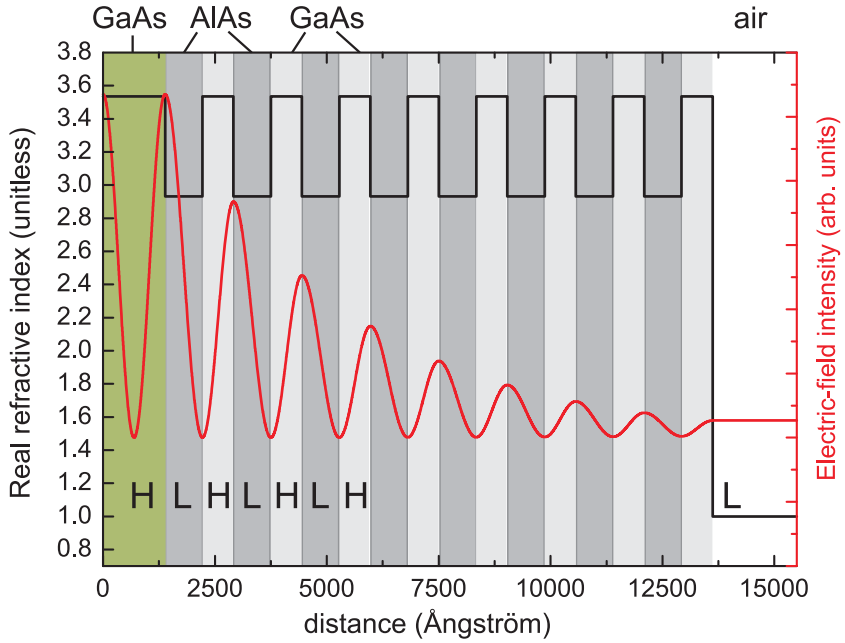

Figure 2.6.: Real refractive index and the electric field intensity profile for an 8-period distributed Bragg reflector (DBR) with eight equal DBR pairs. The substrate has the same real refractive index as the high refractive index layers of the DBR. H and L indicate the relative high and low real refractive index layers of the DBR. Light is incident from the GaAs substrate to the right toward air.

refractive index contrast Δn is 0.6 for the first four binary AlAs/GaAs mirrors counted from the GaAs-substrate and reduces to 0.46 and 0.33 for the following ternary $Al_xGa_{1-x}As$-DBR pairs. In the second example DBR in Figure 2.7 the difference of the electric field intensity as compared to the all binary DBR seems not to be very large. The second DBR with the same number of DBR pairs but with 4 DBR pairs with smaller Δn has a smaller power reflectance of 90.94% (R = 0.9094) at 980-nm. The electric field intensity and the refractive index profile of the DBR structure with varying refractive index constrast is shown in Figure 2.7.

The third example DBR is a purely binary layer DBR where the high refractive index layer of the fourth DBR period has an optical thickness of $(3\lambda)/4$ instead of $\lambda/4$. The additional $\lambda/2$ layer of GaAs is optically inactive with respect to the power reflectance at the design wavelength of the DBR, thus the relative maximum amplitude of the electric field intensity does not change within the $\lambda/2$-thick layer leading to a second peak of the exact same amplitude. Each layer with an optical thickness of an integer multiple of $\lambda/2$ is optically inactive (if absorption is zero) and adds additional electric field intensity peaks. Thus a layer with the thickness of $d = n \cdot \lambda/2$ will have n additional peaks of the electric field intensity, all of the same amplitude. The

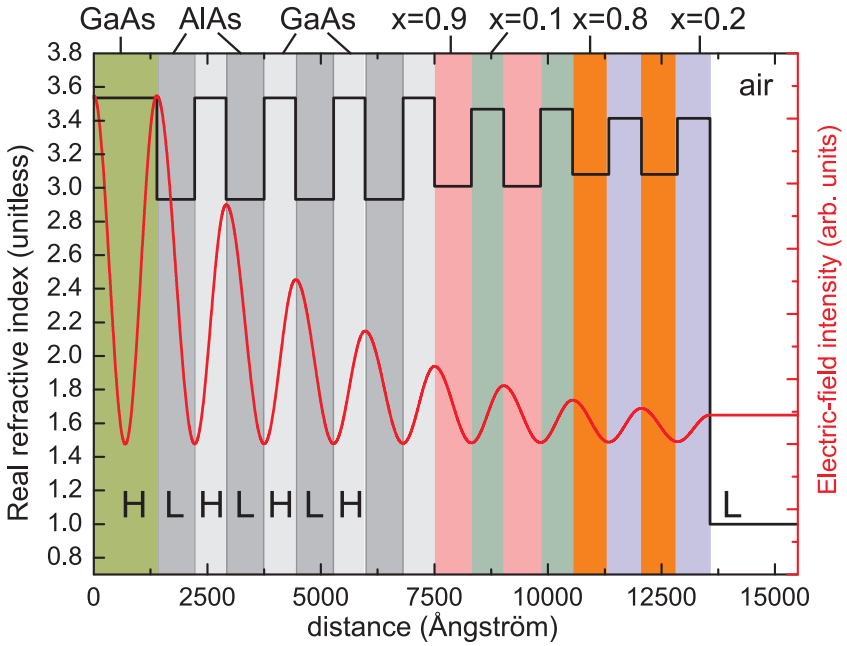

Figure 2.7.: Real refractive index and the electric field intensity profile for a distributed Bragg reflector (DBR) with eight DBR pairs. The substrate has the same real refractive index as the high refractive index layers of the DBR. The first four DBR pairs are the same as in Figure 2.6, followed twice by 2 periods with decreasing refractive index contrast. H and L indicate the relative high and low real refractive index layers of the DBR.

electric field intensity and the refractive index profile of the DBR structure with an inserted extra $\lambda/2$-thick GaAs-layer are shown in Figure 2.8.

At the design wavelength λ_0 of 980-nm both binary DBR mirrors with and without the extra $\lambda/2$-layer yield the same phase and power reflectance. The more the wavelength deviates from the design wavelength the extra layer becomes a larger deviation from the periodicity as compared to the DBR without the extra $\lambda/2$ layer, resulting in a decrease of the power reflectance. For application in VCSELs it is desired that the DBR functions as a high reflectance mirror in a broader range of wavelengths, thus the power reflectance versus the wavelength is of importance. The width of the DBR stop band can be used to compare DBR power reflectance spectra. The stop band width is defined as the width between the two wavelengths at which the DBR power reflectance has dropped to 90%. Of the three presented 8-period DBRs, the all binary DBR with all layers having an optical thickness of $\lambda/4$ achieves the broadest band width of 88 nm which reduces to 75 and 35 nm for the DBR with an extra $\lambda/2$ layer and for the DBR with the variation in the refractive index contrast, respectively. Due to the lower average refractive index contrast of the DBR with different Δn but the same number of periods also the maximum

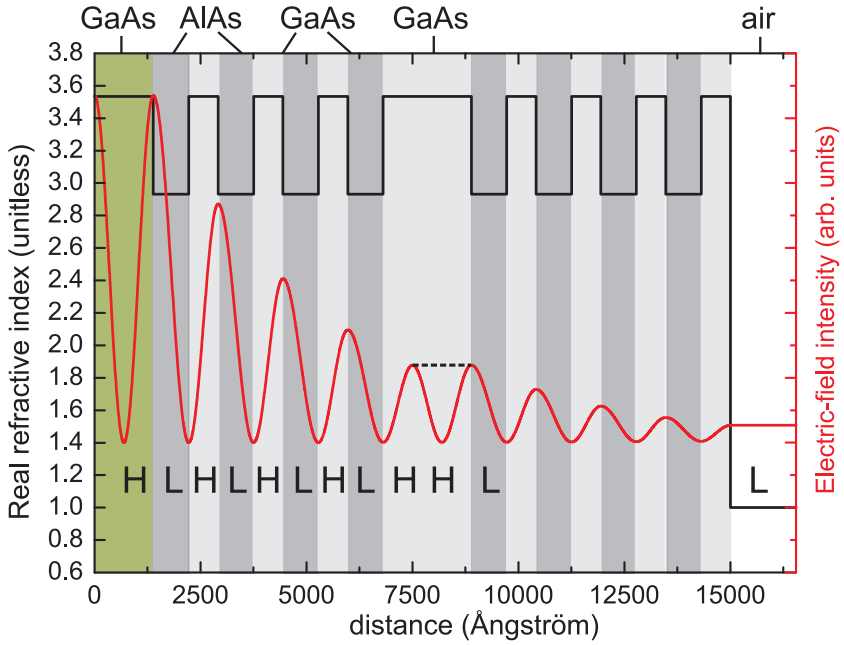

Figure 2.8.: Real refractive index and the electric field intensity profile for a distributed Bragg reflector (DBR) with eight DBR pairs. The substrate has the same real refractive index as the high refractive index layers of the DBR. The optical thickness of the high refractive index layer of the fourth DBR pair is $\lambda/2$ thicker than $\lambda/4$. H and L indicate the relative high and low real refractive index layers of the DBR.

power reflectance at the design wavelength is lower than that of the two different AlAs/GaAs-DBRs. Because the mean refractive index contrast at the design wavelength remains unchanged when introducing an extra $\lambda/2$-layer the power reflectance at this wavelength also does not change. For the other wavelengths this extra layer is not of the optical thickness of $\lambda/2$ and thus further reduces the reflectance for these wavelength. As a consequence the width of the DBR stop band reduces when inserting an extra $\lambda/2$-layer. The calculated reflectance spectra of the three different 8-period DBR mirrors are shown in Figure 2.9.

Extra $\lambda/2$-layers or layers with an optical thickness of an integer multiple of $\lambda/2$ can serve various purposes and are often used as contact layers in VCSELs with intra-cavity or intra-DBR contacts [26]. Parts of these layers will then be highly doped to facilitate lateral current transport. In order to avoid absorption the high doping concentrations will be positioned at the antinodes, e.g. at the minima, of the electric field intensity. Thus $n \cdot \lambda/2$-thick layers (n = 1,2,3,...) allow us to add more highly doped material into the DBR without affecting the power reflectance at the design wavelength λ_0. These added absentee layers may also be used to facilitate current spreading inside the DBRs in VCSELs where the current is injected from contact layers below

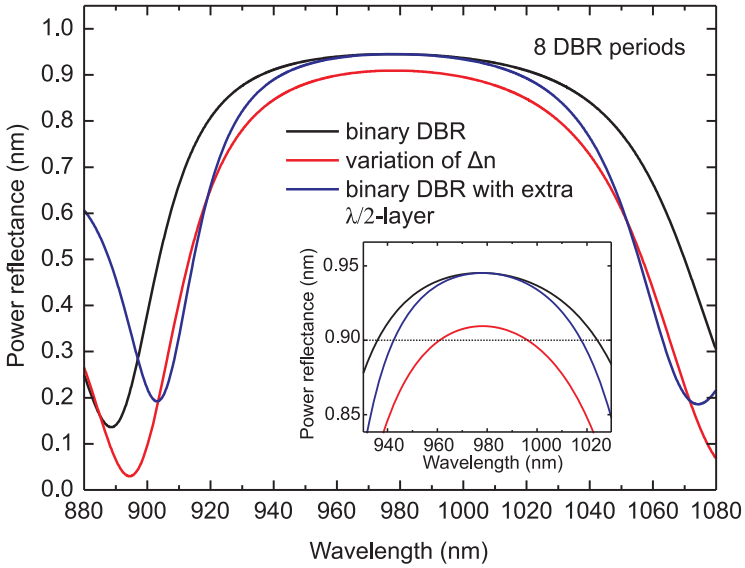

Figure 2.9.: Calculated power reflectance versus wavelength at normal incidence for three $Al_xGa_{1-x}As$-DBR structures with 8 periods. The inset shows a zoomed-in plot of the spectra demonstrating the different widths of the stop band of the DBR with a design wavelength of 980-nm.

and above the bottom and top DBR, respectively.

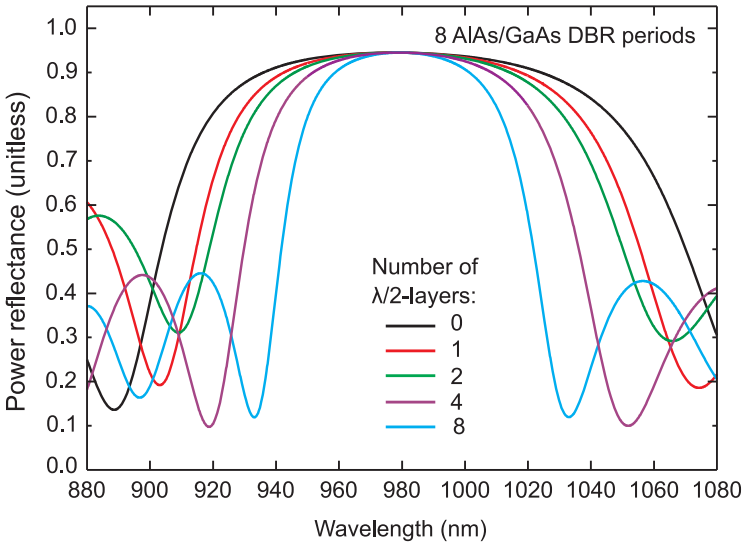

Figure 2.10.: Calculated power reflectance versus wavelength at normal incidence for binary AlAs/GaAs DBRs with 8 periods and 0, 1, 2, 4, and 8 additional $\lambda/2$ GaAs-layers with a design wavelength of 980-nm.

The stop band width of the DBR decreases with increasing number of inserted $\lambda/2$-layers. For the given binary AlAs/GaAs example DBR with 8

periods in Figure 2.6, the width of the stop band is 88 nm without any additional $\lambda/2$-layers and decreases to 75, 68, 57, and 43 nm for 1, 2, 4, and 8 inserted $\lambda/2$-layers, respectively, where each single additional $\lambda/2$-layer is added to separate high refractive index GaAs-layers. In the last case of 8 extra $\lambda/2$-layers each high refractive index layer of the DBR has an extra $\lambda/2$ of GaAs. The calculated power reflectance spectra for binary AlAs/GaAs-DBRs with different numbers of $\lambda/2$-layers and a design wavelength of 980-nm are plotted in Figure 2.10.

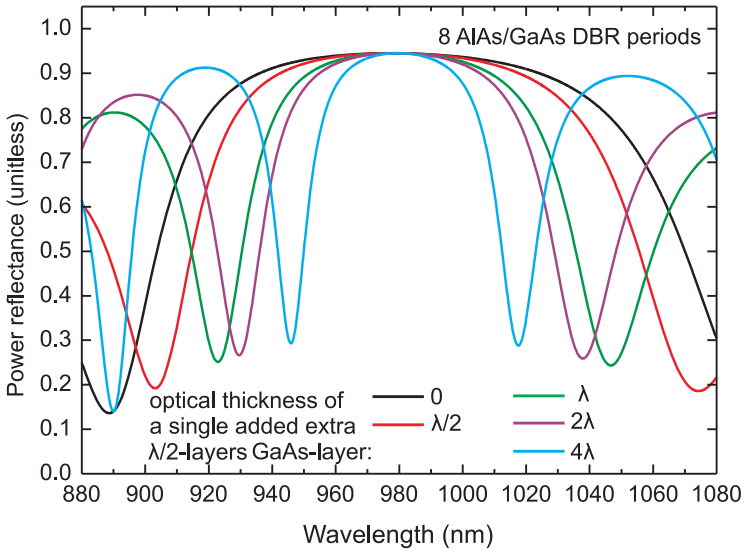

Figure 2.11.: Calculated power reflectance versus wavelength for binary AlAs/GaAs DBRs with 8 periods with and one without an added GaAs layer with an optical thickness of $\lambda/2$, λ, 2λ, and 4λ.

Instead of inserting separate $\lambda/2$-layers to several separate DBR pairs, one can also add layers that have an optical thickness of an integer multiple of $\lambda/2$ to a single DBR pair. This also changes the power reflectance spectra. Compared to DBRs where single $\lambda/2$ layers are added to separate DBR pairs, adding a single layer of the same accumulative optical thickness of the individual $\lambda/2$-layers, leads to different power reflectance spectra. The power reflectance remains unaffected at the Bragg design wavelength, but the width of the stop band reduces with increasing optical thickness and the maximum power reflectance of the sidelobes of the DBR significantly increase with increasing optical thickness of the added layers. Thus while having the same optical thickness at the design wavelength the impact on the power reflectance spectra of the DBRs is different for adding several separate $\lambda/2$-layers or one thick layer with the same accumulative optical thickness. As previously stated the width of the stop band is 88 and 75 nm without and with a single $\lambda/2$-layer. It further reduces to 65, 51, and 35 nm for an optical thickness of λ, 2λ, and 4λ, respectively. In the case of the 4λ optically thick additional GaAs-layer, one

sidelobe of the DBR reaches a maximum power reflectance value of 91.28% at a wavelength of 919 nm. This sidelobe was not included in the determination of the stop band width. The power reflectance spectra for AlAs/GaAs DBRs with 8 periods without extra $\lambda/2$-layer and with extra layers of the optical thickness of $\lambda/2$, λ, 2λ, and 4λ are shown in Figure 2.11.

Due to the periodic nature of the DBR mirrors large power reflectance values can be achieved by simply increasing the number of DBR pairs. For an infinite number of DBR pairs the power reflectance at the Bragg wavelength λ_0 approaches 100%. The required number of DBR pairs in order to achieve a given reflectance value at λ_0 decreases with increasing refractive index contrast of the two materials used for the $\lambda/4$-layers. The $Al_xGa_{1-x}As$ material system is well-suited and widely used for VCSELs emitting at 850 and 980-nm. The maximum refractive index contrast Δn in the $Al_xGa_{1-x}As$-system is achieved for mirrors consisting of binary AlAs/GaAs-DBR pairs and is Δn =0.60 at a wavelength of 980-nm. Although the DBR layers of a given design will be only for one wavelength of the exact optical thickness of $\lambda/4$, the resulting reflectance spectrum shows a broader so-called stop band providing high values of power reflectance for wavelengths shorter and longer than the design wavelength λ_0 of the DBR. The power reflectance versus the wavelength for binary AlAs/GaAs-DBRs with 5.5, 10.5, and 20.5 DBR pairs is shown in Figure 2.12. The maximum power reflectance value increases with increasing number of DBR pairs and a flat stop band is formed when the number of DBR pairs is large (more than ~20 periods). The stop band with a maximum power reflectance given as a percentage of 99.94% and a stop band width of 113 nm can clearly be seen for the mirror with 20.5 DBR pairs. The width of the stop band is determined at the distance between the two wavelengths at which the power reflectance reaches 90% as done previously for the DBR examples with 8 mirror pairs. The calculated power reflectance values given as a percentage at 980-nm are 97.57% and 85.19% for the DBRs with 10.5 and 5.5 DBR pairs, respectively. The width of the stop band is 107 nm for the DBR with 10.5 DBR pairs and is not given for the mirror with only 5.5 pairs, because this DBR does not achieve reflectance values of 90%.

In a VCSEL both mirrors typically have to achieve power reflectance values close to 100% to enable lasing. At 980-nm a DBR consisting of 25.5 pairs of binary AlAs/GaAs $\lambda/4$ pairs achieves a calculated power reflectance of 99.99% with a stop band width of 112 nm. By adding more DBR pairs the power reflectance can not significantly increased anymore, because the limit of 100% can only be theoretically achieved by an infinite number of DBR pairs. Thus one simply adds more 9s behind the comma of the power reflectance by further adding DBR pairs. The power reflectance and the reflectivity phase of a DBR with 25.5 AlAs/GaAs $\lambda/4$ pairs and a design wavelength λ_0 of 980-nm are plotted versus the wavelength in Figure 2.13.

The saturation behavior of the power reflectance of a DBR can be shown by removing material from the top of the DBR, modeling the power reflectance

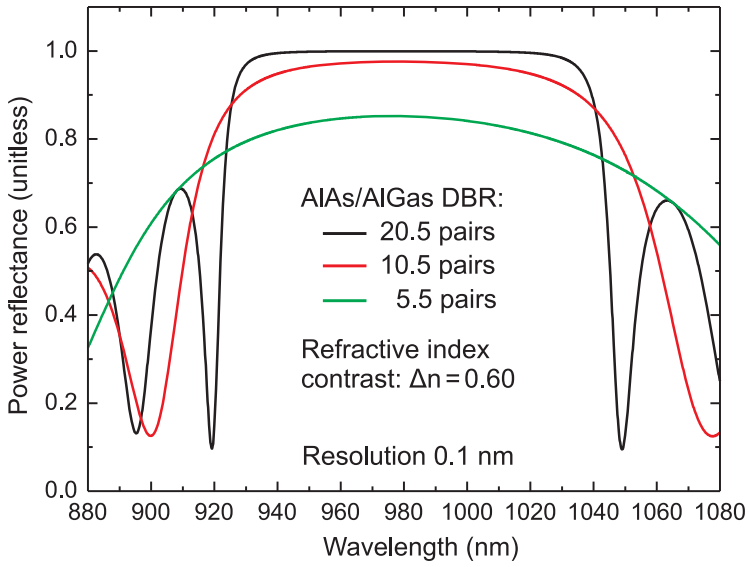

Figure 2.12.: Calculated power reflectance versus wavelength at normal incidence for three binary AlAs/GaAs-DBR structures on a GaAs substrate with with 5.5, 10.5, and 20.5 DBR periods and with air as the incident medium.

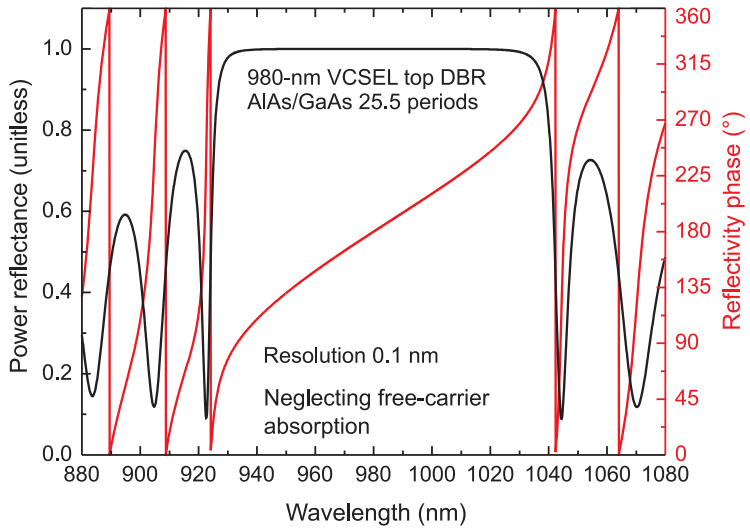

Figure 2.13.: Calculated power reflectance and reflectivity phase spectrum for an AlAs/GaAs DBR on a GaAs substrate with 25.5 mirror pairs and with air as the incident medium.

R and plotting R versus the thickness of the removed material or equivalently versus the etch depth from the top DBR surface. The power reflectance versus etch-depth shows an oscillating behavior and reaches local maxima when a complete DBR period is removed and local minima when a $\lambda/4$ layer is com-

pletely removed as shown in Figure 2.14. The difference of two neighbor local maxima increases with increasing etch-depth. This is equivalent to the fast increase in power reflectance when DBR pairs are added to a DBR with a low number of periods and the saturation of the power reflectance once the power reflectance reaches values above approximately 90% (R = 0.90).

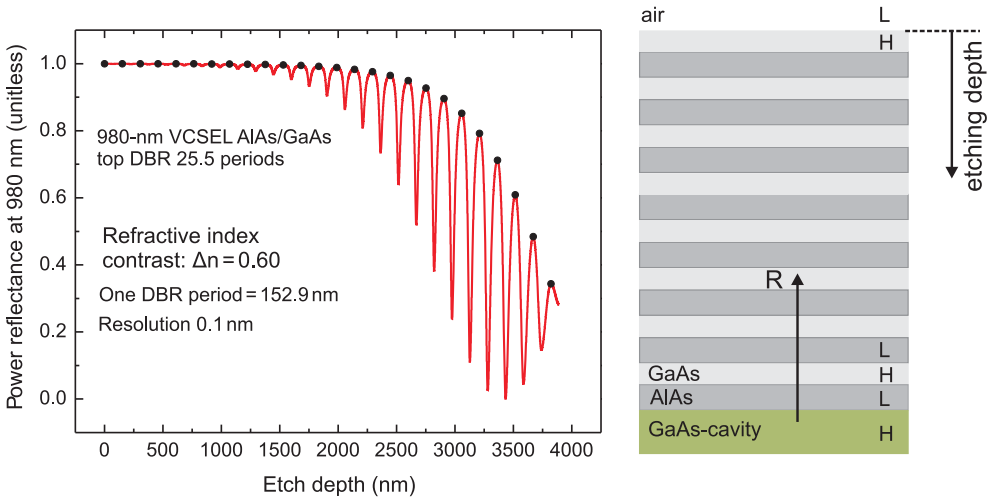

Figure 2.14.: Calculated power reflectance R normal incidence at 980-nm versus the etch depth of an AlAs-DBR with 25.5 mirror pairs. The R is as seen by photons in the cavity looking up through the DBR toward air.

The power reflectance of the DBR stop band increases with the refractive index contrast Δn and with the number of the DBR pairs. For a larger Δn the power reflectance increases faster with increasing number of periods. The power reflectance at the design wavelength is plotted for different refractive index contrasts Δn of 0.60, 0.46, and 0.33 versus the number of DBR pairs in Figure 2.15 and the power reflectance for 25.5 DBR pairs of the given Δn values is plotted versus the wavelength in Figure 2.16. For 25.5 DBR pairs the maximum power reflectance at the design wavelength of 980-nm is 99.99, 99.91, and 99.34% and the width of the stop band is 112, 75, and 63 nm for a refractive index contrast of 0.60, 0.46, and 0.33, respectively.

So far only single DBRs have been considered. In order to build a cavity two DBRs are required, one on each side of the active optical cavity region that contains the gain material. The shortest possible cavity-length has an optical thickness of $\lambda/2$. The 980-nm VCSEL design that is presented in this dissertation in Chapter 6 has a short $\lambda/2$-cavity to improve the dynamic properties of the VCSEL. Although in real VCSEL structures the active region in between the DBRs typically consists of different material compositions including the quantum wells or quantum dots, barrier layers, compositionally-graded or abrupt separate confinement heterostructure layers, etc., an average real refractive index can be determined that represents the materials in the

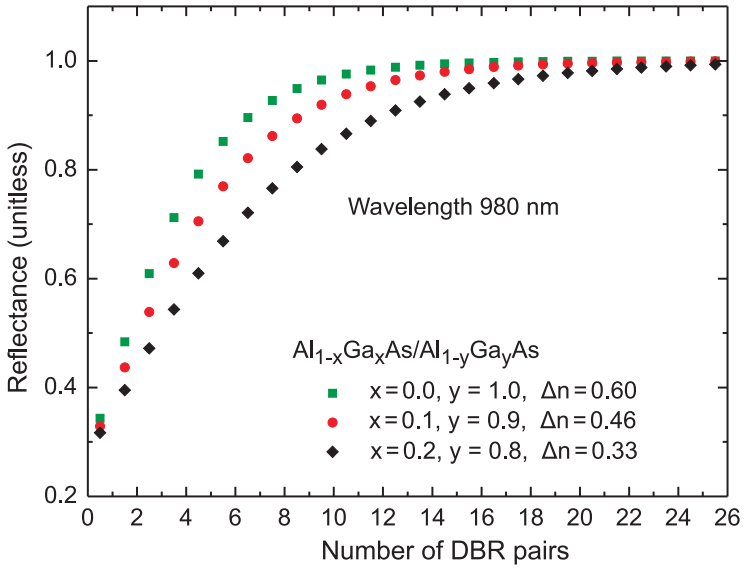

Figure 2.15.: Calculated power reflectance R at normal incidence versus the number of distributed Bragg reflector pairs for $Al_xGa_{1-x}As$-DBRs with different refractive index contrasts Δn.

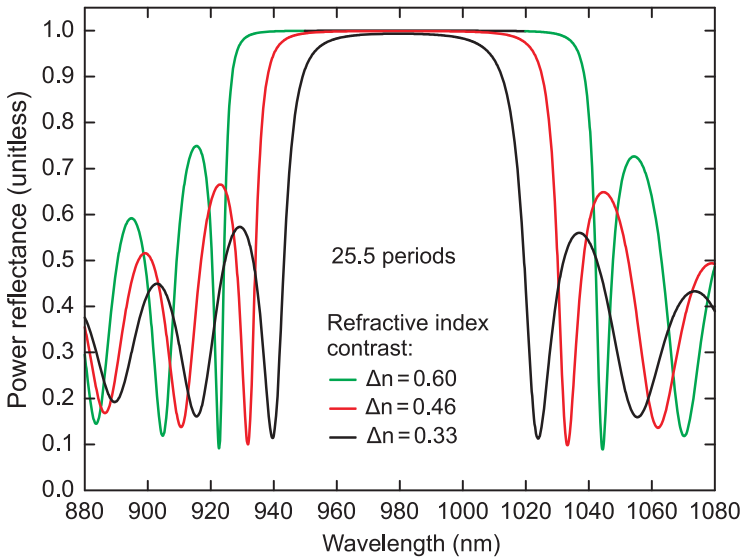

Figure 2.16.: Calculated power reflectance R at normal incidence from air as the incident medium versus the wavelength of 25.5 $Al_xGa_{1-x}As$-DBR pairs with different refractive index contrasts Δn.

cavity for the modelling of the electric field intensity. The optical thickness of course remains constant. In the model only the physical thickness of the material with the calculated average real refractive index has to be adjusted accordingly. In a $\lambda/2$ optically-thick cavity the electric field intensity has an

anti-node (peak) in the center of the cavity, when the average real refractive index of the optical cavity is lower than the real refractive of the neighbor layers [49]. The active material, such as the quantum wells, are then typically placed at the position where the maximum of the electric field intensity is achieved. Compared to a longer $3\lambda/2$-cavity the overlap of the gain material and the electric field intensity can be increased via a $\lambda/2$-cavity [21] which is advantageous for the overall VCSEL properties, especially for achieving large modulation bandwidths. The placement of five quantum wells relative to the maximum of the electric field intensity in a $\lambda/2$-cavity is shown for the 980-nm VCSEL presented in this dissertation in Figure 6.4 in Chapter 6.

The real refractive index and the electric field intensity versus the distance from the wafer surface for a passive (i.e. without optical gain) multilayer asymmetric etalon formed by binary GaAs/AlAs-DBRs with a $\lambda/2$-cavity are shown in Figure 2.17. Air is assumed above the top DBR and the structure is placed onto a GaAs-substrate. Both the air and the GaAs-substrate are assumed to have an infinite thickness. The top-DBR and bottom DBR consist of 11.5 and 18 binary GaAs/AlAs DBR pairs, respectively. For the design wavelength of 980-m, this structure is resonant leading to the increase of the electric field intensity towards the center of the cavity structure.

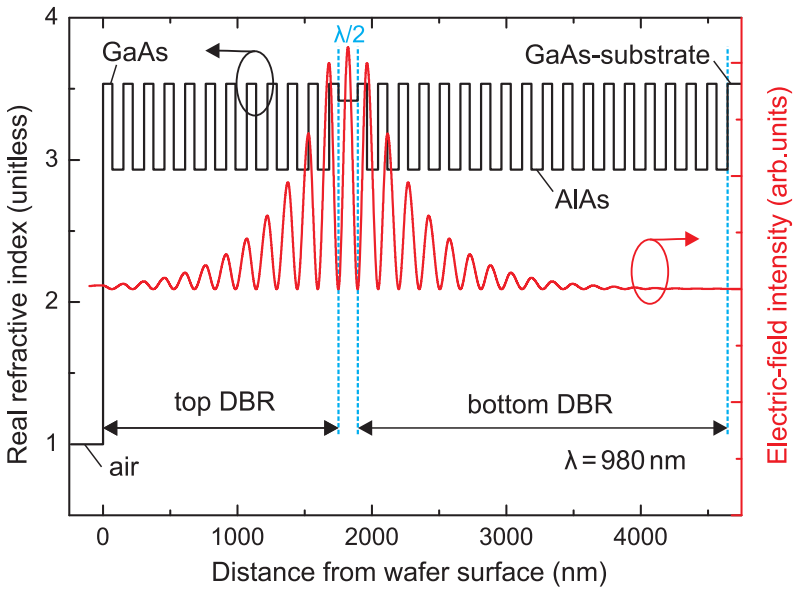

Figure 2.17.: Real refractive index and the normalized electric field intensity versus the distance from the top epitaxial surface of of a 980-nm passive etalon with binary GaAs/AlAs distributed Bragg reflectors and a $\lambda/2$-cavity on a GaAs-substrate. Light at 980-nm (modeled as plane waves) is incident from air looking down onto the passive multilayer asymmetric etalon. The light is reflected and also passes through the etalon exiting into the GaAs substrate.

Multiple nonabsorbing absentee layers that are optically inactive for the

design wavelength can be added to the etalon structure to serve different purposes such as to function as current spreading layers or intracavity ohmic contact layers. Because only the optical thickness matters, these absentee layers can be of the same low or high refractive index as the used $\lambda/4$-layers of the DBR material or in general it can have any other real refractive index. Figure 2.18 shows the same structure from Figure 2.17 but with a $5 \times \lambda/2$ optically-thick GaAs absentee layers added to the top DBR and a $3 \times \lambda/2$ optically-thick AlAs-layer placed within to the bottom DBR. These layers are not optical cavities, because the maxima of the electric field intensity of the neighbor layers are lower and higher, respectively. The absentee layers do not lead to the building up of the electric field intensity as is the case for a resonant optical cavity. An SEM image of a VCSEL structure with three absentee layers, two close to the active region and one closer to the wafer surface is shown in Figure 2.19.

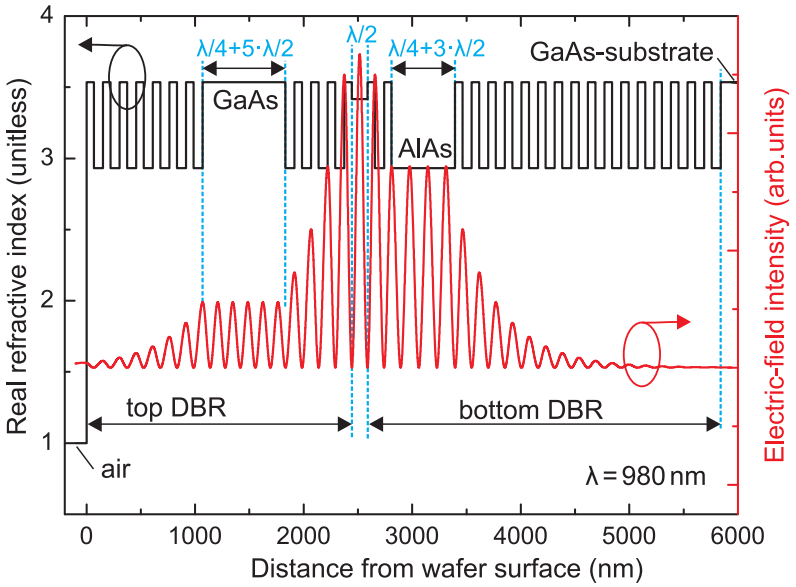

Figure 2.18.: Real refractive index and the normalized electric field intensity versus the distance from the top epitaxial surface of of a 980-nm passive etalon with binary GaAs/AlAs distributed Bragg reflectors (DBRs) and a $\lambda/2$-cavity on a GaAs-substrate. The top and bottom DBR each contain additional absentee layers with an optical thickness of a multiple of $\lambda/2$.

In addition to the optical properties such as power reflectance and reflectivity phase, also the thermal conductance and the electrical resistance are important for the CW and dynamic VCSEL properties. In order to reduce the mirror resistance, abrupt interfaces between the high and low refractive index materials can be replaced with different kinds of material compositional gradings. The simplest grading would be a linear grading from the low refractive index material to the high index material or vice versa. The doping

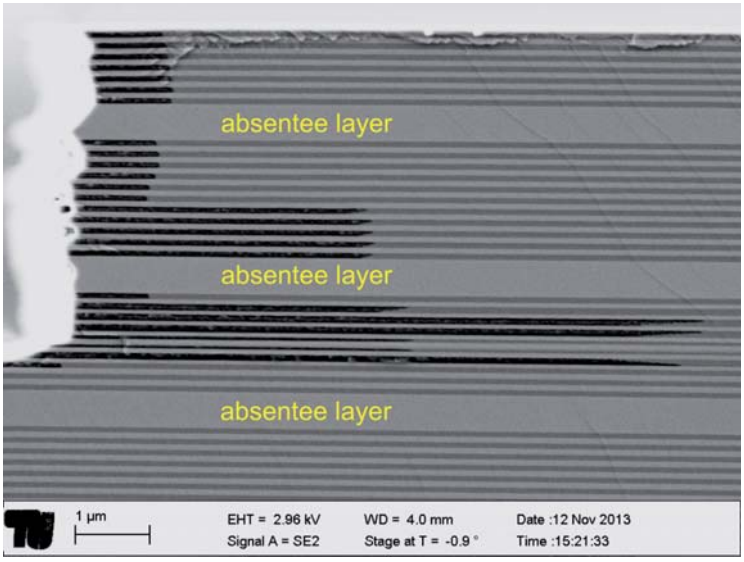

Figure 2.19.: Scanning electron microscope (SEM) image of a 980-nm VCSEL structure with three absentee layers.

is also very important for achieving a low mirror resistance. High doping levels are used only at the nodes of the electric field intensity in order to avoid free-carrier absorption losses which lead to heat creation in the DBRs. The emission wavelength of the VCSEL also limits the choice of possible materials or material compositions for the DBR, because of the wavelength dependance of the real refractive index and the absorption. For example GaAs can not be used as a mirror material for 850-nm VCSELs, because it absorbs all light at wavelengths shorter than about 870-nm. At 980-nm GaAs is transparent and can therefore be used in the DBRs of 980-nm VCSELs. Because of its high real refractive index and high thermal conductivity it is desirable to use GaAs-layers as the high refractive index material in DBRs. The 980-nm VCSEL design presented in Chapter 6 uses GaAs-layers as the high refractive index material in the top and bottom DBRs.

2.2.2. Oxide-apertures in VCSELs

Distributed Bragg reflectors confine the light in the longitudinal direction, e.g. vertical to the wafer surface. In order to improve the static and dynamic VCSEL properties a transverse optical confinement is required as well. This can be realized by simply etching a mesa as schematically shown in Figure 2.21 (a). The disadvantages of such a simple approach is that non-radiative surface recombination can occur at the etched sidewalls of the mesa and that relatively large bias currents are required to reach lasing threshold, because a large area needs to be pumped. Thus it is desired to realize transverse optical and current confinement to enable efficient laser operation and low

laser threshold currents.

Many different approaches for achieving transverse optical and current confinement in VCSELs exist, each with its own specific advantages and draw backs. Oxide-layers formed by the selective wet-oxidation of aluminum-rich $Al_xGa_{1-x}As$-layers [50] have many applications in semiconductor lasers [51]. Such oxide-layers formed by oxidation of $Al_xGa_{1-x}As$-layers were first used in edge-emitting lasers and then soon applied in VCSELs in 1994 [52] as current confining layers in oxide-confined VCSELs. Choquette *et al.* demonstrated the first oxide-confined VCSEL with conducting all semiconductor DBRs in the same year, which is the first VCSEL technology similar to the VCSELs presented in this dissertation. Oxide-confinement has led to a significant reduction in the threshold current [53] and increase of the wallplug efficiency of VCSELs [54, 55] and finally also enabled the presently fastest VCSELs.

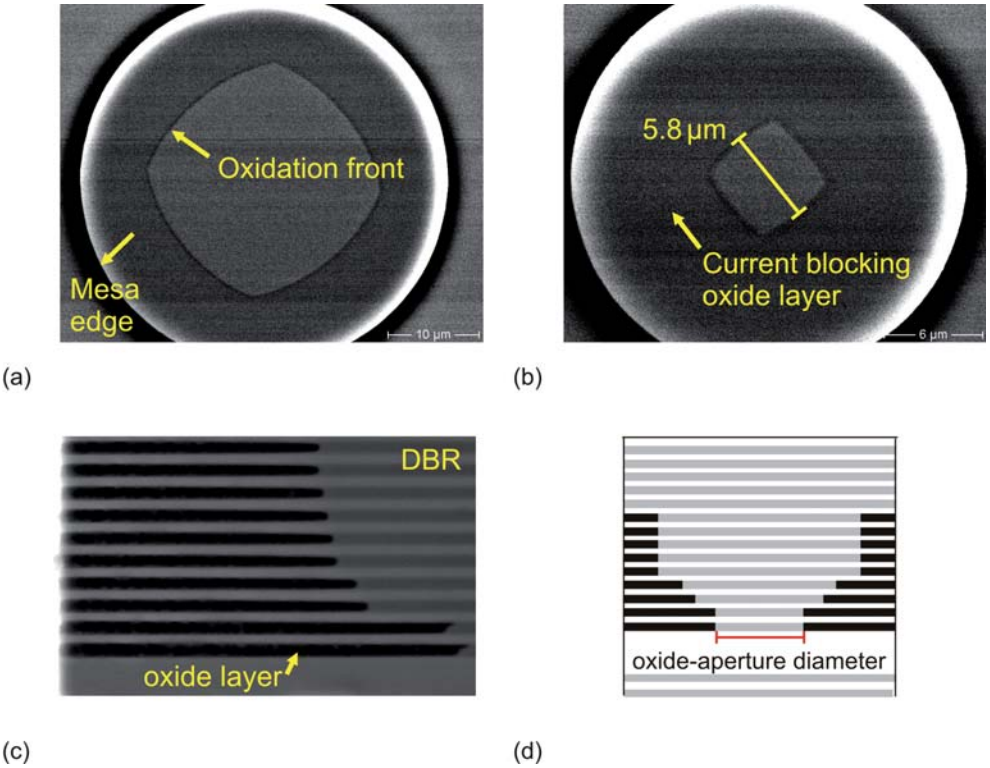

Figure 2.20.: Scanning electron microscope (SEM) image of oxidation test structures. The oxidized aluminum-rich $Al_xGa_{1-x}As$-layers can be seen under a thin GaAs cap layer for a (a) 41 µm mesa diameter (b) and 24 µm mesa diameter test structure. (c) SEM image of a cross section of oxidized $Al_xGa_{1-x}As$-layers. (d) Schematic of a mesa structure with deep oxidation and oxide-aperture layers of different lengths.

Oxide-layers in VCSELs are formed by the wet oxidation at high temperatures of $Al_xGa_{1-x}As$-layers with a high aluminum-content [50, 51, 56]. The formation of the oxide-apertures is typically performed at temperatures higher

than 350°C in a saturated N_2/H_2O atmosphere. The oxide-apertures of the VCSELs presented in this dissertation were formed at 420°C as explained in Chapter 5. The oxidation rate of aluminum-rich $Al_xGa_{1-x}As$-layers depends on many different parameters, such as the aluminum-content, the layer thickness, crystalline quality, doping, material composition and doping of the neighbor layers, the temperature and other parameters. Thus very accurate control of the thickness and material composition is required during the epitaxial growth to successfully realize (multiple) oxide-aperture layers. Binary AlAs is easier to epitaxially grow with a guaranteed material composition as compared to for example $Al_xGa_{1-x}As$ with $x = 0.98$ where the exact aluminum-content can only be realized with a certain maximum accuracy. Even a small deviation from the desired aluminum-content impacts the oxidation rate significantly [56]. In present state-of-the-art high-speed VCSELs typically $Al_{0.98}Ga_{0.02}As$-layers are employed that form the oxide-apertures during the oxidation process [9, 22, 57, 58]. A slightly lower aluminum-content of 98% is used instead of binary AlAs, in order to reduce the strain induced by shrinkage of the oxidized layers [56] as compared to the non-oxidized layers. The shrinkage reduces with decreasing aluminum-content and is about 12-13% for oxidized AlAs [56]. A different approach is to remove oxide-layers via selective chemical wet etching [59] in order to form air gaps and thus remove the majority of the strain. The strain induced by the oxide-layers is critical for the lifetime of the VCSELs. Because oxide-layers are typically placed close to the active region in order to effectively confine the current in the region with gain, the geometric distance to the active region is relatively small. Thus any defects that might be created at the tip or along the length of a strained oxide layer will eventually propagate to the active region and therefore drastically reduce the lifetime of the VCSEL. In order to reduce the strain of the oxidized layers, the thickness of the $Al_{0.98}Ga_{0.02}As$-layers prior to the oxidation is typically chosen to be between 20 and 30 nm [9, 22, 58]. Due to differences in the oxidation rates for different crystal axis, the oxide-aperture for a circular mesa can deviate from a circular shape. Thus square oxide-apertures are possible depending on the epitaxial layer design and the conditions during the wet oxidation, even for round mesa structures. Top views of oxide-aperture test structures are shown in Figure 2.20 (a) and (b). Oxidized layers in a DBR structure with different oxidation depths are shown in a cross section scanning electron microscope (SEM) image and a schematic illustrating the application of such oxidation layers in a VCSEL mesa are shown in Figure 2.20 (c) and (d), respectively.

Oxide-apertures can simultaneously provide optical and current confinement. The oxidized and non-oxidized $Al_xGa_{1-x}As$-layers differ in the refractive index, where the selectively oxidized material has a low refractive index of ~1.6 [56]. Thus there is a lateral refractive index profile leading to lateral optical confinement and the formation of modes. The impact of the oxide-layers on the optical properties of the VCSEL depends on the number, thickness, and position of the oxide-layers. Simultaneously the oxide-layers serve as current-

blocking layers forcing the current to flow through the oxide-aperture where the $Al_xGa_{1-x}As$-layer is not oxidized and which has typically a much smaller diameter than the etched mesa. This allows one to achieve high current densities at comparably low bias currents. Schematic cross sections of a VCSEL and the current flow with and without oxide-confinement is shown in Figure 2.21 (a) and (b), respectively.

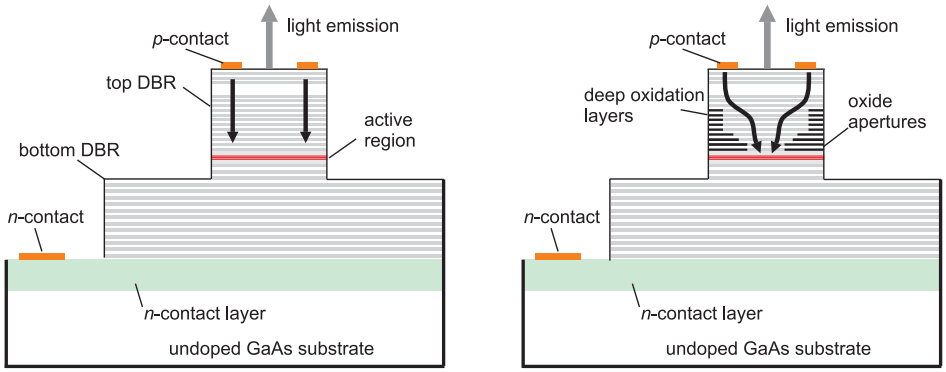

Figure 2.21.: Schematic cross section of top-emitting VCSELs with doped semiconductor top and bottom distributed Bragg reflectors (a) without oxide-apertures and (b) with current confining multiple oxide-apertures and deep oxidation layers. The thick black arrows indicate the difference of the current flow in the two structures.

For data transmission across long distances of multimode optical fiber a low spectral width at a simultaneously low current density is desired. The current density is directly related to the lifetime of the VCSELs and in order to realize reliable operation for commercial application the current density is desired to be below $10\,kA/cm^2$ [31]. The spectral width limits the maximum transmission distance across a particular type of MMF of a given of a given modal bandwidth (GHz·km) and a given attenuation (dB/km) as functions of wavelength [60, 61]. A small spectral width allows to transmit across longer distances of multimode fiber. Error-free operation of 850-nm single-mode VCSELs (side-mode suppression ratio $> 40\,dB$) has been demonstrated at $10\,Gb/s$ up to a MMF transmission distance of a record-long $2820\,m$ [62]. Typically the maximum transmission distance of single-mode VCSELs across MMF is limited by the relatively small output power of the VCSEL and the attenuation of the fiber. Thus many approaches of increasing the output power of the VCSEL while maintaining the single-mode emission have been investigated.

Without any other further modification the diameters of the optical and current aperture are the same. Thus several approaches have been developed to add additional transverse optical confinement or laterally varying losses to a VCSEL in order to modify the spectral width. The main approaches are photonic crystals (PhC) [63] where vertical holes are etched into the top DBR

in order to modify the effective index or surface relief structures of different geometries which introduce mode selective losses [41, 43, 64]. Both approaches have led to an increase of single-mode output power [43] and an increase of the multimode optical fiber distance at simultaneously lower current density [12, 44], but both approaches also share the need for additional processing steps with a high precision, which might be cost-ineffecient and detrimental for mass production and commercialization. Photonic crystals and surface reliefs typically introduce additional losses which is detrimental for energy-efficient data transmission. In this dissertation extremely energy-efficient data transmission across long distances of MMF is be demonstrated with oxide-confined VCSELs without any further modification of the top DBR. While the bit rate and MMF distance is comparable to those results obtained with PhC and surface relief VCSELs, the energy efficiency is much better without additional modification of the top DBR [65].

In addition to oxide-aperture layers, deep-oxidation layers [66] can be used to reduce parasitic capacitances and thus increase the electrical bandwidth of VCSELs for optical interconnects. Deep oxidation layers are $Al_xGa_{1-x}As$-layers which have a lower oxidation rate and thus a shorter oxidation-depth than the layer(s) that form the oxide-aperture(s). Since the oxidation rate depends on both the aluminum content as well as on the layer thickness [56], the deep-oxidation layers have either to be thinner than the oxide-aperture layers or have a lower aluminum-content than the layers that are designed to form the oxide-apertures. Figure 2.22 shows the SEM image of a cross section of an oxidized VCSEL waferpiece of the 980-nm design presented in this dissertation. The oxidized high aluminum-content layers can be seen (dark horizontal layers). This image is a zoom-in of the 980-nm VCSEL structure shown in Section 6.2 in Figure 6.6 and shows six tapered deep oxidation layers of different thickness and different taper design, but with the same oxidation depth. The taper is realized by using a grading of the Al-content in the $Al_xGa_{1-x}As$-layers. The design of the deep oxidation layers just above and below the two oxide-aperture layers is different, resulting in a much thinner tip of the oxidized layer due to the much longer taper. Oxide-aperture layers are typically tapered in order to decrease optical scattering losses [67].

For top-emitting VCSELs with epitaxially grown doped semiconductor DBRs, such as presented in this thesis, the top metal contact is usually designed in a circle, leaving the center of the topmost DBR layer free from metal. This contact shape leads to an inhomogenous lateral current-density distribution inside the top DBR. In VCSELs with current-confining oxide-apertures, e.g. oxide-confined VCSELs, the oxide-aperture is typically smaller than the diameter of the top metal contact ring in order to prevent the metal contact from blocking and absorbing the light. This leads to current-crowding at the edge of the oxide-aperture where the current density is much higher than in the center of the conducting aperture, which may negatively impact the VCSEL performance by inhomogeneous heating resulting in a thermal lens or spatial

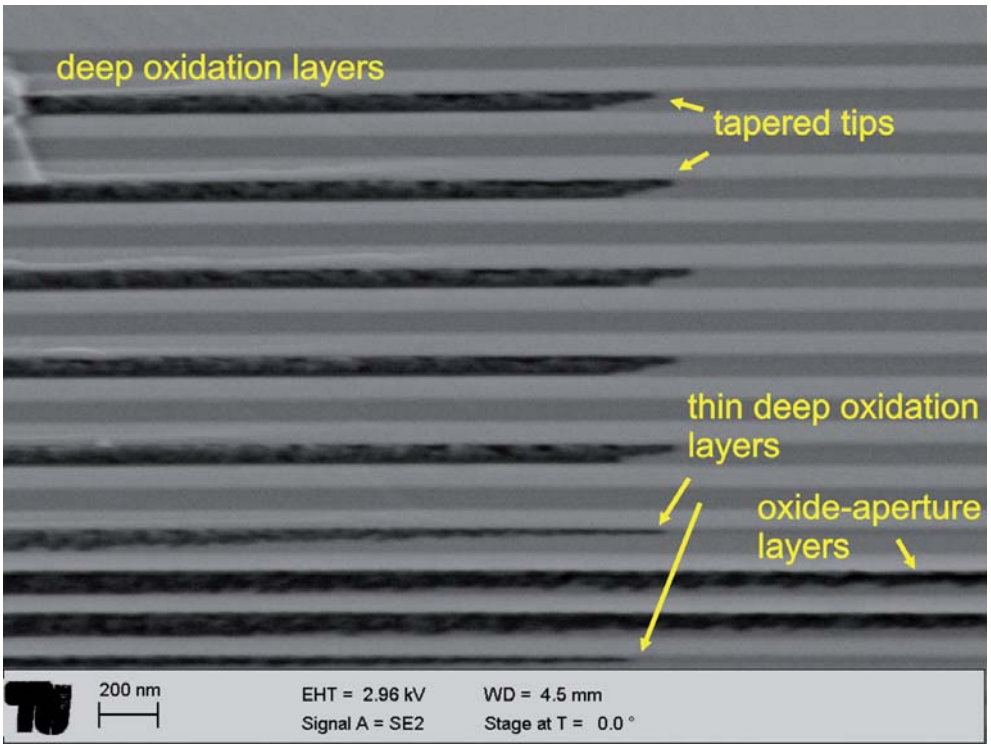

Figure 2.22.: Scanning electron microscope image of an oxidized 980-nm VCSEL wafer piece that was oxidized for 66 min at 420°C at 50 mbar. Six deep oxidation layers are shown above two oxide-aperture layers.

hole burning. Current crowding is even a larger issue in VCSELs with intracavity contacts in which the vertical distance between the oxide-aperture layer and the layer in which the current is injected, is much smaller.

Because of the potential strain-induced reliability issues of oxide-confined VCSELs and the low heat conductance of the oxide-layers, the development of oxide-free VCSELs is a modern subject of research [68, 69, 70]. In such VCSELs the current apertures are lithographically defined and at least one etch and regrowth step is required. However the exact fabrication of such oxide-free VCSELs as well as the dynamic modulation properties have not been published. The published CW properties are very promising, because large optical output powers at small current-aperture diameters are achieved, for example 3 µm aperture-diameter devices achieve a maximum output power of 12 mW [69, 70], and the LI-curves are very insensitive to temperature changes. While the issue of the large differential resistance of small current-confining apertures remains unsolved, the achieved large photon densities might lead to large D-factors and the large output power at single-mode emission might enable longer MMF transmission distances at higher bit rates.

Chapter 3.

Dynamic properties of oxide-confined VCSELs

The theoretical background to gain a basic understanding of the dynamic properties of VCSELs is introduced in this Chapter. Starting with the standard rate-equations for laser diodes the concept of small-signal modulation analysis and the impact of the oxide-aperture diameter on the dynamic VCSEL properties are explained.

3.1. Rate equations

The modeling of the static and dynamic properties of VCSELs is a very complex task that requires full three dimensional self-constistent modeling of the thermal, electrical, and optical properties. Self-heating and other thermal effects play an important role in VCSELs making it especially hard to draw proper conclusions from modeling that does not include temperature effects.

To gain a basic understanding of the dynamic properties and limitations of a given laser diode simple rate-equation models are very helpful despite the many simplifications and assumptions. The derivation of the standard rate-equation models for semiconductor laser diodes and all the assumptions and approximations that are made are explained in great detail in Ref. [39] in Chapter 5 and are therefore not repeated here.

The single-mode *density* rate-equations describe the change of charge carrier and photon-densities inside the VCSEL with time. The dependance of the charge carrier density N and photon density N_p on the time is given by Equation (3.1) and Equation (3.2), respectively:

$$\frac{d}{dt}N = \frac{\eta_i I}{qV} - (R_{sp} + R_{nr} - v_g g N_p) \tag{3.1}$$

$$\frac{d}{dt}N_p = \left(\Gamma v_g g - \frac{1}{\tau_p}\right) N_p + \Gamma R'_{sp} \tag{3.2}$$

where η_i is the internal efficiency, I is the bias current and V the active region volume, e.g. the carrier reservoir formed by the quantum wells, q is the elementary charge, R_{sp} and R_{nr} are the spontaneous and non-radiative recombination rates, v_g is the group velocity, g the optical gain, Γ is the ratio of V over the mode-volume, τ_p is the photon-lifetime, and R'_{sp} is the rate of the spontaneous emission that emits into the lasermode. Gain compression is accounted for in $g = g_0/(1 + \epsilon \cdot N_p)$ by the empirical gain compression factor ϵ which leads to an nonlinear dependance of g on N_p

Equations (3.1) and (3.2) can be solved for constant current values or any signal superimposed on a constant current value. This can be a sinusoidal signal for small-signal modulation or any type of bit patterns for modeling rise times or optical eye-diagrams of large-signal modulation. The rate-equations can not be solved analytically in the presented form.

For this work the small-signal modulation properties of VCSELs are of large interest. Assuming that the change of the charge carrier and photon density induced by the modulation signal is very small compared to the CW charge carrier and photon density allows to form the differential form of equations (3.1) and (3.2) [39] in a compact matrix form where dI, dN, and dN_p are independent differentials:

$$\frac{d}{dt}\begin{bmatrix} dN \\ dN_p \end{bmatrix} = \begin{bmatrix} -\gamma_{nn} & -\gamma_{np} \\ \gamma_{pn} & -\gamma_{pp} \end{bmatrix} \begin{bmatrix} dN \\ dN_p \end{bmatrix} + \frac{\eta_i}{qV}\begin{bmatrix} dI \\ 0 \end{bmatrix}. \tag{3.3}$$

For small-signal modulation one assumes a sinusoidal bias current modulation dI. It is further assumed that modulation will result in a similarly sinusoidal modulation response of the charge carrier and photon densities dN and dN_p, respectively. This can be expressed using following complex ansatz:

$$dI(t) = I_1 e^{j\omega t} \tag{3.4}$$
$$dN(t) = N_1 e^{j\omega t} \tag{3.5}$$
$$dN_p(t) = N_{p1} e^{j\omega t} \tag{3.6}$$

where I_1, N_1, and N_{p1} are the complex constant amplitudes. Putting equations (3.4), (3.5), and (3.6) into equation (3.3) one can solve for N_1 and N_{p1} using the determinant Δ of the matrix in equation (3.3).

$$N_1 = \frac{\eta_i I_1}{qV}\frac{\gamma_{pp} + j\omega}{\omega_r^2} \cdot H(\omega) \tag{3.7}$$
$$N_{p1} = \frac{\eta_i I_1}{qV}\frac{\gamma_{pn}}{\omega_r^2} \cdot H(\omega). \tag{3.8}$$

$H(\omega)$ is the two-pole transfer function:

$$H(\omega) = \frac{\omega_r^2}{\omega_r^2 - \omega^2 + \gamma j\omega} \tag{3.9}$$

where ω_r and γ are the relaxation resonance frequency and the damping, respectively. Setting $f_r = \omega_r/2\pi$ and expanding the matrix elements in equations (3.7) and (3.8) while making several assumptions and estimations as precisely explained in Ref. [39] the value of the relaxation resonance frequency f_r (GHz) and the damping γ (ns) can be expressed as follows:

$$f_r = D\sqrt{I - I_{th}} \tag{3.10}$$

$$\gamma = K f_r^2 + \gamma_0 \tag{3.11}$$

where D ($\mathrm{GHz}/\sqrt{\mathrm{mA}}$) and K (ns) are the so called D- and K-factors, $\mathrm{I_{th}}$ (mA) is the threshold current of the VCSEL and γ_0 (ns) is the damping offset. D and K can be expressed as

$$D = \frac{1}{2\pi}\sqrt{\frac{\eta_i \Gamma \nu_g}{q V_a}\frac{\partial g/\partial n}{\chi}} \tag{3.12}$$

$$K = 4\pi^2\left(\tau_p + \epsilon\frac{\chi}{\nu_g(\partial g/\partial n)}\right) \tag{3.13}$$

where η_i (unitless) is the internal quantum efficiency, Γ (unitless) is the optical confinement factor, ν_g (cm/s) is the group velocity of light, q is the elementary charge (coulomb), V_a (cm^3) is the active volume, $\partial g/\partial n$ (cm^2) is the differential gain, χ (unitless) is the transport factor, τ_p (ps) is the photon lifetime, and ϵ (cm^3) is the empirical gain compression factor. The active volume V_a is the product of the aperture area and the thickness of the active material, given for example by the cumulative quantum well thickness.

According to Equations 3.10 and 3.11 the dynamic properties of a VCSEL under small-signal modulation is characterized by the D- and K-factor as well as the damping offset γ_0. The relaxation resonance frequency and damping follow the linear theory until current-induced self-heating at larger bias currents cause the D-factor to decrease and the K-factor to increase. As will be shown in this thesis, for extremely energy-efficient VCSEL operation resulting in low consumed or dissipated energy per bit, VCSELs need to be operated at low currents, where the resonance frequency and damping follow the linear dependance and current-induced self-heating is not yet important. Therefore also the different possible limitations of the maximum possible modulation bandwidth f_{3dB} of a given VCSEL, such as damping and electrical RC-limitations, are not discussed in detail here, because they are typically reached at much higher currents that are not the main focus of this work.

3.2. Small-signal modulation

The relaxation resonance frequency and the damping of a VCSEL at a given bias current can be determined by measuring the small-signal modulation response as discussed in this Section.

The values of the relaxation resonance frequency f_{r} and the damping rate γ can be determined by performing small-signal modulation response (S21) measurements:

$$S21 = 20 \cdot log\,|H|\,. \tag{3.14}$$

Fitting the measurements at given bias currents allows to determine the relaxation resonance frequency f_r, the damping γ, and the parasitic frequency at these respective currents. The parasitic frequency accounts for electrical parasitics such as parasitic capacitances of the VCSEL. In order to successfully determine the intrinsic laser parameters without the influence of the measurement setup or configuration, careful calibration of the network analyzer and a known detector response are required. Then the evaluated D- and K-factors and the damping offset reflect purely intrinsic properties of the VCSEL. Therefore the energy efficiency of VCSELs will later be investigated by analyzing their dynamic properties obtained by small-signal modulation response measurements rather than from data transmission experiments which typically reflect the combined performance the complete measurement setup configuration including amplifiers and detectors.

As can be seen in the Equations (3.10) and (3.11) the modulation response S21 varies with the bias current of the VCSEL. The relaxation resonance frequency f_r increases with increasing current above threshold current. The damping rate γ increases with increasing f_r. A measure of the high-speed modulation capability of the VCSEL at a given bias current is the -3dB modulation bandwidth f_3dB which is defined as the frequency at which $S21 = -3\mathrm{dB}$. As well as f_r and γ the modulation bandwidth f_3dB varies with bias current. Similarly to the equation (3.10) the dependance of f_3dB on the bias current can be expressed as:

$$f_{3dB} = MCEF\sqrt{I - I_{th}} \tag{3.15}$$

where MCEF ($\mathrm{GHz}/\sqrt{\mathrm{mA}}$) is the modulation-current efficiency factor [71]. In a first order approximation the f_3dB is directly related to the bit rate at which the VCSEL can be operated. Therefore the MCEF is desired to be as large as possible in order to achieve large bit rates at low currents.

The modeled S21-response of an example VCSEL for different bias currents is shown in Figure 3.1 (a). This modeling does not include any temperature effects such as current-induced self-heating and its purpose is to demonstrate the impact of the bias current on the S21-response. At low bias currents there is a pronounced resonance peak, because the damping is relatively low due to the small f_r. With increasing current f_r increases, leading to a corresponding increase in γ. Therefore the amplitude of the resonance peak decreases until the S21-modulation response curve is flat, here at a bias current of 8.0 mA. A further increase in bias current and consequently of f_r and therefore also γ finally leads to a decrease in the modulation bandwidth f_3dB. The dependance of f_3dB on the bias current is shown in Figure 3.1 (b).

In addition to damping the maximum f_3dB in real VCSELs can also be limited by thermal effects. Especially for small oxide-aperture diameter VCSELs current-induced self-heating typically leads to saturation of f_3dB before the damping limit is reached.

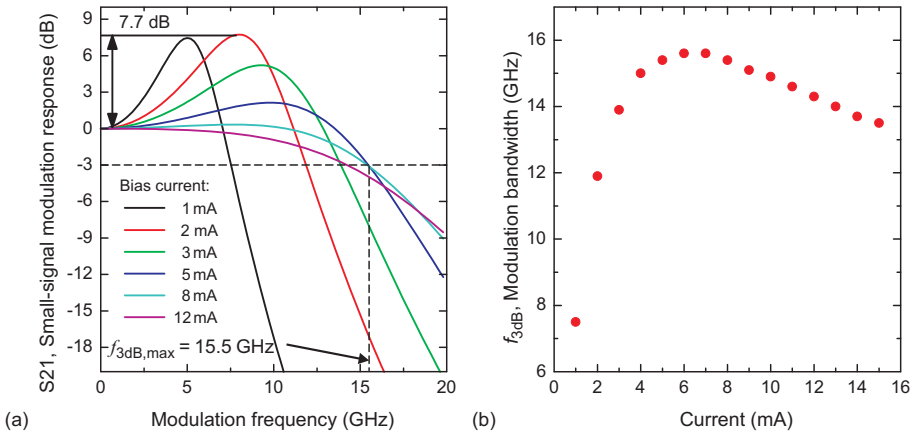

Figure 3.1.: (a) Modeled S21-response versus the modulation frequency for different bias currents. (b) Modulation bandwidth $f_{3\mathrm{dB}}$ versus bias currents for the modeled results of (a).

As given in Equation (3.12) the D-factor is inversely proportional to the square-root of the active volume $\mathrm{V_a}$ which is the product of the aperture-area and in case of quantum-well (QW) based active regions the QW-thickness. Thus the D-factor is inverse proportional to the oxide-aperture diameter $\mathrm{d_A}$:

$$D \propto \frac{1}{\sqrt{V_A}} \propto \frac{1}{d_A}. \tag{3.16}$$

Therefore VCSELs with smaller oxide-aperture diameters have larger D-factors and achieve larger f_r at a given bias current as compared to VCSELs with larger oxide-aperture diameters. Due to the larger f_r also the damping γ is larger at a given bias current, typically leading to slightly smaller maximum $f_{3\mathrm{dB}}$ values of VCSELs with smaller oxide-aperture diameters. VCSELs with larger oxide-aperture diameter have a smaller D-factor, but also a smaller K-factor. Therefore a flat modulation response is achieved at much higher currents for those VCSELs as compared to VCSELs with smaller oxide-aperture diameter. At very small bias currents, as desired for energy-efficient operation, the small-signal modulation response curves of large oxide-aperture diameter VCSELs have large resonance peaks as shown in Figure 3.1 (a) which is detrimental for data transmission where typically a flat modulation response is desired to achieve large optical eye-openings.

As shown later in Section 7.2.1 in Figure 7.5 we find that for VCSELs with oxide-aperture diameters larger than approximately 4 µm the MCEF is proportional to the D-factor. Then the ratio X = MCEF/D is constant. Therefore for VCSELs with larger oxide-aperture diameters the MCEF is inverse proportional to the aperture diameter. For VCSELs with oxide-aperture diameters smaller than 4 µm the MCEF still increases with decreasing oxide-aperture diameter but at a lower rate.

All static and dynamic properties of the VCSEL, such as for example the maximum output power, the differential quantum efficiency, maximum f_{3dB}, D-factor, and MCEF, etc. scale with the oxide-aperture diameter of the VCSEL. Therefore for a given epitaxial VCSEL design the oxide-aperture diameter is one key parameter for optimizing the VCSEL for certain performance goals. While it is well-known that larger oxide-aperture diameter VCSELs have larger maximum wallplug efficiencies and can be modulated at the highest bit rates, the impact of the oxide-aperture diameter on the dynamic energy efficiency and its temperature stability have not been investigated yet. As shown in Chapters 7 and 8, the oxide-aperture diameter is a key parameter to enable energy-efficient and temperature-stable data transmission with a given epitaxial VCSEL design. The figures-of-merit and methods for comparing the energy efficiency of VCSELs are introduced and explained in the next Chapter of this thesis.

Chapter 4.

Dynamic energy efficiency

The term *energy efficiency* is often used in the context of semiconductor lasers but it is not a set term with an established definition. Even when only semiconductor laser diodes for optical communications are considered, *energy efficiency* can have several different meanings, leading to confusion when in presentations or publications, intentionally or unintentionally, different energy efficiencies are compared. In this Chapter the energy-to-data ratio (*EDR*) and the heat-to-bit rate ratio (*HBR*) are defined and introduced as useful figures-of-merit for comparing the dynamic energy efficiency of laser diodes for data communication. By introducing the modulation factor M, a new method of comparing the energy efficiency of VCSELs and their suitability for application in different optical interconnect technologies is introduced and explained in detail.

4.1. Dissipated heat-to-bit rate ratio (HBR) and energy-to-data ratio (EDR)

In order to compare the suitability of different VCSEL designs for low energy dissipating and consuming optical interconnects the electrical energy-to-data ratio (*EDR*) (fJ/bit) and the dissipated heat-to-bit rate ratio (*HBR*) (mW/Tbps or in fJ/bit) are defined as follows [72, 73, 74]:

$$EDR = \frac{I \cdot V}{BR} \tag{4.1}$$

$$HBR = \frac{I \cdot V - P_{opt}}{BR} \tag{4.2}$$

$$\tag{4.3}$$

where V and I are the continuous (CW) bias voltage (V) and current (mA), P_{opt} (mW) is the optical output power of the VCSEL, and BR (Gb/s) is the bit rate at error-free operation.

One purpose of defining *EDR* and *HBR* is to provide the basis for an easy comparison of published VCSEL data transmission results. In most cases the values of P_{el} and P_{opt} are given in publications allowing one to calculate the respective *EDR* and *HBR* values at error-free data transmission. The values of *EDR* and *HBR* are the CW electrical power and dissipated power per bit rate, respectively, of the VCSEL at the bias current of error-free transmission. This means that the modulation energy of the electrical signal is not included

in the above definition for the *energy efficiency* of VCSELs for optical data transmission.

The modulation energy that actually enters the VCSEL and eventually creates the bits is nontrivial to accurately determine. In order to *estimate* the total energy dissipation and consumption per bit of the VCSEL, the fraction of the modulation energy that is dissipated and consumed in the VCSEL can be *estimated* by measuring the root mean square (RMS) power P_{BPG} provided by the bit pattern generator (BPG) at the given bit rate and also the modulation peak-to-peak voltage V_{PP}.For standard on-wafer high frequency (HF) testing of VCSELs the device impedance is typically not matched to the 50 Ω impedance of the HF probe. Especially for VCSELs with smaller oxide-aperture diameters a large impedance mismatch exists. As a result, part of the power that modulates the VCSEL is reflected and does not contribute to the generation of the bits. The amplitude reflection coefficient r (unitless, in general a complex number) is calculated as follows (4.4):

$$r = \frac{Z_A - Z_L}{Z_A + Z_L} \qquad |r| \leq 1 \tag{4.4}$$

where Z_A is the impedance up to the HF probe tips, and of the VCSEL and Z_L is the transmission line impedance, and both terms are a function of frequency. The impedance Z_L of the standard high frequency transmission lines used for the data transmission experiments is 50 Ω. In general the 50 Ω impedance can be replaced by 100 Ω or another value to better match the impedance of the VCSEL and thus reduce the reflection. The impedance Z_A of the VCSEL can be approximated with the differential resistance $R_d(I)$ of the VCSEL at the bias current of the data transmission experiment. The fraction of the power that is reflected due to the impedance mismatch is given by the square of the magnitude of r as given in (4.4).

Taking the modulation power used to drive the VCSEL into account the *EDR* defined in (4.1) can be extended to *estimate* EDR_{mod} (4.5) [73]:

$$EDR_{mod} = \frac{I \cdot V}{BR} + \frac{P_{BPG}}{BR}(1 - |r|^2)WPE(I) \tag{4.5}$$

where WPE(I) is the static wallplug efficiency of the VCSEL, evaluated at the bias current of the large-signal modulation experiment I and $(1 - |r|^2)WPE(I)$ is the fraction of the power P_{BPG} that enters the VCSEL and is converted into optical power. The equivalent addition to *HBR* leads to an *estimate* for HBR_{mod} (4.6) [73]:

$$HBR_{mod} = \frac{I \cdot V - P_{opt}}{BR} + \frac{P_{BPG}}{BR}(1 - |r|^2)(1 - WPE(I)) \tag{4.6}$$

where $(1 - |r|^2)(1 - WPE(I))$ is the fraction of the power P_{BPG} that enters the VCSEL but is turned into dissipated heat and thus does not contribute to the creation of the bits but to heating of the VCSEL.

Because the modulation energy dissipated inside the VCSEL can only be estimated with a rather large uncertainty, it is neglected in the further analysis of the energy efficiency of VCSELs. As the *EDR* and *EDR* values of VCSELs decrease and become comparable to the modulation energy per bit, the determination of the modulation energy will become more important. The fraction of the estimated modulation energy consumed and dissipated in the VCSEL of EDR_{mod} and HBR_{mod}, respectively, is 7.7% for 850-nm VCSELs with different oxide-aperture diameters presented in Chapter 7. Thus more than 90% of the total energy consumption and dissipation is caused by the CW energy consumption and dissipation per bit as determined with Equations (4.1) and (4.2).

4.2. Modulation factor M

Although the *EDR* and *HBR* values determined with Equations (4.1) and (4.2) are good figures-of-merit for comparing published VCSEL results with each other, they do not reflect purely intrinsic properties of the VCSELs alone, but reflect the energy efficiency of the VCSEL in the measurement setup or configuration that was used to perform the data transmission. The experimentally measured maximum bit rate at the given bias current at which the VCSEL operates error-free largely depends on the measurement setup, for example the electrical amplifiers and available detectors or receivers. Therefore the *EDR* and *HBR* values determined using the bit rate of a large-signal modulation experiment do not purely reflect the energy efficiency of the VCSEL alone, but are impacted by the way the large-signal modulation experiment is performed. Therefore it is hard to draw valuable conclusions or to predict the performance of such a VCSEL in other measurement configurations, e.g. in a packaged optical interconnect module with a matched driver circuit, or for different modulation schemes, such as feed forward equalization. In order to better analyze the dynamic energy efficiency of a VCSEL and to account for the influence of the system in which the VCSEL is incorporated, the bit rate BR is replaced by the product of the modulation bandwidth $f_{3\mathrm{dB}}$ and the modulation factor M in units of (b/s)/Hz [75].

$$EDR = \frac{I \cdot V}{M \cdot f_{3dB}} = \frac{P_{el}}{M \cdot f_{3dB}} \tag{4.7}$$

$$HBR = \frac{I \cdot V - P_{opt}}{M \cdot f_{3dB}} = \frac{P_{diss}}{M \cdot f_{3dB}} \tag{4.8}$$

The error-free bit rate of a VCSEL is related to $f_{3\mathrm{dB}}$ and depends on the measurement or optical interconnect system. Thus M describes the overall optical interconnect system, whereas the electrical power and $f_{3\mathrm{dB}}$ reflect intrinsic properties of the VCSEL. For a given optical interconnect the value

of the M-factor is determined by the ratio of the bit rate to the modulation bandwidth $f_{3\mathrm{dB}}$:

$$M = \frac{BR}{f_{3dB}}. \tag{4.9}$$

As a first approximation the M-factor is considered to be constant for a given VCSEL and a given optical interconnect. The average M-factor for 11 published room temperature data transmission results of VCSELs with emission wavelengths of 850, 980, and 1060-nm and across multimode optical fiber transmission distances up to 100 m is 1.62 [33] including oxide-confined, photonic crystal, and tunnel junction VCSELs. For these results the M-factor varies between values of 1.25 and 1.80 (b/s)/Hz. Recently the error-free bit rate has been dramatically increased for 850-nm and 980-nm VCSELs. This increase in bit rate is not only caused by the large reported increase of the $f_{3\mathrm{dB}}$ of the VCSELs, but also by improvements of amplifiers, detectors, and other components, resulting in a large increase of the M-factor. Using the same university-produced 850-nm VCSEL technology [9] the error-free bit rate achieved with packaged VCSELs and feed forward equalization could be increased from 64 Gb/s [76] in 2014 to 71 Gb/s in 2015 [29]. This corresponds to an increase of the M-factor from 2.46 to 2.73 (b/s)/Hz. Table 4.1 shows selected M-factors equal to or larger than 2.0, including the 980-nm data transmission results presented in this dissertation.

Table 4.1.: M-factors for error-free data transmission with 850-nm and 980-nm VCSELs

Affiliation	TUB	TUB	IBM/CTH	IBM/CTH	IBM/CTH
M-factor ((b/s)/Hz)	2.1	2.0	2.46	2.38	2.73
Bit rate (Gb/s)	50	46	64	50	71
Temperature (°C)	25	85	25	90	25
Wavelength (nm)	980	980	850	850	850
Year of publication	2014	2014	2014	2014	2015
Reference	[58]	[58]	[76]	[77]	[29]

In the following analysis the M factor is assumed to be constant for any $f_{3\mathrm{dB}}$ of the given VCSEL and for a given VCSEL optical interconnect configuration. As already mentioned in Chapter 3, large resonance peaks in the small-signal modulation response are detrimental for good optical eye-quality and thus error-free operation at the respective bit rate. A flat modulation response typically yields a good eye-quality. Thus two VCSELs with the same $f_{3\mathrm{dB}}$ but one with very low damping and a large resonance peak in the S21-curve and the other with a perfectly flat small-signal modulation response would most likely achieve different maximum bit rate values. This is in agreement

with large-signal modulation experiments performed with the 850-nm VCSELs having different oxide-aperture diameters presented in Chapter 7. At low bias currents where the damping is small for large oxide-aperture diameter VCSELs resulting in pronounced resonance peaks in the small-signal modulation responses, no open optical eyes can be achieved. In constrast clearly open eye-diagrams are achieved with smaller oxide-aperture diameter VCSELs having a comparable f_{3dB} but larger damping. The non-trivial impact of damping on important large-signal modulation parameters have been studied on 850 nm VCSELs with different photon lifetimes in Ref. [78]. The optimal damping for a given VCSEL varies with the bit rate [78], thus different dampings will most likely result in slightly different maximum error-free bit rates. However, the M-factors of the 850 nm VCSELs at error-free 40 Gb/s operation as shown in Ref. [78] vary from 1.96 to 2.20 (b/s)/Hz for a rather large variation of the K-factor values from 0.2 to 0.4 ns with a rather small change in the bit-error ratio curve versus the received optical power. Therefore, assuming M to be constant for a given VCSEL operated at different bias currents resulting in different f_{3dB} values with different damping is a good first approximation. A bias current dependent correction factor that accounts for resonance peaks in the small-signal modulation response and therefore acts as a quality factor for f_{3dB} can be added to the M-factor without changing the general value of the evaluation method introduced in the following Chapters of this dissertation. As will become clear from the analysis of the results presented in this dissertation, assuming a bias current independent constant M-factor for a given oxide-aperture diameter and optical interconnect system does not result in misleading conclusions.

The modulation factor M can also more generally be related to the Shannon-Hartley Theorem from the field of the Information Theory that allows one to calculate the maximum channel capacity of a given communication channel [79, 80]. The general conclusions of the Information Theory apply to all kinds of communication and are not restricted to the communication of Shannon's days or the present communication technologies. According to the Information Theory the capacity C (in general in units of symbols/s) of error-free information transfer, (error-free defined by Shannon as an "arbitrarily-small frequency of errors" [79]) of an ideal ideal system with *white noise* that transfers binary digits, e.g. bits, can be expressed by the following equation:

$$C = B \cdot log_2(1 + S/N) \tag{4.10}$$

where B is the bandwidth of the channel, S and N are the average signal and noise powers in Watts, and S/N is then the unitless signal-to-noise ratio. Thus the channel capacity C for a given bandwidth B increases with increasing S/N of the system. This capacity is the ideal limit that can only be approached, but not achieved in real systems. The M-factor is then equivalent to the term $log_2(1 + S/N)$ with units of (b/s)/Hz as can also be seen in Equation 4.9. An

S/N of 4.0 therefore corresponds to an M-factor of 2.32 (b/s)/Hz. The general dependence of M on the S/N is shown in Figure 4.1.

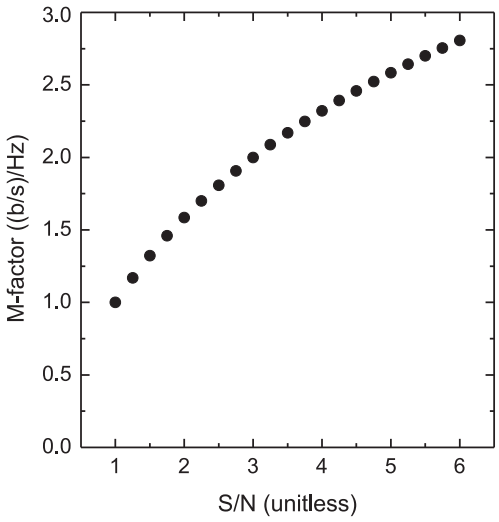

Figure 4.1.: Calculated modulation factor M for a digital communication system versus the signal-to-noise ratio.

In the simplified case of transmission of binary data such as the nonreturn-to-zero modulation of a VCSEL, one can replace B with the modulation bandwidth $f_{3\mathrm{dB}}$ of the VCSEL and the capacity of the channel equals then the maximum bit rate BR for this given system. In general B is the bandwidth of the entire system. Thus by using the modulation bandwidth $f_{3\mathrm{dB}}$ of the VCSEL as the bandwidth B, one assumes that the bandwidth of the photo detector of the optical interconnect is as large or larger than the modulation bandwidth of the VCSEL. In the Information theory the ratio of the channel capacity C to the bandwidth B of the communication channel is called the spectral efficiency η, which equals exactly the definition of the M-factor as given by Equation 4.9:

$$\eta = C/B = \frac{BR}{f_{3dB}} = M((b/s)/Hz). \tag{4.11}$$

A fundamental trade-off exists between low energy per transmitted bit and a large M-factor [81]. Large signal-to-noise ratios are required for large M-factors, which means that the average signal power has to be large compared to the average noise power. Assuming a constant minimum average noise power a low energy per transmitted bit corresponds to a small average signal power and thus smaller signal-to-noise ratio, leading to a small M-factor. Thus information can be transported very energy efficiently for systems with low M-factors only. Or in other words, the fundamental limit of the minimum energy per bit in systems with a large M-factor is larger than the fundamental limit for systems with a smaller M-factor.

Applying this general conclusion from Information theory to optical interconnects leads to the conclusion that VCSELs for very energy-efficient interconnects need to operate well at small M-factors. In this dissertation it is demonstrated that VCSELs with small oxide-aperture diameters are especially well-suited for application in optical interconnects with small M-factors.

From published results of optical interconnects, it can be empirically observed that those systems and modulation schemes with a larger spectral efficiency consume much more energy than those with a smaller spectral efficiency [2]. A similar trend can be seen for state-of-the-art VCSEL-based optical interconnects, where optical interconnects with a large M-factor consume much more energy per bit than optical interconnects with smaller M-factors. Optical interconnects using 850-nm VCSELs and SiGe-based integrated circuits achieve record-large error-free bit rates and very large M-factors (calculated with Equation 4.9) in excess of 2.0 (b/s)/Hz [29, 76, 77] as shown in Table 4.1, but have a large total energy consumption. For example 13.4 pJ/bit are consumed at 71 Gb/s and a M-factor of 2.73 (b/s)/Hz [29]. Optical interconnects using SOI CMOS-based integrated circuit technology have been demonstrated to be very energy-efficient [30, 82]. In recent work error-free operation at 26 Gb/s is demonstrated with 1060 nm VCSELs with a total optical interconnect power consumption of 1.1 pJ/bit and an M-factor of 1.44 (b/s)/Hz [28].

Thus in this work the M-factor is the *equivalent* to the spectral efficiency η of the Information Theory for VCSEL-based optical interconnects. By varying the M-factor, the performance of the VCSEL in optical interconnects with different spectral efficiencies is determined. The *EDR* and *HBR* values can now be calculated with Equations (4.7) and (4.8) for a given M-factor from the measured intrinsic $f_{3\mathrm{dB}}$ and electrical and dissipated powers.

For a given optical interconnect system, thus for a given combination of for example the driver, transmission line impedance, detector, etc. the M-factor is different for VCSELs with different oxide-aperture diameters, because the static and dynamic properties of the VCSEL vary with the oxide-aperture diameter. Thus if in the following analysis the M-factor is assumed to have a certain value of X for different VCSELs, the specific optical interconnect systems represented by the fixed M-factor value of X are different combinations of drivers, detectors etc., all resulting in the same M = X for the respective VCSEL. Assuming a value for the M-factor allows one to compare the suitability of different VCSEL technologies at particular *EDR* and *HBR* values for application in different optical interconnect systems represented by the respective M-factor. In this dissertation the M-factor dependent evaluation of the energy efficiency is used to demonstrate important trade-offs between bit rate and energy per bit as well as the temperature stability of the energy efficiency.

4.3. Impact of the oxide-aperture diameter on the energy efficiency

All of the static and dynamic properties of the VCSEL vary with the oxide-aperture diameter of the VCSEL and therefore the energy efficiency of VCSELs varies with the oxide-aperture diameter as well.

The static wallplug efficiency (WPE) and the differential quantum efficiency (DQE) alone are no valid indicators of the possibility of VCSEL operation with a low energy consumption per bit. These values refer to the static conversion of electrical to optical power only and do not account for the dynamic properties of a given VCSEL. Typically the WPE and DQE values are larger for larger oxide-aperture diameters, because smaller oxide-aperture diameter VCSELs experience increased diffraction losses at the oxide-layers [83, 84] leading also to increased threshold current densities. These optical losses are observed for the 850-nm VCSELs presented in Chapter 7. While a large WPE is advantageous, because then more power is converted into potentially useful optical power, VCSEL designs that optimize the WPE may deteriorate the dynamic properties of the device leading to a larger energy per bit required for error free transmission. The static and dynamic VCSEL properties must be evaluated simultaneously in order to draw proper conclusions about the energy efficiency of VCSELs and the impact of the oxide-aperture diameter on the energy efficiency. The WPE can be derived using the *HBR* and *EDR* as (4.12):

$$WPE = 1 - HBR/EDR \tag{4.12}$$

where the bit rate in each term cancels out, resulting in a unitless continuous wave WPE value. For simplicity only the impact of the oxide-aperture diameter on the electrical power consumption P_{el} and on the dynamic properties is analyzed in the following paragraphs. The electrical power P_{el} can be written as:

$$P_{el} = V_{th} \cdot I_{th} + R_{d,th}(I - I_{th})^2 \tag{4.13}$$

where V_{th} is the threshold voltage, I_{th} is the threshold current, and $R_{d,th}$ is the differential resistance at I_{th}. All three of these parameters vary with the oxide-aperture diameter of a given VCSEL. Small-aperture devices have small threshold powers P_{th} defined as the product of I_{th} and V_{th}, but typically large values of R_d. Due to the large R_d the electrical power is larger at a given current for small oxide-aperture diameter devices compared to VCSELs with a larger oxide-aperture diameter. As discussed in the previous Chapter, the D-factor is inversely proportional to the oxide-aperture diameter and the modulation-current efficiency-factor MCEF follows this proportionality for oxide-aperture diameters larger than some particular oxide-aperture diameter, e.g. ~3.5 µm. Due to the dependence of the electrical power and the D-factor on the oxide-aperture diameter, the resonance relaxation frequency

f_r at a given bias current increases with decreasing oxide-aperture diameter, but also the VCSEL driving power increases. The modulation bandwidth f_{3dB} increases with decreasing oxide-aperture diameter as well, but for smaller oxide-aperture diameters this increase is smaller than the increase of the f_r. The impact of the oxide-aperture diameter on the dynamic energy efficiency of the VCSEL can be illustrated by the following simple modeling. The threshold voltage V_{th}, the threshold current I_{th}, and differential resistance R_d are used from LIV-measurements of the 850-nm VCSELs presented in Chapter 7 and the electrical power P_{el} is calculated using Equation 4.13. The measured D-factors and the ratios $X = MCEF/D$ are used to calculate the relaxation resonance frequency f_r and the modulation bandwidth f_{3dB} for a given bias and oxide-aperture diameter. Figure 4.2 shows the measured and calculated electrical power values plotted against f_r. For some oxide-aperture diameters there is a larger difference between the measured and calculated values. This is most likely due to the uncertainty of the oxide-aperture diameter, especially for the small oxide-aperture diameters. The dependence of the D-factor on the oxide-aperture diameter is fitted and and then the D-factors for the respective oxide-aperture diameters are determined from the fits.

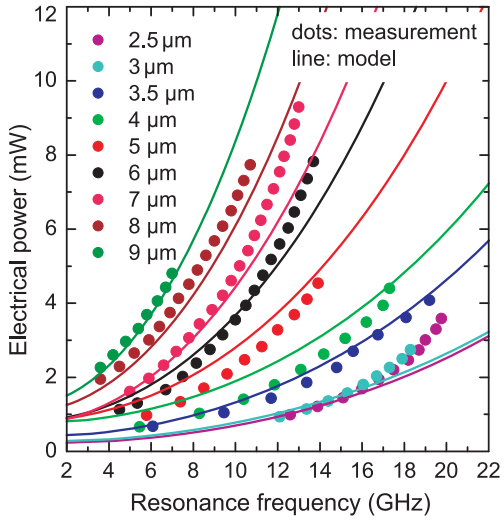

Figure 4.2.: Calculated (lines) and measured (dots) electrical power versus the relaxation resonance frequency f_r for 850-nm VCSELs with oxide-aperture diameters ranging from 2.5 to 9 µm.

Despite the differences between the measured and calculated data, the general trend is well reproduced. At a given f_r the required electrical power increases with increasing oxide-aperture diameter. Thus larger oxide-aperture diameter VCSELs require more power in order to achieve the same f_r as similar VCSELs with smaller oxide-aperture diameters. Using the known ratio $X = MCEF/D = f_{3dB}/f_r$ for calculating f_{3dB} from f_r, the bandwidth-to-electrical power ratio (f_{3dB}/P_{el}) is plotted versus the modulation bandwidth

f_{3dB}, as shown in Figure 4.3 (a). Because no damping or other effects such as the saturation of the f_r due to heating are included, the f_{3dB} values in this model would infinitely increase with increasing bias current, thus the results are only plotted up to a realistic bandwidth of 30 GHz. The energy efficiency of the VCSEL is directly related to the ratio f_{3dB}/P_{el}. In fact, f_{3dB}/P_{el} is an intrinsic dynamic energy efficiency of the VCSEL itself, in contrast to the *EDR* which always contains an impact of a system via the M-factor. The potential for error-free operation at large bit rates and simultaneously low energy consumption increases with increasing f_{3dB}/P_{el}. The bandwidth-to-dissipated power ratio (f_{3dB}/P_{diss}) is the corresponding intrinsic counterpart to the *HBR*. At any given f_{3dB} the ratio f_{3dB}/P_{el} increases with decreasing oxide-aperture diameter of the VCSEL. The ratio of f_{3dB}/P_{el} first increases with increasing modulation bandwidth f_{3dB} up to a maximum value between 5 to 10 GHz and then decreases again with a further increase in f_{3dB}. The peak of f_{3dB}/P_{el} is more pronounced for smaller oxide-aperture diameters. A large ratio f_{3dB}/P_{el} corresponds to a low consumed energy per bit, thus a low *EDR*. The *EDR* for $M = 2.0$ (b/s)/Hz is plotted for the VCSELs with oxide-aperture diameters ranging from 2.5 to 9 µm versus the calculated bit rate in Figure 4.3 (b).

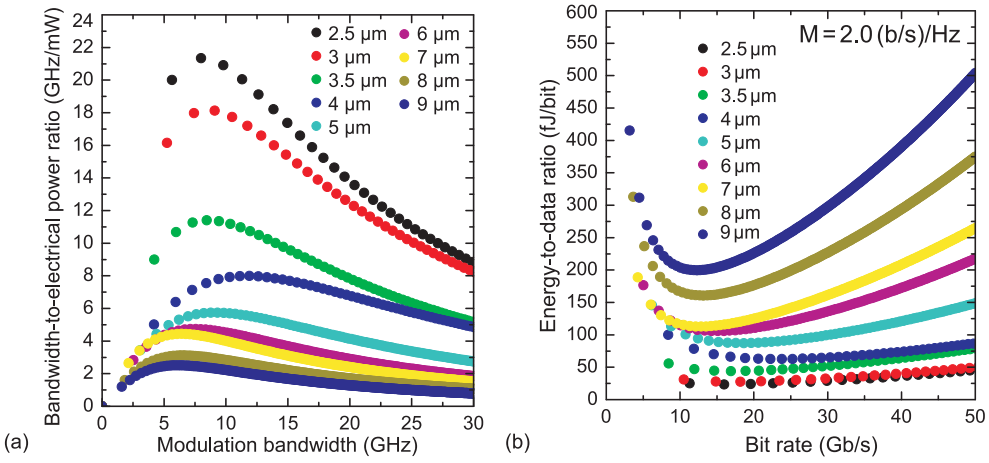

Figure 4.3.: (a) Calculated bandwidth-to-electrical power ratio versus the modulation bandwidth f_{3dB} for 850-nm VCSELs with oxide-aperture diameters ranging from 2.5 to 9 µm. (b) Calculated energy-to-data ratio (*EDR*) versus the calculated bit rate for $M = 2.0$ (b/s)/Hz for 850-nm VCSELs with oxide-aperture diameters ranging from 2.5 to 9 µm.

Corresponding to the peaks of f_{3dB}/P_{el} at the bandwidth values $f_{3dB,peak}$, the *EDR* has minima at the bit rates $M \cdot f_{3dB,peak}$. Because the *EDR* is calculated from the inverse of f_{3dB}/P_{el}, the *EDR* curve versus the bit rate is flatter for the VCSELs with smaller oxide-aperture diameters as compared to the curves for the large oxide-aperture diameter VCSELs. It is important to remember that this basic modeling does not account for damping or any

other effects that lead to a saturation of f_r and thus f_{3dB} or even a reduction of f_{3dB} at high bias currents. Thus the assumption is that f_r and therefore f_{3dB} follow the linear theory as given in Chapter 3 in Equations 3.12 and 3.15 and conclusions from these plots should only be drawn from the results at low currents where damping, thermal, and other limitations do not yet need to be taken into account. As discussed in the previous Chapter, the maximum modulation bandwidth f_{3dB} is smaller for VCSELs with smaller oxide-aperture diameters, due to the faster increase of f_r (and thus increase of damping) with current for the smaller oxide-aperture diameter VCSELs.

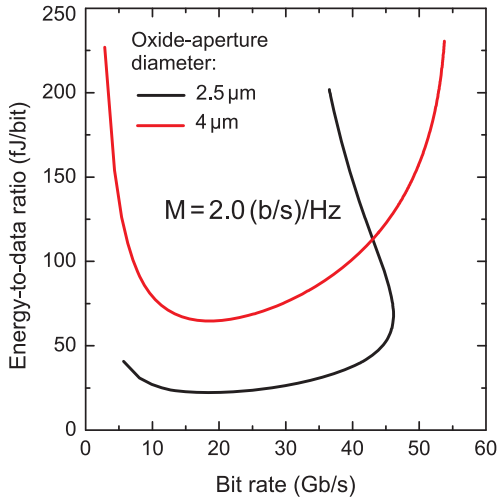

Figure 4.4.: Calculated energy-to-data ratio (*EDR*) versus the bit rate for two 850-nm VCSELs with oxide-aperture diameters of 2.5 and 4 µm for $M = 2.0\,(\mathrm{b/s})/\mathrm{Hz}$.

Figure 4.4 shows the calculated *EDR* values for VCSELs with oxide-aperture diameters of 2.5 and 4 µm versus the bit rate for $M = 2.0\,(\mathrm{b/s})/\mathrm{Hz}$. In this calculation the damping γ is added. This leads to a saturation of the f_{3dB} and thus also the bit rate. Once the maximum bit rate is achieved a further increase of bias current and thus the operating electrical power leads to a decrease of the bit rate which dramatically increases the *EDR*. The VCSEL with the larger oxide-aperture diameter of 4 µm achieves a larger maximum bit rate than the smaller oxide-aperture diameter VCSEL. Thus for every given bit rate there exists an optimum oxide-aperture diameter that results in the lowest *EDR* and there is a trade-off between very low *EDR* and a very large bit rate.

In the following Chapters the basic principles of energy-efficient data transmission with VCSELs will be verified by small- and large-signal modulation measurements of 850 and 980-nm VCSELs.

Chapter 5.

Fabrication of high-speed VCSELs

The process flow as well as the geometric VCSEL design can impact the static and in particular the dynamic properties of the resulting VCSEL devices. Therefore the process flow that is developed and used for this dissertation for fabricating oxide-confined VCSELs in a geometric design that is capable of at least 50 Gb/s modulation is presented in this Chapter. The formation of the oxide-aperture layers by *in situ*-controlled selective wet-oxidation, one of the key processing steps, is explained with a focus on the used oxidation monitor fields. The research mask-set that I developed for this dissertation contains many systematic geometric design variations that are explained in the following Chapter as well.

5.1. Process flow overview

The fabrication of high bit rate VCSELs includes numerous complex processing steps such as dry and wet etching, thin metal and dielectric layer deposition, selective wet oxidation, lithography, and planarization with high dielectric constant polymers. To enable reliable, fast, and cost-efficient processing the number and complexity of the processing steps should be kept as low as possible. The processing steps are optimized to yield a reliable and homogenous process flow across a quarter of a 3-inch diameter wafer piece. All of the processing steps that I used are fully compatible with the standard processing in existing foundries.

The step-by-step fabrication flow is illustrated in Figure 5.1. After cleaving the wafers into quarter-wafer pieces, an initial cleaning step is performed using isopropanol and acetone. Depending on the samples the initial cleaning can include short dips in an HCl:H_20 solution or plasma oxidation in an O_2 plasma. The alignment markers for all of the following masks are defined in the first metal deposition step of the top p-contact rings. All processed VCSEL designs presented in this dissertation employed p-type top DBRs. The top p-metal contact is evaporated after a 30 s dip in HCl:H_20 1:5 solution. An electron beam metal deposition machine is used for evaporation of the Ti/Pt/Au layers where the typical thickness of the titanium, platinum, and gold layers is 20, 50, and 300 nm, respectively. Next the first mesa (mesa 1) is etched in an inductively coupled plasma reactive ion etching machine (ICP-RIE). A Cl_2 and BCl_3 plasma process is used resulting in a ~300 nm per minute etch-rate of GaAs. Precise *in situ*-control of the etch process is realized by monitoring

the reflected intensity of an He-laser. The alternating high- and low aluminum-content $Al_XGa_{1-X}As$ distributed Bragg reflector layers can be distinguished by the lower and higher reflected intensity signal. Precise control of the etch depth is of high importance for the processing of structures that contain binary bottom DBRs. Overetching can lead to AlAs-layers that are exposed to the N_2 and H_2O atmosphere during the oxidation process. Since the AlAs-layers typically oxidize much faster than the the AlGaAs-layers that are designed to form the oxide-aperture, overetching can consequently lead to a loss of a complete waferpiece. Typically, AlGaAs-layers with an aluminum content of ~98% are employed for the oxide-aperture layers, since the slightly lower Al-content results in much less strain than compared to AlAs. After the first mesa etch the oxide-apertures are formed by the selective wet oxidation of the aluminum-rich aperture layers using a home-built *in situ*-controlled oxidation furnace. The oxide-apertures are formed at 420°C in a saturated N_2 and H_2O atmosphere at a pressure of 50 mbar. A zoom-microscope with coaxial illumination using a commercial 850 or 940-nm high power light emitting diode array as the illumination source and a Si-CCD camera as the photodetector are used for optical *in situ* oxidation monitoring and process control.

After formation of the oxide-apertures the second (bottom) mesa (mesa 2) is etched using the same dry etching process as for the first mesa. The etching is stopped in the highly n-doped contact layer residing just above the undoped GaAs substrate and Ni/Au:Ge/Au n-contacts are evaporated using an electron beam metal depositon machine or a thermal metal evaporation system where the typical thickness of the nickel, gold-germanium, and gold layers is 20, 100, and 300 nm, respectively. In order to minimize parasitic capacitances formed by the overlap of the p-type source pad contact metal and the n-type bottom contact layer, photosensitive bisbencozyclobutene (BCB) is placed onto the wafer in a process analogous to the placement, exposure, development and baking of photoresist. An ~8 µm thick BCB layer is used for planarization. In the final step coplanar ground-signal-ground (GSG) metal pad contacts are evaporated for the ease of on-wafer probing and automatic continuous wave (CW) characterization. For some wafer pieces the process flow was slightly varied. For example the oxidation was performed after the p-metallization, first and second mesa etch, and n-type bottom contact metalilzation. Also for some process runs dry-etch BCB was used instead of photosensitive BCB. Since these processing variations do not significantly impact the resulting VCSEL device performance these processing variations are not discussed in greater detail here.

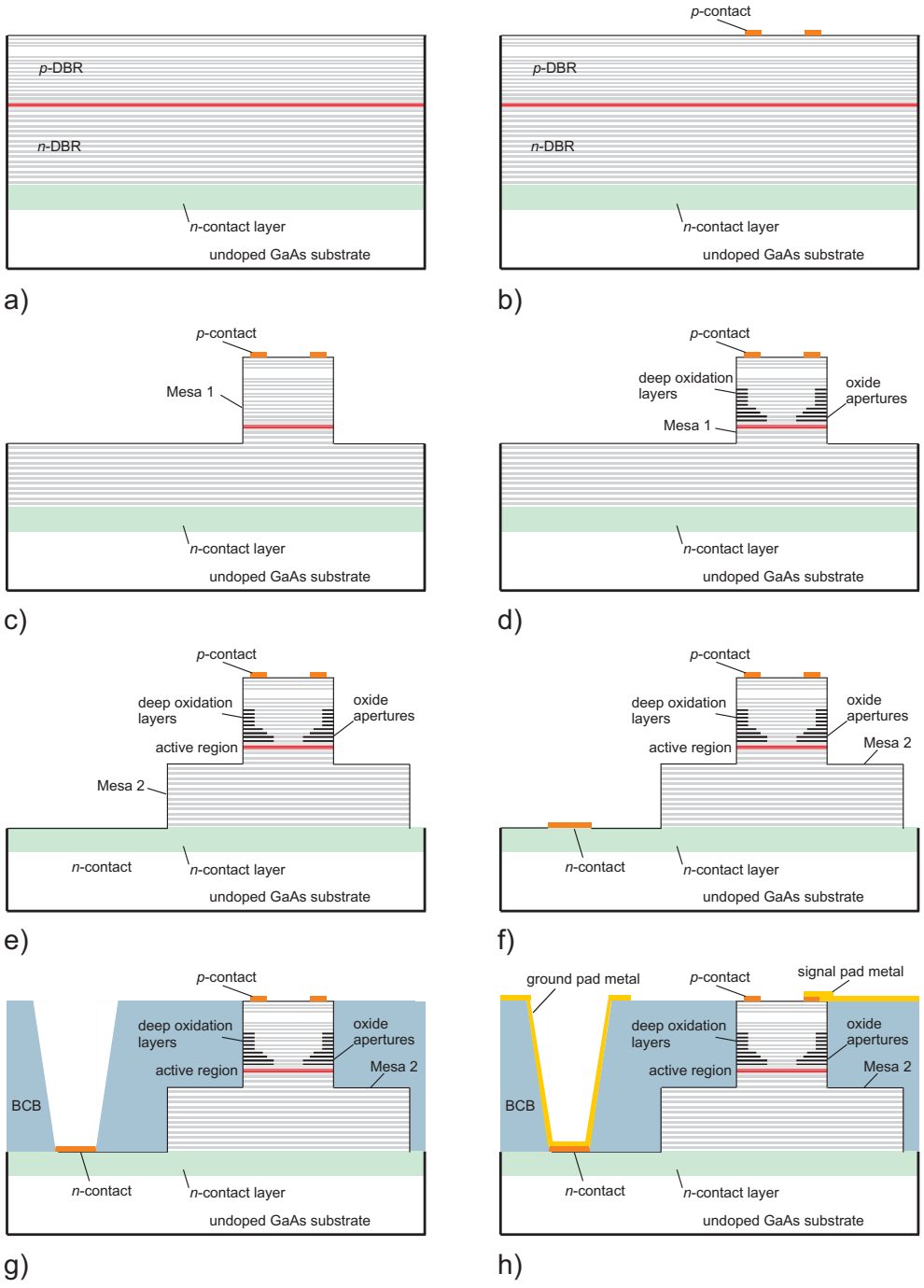

Figure 5.1.: Process flow for directly modulated oxide-confined high-speed VCSELs. Starting from the as-grown wafer (a), the p-type top contacts are evaporated (b), then the first mesa is etched (c) and the oxide-apertures are formed by selective wet oxidation (d) followed by the second mesa etch (e) and the bottom n-contact metallization (f). After the BCB-planarization (g) and evaporation of the coplanar contacts in a high-frequency layout (h) the devices are ready for measurements.

5.2. In situ-controlled selective wet oxidation

The formation of the current-confining oxide-apertures by the selective wet oxidation of aluminum rich AlGaAs-layers is one of the most crucial steps of the VCSEL processing. In commercial VCSEL fabrication the selective wet oxidation is often performed using lamp heaters leading to a high temperature homogeneity, but prohibiting optical *in situ*-control of the oxidation progress. Since in commercial VCSEL fabrication often many wafers of an identical design that require one fixed oxide-aperture diameter for all wafers are simultaneously oxidized, *in situ*-control of the oxidation process is less important than achieving the highest possible homogeneity. Pre-oxidation tests of the epitaxial material and *ex situ*-control of the oxidation process are then performed.

In research a lot of different epitaxial designs with varying number, position, thickness and composition of the Al-rich layers for forming the oxide-apertures are used. All these design parameters greatly impact the oxidation rate. Oxidation tests of unprocessed material and oxidation depth measurements with an SEM are time consuming, therefore *in situ*-control of the oxidation process is useful for processing many different VCSEL epitaxial designs.

For an homogeneous, reproducible, and *in situ*-controlled oxidation process, an oxidation furnace with a 4-inch diameter heater suitable for the oxidation of full 3-inch diameter wafers was built. To achieve the highest possible homogeneity the furnace was designed to have cylindrical symmetry. The gas outlet is realized by a tube that has a ring shape and is placed 3-4 cm above the heater surface. The ring with equidistant holes in the inner side has a diameter slightly larger than the 4-inch diameter heater. To increase the temperature homogeneity a heatshield made from tantalum is used. The H_2O/N_2 process gas mixture leaves the tube from holes in the inner side of the ring. Two independently controlled heater zones ensure a high temperature homogeneity across the inner 3-inch diameter circle of the heater. The oxidation of the aluminum-rich AlGaAs-layers is performed in a saturated H_2O/N_2 atmosphere at 50 mbar and a heater temperature of 420°C. The H_2O is evaporated and mixed with the N_2 in a controlled evaporation and mixing system (CEM) from Bronkhorst Mättig GmbH, employing two mass flow controllers with high precision. The pressure of the vacuum chamber is controlled by a throttle valve. Optical *in situ*-control is realized by a near infrared zoom-microscope with coaxial illumination. The difference between oxidized and non-oxidized Al-rich layers can be seen as a contrast between light and dark areas. The oxidation is performed with H_2O and N_2-flows of 0.8 l/min.

Several oxidation control fields for *in* and *ex situ*-control of the oxidation process are designed in the new UV contact lithographic mask set. Because the contrast between oxidized and non-oxidized material is sometimes difficult to see, especially when looking on the real VCSEL structures having their ring-shape metal contact on top of mesa 1, oxdiation test structures with

various geometries are designed in the new mask set. These structures differ in shape, size and orientation. The structures include circles, triangles, squares, rhomboids, and other shapes and are definded during the mesa 1 and/or mesa 2 etching step. *In situ*-images of the oxidation test structures are shown in Figure 5.2. The contrast between the oxidized (light) and non-oxidized (dark) material can clearly be seen and if necessary enhanced using the video software that controls the camera. The contrast of the images was artificially increased to make the oxidation front easier to see on the printed images. During the processing the microscope image is viewed with a 19-inch monitor and the contrast can be clearly seen. The samples shown in Figure 5.2 are 980-nm VCSELs with 22 top DBR pairs having a high power reflectance. The sample is illuminated with a high power 850-nm light emitting diode array and the image is taken with a standard Si-CCD camera.

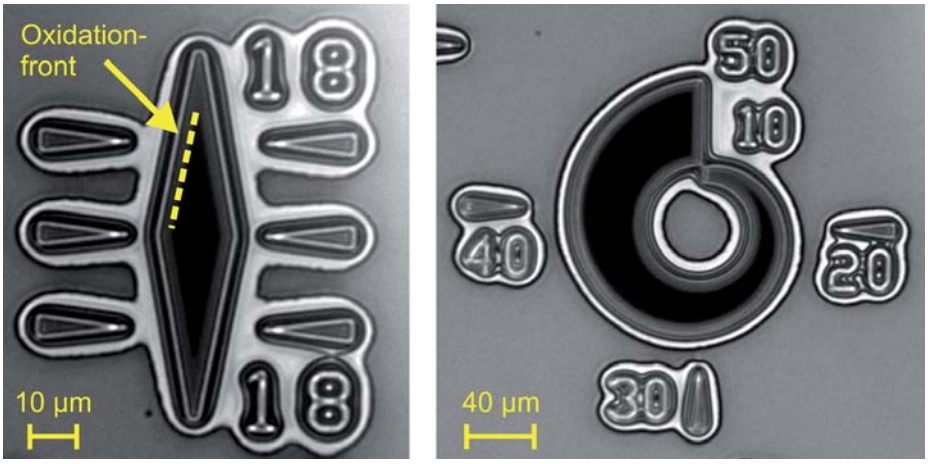

Figure 5.2.: *In situ*-image of a 980-nm VCSEL. The contrast between the oxidized (light) and non-oxidized material (dark) can clearly be seen through the more than 20 DBR pairs. Rhomboid (left) and spiral horn (right) test structures on the same waferpiece. The oxidation front is marked with a yellow dashed line on the rhomboid structure. The contrast of the images was increased so that the oxidation front can be better seen on the printed images.

Depending on the epitaxial design and the conditions during the oxidation-process the oxidation-rate can depend on the crystal axis resulting in square oxide-apertures as mentioned in Chapter 2. The difference of the oxidation rates can also be seen at asymmetric test structures that have different orientations. Such test structures are shown in Figure 5.3 where there is a clearly open oxide-aperture for the structures that are oriented horizontally and vertically and the oxide-aperture is already nearly closed for those structures that are rotated by 45°.

For samples where the contrast between oxidized and non-oxidized material can be very clearly seen, it is in most cases not necessary to use a large magnification as shown in Figure 5.4. Then the progress of the oxidation can

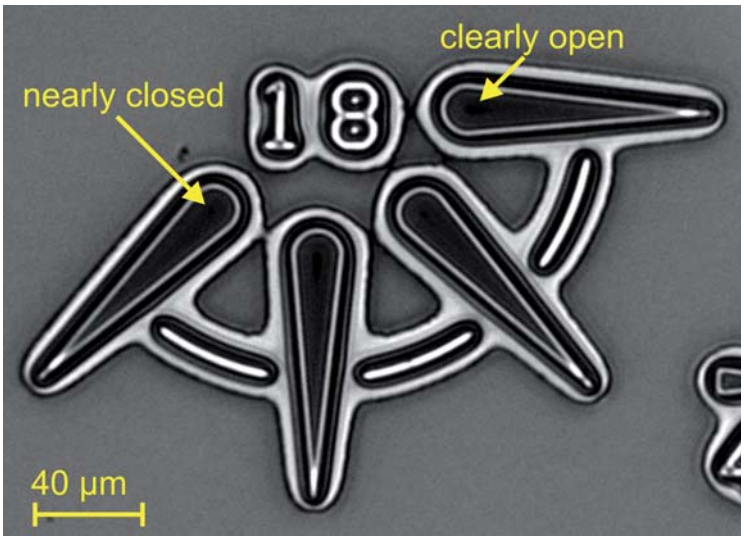

Figure 5.3.: *In situ*-image of a 980-nm VCSEL. The dependence of the oxidation rate on the crystal axis results in different oxide-aperture diameters for the differently orientated test structures. The contrast of the image was increased so that the oxidation front can be better seen on the printed images.

be monitored by simultaneously looking on many mesa test structures with different diameters. In the given example the mesas with a diameter of 17 µm and larger have clearly open oxide-apertures.

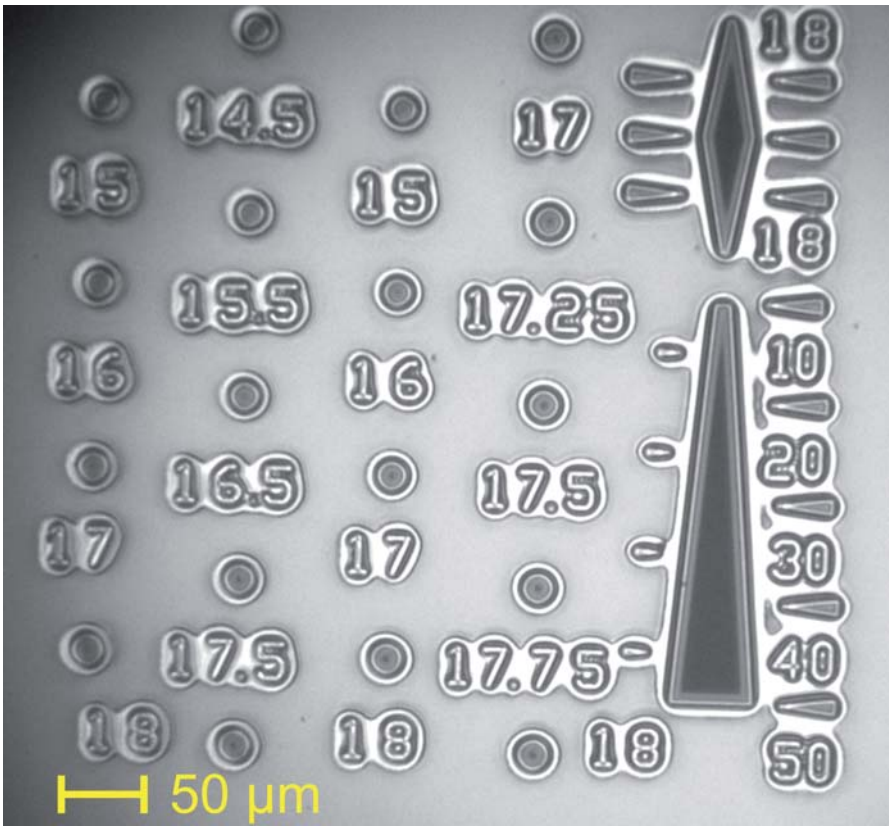

Figure 5.4.: *In situ*-image of a 980-nm VCSEL. The oxide-apertures can be clearly seen as dark circles in the center of the circular mesas. The contrast of the image was increased so that the oxidation front can be better seen on the printed images.

5.3. High-frequency mask layout

The VCSEL geometry defined by the mask set and process flow is of high importance as it may limit or enable high-speed performance of the VCSEL. If the electric parasitics of a VCSEL device are too large due to the layout of the high-frequency contact transmission lines or other geometric parameters, the VCSELs can not reach the high bit rate limits of the epitaxial design.

Because the homogeneous process flow allows processing of quarter wafer pieces from a 3-inch diameter wafer the use of large unit cells is possible. The developed mask set allows various processing options and alternative process flows due to the large unit cells. These cells have dimensions of 10.2 x 10.2 mm. Each unit cell includes 240 VCSELs in a high-speed double mesa design, 16 VCSELs for high-power and other studies and several process monitoring and test structures as well as different linear and circular VCSEL arrays. The high-speed VCSELs are arranged in a 16×15 array with a 600 µm pitch, where all VCSELs of one row have the same top mesa diameter. The first (top) mesa

diameter d_{top} of the VCSELs in the first row is 18 µm and d_{top} is 31 µm for the devices in the last row. In the first four rows d_{top} increases from row to row by $\Delta d_{top} = 0.5$ µm. For the other rows the top mesa diameters differ by $\Delta d_{top} = 1.0$ µm.

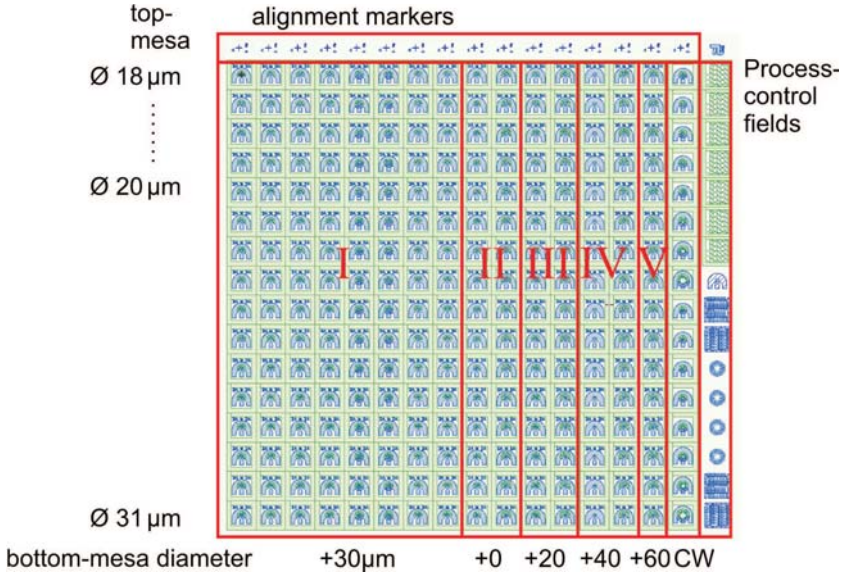

Figure 5.5.: Schematic of a complete unit cell of the TUB mask set TUB_SE2010 with systematic geometric design variations. The double mesa high-speed VCSELs are arranged in a 16 rows×15 columns array, where all devices in given row have the same top mesa diameter. The VCSELs in the groups I, II, III, and IV differ in the double mesa design and the geometric design and position of the bottom contact. The last row marked with CW contains devices with large mesa diameters up to 400 µm designed for high-power studies.

While all VCSELs in a given row have the same top mesa diameter d_{top}, the double mesa design differs for different columns. In the first eight columns (group I) the bottom mesa diameter d_{bottom} is 30 µm larger than d_{top}. Group II is formed by two columns of VCSELs without a bottom mesa, this means that these devices consist of a single pillar from top to the bottom. In the following groups III, IV, and V d_{bottom} is 20, 40, and 60 µm larger than d_{top}, respectively. A schematic of a complete unit cell is shown in Figure 5.5.

The footprint of a fully processed high-speed VCSEL device is 420 µm×420 µm, which is rather large compared to commercial VCSELs (typically 250 µm×250 µm). Since the purpose of the mask set was mainly to be able to investigate all VCSELs automatically with the home-built automatic measurement and evaluation system, a rather large contact pad size of 80 µm×80 µm was chosen. This increases the alignment tolerance for automatic probing. The computer mask layout of a VCSEL with a high-frequency pad layout is shown in Figure 5.6. In this example the VCSEL does not have a larger bottom mesa (thus it is a group II VCSEL). The inset in the upper right corner of Figure 5.6 shows

a zoom-in of the top ring contact and the source transmission line ending in a u-shape. This increased overlap between the source transmission line and the top ring-contact due to the u-shape potentially increases the yield in case residual BCB remained on the ring-contact after the BCB etch step.

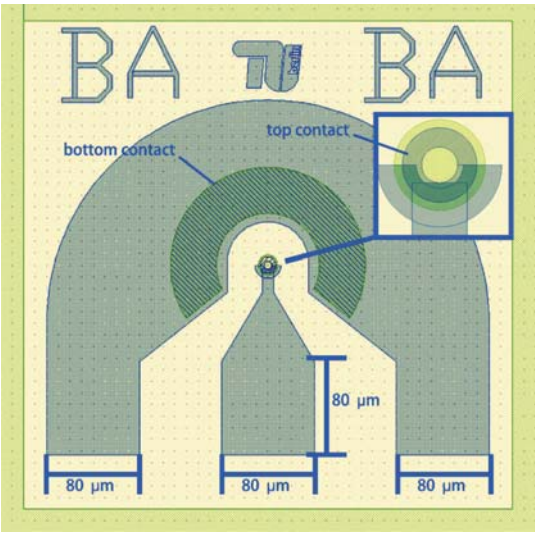

Figure 5.6.: Schematic of the high-frequency GSG layout of a high-speed VCSEL of the TUB mask set TUB_SE2010. The contact pads have dimensions of 80 µm x 80 µm and the fully processed VCSEL device has dimensions of 420 µm x 420 µm.

Figure 5.7 is an optical microscope image of a fully processed VCSEL with dimensions of 420 µm x 420 µm. The bottom mesa 2 is 30 µm larger in diameter than the top mesa 1. Figure 5.7 (right) shows a zoom-in on the VCSEL top mesa 1 and the emitting aperture.

Taking into account that some material is lost due to edge bead removal and inhomogeneous processing near the edge of the wafer piece a fully processed quarter piece of a 3-inch diameter wafer typically contains about 2000 working high-speed VCSELs. While this number of working devices is more than enough for research purposes, commercial VCSEL processing aims at a much smaller footprint in order to produce more devices from the costly epitaxial material. The developed VCSEL and mask design is suitable to be scaled down by reducing contact pitch and size and by reducing the pitch between the single devices without losing the high-speed capability of the device pad layout.

Various fully processed VCSELs with systematic geometric design variations such as different top and bottom mesa diameters and different shapes of bottom contacts are shown in the optical micrograph image in Figure 5.8.

Figure 5.9 shows the mapping of a wafer piece that is slightly smaller than a quarter 3-inch diameter wafer piece. The size of the unit cells is marked with thin green lines. The small blue to red boxes correspond to single VCSELs

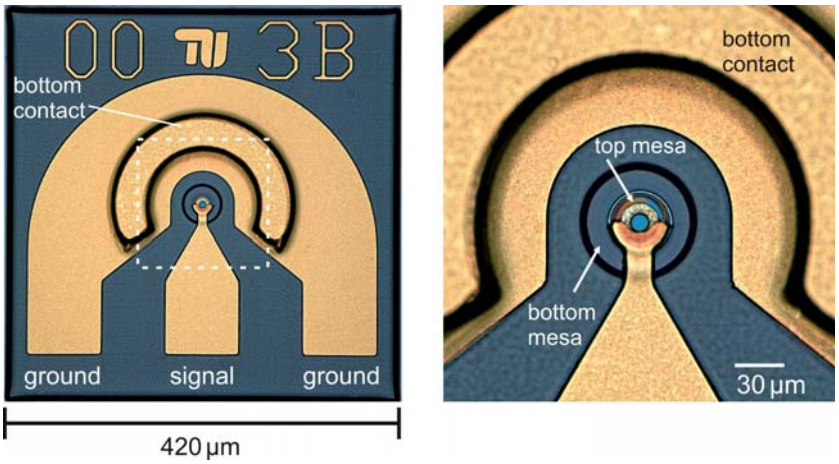

Figure 5.7.: (Left) Micrograph of a fully processed VCSEL with dimensions of 420 µm x 420 µm m with a high frequency ground-signal-ground (GSG) pad layout. (Right) Detailed view of the double-mesa structure. The second bottom mesa is 30 µm larger in diameter than the first top mesa. The apparently dark orange area in the upper left part of the top mesa is caused by residiual photo-BCB. [73] © 2013 IEEE.

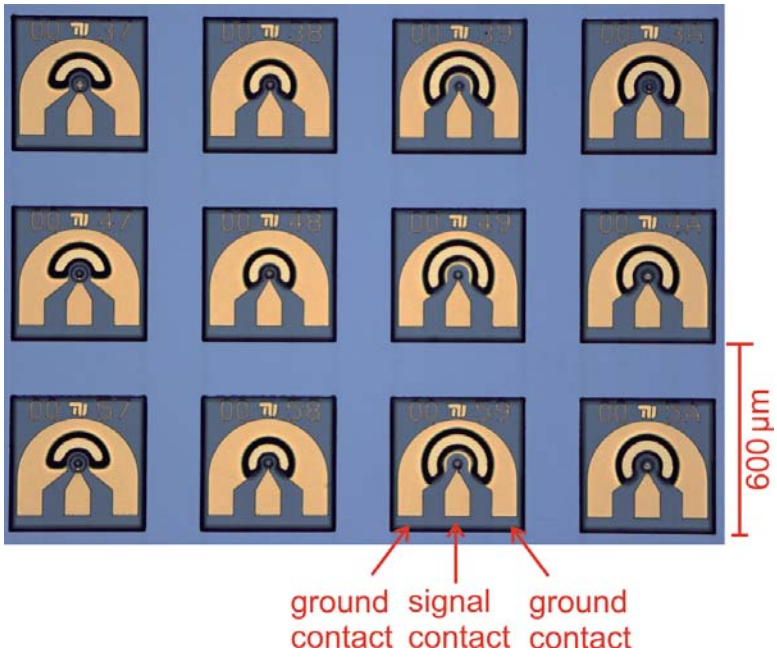

Figure 5.8.: Optical micrograph of an array of high-speed VCSELs processed using the TUB mask set TUB_SE2010 with systematic geometric design variations. [85] © SPIE 2012.

and the color code indicates the value of a certain CW parameter in this case the magnitude of the rollover current. The approximate shape of the wafer

piece is marked with a thick yellow line. Black squares stand for VCSELs that do not work. Because during a wafer piece mapping only full unit cells can be measured the mapping system also tries to measure VCSELs where no VCSELs exist. This can be seen in Figure 5.9 in the lower right corner. The prober tries to contact a VCSEL although due to the shape of the waferpiece no VCSELs exist in these off-wafer locations.

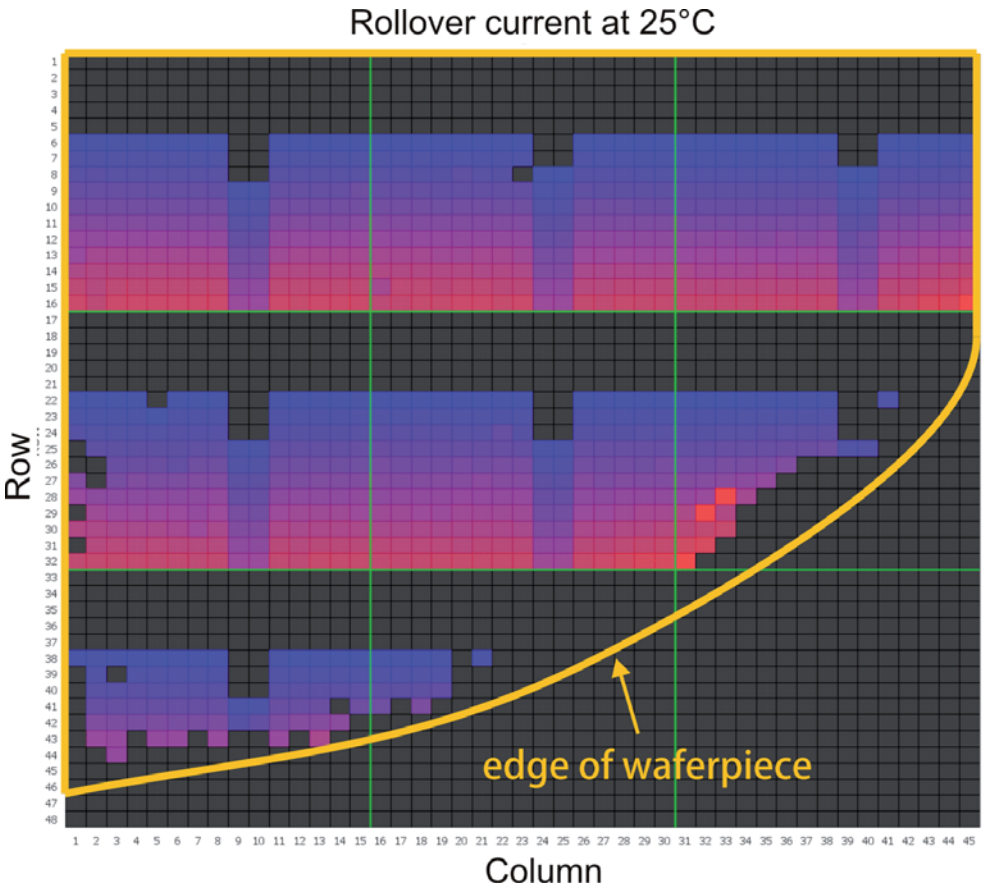

Figure 5.9.: Colorized wafer map representing the variation in the rollover current of a wafer piece slightly smaller than a quarter 3-inch diameter wafer piece. Blue colors correspond to small and red colors to large rollover currents. The VCSELs in the top 5 rows of each unit-cell do not work, because the oxide-apertures are closed.

Chapter 6.

VCSEL Design

One main focus of this thesis is to develop general principles about the energy efficiency of VCSELs in terms of dissipated or consumed energy per bit, that apply to all different designs of oxide-confined VCSELs. These principles are verified by measurements of several different epitaxial VCSEL designs emitting at 850-nm and 980-nm, respectively. In the following the design of those VCSELs that are measured for this dissertation is roughly described in order to prove that the designs are comparable to various other published designs and thus the conclusions presented here are valuable for other designs as well. The VCSELs of all three presented epitaxial VCSEL designs are processed using the same processing flow and the same lithographic mask set and thus the difference in performance of the VCSELs should be caused only by the different epitaxial designs.

6.1. Oxide-confined 850-nm VCSELs for optical interconnects

Measurement data from two different epitaxial VCSEL designs emitting at 850-nm are presented in this dissertation. The impact of the oxide-aperture diameter on the static characteristics and on the dynamic properties of oxide-confined VCSELs is demonstrated by measuring VCSEL devices of design B. Data transmission experiments are performed using VCSELs of design A and B.

The 850-nm VCSEL structures of design A and B are grown on undoped GaAs-substrates by metal-organic vapor-phase deposition (MOCVD) [86, 87, 88] by a commercial foundry [87, 89, 90, 91]. Ternary $Al_xGa_{1-x}As$ top and bottom distributed Bragg reflectors (DBRs) are used for vertical optical confinement. For Design A (B) the top and bottom DBRs consist of 23 (21) and 34.5 (33.5) $Al_{0.12}Ga_{0.88}As$ and $Al_{0.90}Ga_{0.10}As$ DBR pairs [87], respectively. Five thin compressively strained InGaAs quantum wells (QWs) [87, 88, 91, 92, 93], surrounded by $Al_xGa_{1-x}As$-barriers form the active region. Multiple oxide apertures [87, 88, 91, 92, 93] are used for lateral optical and current confinement. Current spreading regions are used [86, 87, 88, 91, 92, 93] to reduce the differential resistance of the VCSELs and thus reduce the dissipated and consumed energy at a given bias current.

Design A and B mainly differ in the QW and DBR design, resulting in larger D-factors and higher maximum modulation bandwidths f_{3dB} for Design B. Due to the different number and location of the current spreading regions,

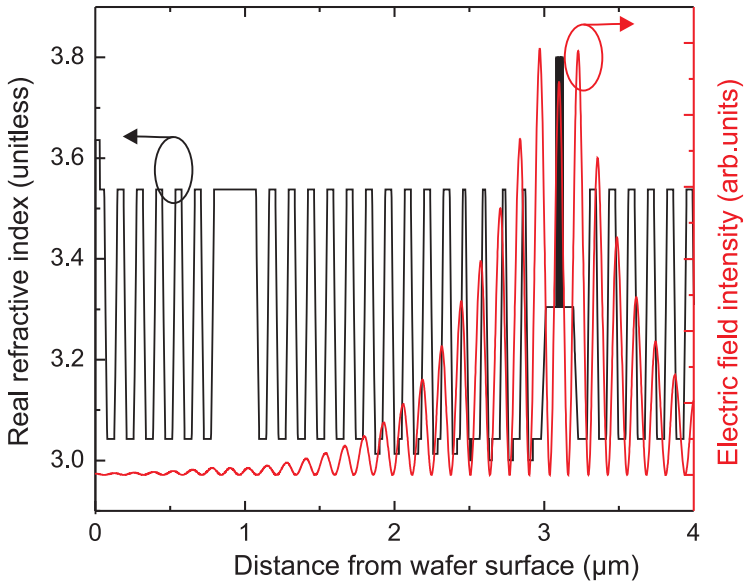

Figure 6.1.: Real refractive index and the normalized electric field intensity versus the distance from the top epitaxial surface for the complete top distributed Bragg reflector (DBR) and the active region of a 850-nm epitaxial structure with deep oxidation and multiple oxide-aperture layers. [73] © 2013 IEEE.

design B has a lower differential resistance for a given oxide-aperture diameter as compared to Design A. The real refractive index profile and the electric field intensity versus the distance from the wafer surface of the top DBR to below the cavity from Design B are plotted in Figure 6.1. The details of these two particular epitaxial designs are not the main focus of this dissertation. The 850-nm VCSELs of design B are used to demonstrate general principles that may apply for all oxide-confined VCSELs. The conclusions are verified by data transmission experiments using VCSELs of the two different 850-nm epitaxial designs.

6.2. Oxide-confined 980 nm VCSELs for optical interconnects

The 980-nm VCSEL design aims at achieving large modulation bandwidths at low consumed and dissipated power, especially at high external temperatures. The design has a short $\lambda/2$ optically-thick cavity with five InGaAs-quantum wells (QWs) and the optical confinement in the vertical direction is realized by 21.5 and 35 pairs of binary/ternary GaAs/$Al_xGa_{1-x}As$ layers for the top and bottom DBR, respectively. Two oxide-apertures are used for both lateral optical and current confinement and 7 additional deep oxidation layers are employed to reduce parasitic capacitances. Two current spreading regions are used to facilitate current spreading in the top and bottom DBR. The real refractive index and the normalized electric field intensity versus the distance

from the top epitaxial surface for the complete 980-nm VCSEL epitaxial structure is shown in Figure 6.2. In the following the design is explained in greater detail.

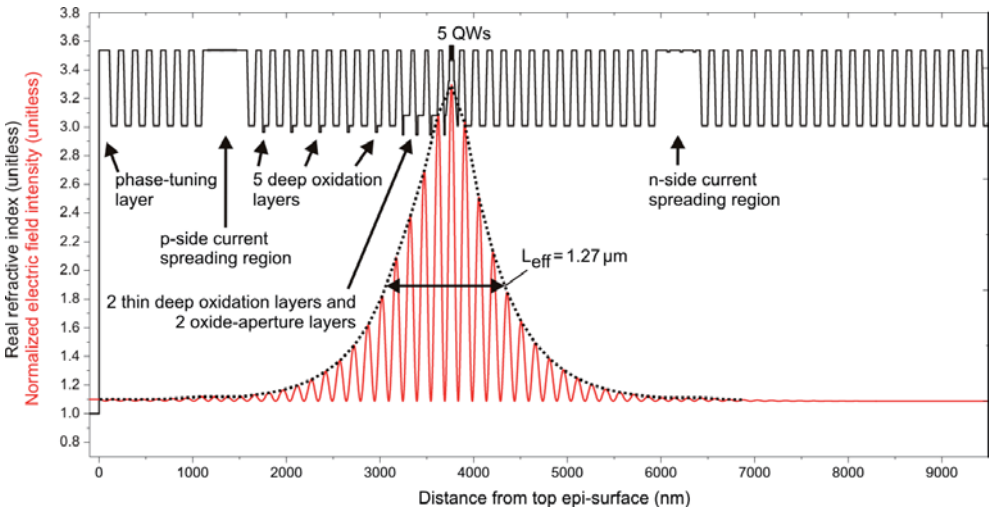

Figure 6.2.: Real refractive index and the normalized electric field intensity versus the distance from the top epitaxial surface for a complete 980-nm VCSEL epitaxial structure. The approximate effective cavity length (L_{eff}) is shown as the distance between the points at which the electric field intensity has dropped to 1/e of its maximum value is given. The two high refractive-index current-spreading regions in the top and bottom distributed Bragg reflectors are shown.

The VCSEL epitaxial structure is grown by a commercial foundry (IQE plc, Cardiff, Wales, UK) on undoped 3-inch diameter GaAs-wafers using MOCVD. To achieve the smallest possible mode-volume in the vertical direction and thus to increase the D-factor, a short $\lambda/2$ optically-thick cavity is used. The *effective* cavity length L_{eff} , determined as the distance between the two points at which the electric field intensity has dropped to the fraction of 1/e of its maximum value, is 1.27 µm. The top p-type DBR consists of 21.5 carbon doped $GaAs/Al_{0.9}Ga_{0.1}As$ $\lambda/4$-pairs with 18 nm-thick linear compositional interface gradings [58, 75]. The thermal resistivity of $Al_xGa_{1-x}As$ has a maximum at $x = 0.5$ and continuously decreases for lower and larger x-values [94], respectively. Thus GaAs and AlAs have lower thermal resistivity values than any other $Al_xGa_{1-x}As$-composition [94]. Therefore GaAs-layers are used in the DBRs for the high refractive index layers. The transparency of GaAs at 980-nm allows the use of GaAs in the top DBR which is one of the advantages of the wavelength of 980-nm as compared to 850 nm. AlAs-layers in the top DBR are not easily compatible with a process flow that includes oxide-aperture formation by *selective* wet-oxidation. Because AlAs layers oxidize faster than any other $Al_xGa_{1-x}As$-compositions with a lower aluminum-content, assuming that no extreme differences in the layer thicknesses exist, a *selective* ox-

idation process is not possible anymore for formation of the oxide-apertures. Therefore the AlAs-layers of the DBR that are not supposed to be oxidized, need to be prevented from being exposed to any oxygen during the oxidation process. Thus a reliable sealing process [95] is required for the processing of oxide-confined VCSEL structures incorporating AlAs-layers as low refractive index layers in the top DBR. The bottom silicon n-doped DBR has a similar design to the top DBR, but with 35 DBR pairs and a different modulation doping scheme. The topmost-GaAs layer of the top DBR is optically 0.18λ (physically ~50 nm) thicker than $\lambda/4$ and serves as a reflectivity phase-tuning layer. Thus the top DBR is out of phase by design.

The 8^{th} high-refractive index GaAs region counted from the wafer top surface, or the 15^{th} counted from the quantum well based active region, acts as the top current spreading region with negligible impact on the top DBR's reflectivity. This current spreading region is optically 1.75λ thick and thus optically inactive, e.g. the maxima of the optical field intensity do not decrease inside this region. Therefore the mode volume slightly increases as compared to a VCSEL without such a current spreading region. At the nodes of the electric field intensity the GaAs is highly p-doped in order to facilitate current spreading and thus help to reduce the differential resistance of the VCSELs. The current spreading regions can also be used as a contact layer and thus provide the opportunity to process VCSELs with intra-DBR contacts. The bottom DBR contains a similar current spreading region of the same thickness, but with n-doping. Similarly to the top current spreading region it is the 15th high refractive index layer counted from the active region. The current spreading regions in the top and bottom DBRs are placed further away than the point at which the electric field intensity is 1/e of its maximum value, e.g. outside of the effective cavity as defined by L_{eff}, thus the slight increase of the mode volume is negligible. The real refractive index profile and the electric field intensity versus the distance from the top epitaxial surface of the top p-type current spreading region is shown in Figure 6.3.

Five compressively strained 4 nm-thick InGaAs-QWs with 21.1% In-content surrounded by 5.1 nm-thick GaAsP-barrier layers form the active region, designed to provide large differential gain at a low current density. With a phosporus content of 10% the GaAsP-barriers are tensile strained and thus partially compensate the compressive strain of the QWs [58, 75]. The nominal QW gain-to- etalon wavelength offset at room temperature is -16 nm to improve the static and dynamic properties of the VCSEL at elevated ambient temperatures. $Al_xGa_{1-x}As$-cladding layers with an aluminum-content of 38% are used. Next to the p-doped claddding layer, a 10 nm-thick thin $Al_xGa_{1-x}As$ deep oxidation layer with an aluminum-content of 98%, followed by two 20 nm-thick oxide-aperture layers of the same material composition and again a 10 nm-thick deep oxidation layer are employed for reducing parasitic capacitances and optical and current confinement, respectively. The thickness and material composition of neighbor layers greatly impact the oxidation rate

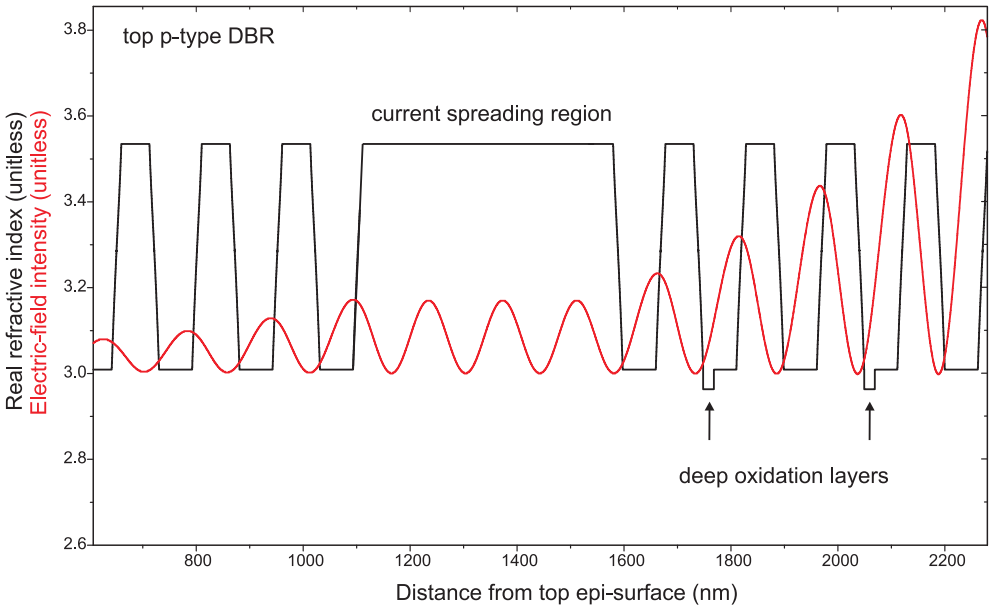

Figure 6.3.: Real refractive index and the normalized electric field intensity versus the distance from the top epitaxial surface of of a 980-nm VCSEL epitaxial structure. The high refractive index current-spreading region and the top two deep oxidation layers of the top p-type distributed Bragg reflector are labeled.

and the taper of the oxide-aperture and deep oxidation layers. The material compositions of the neighbor layers next to the oxide-aperture layer and the thin deep-oxidation layers are similar. The layers only slightly differ in thickness and composition. The neighbor layers closer to the active region consist of $Al_xGa_{1-x}As$ with an aluminum-content of 80%. For the two 20 nm-thick oxide-aperture layers the $Al_{0.8}Ga_{0.2}As$ layers have a nominal thickness of 60.6 nm and for the bottom and top thin oxidation layers the neighbor layer thickness is 10.0 and 65.2 nm, respectively. There is no compositional grading, but a step of the Al-content from 80 to 98%, followed by a linear compositional-grading from 90 to 0% aluminum, e.g. from $Al_{0.9}Ga_{0.1}As$ to GaAs. This compositional grading is the same for all DBR pairs in the top and bottom DBR and has a thickness of 18 nm as mentioned previously. The real refractive index profile and the electric field intensity versus the distance from the top epitaxial surface of the active region is shown in Figure 6.4.

The calculated power reflectance value at 980-nm is 99.23% for the top DBR and 99.99% for the bottom DBR of the VCSEL. The calculated power reflectance spectra for the top and bottom DBR of the 980-nm VCSEL epitaxial design are shown in Figure 6.5 (a) and (b), respectively.

As compared to the oxide-aperture layers and the thin deep oxidation layers the five thicker deep oxidation layers consist of 20 nm-thick $Al_{0.96}Ga_{0.04}As$-layers. The neighbor $Al_xGa_{1-x}As$ layers closer to the active region are 42.1 nm-

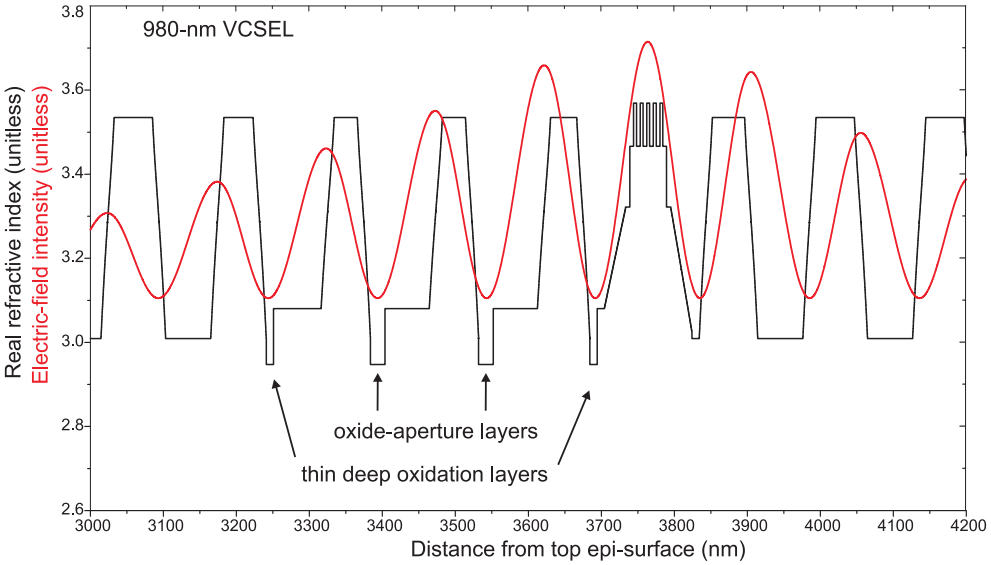

Figure 6.4.: Real refractive index and the normalized electric field intensity versus the distance from the top epitaxial surface to below the QW active region of a 980-nm VCSEL epitaxial structure. One thin deep oxidation layer is positionend above and below of the two oxide-aperture layers. The deep oxidation and oxide-aperture layers are positioned in the nodes of the electric field intensity whereas the five quantum wells are positioned in the antinode of the electric field intensity. A graded-index separate-confinement heterostructure active region design is used.

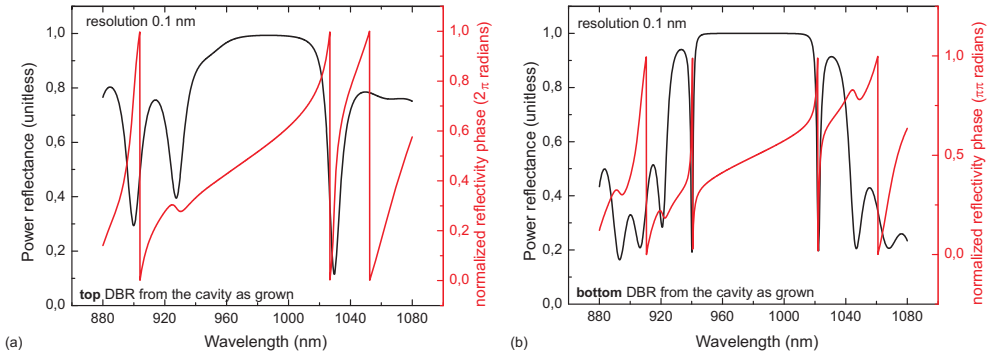

Figure 6.5.: Calculated power reflectance at normal incidence versus wavelength for the grown (a) top and (b) bottom DBR of the 980-nm VCSEL, as seen from the optical cavity.

thick and have an aluminum content of 90%. The neighbor layers on the other side are 18 nm-thick linear compositional gradings from an aluminum content of 90 to 0% as for all the other DBR layers. The design of the thicker deep oxidation layers leads to a rather short taper with 0.15-0.20 µm length, whereas the taper of the thin deep oxidation layers is 1.93 µm long and correspondingly thinner. Also the tip of the oxidized aperture layer is thinner for the 10 nm-thin

$Al_{0.98}Ga_{0.02}As$-layers as compared to the 20 nm-thick $Al_{0.96}Ga_{0.04}As$-layers. After a 66 min oxidation in the oxidation furnace at 420°C at 50 mbar the oxidation-depth of the thin and thick deep oxidation layers differ only by 150-200 nm. A scanning electron microcsope (SEM) image of the 20 nm-thick $Al_{0.96}Ga_{0.04}As$ deep oxidation layers are shown in greater detail together with the thin deep oxidation layers after 66 min oxidation at 420°C at 50 mbar in Figure 2.22 in Chapter 5.2.

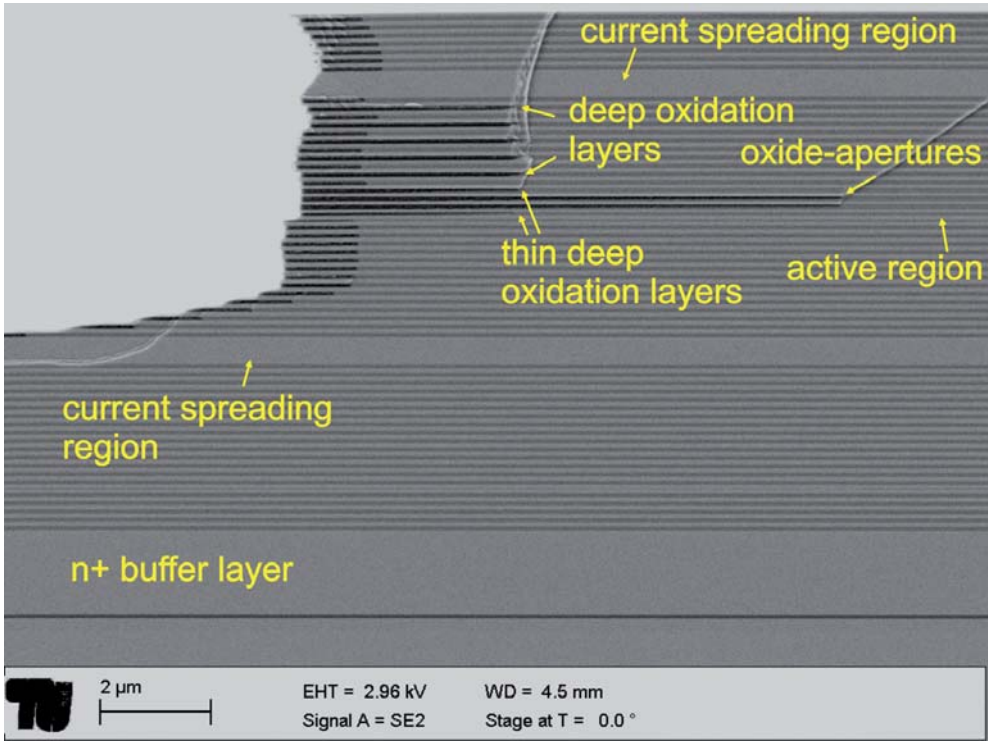

Figure 6.6.: Scanning electron microscope image of a cleaved wafer piece of the 980-nm VCSEL design that was oxidized for 66 min at 420°C and at 50 mbar. The oxidized layers with high aluminum content can be clearly seen as dark layers. The rough side-wall indicates that in this case the dry-etch process for defining the first mesa did not work perfectly at desired.

The SEM image of a cleaved test wafer piece after the first mesa etch and after a 66 min oxidation shows all deep oxidation layers, the oxide-aperture layers, and the two current spreading regions and is given in Figure 6.6. The relatively rough side-wall indicates that in this test process run the dry-etch process for defining the top first mesa did not work perfectly. But given the oxidation depth of the oxide-aperture layers of 9.8 µm the rough side-walls shouldn't negatively impact the performance of the VCSEL. The oxidation depth of all deep oxidation layers varies only by 0.15-0.20 nm and ranges from ~3.85 to 4.05 µm. With a smoother sidewall the deep oxidation layer depth would become even more homogeneous. The dry-etch process of the test-

piece shown in Figure 6.6 as well as of the processed 980-nm VCSEL devices presented in the following Chapter is stopped within the bottom n-doped GaAs buffer layer to allow the placement of ohmic contacts onto this buffer layer.

In order to investigate the impact of the photon lifetime τ_p on the static and dynamic VCSEL properties, τ_p is reduced by depositing 55 nm of Si_xN_y with a 100°C ICP-PECVD process on top of the outcoupling DBR. The photon lifetime τ_p can be calculated in the following way. Using Equation 3.2 from Chapter 3 that describes the change of the photon density with time, assuming a steady-state condition ($dN_p/dt = 0$), and neglecting the spontaneous emission R'_{sp} that contributes to the laser mode yields [39]:

$$\frac{1}{\tau_p} = v_g \Gamma g_{th} \tag{6.1}$$

where v_g is the group velocity, g_{th} is the threshold gain as given by Equation 2.20 in Chapter 2, and Γ is in the one-dimensional case the ratio of the cavity length and the *effective* cavity length L_{cav}/L_{eff}. Inserting Equation 2.20 into Equation 6.1 yields:

$$\frac{1}{\tau_p} = v_g \left(\frac{L_{cav}}{L_{eff}} \alpha + \frac{1}{2L_{eff}} ln \left(\frac{1}{R_{top} R_{bot}} \right) \right) = v_g \left(\frac{L_{cav}}{L_{eff}} \alpha + \alpha_m \right) \tag{6.2}$$

where α_m is the mirror loss as described in Chapter 2 and α stands for all the other optical losses in the cavity such as absorption and scattering. Thus in order to be able to calculate the photon lifetime the effective cavity length L_{eff} and the losses α have to be determined. The effective cavity length L_{eff} is shown for the 980-nm VCSEL in Figure 6.2 as determined by the distance between the two points at which the calculated electric field intensity has reduced to 1/e of the maximum value achieved in the cavity. L_{eff} can also be calculated using:

$$L_{eff} = L_{top} + L_{cav} + L_{bot} \tag{6.3}$$

where L_{cav} is the geometric cavity length and L_{top} and L_{bot} are the phase penetration depths of the electric field intensity into the top and bottom DBR, respectively. L_{cav} is given by the epitaxial structure and L_{top} and L_{bot} can be calculated by [96]:

$$L_p^{top,bot} = \frac{\lambda_0^2}{4\pi \langle n_{gr} \rangle} \frac{d\varphi}{d\lambda} \tag{6.4}$$

where λ_0 is the design wavelength, $\langle n_{gr} \rangle$ is the spatial average of the group index of refraction of the cavity and $d\varphi/d\lambda$ is the slope of the mirror reflectivity phase versus the wavelength at the design wavelength λ_0. Thus the phase penetration depth into the top and bottom DBR differ only due to their different phase-slopes $d\varphi/d\lambda$. The phase spectra of the top and bottom DBRs

of the 980-nm VCSELs are plotted in Figure 6.5 (a) and (b), respectively. Finally, α can be determined by changing the top DBR reflectance of a VCSEL and evaluating the LI-slope for different mirror losses α_m. This has been done for the 980-nm VCSEL [97] and the calculated photon lifetimes in this dissertation are based on this evaluation.

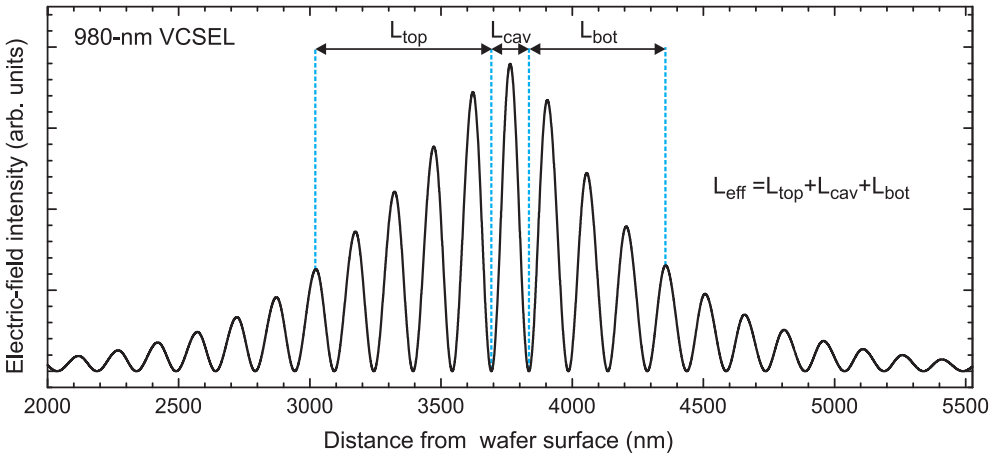

Figure 6.7.: Calculated electric field intensity versus the distance from the wafer surface for the as-grown 980-nm VCSEL. The cavity length L_{cav} and the approximate mirror penetration depths L_{top} and L_{bot} are indicated.

At the design wavelength of 980-nm the measured refractive index of the Si_xN_y is 1.896. The photon lifetime of the VCSEL without further modification of the top DBR is 3.7 ps and reduces to 1.8 ps when 55 nm of Si_xN_y is added to the topmost GaAs-layer. The photon lifetime of 1.8 ps is close to the local minimum of τ_p, which is calculated to be achieved at a Si_xN_y-thickness of 59.6 nm. The calculated difference of τ_p for 55.0 and 59.6 nm of Si_xN_y is only 0.01 ps which is certainly smaller than the accuracy of the control of the optical thickness of the additional Si_xN_y-layer. The calculated photon lifetime versus the thickness of the removed top DBR material or the thickness of the added Si_xN_y is plotted in Figure 6.8.

The calculated power reflectance at 980-nm is 99.23% for the as-grown structure and reduces to 98.38% for an additional layer of 55 nm of Si_xN_y. The local minimum of the power reflectance is 93.36%. The calculated power reflectance at 980-nm versus the removed top DBR material thickness or the thickness of the added Si_xN_y is shown in Figure 6.9.

Double-mesa VCSELs processed from this epitaxial design are used in the following Chapters for oxide-aperture diameter dependent analysis of the temperature stability of the static and dynamic properties as well as of the energy efficiency, e.g. the *EDR* and *HBR* as defined in Equations 4.7 and 4.8 on page 48. This epitaxial design enables VCSELs with record-large f_{3dB} at 85°C and by far the fastest 980-nm VCSELs produced to date.

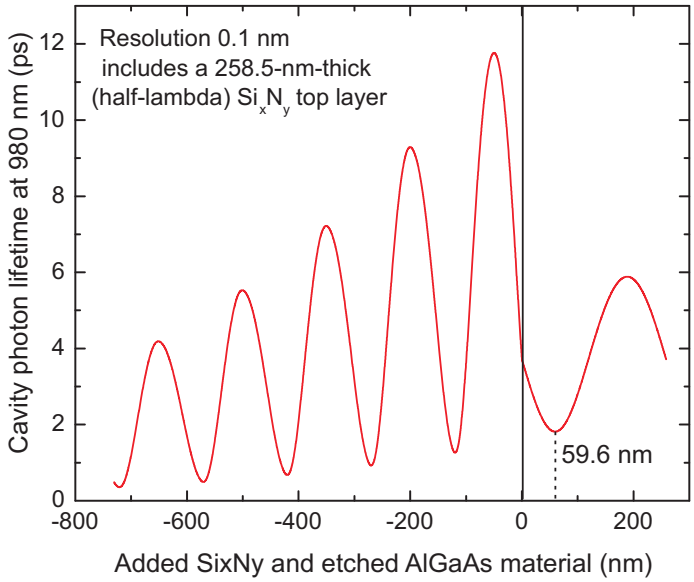

Figure 6.8.: Calculated photon lifetime τ_p versus the etch depth of removed mirror material or the thickness of added Si_xN_y.

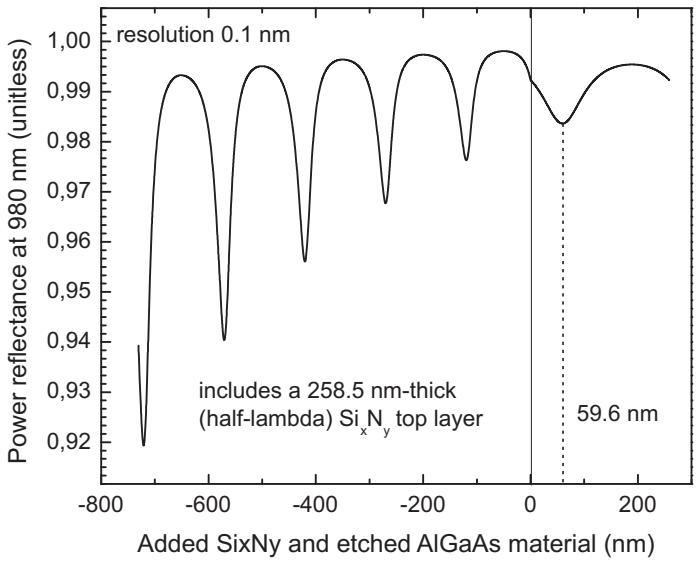

Figure 6.9.: Calculated power reflectance at 980-nm versus the etch depth of removed mirror material or the thickness of added Si_xN_y.

Chapter 7.

850-nm VCSEL results

Optical interconnects based on 850-nm oxide-confined VCSELs and multimode optical fiber (MMF) dominate the short-range (up to 300 m) data communication in modern data centers and supercomputers. At distances larger than 300 m optical interconnects (OIs) based on edge-emitting distributed feedback (DFB) lasers emitting at about 1300 nm and single-mode fiber are typically used. The power consumption of such an edge-emitting laser is at least an order of magnitude larger than that of VCSELs, so replacing edge-emitter based interconnects with energy-efficient VCSEL-based interconnects can save a large amount of energy. The new larger "mega-data centers" require 25 Gb/s transmission across distances of 1-2 km of MMF.

The dependence of the most important static and dynamic VCSEL properties such as the threshold current and power consumption on the oxide-aperture diameter of the VCSEL is investigated at room temperature in the following Sections. The energy efficiency of VCSELs with different oxide-aperture diameters is compared by investigating the ratio of the consumed and dissipated energy over the modulation bandwidth $f_{3\mathrm{dB}}$ and it is demonstrated that VCSELs with small oxide-aperture diameters achieve much smaller power-to-bandwidth ratios than similar VCSELs with larger oxide-aperture diameters especially at small current-densities. Using the M-factor as a parametric factor the optimal oxide-aperture diameter for operation at different *EDR*-values is determined. Finally, the general principles derived in this chapter are verified by large signal modulation experiments, resulting in record energy-efficient data transmission across various lengths of multimode optical fiber.

7.1. Static properties

The impact of the oxide-aperture diameter on the static (continuous wave, CW) *LIV*-characteristics of VCSELs has been studied since the realization of the first oxide-confined VCSELs and the increased scattering loss of very small oxide-aperture diameters has been identified as a severe drawback for VCSELs with small oxide-aperture diameters [83]. Large optical output powers at simultaneously low current densities are usually desired for application in optical interconnects, which has led to the use of VCSELs with large oxide-aperture diameters that also achieve large wallplug efficiencies. But as the energy efficiency, e.g. the energy consumption and dissipation per transmitted bit, becomes at least as important as the bit rate, the CW energy consumption is

gaining importance. Thus in the following Sections one main focus is on the trade-offs between a low CW energy consumption of the oxide-confined VCSELs and all other important CW parameters including optical output power, current density, and differential resistance.

7.1.1. LIV-characteristics at room temperature

The static *LIV*-characteristics of a complete waferpiece (a quarter of a 3-inch diameter wafer) of VCSEL design B are measured automatically at room-temperature using our home-built automatic wafer prober. In order to demonstrate the impact of the oxide-aperture diameter on the VCSEL performance a detailed evaluation of the *LIV*-characteristics is performed on a column of 9 VCSELs with different oxide-aperture diameters ranging from 2.5 to 9 µm. This array of VCSELs is located close to the center of the processed wafer piece. The oxide-aperture diameters of the 4 smallest VCSELs increase in steps of 0.5 µm (from 2.5 to 4 µm) whereas the oxide-aperture diameters of the larger VCSELs increase in steps of 1.0 µm (from 4 to 9 µm). The diameter of the first mesa is 18.5, 19, 19.5, and 20 µm for the VCSELs with oxide-aperture diameters of 2.5, 3, 3.5, and 4 µm, respectively. For the larger oxide-aperture diameter VCSELs the first mesa diameter increases in steps of 1 µm as does the oxide-aperture diameter. For all VCSELs the second mesa diameter is 60 µm larger in diameter than the first mesa diameter. The VCSEL with the smallest oxide-aperture diameter of 2.5 µm has a low threshold current I_{th} of 150 µA. I_{th} increases to 800 µA for the VCSEL with an oxide-aperture diameter of 9 µm. For VCSELs with oxide-aperture diameters of approximately 5 µm and larger the threshold current density J_{th} is around 1.3 kA/cm^2, whereas J_{th} increases with decreasing oxide-aperture diameter to 3.1 kA/cm^2 for the VCSEL with an oxide-aperture diameter of 2.5 µm. An increased J_{th} for the VCSELs with smaller oxide-aperture diameters is a well-known effect and related to the increased scattering loss of such small oxide-aperture diameter devices [83, 84]. The static *LIV*-characteristics at 25°C for 850 nm VCSELs with oxide-aperture diameters ranging from 2.5 to 9 µm are shown in Figure 7.1 (a) and the dependence of I_{th} and J_{th} on the oxide-aperture diameter is given in Figure 7.1 (b).

The threshold voltage V_{th}, defined as the voltage at I_{th} is 1.55 V for VCSELs with oxide-aperture diameters of 5 µm and larger. Similarly to J_{th} the value of V_{th} increases for VCSELs with decreasing oxide-aperture diameters smaller than 5 µm and is 1.71 V for the VCSEL with an oxide-aperture diameter of 2.5 µm. The threshold power P_{th} is defined as the product of I_{th} and V_{th} and is therefore the minimum of electrical power P_{el} that is required to operate the diode in the laser mode. Despite the increased V_{th}, the threshold power is smallest for the VCSEL with the smallest oxide-aperture diameter and increases with increasing oxide-aperture diameter. P_{th} is 0.26 mW for the VCSEL with an oxide-aperture diameter of 2.5 µm and increases to 1.24 mW

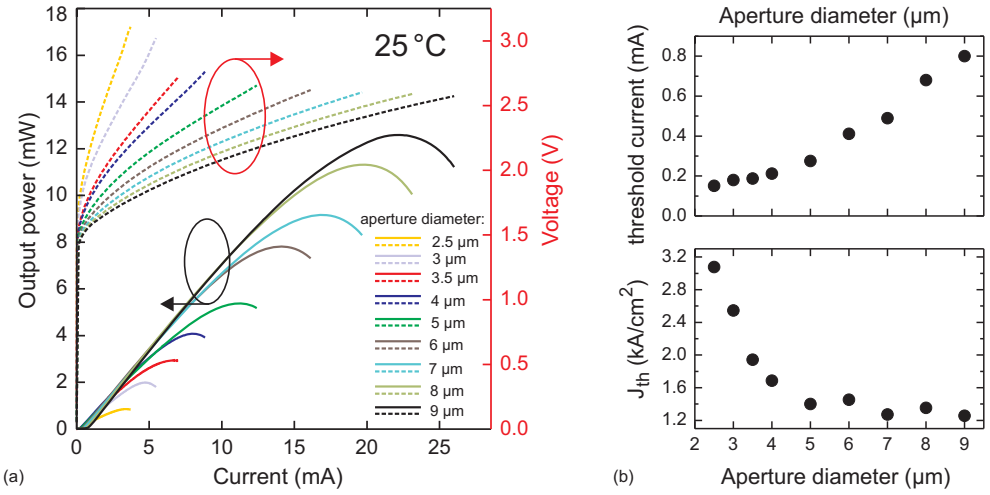

Figure 7.1.: Static *LIV*-characteristics at 25°C (a) of 850-nm VCSELs with oxide-aperture diameters ranging from 2.5 to 9 µm. (b) Threshold current I_{th} (top) and threshold current density J_{th} (bottom) versus oxide-aperture diameter. [73] © 2013 IEEE.

for the VCSEL with an oxide-aperture diameter of 9 µm. A low P_{th} is one key parameter to enable energy-efficient high-speed operation at low energy consumption per bit.

The differential resistance R_{d} of the VCSELs is evaluated at the rollover current I_{RO} (current at the maximum of the optical output power) of each VCSEL. R_{d} varies with the oxide-aperture diameter, because it is inversely proportional to the aperture area of the VCSEL. Therefore VCSELs with smaller oxide-aperture diameters below 5 µm have a significantly larger R_{d} as compared to similar VCSELs with larger oxide-aperture diameters. R_{d} is 350 Ω for the VCSEL with an oxide-aperture diameter of 2.5 µm and reduces to below 50 Ω for VCSELs with oxide-aperture diameters of approximately 5 µm or larger. The thermal rollover current I_{RO} of the VCSEL increases linearly with increasing oxide-aperture diameter, from 3.38 mA for the 2.5 µm oxide-aperture diameter VCSEL to 22.19 mA for the VCSEL with an oxide-aperture diameter of 9 µm.

The maximum values of the static efficiencies, e.g. the differential quantum efficieny (DQE) and the wallplug efficiency (WPE), both depend on the oxide-aperture diameter. For VCSELs with oxide-aperture diameters of approximately 5 µm and larger the maximum DQE and WPE saturate and are 50-55% and 35%, respectively. For smaller oxide-aperture diameter VCSELs these values decrease with decreasing oxide-aperture diameter. The maximum DQE and WPE are 23% and and 15%, respectively, for the VCSEL with an oxide-aperture diameter of 2.5 µm. It is important to note that the static DQE and WPE values alone are not sufficient to draw proper conclusions about the

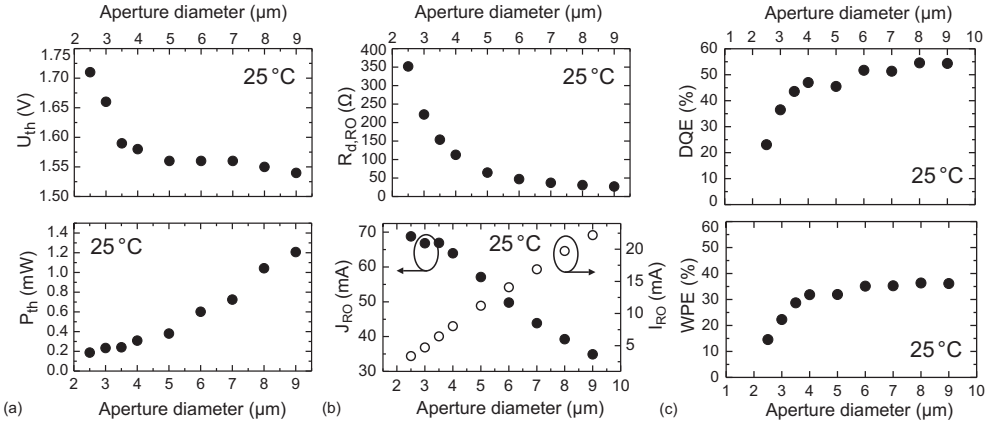

Figure 7.2.: (a) Threshold voltage V_{th} (top) and threshold power P_{th} (bottom); (b) differential resistance at rollover current $R_{\mathrm{d,RO}}$ (top), rollover current I_{RO} and rollover current density J_{RO} (bottom); (c) maximum differential quantum efficiency (DQE) (top) and maximum wall plug efficiency (WPE) (bottom) versus the oxide-aperture diameter. All values are derived from the same devices shown in Figure 7.1 (a). [73] © 2013 IEEE.

energy efficiency in terms of energy per bit, because these efficiencies do not inlcude any information about the dynamic properties of the VCSEL.

For commercial applications in an optical interconnect the operating current density J of the VCSEL is more important than an absolute current value, because it is directly related to the VCSEL reliability (lifetime) [31]. Operation at increased J can dramatically limit the device lifetime. The rollover current density J_{RO} is largest for the smallest oxide-aperture diameter VCSELs and decreases linearly from 68.8 to 34.9 kA/cm^2 for the largest VCSEL with an oxide-aperture diameter of 9 µm. The dependence of V_{th}, P_{th}, R_{d}, I_{RO}, and J_{RO} on the oxide-aperture diameter are given in Figure 7.2 (a) and (b). The maximum DQE and WPE versus the oxide-aperture diameter are shown in Figure 7.2 (c) top and bottom, respectively.

While the J_{th} values differ at most by 1.8 kA/cm^2, J_{RO} is reduced by 33.9 kA/cm^2 when the oxide-aperture diameter increases from 2.5 to 9 µm. Therefore VCSELs with smaller oxide-aperture diameter can operate in a much larger current density range as compared to VCSELs with larger oxide-aperture diameters. If operation at a given current density is specified for a commercial application, VCSELs with smaller oxide-aperture diameter therefore have the advantage of operating further away from J_{RO} as compared to VCSELs with larger oxide-aperture diameter.

In current commercial VCSEL-based optical interconnects typically VCSELs with oxide-aperture diameters of ~7-11 µm are employed. VCSELs with such large oxide-aperture diameters have the advantage of a small differential resistance and a large output power at a simultaneously low current density. In addition, the differential resistance does not deviate very much across an

entire 4-inch diameter wafer even if the oxidation is slightly inhomogeneous, making such VCSELs easier to process in large volumes than VCSELs with a significantly smaller oxide-aperture diameter. While using VCSELs with a large oxide-aperture diameter is advantageous when only aiming at high bit rate operation at low current density and high output power, it becomes detrimental for simultaneously achieving a very energy-efficient operation with low energy consumption or dissipation per bit.

The optical output power is plotted versus the current density in Figure 7.3 (a) for the same set of VCSELs with oxide-aperture diameters ranging from 2.5 to 9 µm that are shown in Figure 7.1. At a given current density the optical output power increases with an increase of the oxide-aperture diameter of the VCSEL. Therefore if a high output power at a simultaneously low current density is required by an application, VCSELs with a comparably large oxide-aperture diameter have to be used. But it can also clearly be seen that the thermal rollover is reached at much smaller current densities for VCSELs with larger oxide-aperture diameters, which is potentially disadvantageous for temperature-stable device performance (see: Section 8.1).

Because the differential resistance is larger for smaller oxide-aperture diameters, those VCSELs require more electrical power P_{el} at a given bias current than VCSELs with larger oxide-aperture diameters and therefore smaller R_{d}. Plotting P_{el} versus J, shows that at any given J, the electrical power P_{el} increases with increasing oxide-aperture diameter of the VCSEL. Therefore if it is desired to operate VCSELs at simultaneously a low current-density and a low electrical power consumption, VCSELs with smaller oxide-aperture diameters are beneficial. The only two drawbacks are lower optical output power and a larger differential resistance.

In addition to current-confinement, the oxide-aperture also leads to optical confinement, because of the difference in the refractive index of the oxidized and non-oxidized material. The oxide-aperture diameter has therefore a large impact on the number of lasing modes and on the optical output power of a VCSEL. The optical emission spectra of VCSELs with oxide-aperture diameters of 3.5, 4, and 5 µm are shown at the bias currents of error-free 25 Gb/s data transmission (Section 7.3.1) in Figure 7.4. The number of lasing modes increases with increasing oxide-aperture diameter leading to a corresponding increase of the spectral-width $\Delta\lambda$ which is 0.08, 0.22, and 0.42 nm for the 3.5, 4, and 5 µm oxide-aperture diameter VCSELs, respectively. The side-mode suppression ratio decreases with increasing oxide-aperture diameter and is 29, 16, and 8 dB for the 3.5, 4, and 5 µm oxide-aperture diameter VCSELs, respectively. The spectral-width limits the maximum possible transmission distances across multimode optical fiber (MMF). Thus small spectral-width values and large side-mode suppression ratios are desired for data transmission across long distances of MMF. Ideally single-mode emission enables the longest MMF transmission distances. But single-mode lasers usually suffer from low output power. The most important figures-of-merit for the optical

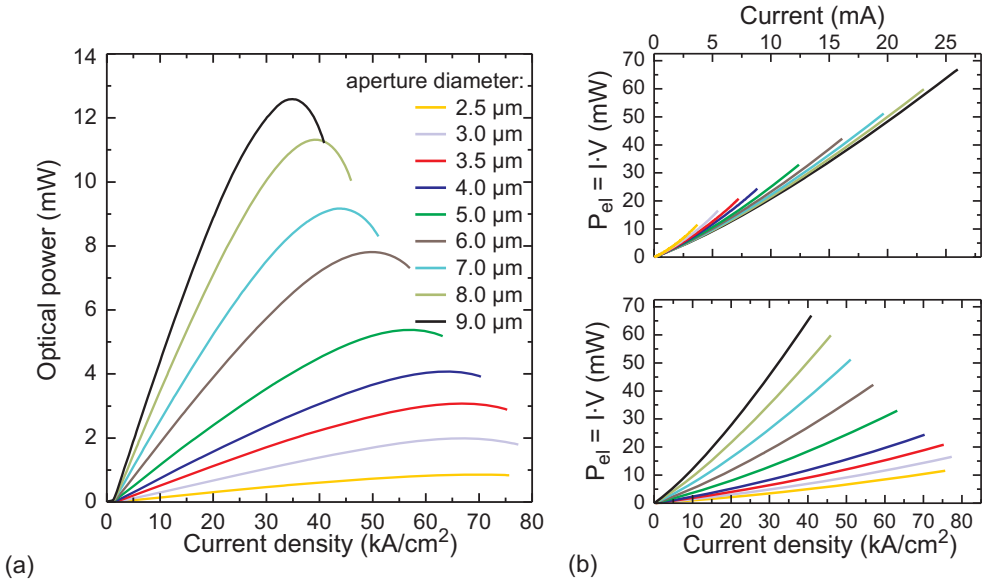

Figure 7.3.: Optical output power versus current density (a) for VCSELs with oxide-aperture diameters ranging from 2.5 to 9 µm at 25°C. (b) Electrical power P_{el} versus bias current (top) and versus current density for the same devices as shown in (a). [98] © 2014 SPIE.

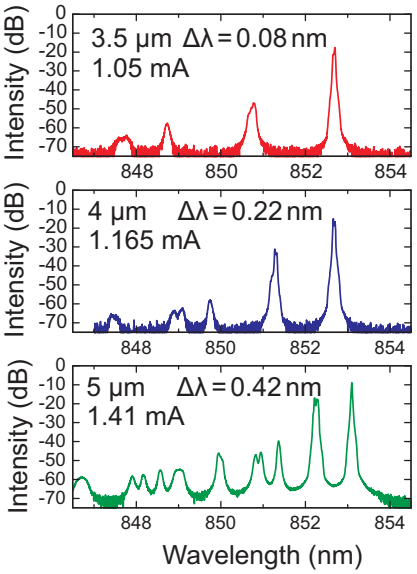

Figure 7.4.: Optical emission spectra of VCSELs with oxide-aperture diameters of 3.5, 4.0, and 5.0 µm at the bias current of error-free 25 Gb/s operation. The spectral-width $\Delta\lambda$ increases with increasing oxide-aperture diameter. [86] © IET 2012.

emission spectra are summarized in Table 7.1.

Table 7.1.: Side-mode suppression ratio and spectral width of 850-nm VCSELs with oxide-aperture diameters of 3.5, 4.0 and 5.0 µm.

Oxide-aperture diameter (µm)	3.5	4.0	5.0
Current density (kA/cm^2)	11	9	7
Side-mode suppression ratio (dB)	29	16	8
Spectral width $\Delta\lambda$ (nm)	0.08	0.22	0.42

Large oxide-aperture diameter devices have lower rollover current densities. As will be shown in the next Chapter these large oxide-aperture diameter VCSELs need to be operated close to the rollover current, e.g. at large currents, in order to achieve large bandwidth values. Because the rollover current density is quite low, this will still result in low current density operation. While this is advantageous for VCSELs to achieve low current density operation with large optical output powers, it is detrimental for energy-efficient operation, because these VCSELs have a huge energy consumption. Operating a VCSEL close to its thermal rollover current is also detrimental for temperature-stable operation at changing or high ambient temperatures.

7.2. Small-signal modulation response

In order to investigate and determine the impact of the oxide-aperture diameter on the dynamic energy efficiency of VCSELs, small-signal modulation response (S21) measurements of the VCSEL array shown in Figure 7.1 are performed using an HP 8722C network analyzer and a New Focus 1434-50-M photodetector module. The S21-curves are fitted to Equation (3.14) to extract f_r and γ, and the f_{3dB} values are directly determined from the S21-measurement curves. The main goal of the following evaluation is to determine the impact of the oxide-aperture diameter and the bias current on the energy efficiency of the VCSELs and not to investigate the factors that limit the maximum modulation bandwidth and thus bit rate of the VCSELs. Therefore the focus is on the performance of the VCSELs at comparably low bias currents, where the maximum f_{3dB} value might not yet be reached for VCSELs with larger oxide-aperture diameters. Thus the effects that limit the maximum modulation bandwidth of the VCSELs are not further discussed in this Chapter.

7.2.1. D-factor and MCEF versus oxide-aperture diameter

The D-factors and modulation-current efficiency factor (MCEF) values [71], obtained by linear fits of the dependence of the relaxation resonance frequency f_r and the modulation bandwidth f_{3dB} on the square-root of the current above the threshold current, are valuable intrinsic dynamic VCSEL figures-of-merit for comparing the dynamic properties of VCSELs. As explained in Chapter

3, the D-factor can be directly related to the rate-equations, whereas this is generally not the case for f_{3dB}. As shown in this Section the MCEF is proportional to the D-factor, but only for oxide-aperture diameters larger than a certain oxide-aperture diameter, in our case approximately 4 µm.

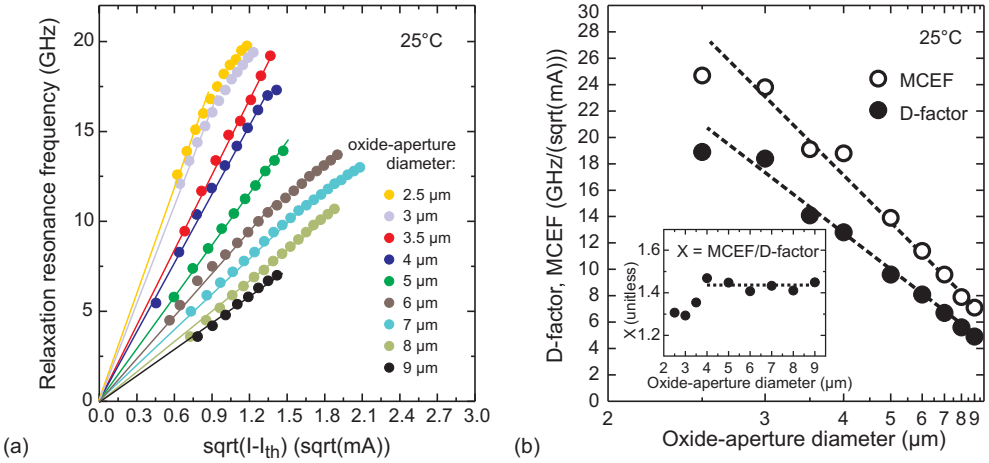

Figure 7.5.: Relaxation resonance frequency f_r versus the square-root of the current above threshold current (a) at 25°C of 850-nm VCSELs with oxide-aperture diameters ranging from 2.5 to 9 µm. The colorful lines indicate the linear fits for obtaining the D-factors. The slope of the fits decreases with increasing oxide-aperture diameters [73] © 2013 IEEE. (b) D-factor and modulation current efficiency factor (MCEF) versus the oxide-aperture diameter plotted on a nonlinear scale. Inset: the ratio of the MCEF and the D-factor versus the oxide-aperture diameter.

The values of f_r versus the square-root of the current above threshold current for the 9 different VCSELs are shown in Figure 7.5 (a). For simplicity and clarity of the plots, the f_r values are only shown before the saturation of f_r occurs. The VCSELs are investigated in the bias current range where f_r follows the linear theory as discussed in Sections 3.1 and 3.2. The straight lines show the linear fits from which the respective D-factors are obtained. The slopes of the shown fits and therefore the D-factors of the VCSELs decrease with increasing oxide-aperture diameter. The D-factor is 19.3 GHz/$\sqrt{\text{mA}}$ for the VCSEL with the smallest oxide-aperture diameter of 2.5 µm and reduces to 5.0 GHz/$\sqrt{\text{mA}}$ for the VCSEL with an oxide-aperture diameter of 9 µm. In Figure 7.5 (b) the D-factor for the 9 different VCSELs is plotted versus the oxide-aperture diameter. The shown linear fit, using a reciprocal scale for the x-axis, demonstrates that the D-factor is inverse proportional to the oxide-aperture diameter as given in Equation (3.12) [39, 33]. Therefore VCSELs with smaller oxide-aperture diameter achieve larger f_r values at lower bias currents above the threshold current than similar VCSELs with larger oxide-aperture diameters. The MCEF values versus the diameter of the oxide-aperture are also shown in 7.5 (b). For VCSELs with oxide-aperture diameters of 4 µm and

larger the MCEF is, similarly to the D-factor, inversely proportional to the oxide-aperture diameter. Consequently VCSELs with smaller oxide-aperture diameter reach larger f_{3dB} values at the same currents above the threshold current than VCSELs with larger oxide-aperture diameter. The ratio X of the MCEF- and D-factor versus the oxide-aperture diameter is shown as an inset in Figure 7.5 (b). For VCSELs with oxide-aperture diameters of 4 µm and larger X is around 1.44 (dashed line) whereas it is significantly smaller for the VCSELs with smaller oxide-aperture diameters. X is 1.29 for the VCSEL with an oxide-aperture diameter of 3.0 µm.

In addition to having larger D-factors and MCEF-values VCSELs with smaller oxide-aperture diameters also have smaller threshold currents I_{th} and threshold powers P_{th} as compared to VCSELs with larger oxide-aperture diameters as is discussed on page 80. Therefore VCSELs with smaller oxide-aperture diameter are especially well-suited for achieving large f_{3dB} at low currents and electrical powers. For application in an energy-efficient optical interconnect not only f_{3dB} is of importance. The energy-consumption per bit, the power dissipated as heat, and the optical output power are important parameters as well that can be detrimental for VCSELs that will be integrated in future energy-efficient densely packed optical interconnects. While it is crucial that a large bandwidth is achieved at a very low dissipated and consumed energy, the only drawback of the low output power of VCSELs with small oxide-aperture diameter is that sensitive detectors are required to ensure error-free operation of the optical link. Typically detectors with a very high bandwidth are less sensitive than more sensitive detectors with larger active diameter and smaller bandwidth. In case the output power of the VCSEL is large enough for the detector, resulting in optical eye diagrams that meet the signal-to-noise and eye-opening requirements of the specific application, there is no advantage in having larger than necessary output powers of the VCSEL.

7.2.2. Power-to-bandwidth ratio and energy per bit for a 3 µm oxide-aperture diameter VCSEL

In order to investigate the energy efficiency of VCSELs the static and dynamic properties of the VCSELs are investigated simultaneously by relating the electrical power P_{el} and the dissipated power P_{diss} to the dynamic parameters such as the relaxation resonance frequency f_r and the modulation bandwidth f_{3dB}. In Figure 7.6 (a) the electrical power P_{el}, the dissipated power P_{diss}, and the optical output power P_{opt} of a 3 µm oxide-aperture diameter VCSEL are plotted versus f_r. The values of P_{el}, P_{diss}, and P_{opt} are obtained from the static *LIV*-measurements performed with the integration sphere. An optical coupling efficiency of 100% is assumed by measuring the optical output power with the integration sphere. For the S21-measurements or application of the VCSEL in an actual optical interconnect where the light is coupled into cleaved multimode optical fiber, lensed fibers, or an other light guiding media,

the coupling efficiency can be much lower than 100%. The coupling efficiency depends also very much on the modal properties of the VCSEL which also change with the oxide-aperture diameter of the VCSEL. The oxide-aperture diameter dependent coupling efficiencies for different coupling schemes and therefore the suitability for different optical interconnect configurations is not studied and is therefore not included in the following analysis.

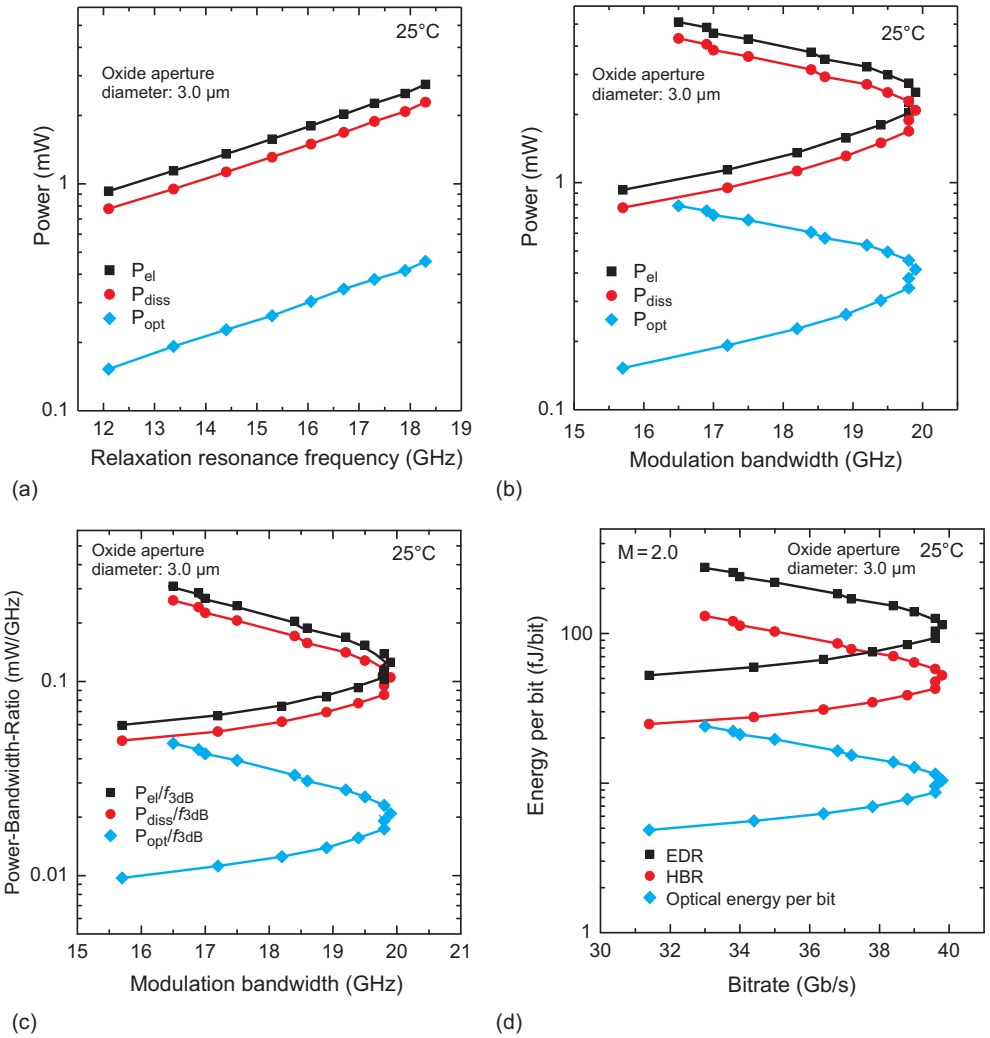

Figure 7.6.: Electrical power P_{el}, dissipated power P_{diss}, and optical power P_{opt} versus the relaxation resonance frequency f_{r} (a) and (b) versus the -3dB modulation bandwidth $f_{3\mathrm{dB}}$ for an 850-nm VCSEL with an oxide-aperture diameter of 3.0 µm at 25°C. (c) Electrical-, dissipated-, and optical-power bandwidth ratio versus the modulation bandwidth $f_{3\mathrm{dB}}$. (d) Calculated *EDR*, *HBR* and optical energy per bit versus the bit rate for M = 2.0.

As can be clearly seen in Figure 7.6 (a), P_{el}, P_{diss}, and P_{opt} increase with increasing f_{r}. The y-axis is in a logarithmic scale. Therefore the power con-

sumption and dissipation increase faster than f_r which means that the power per bandwidth ratio is smaller at smaller bias currents of the VCSEL. Because f_{3dB} is directly related to the achievable bit rate, f_{3dB} is more important than f_r when judging the suitability of a VCSEL for large-signal modulation. In Figure 7.6 (b) P_{el}, P_{diss}, and P_{opt} of the same VCSEL are plotted versus f_{3dB}. One can clearly see that the VCSEL reaches a maximum of the f_{3dB} at a certain power. When the electrical pump power is further increased, f_{3dB} does not increase but decreases due to damping and self-heating. The maximum of the f_{3dB} is approximately 20 GHz. Dividing P_{el}, P_{diss}, and P_{opt} by f_{3dB} yields the electrical, dissipated, and optical power-bandwidth-ratios, respectively. From these power-bandwidth-ratios one can calculate the electrical, dissipated, and optical energy per bit versus the respective bit rate for given M-factors using Equations (4.7) and (4.8). For M = 2.0 (b/s)/Hz the maximum bit rate of the 3 µm oxide-aperture diameter VCSEL is 40 Gb/s.

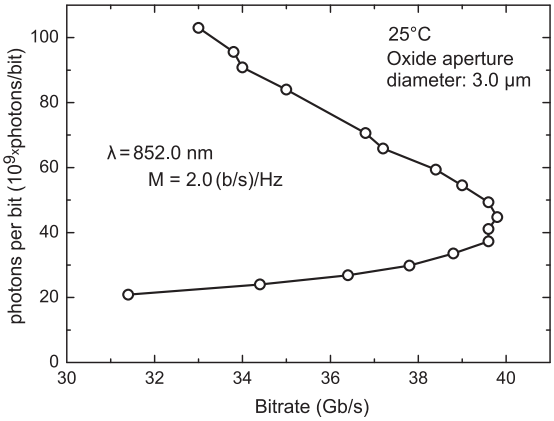

Figure 7.7.: Number of photons per bit versus the bit rate calculated with M = 2.0 (b/s)/Hz and with a fixed λ_0 = 852-nm for a 3 µm oxide-aperture diameter VCSEL.

In the shown measurement range the optical output power P_{opt} of the 3 µm oxide-aperture diameter VCSEL is below 1 mW. As can be seen in Figure 7.1 (a) and in Figure 7.3 (a) on page 80 and 83, respectively, the 3 µm oxide-aperture diameter VCSEL has a maximum output power of nearly 2 mW, but at a high current density exceeding 65 kA/cm^2. Because the maximum bandwidth is achieved at a much lower current density of approximately 15 kA/cm^2, this device was not measured at current densities close to the thermal rollover. Thus the 3 µm oxide-aperture diameter VCSEL is not suitable for highly energy-efficient data transmission if larger output powers exceeding 1 mW are required due to the detector's sensitivity. Then a VCSEL with larger oxide-aperture diameter should be used that provides more optical output power at a simultaneously smaller current density. As will be shown in the following sections, the larger oxide-aperture diameter can be disadvantageous for

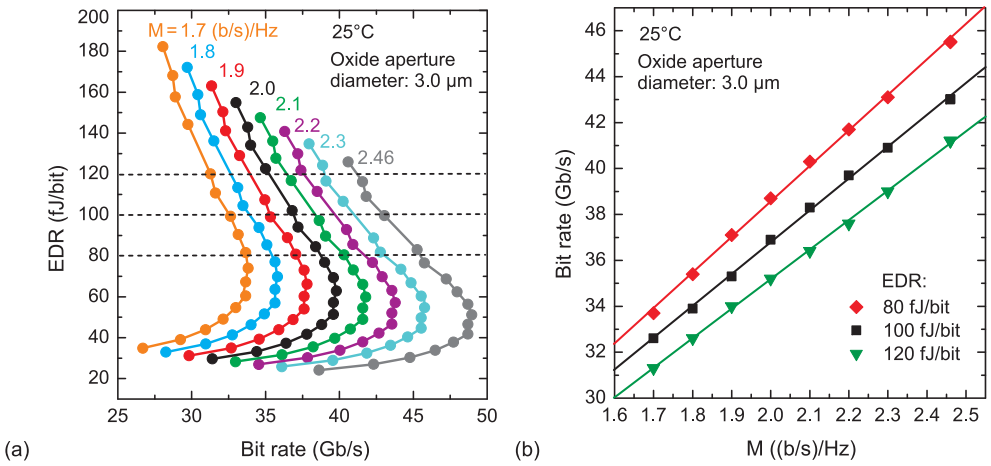

Figure 7.8.: (a) Calculated electrical energy-to-data ratios *EDR* versus the bit rate for varying M-factor values. The *EDR* values are calculated from the electrical power-to-bandwidth ratios shown in Figure 7.6 (c). (b) Bit rate at *EDR* values of 80, 100, and 120 fJ/bit versus the M-factor for an 850-nm VCSEL with an oxide-aperture diameter of 3 µm.

achieving extremely energy-efficient data transmission with the VCSEL. The number of emitted photons per transmitted bit can be calculated using the optical emission wavelength and the optical power at the respective bit rate and is shown versus the bit rate in Figure 7.7.

The *EDR* and *HBR* values in Figure 7.6 (d) are calculated from the electrical and dissipated power-to-bandwidth ratios with M = 2.0 (b/s)/Hz. In order to determine the *EDR* and *HBR* values of the VCSEL in different optical interconnects represented by different M-factors the M-factor is varied in the following analysis. The *EDR* versus the bit rate for the VCSEL with an oxide-aperture diameter of 3 µm and M-factors ranging from 1.7 to 2.46 (b/s)/Hz is shown in Figure 7.8 (a). The *EDR* does not show a minimum in the measured range of f_{3dB} values, the *EDR* initially increases with increasing bit rate toward a maximum bit rate. The maximum bit rate as well as the bit rate at a given *EDR* vary with M. The bit rate at a given *EDR* and M-value can be used as a measure of a VCSEL's energy efficiency. In Figure 7.8 (b) the bit rates at *EDR* values of 80, 100, and 120 fJ/bit are plotted versus the M-factor. These data points can be fitted linearly. In the investigated *EDR* range from 80 to 120 fJ/bit, the bit rate at a given M-factor decreases with increasing *EDR* for the 3 µm oxide-aperture diameter VCSEL. For M = 2.0 (b/s)/Hz the bit rates at 80, 100, and 120 fJ/bit are 38.7, 36.9, and 35.2 Gb/s, respectively. For a smaller M of 1.7 (b/s)/Hz the bit rates reduce to 33.7, 32.6, and 31.3 Gb/s for *EDR* values of 80, 100, and 120 fJ/bit, respectively. As can be seen in Figure 7.8 (a) the maximum bit rate of the 3 µm oxide-aperture diameter VCSEL is already reached at *EDR* values below 80 fJ/bit in the investigated range of

M-factors. Therefore the bit rate of the VCSEL reduces when the *EDR* is further increased. Thus in this case allowing a larger *EDR* does not lead to an increase in bit rate but to an undesired decrease of the bit rate. If the optical interconnect application allows larger *EDR* values then a VCSEL with a larger oxide-aperture diameter should be used leading to an increase in bit rate as is discussed in the next Section.

7.2.3. Impact of the oxide-aperture diameter on the energy efficiency: comparison of 3 μm and 5 μm oxide-aperture diameter VCSELs

In order to demonstrate the impact of the oxide-aperture diameter on the energy-efficient high-speed properties of the VCSELs, the 3 μm oxide-aperture diameter VCSEL is compared to a similar neighbor VCSEL from the same epitaxial wafer with an oxide-aperture diameter of 5 μm. The distance between these two VCSELs on the waferpiece is 1.8 mm and therefore inhomogeneities of the growth or processing should be negligible.

Small-signal modulation response results at the same absolute bias currents for VCSELs with oxide-aperture diameters of the 3 and 5 μm are shown in Fig. 7.9 (a) and (b), respectively. At low bias currents of 0.6, 0.8, and 1.0 mA, the f_{3dB} is 17.0, 18.9, and 19.7 GHz for the 3 μm oxide-aperture diameter VCSEL and 8.6, 10.9, and 12.8 GHz for the VCSEL with an oxide-aperture diameter of 5 μm. Because of the smaller threshold current, larger D-factor, and larger MCEF-value the 3 μm oxide-aperture diameter VCSEL achieves larger f_r and f_{3dB} values at the same bias currents as compared to the VCSEL with a larger oxide-aperture diameter of 5 μm. Because of the larger relaxation resonance frequency f_r the 3 μm oxide-aperture diameter VCSEL is also more damped than the larger 5 μm oxide-aperture diameter VCSEL at a lower f_r. At 1.0 mA the f_r is 16.7 and 8.5 GHz for the VCSELs with oxide-aperture diameters of 3 and 5 μm, respectively. The damping γ is 68.5 and 20.9 ns for the 3 and 5 μm oxide-aperture diameter VCSELs at the same bias current. The modulation response of the VCSEL with an oxide-aperture diameter of 3 μm shows a resonance peak of 4.4 dB compared to the initial S21-response at frequencies near 0 GHz at 0.6 mA which reduces to 1.7 dB when the bias current is increased to 1.0 mA. For the 5 μm oxide-aperture diameter VCSEL the resonance peak is 8.0 dB at 0.6 mA and increases to 9.3 dB at 1.0 mA. Large resonance peaks are detrimental for error-free data transmission as they cause overshoots in optical eye-diagrams. For data transmission a flat modulation response curve without any resonance peak would be ideal. In order to obtain a flat modulation response of the 5 μm oxide-aperture diameter VCSEL, the bias current needs to be further increased to larger currents than 1.0 mA leading to a larger f_r and thus also a larger damping but simultaneously to an undesired increase of the power consumption. The extracted f_r, γ, and f_{3dB} values as well as the D-factors and MCEF-values of the VCSELs with oxide-aperture diameters of 3 and 5 μm are given in Table 7.2.

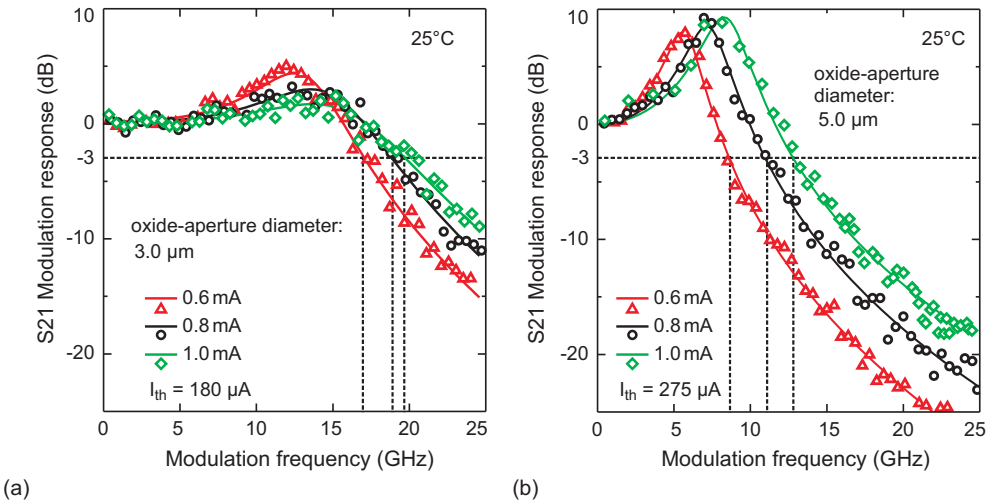

Figure 7.9.: Small-signal modulation response (S21) versus modulation frequency at bias currents of 0.6, 0.8, and 1.0 mA for VCSELs with an oxide-aperture diameter of 3.0 µm (a) and 5 µm (b) both at 25°C.

Table 7.2.: S21-parameters of 850-nm VCSELs with oxide-aperture diameters of 3 and 5 µm.

	Current (mA)	**3 µm VCSEL**	**5 µm VCSEL**
f_r (GHz)	0.6	13.4	5.8
	0.8	15.3	7.4
	1.0	16.7	8.5
γ (ns)	0.6	36.5	14.3
	0.8	50.8	17.2
	1.0	68.5	20.9
f_{3dB} (GHz)	0.6	17.2	8.6
	0.8	18.9	11.0
	1.0	19.8	12.5
D (GHz/$\sqrt{\text{mA}}$)		18.4	9.6
MCEF (GHz/$\sqrt{\text{mA}}$)		23.8	13.9
X = MCEF/D (unitless)		1.29	1.45

Both VCSELs are measured at the same absolute current values. The threshold currents are 180 and 275 µA for the VCSELs with the oxide-aperture diameters of 3 and 5 µm, respectively. So in this case the larger VCSEL is operated at a smaller current above threshold as compared to the smaller 3 µm oxide-aperture diameter VCSEL. But since the goal is to achieve high-speed operation at currents as low as possible, the VCSELs are measured at the same absolute bias current values to directly illustrate the advantage of smaller

oxide-aperture diameters for high-speed VCSELs operated at low currents and current densities.

At the same bias currents the 3 µm oxide-aperture diameter VCSEL achieves larger f_{3dB} values than the VCSEL with a larger oxide-aperture diameter of 5 µm. Due to the smaller oxide-aperture diameter the 3 µm VCSEL is faster at low currents. The D-factor and MCEF for the 3 µm VCSEL are 18.4 and 23.8 GHz/$\sqrt{\text{mA}}$, respectively. For the 5 µm VCSEL the D-factor and MCEF reduce to 9.6 and 13.9 GHz/$\sqrt{\text{mA}}$, respectively. But because of the smaller oxide-aperture diameter the differential resistance is larger and therefore the 3 µm oxide-aperture diameter VCSEL requires more electrical power at equal currents compared to the VCSEL with a larger oxide-aperture diameter of 5 µm. Because of the smaller oxide-aperture diameter the current density J is larger as well. In order to better compare the two VCSELs over a larger current density range, f_{3dB} and P_{el} are plotted versus the current density for both VCSELs in Figure 7.10 (a).

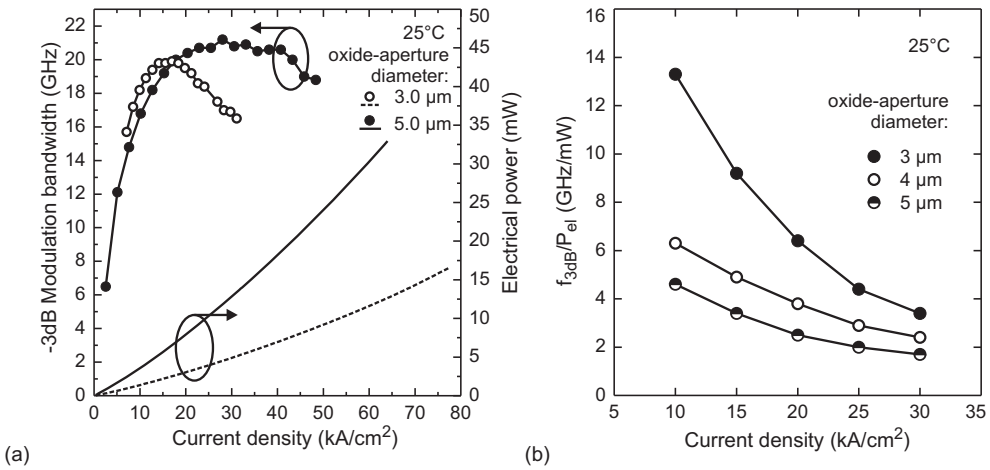

Figure 7.10.: (a) Modulation bandwidth f_{3dB} and electrical power P_{el} versus the current density for 850-nm VCSELs with oxide-aperture diameters of 3 and 5 µm. (b) Bandwidth-power-ratio versus the current density for VCSELs with oxide-aperture diameters of 3, 4, and 5 µm [98] © SPIE 2014.

Within the complete measured *current density* range the electrical power P_{el} is smaller for the 3 µm oxide-aperture diameter VCSEL than for the VCSEL with an oxide-aperture diameter of 5 µm. The 5 µm oxide-aperture diameter VCSEL achieves a maximum f_{3dB} of 21.2 GHz at a current density of 25 kA/cm^2. The maximum f_{3dB} slightly reduces to 19.9 GHz for the 3 µm oxide-aperture diameter VCSEL at a current density of 17 kA/cm^2. At this current density both VCSELs have approximately the same f_{3dB} with a power consumption of 2.5 and 6.6 mW for the 3 and 5 µm oxide-aperture diameter VCSELs, respectively. Providing about the same bandwidth the power requirement of the 5 µm oxide-aperture diameter VCSEL is thus about 260% as

large as that of the 3 µm oxide-aperture diameter VCSEL. The bandwidth to electrical power ratio at 17 kA/cm^2 is 7.96 and 3.02 GHz/mW for the 3 and 5 µm oxide-aperture diameter VCSEL, respectively. From the dependence of P_{el} and $f_{3\mathrm{dB}}$ on the current density it is clear that the bandwidth-to-electrical power ratio varies with the current density also. At current densities below 17 kA/cm^2 the 3 µm oxide-aperture diameter VCSEL achieves a higher $f_{3\mathrm{dB}}$ than the 5 µm VCSEL.

In Figure 7.10 (b) the bandwidth-to electrical power ratio is plotted versus the current density for VCSELs with oxide-aperture diameters of 3, 4, and 5 µm. The electrical bandwidth to power ratio increases with decreasing oxide-aperture diameter of the VCSEL. The advantage of using smaller oxide-aperture diameters is especially significant at lower current densities. At 10 kA/cm^2 the bandwidth to power ratio is 13.3 and 4.6 GHz/mW for the 3 and 5 µm oxide-aperture diameter VCSELs, respectively. In other words the 3 µm oxide-aperture diameter VCSEL provides 289% as much bandwidth per mW as the larger 5 µm oxide-aperture diameter VCSEL. At 30 kA/cm^2 the bandwidth to power ratio reduces to 3.4 and 1.7 GHz/mW for the 3 and 5 µm oxide-aperture diameter VCSELs, respectively. The smaller 3 µm oxide-aperture diameter VCSEL provides exactly double as much bandwidth per driving electrical power as the 5 µm oxide-aperture diameter VCSEL.

The bit rates of the 5 µm oxide-aperture diameter VCSEL at *EDRs* of 80, 100, and 120 fJ/bit versus varying M-factors are plotted in Figure 7.11 (a). In contrast to the same evaluation of the 3 µm oxide-aperture diameter VCSEL shown in Figure 7.8 (b) the bit rate at a given M-factor increases for the 5 µm oxide-aperture diameter VCSEL with increasing *EDR* value. This is due to the fact that the VCSEL achieves the respective *EDR* values before the saturation of the $f_{3\mathrm{dB}}$. Therefore the 5 µm oxide-aperture diameter VCSEL might be better suited for an optical interconnect for which the high bit rate is more important than the energy efficiency. The bit rate versus M-factor plots at different given *EDR* values of the 3 and 5 µm oxide-aperture diameter VCSELs can be used to compare their suitability for different optical interconnects. The M-factor curves of two VCSELs at a given *EDR* have different slopes resulting in an intersection of both curves at a certain M-factor. At this M-factor both VCSELs achieve the same bit rate at the same *EDR*. At smaller M-factors the 3 µm oxide-aperture diameter VCSEL achieves larger bit rates at the given *EDR* than the 5 µm oxide-aperture diameter VCSEL and at larger M-factors the 5 µm oxide-aperture diameter VCSEL is faster. The M-factor at which the M-factor lines cross each other depends on the *EDR* value. Since at a given M-factor the bit rate of the 3 µm oxide-aperture diameter VCSEL decreases with increasing *EDR* whereas the bit rate of the 5 µm oxide-aperture diameter VCSEL increases with increasing EDR, the M-factor of the intersection is decreasing with increasing *EDR* value. The plots of the bit rate versus the M-factor at EDRs of 80, 100, and 120 fJ/bit for the 3 and 5 µm oxide-aperture diameter VCSELs are shown in Figure 7.11 (b), (c), and

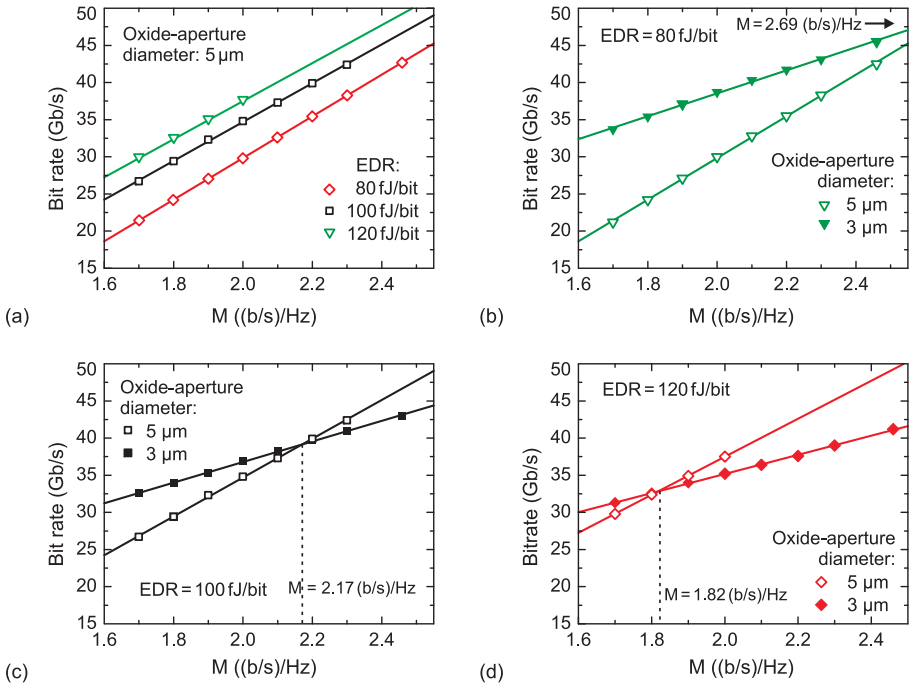

Figure 7.11.: (a) Bit rate at electrical energy-to-data ratios (EDR) of 80, 100, and 120 fJ/bit versus the M-factor for the 850-nm VCSEL with an oxide-aperture diameter of 5 µm. Comparison of the bit rates at an EDR of 80 fJ/bit (b), 100 fJ/bit (c), and 120 fJ/bit (d) versus the M-factor for 850-nm VCSELs with oxide-aperture diameters of 3 and 5 µm, respectively.

(d), respectively. The M-factors at which both VCSELs achieve the same bit rate at 80, 100, and 120 fJ/bit are 2.69, 2.17, and 1.82 (b/s)/Hz, respectively. The M-factors where the linear curves of the two VCSELs cross each other for a given *EDR* are evaluated at *EDR* values ranging from 70 to 120 fJ/bit in steps of 10 fJ/bit and are plotted in Figure 7.12. For the combinations of *EDR* and M-factor values below the red data points in the blue region, the VCSEL with an oxide-aperture diameter of 3 µm achieves a larger bit rate at a given *EDR* and in the bright orange region above the red data points the VCSEL with an oxide-aperture diameter of 5 µm achieves larger bit rates. The *EDR* at which the 5 µm oxide-aperture diameter VCSEL achieves a larger bit rate than the smaller 3 µm oxide-aperture diameter VCSEL decreases with increasing M-factor. Thus VCSELs with smaller oxide-aperture diameters are especially well suited for optical interconnect systems that are represented by a smaller M-factor. If larger *EDR* values can be tolerated and the M-factor of the optical interconnect is large, then VCSELs with larger oxide-aperture diameters achieve larger bit rates at the same *EDR* as smaller oxide-aperture diameter VCSELs, because of the onset of the saturation of f_{3dB} and the smaller maximum f_{3dB} of smaller oxide-aperture diameter VCSELs.

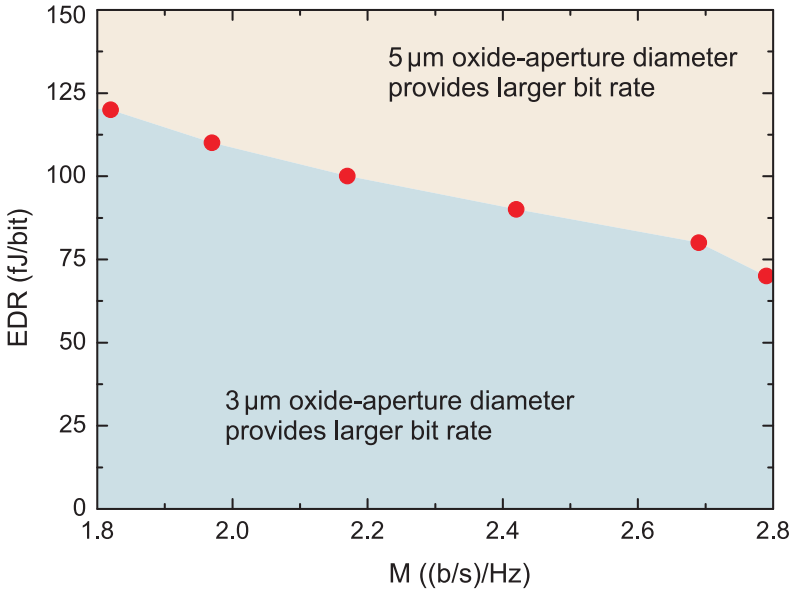

Figure 7.12.: Energy-to-data ratio *EDR* versus the M-factor for VCSELs with oxide-aperture diameters of 3 and 5 µm. At smaller *EDR* values the VCSEL with an oxide-aperture diameter of 3 µm achieves a larger bit rate, whereas the bit rate is larger at larger allowed *EDR* values for the 5 µm oxide-aperture diameter VCSEL.

7.2.4. Determination of the optimum oxide-aperture diameter for energy-efficient operation

In order to determine the optimal oxide-aperture diameter for energy-efficient data transmission all 9 VCSELs with different oxide-aperture diameters of the investigated array are compared in detail. The D-factors and MCEF-values of the VCSELs with oxide-aperture diameters ranging from 2.5 to 9 µm are already shown in Figure 7.5 (a) and (b), respectively. In the following analysis the energy efficiency of the VCSELs will be compared versus the modulation bandwidth, the current density, and for different M-factors. In some of the following examples the goal is to achieve an *EDR* equal to or below 100 fJ/bit and a maximum current density of 10 kA/cm^2. Other requirements such as a certain minimum bit rate or minimum optical output power might lead to a different oxide-aperture diameter that is considered to be the optimum for the respective boundary conditions. Also, if the differential resistance R_d of the VCSEL has to be within a given range in order to avoid a too large impedance mismatch in a given optical interconnect, the choice of possible oxide-aperture diameters can be limited by this condition. The following analysis demonstrates which oxide-aperture diameters of the given VCSELs enable energy-efficient operation with maximum *EDR* values of 100 fJ/bit and a at a maximum current density of 10 kA/cm^2, because a high energy efficiency and reliability are considered to be prerequisites the VCSELs must possess to be

suitable for application in future optical interconnects. Future on-chip interconnects might operate with much lower optical power than current optical interconnects for multimode optical fiber based data transmission up to 300 m. Also the impedance of the transmission lines used in future optical interconnect systems might be larger than the current standard of 50 Ω, decreasing the potential impedance mismatch with small oxide-aperture diameter VCSELs. In addition the differential resistance of small oxide-aperture diameter VCSELs can be reduced by for instance using intra-cavity contacts and by further optimization of the doping and design of the distributed Bragg reflectors or by the use of current spreading regions. Since according to Equations 3.12 and 3.16 the D-factor (and thus potentially also the MCEF) is proportional to the square-root of the differential gain and to the inverse of the oxide-aperture diameter, it is much easier to achieve high energy-efficiencies by using small oxide-aperture diameters than by increasing the differential gain. Even only small reductions of the oxide-aperture diameter of 1-2 µm can lead to large improvements of the energy efficiency as will be demonstrated in the following Sections.

Energy efficiency versus modulation bandwidth

Following the dependence of the D-factor on the oxide-aperture diameter, the VCSELs with smaller oxide-aperture diameters require less P_{el} for a given f_{r} than similar VCSELs with larger oxide-aperture diameter as plotted in Figure 7.13 (a). Next the P_{el} is plotted against f_{3dB}, where the saturation of the f_{3dB} can be seen for the VCSELs with smaller oxide-aperture diameters of 2.5, 3.0, and 3.5 µm. In contrast to the plot of P_{el} versus f_{r}, the VCSEL with the smallest oxide-aperture diameter of 2.5 µm achieves slightly lower f_{3dB} for a given P_{el} as shown in Figure 7.13 (b). Therefore the VCSEL with an oxide-aperture diameter of 3 µm provides more bandwidth per supplied power and therefore potentially yields more energy-efficient data transmission than the 2.5 µm oxide-aperture diameter VCSEL. As shown in Figure 7.1 (b) on page 80 the 2.5 µm oxide-aperture diameter VCSELs has a larger threshold current density J_{th} as compared to all the other VCSELs with larger oxide-aperture diameter. Because of the smaller oxide-aperture diameter also the differential resistance is large (see Figure 7.2 (b) on page 81). Therefore the smallest oxide-aperture diameter VCSEL achieves less bandwidth per power supplied, because of its increased power consumption and despite its larger D-factor.

The dissipated and the optical output power are plotted versus f_{3dB} in Figure 7.14 (a) and (b), respectively. The Figures 7.13 (b) and Figure 7.14 can now be used to determine the optimal oxide-aperture diameter VCSEL for the respective application. For example if a f_{3dB} of at least 12 GHz is required at a maximum supplied power P_{el} of 2 mW, then according to Figure 7.13 (b), a VCSEL with an oxide-aperture diameter of 5 µm or smaller must be used. All VCSELs with larger oxide-aperture diameters require more power

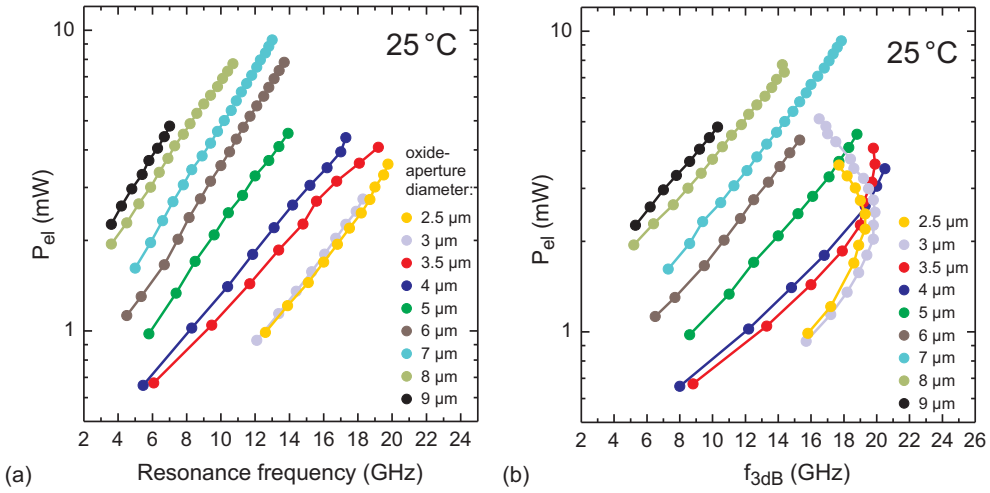

Figure 7.13.: Electrical power P_{el} versus (a) the relaxation resonance frequency f_{r} and (b) versus the -3dB modulation bandwidth f_{3dB} for 850-nm VCSELs with oxide-aperture diameters ranging from 2.5 to 9 µm. [73] © 2013 IEEE.

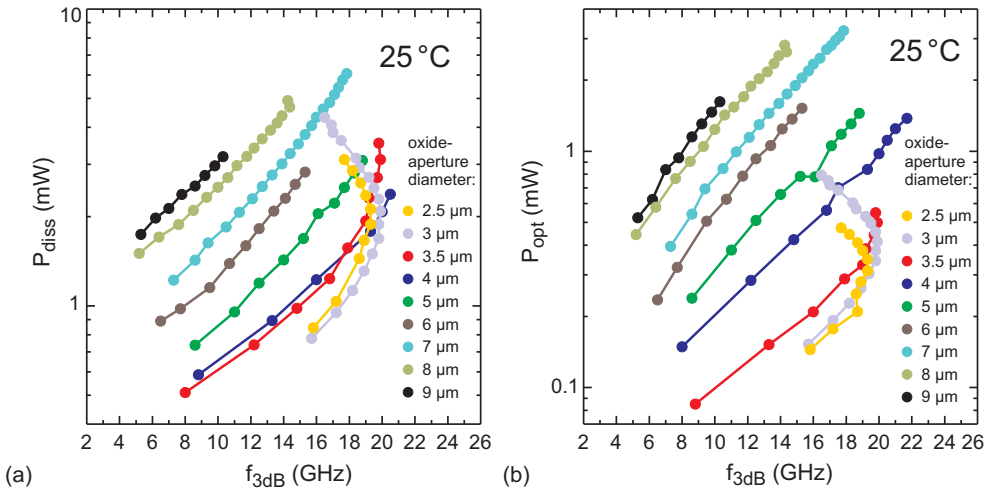

Figure 7.14.: Dissipated power P_{diss} (a) and optical output power P_{opt} versus the -3dB modulation bandwidth f_{3dB} for 850-nm VCSELs with oxide-aperture diameters ranging from 2.5 to 9 µm. (a): [73] © 2013 IEEE.

to achieve a f_{3dB} of 12 GHz. A 5 µm oxide-aperture diameter VCSEL will then dissipate 1.1 mW as heat at 12 GHz. If the power dissipation needs to be lower, a VCSEL with smaller oxide-aperture diameter needs to be used. On the other hand, VCSELs with smaller oxide-aperture diameters provide less optical output power. At 12 GHz the 5 µm oxide-aperture diameter VCSEL achieves an optical output power of 0.45 mW. The VCSEL with an oxide-aperture diameter of 4 µm provides 0.28 mW output power at 12 GHz.

For energy-efficient operation the ratio of the consumed or dissipated power

to the modulation bandwidth must be small. The ratios of P_{el} over f_{3dB} and the ratio of P_{diss} over f_{3dB} are plotted in Figure 7.15 (a) and (b), respectively. The VCSEL with an oxide-aperture diameter of 3 µm achieves the lowest power-to-bandwidth ratio in the presented measurement range. The increased threshold current density of the VCSEL with the smallest oxide-aperture diameter of 2.5 µm leads to a slightly larger power-to-bandwidth ratio as discussed previously in this Section. Some of the curves show a minimum of the power-to-bandwidth ratio at a certain f_{3dB}. At this particular f_{3dB} at the minimum of the power-to-bandwidth ratio the VCSEL can be operated most efficiently and will yield the lowest consumed or dissipated energy per bit. The f_{3dB} value of the minimal bandwidth-to-power ratio slightly increases with decreasing oxide-aperture diameter, but this change is not very large. The power-to-bandwidth ratio curve is relatively flat around its minimum. The curves of the VCSELs with oxide-aperture diameters of 2.5 to 4 µm do not show a minimum power-to-bandwidth ratio in the measured range of f_{3dB}. Before the saturation of f_{3dB} occurs, the power-to-bandwidth ratio increases with increasing oxide-aperture diameter at a given f_{3dB}.

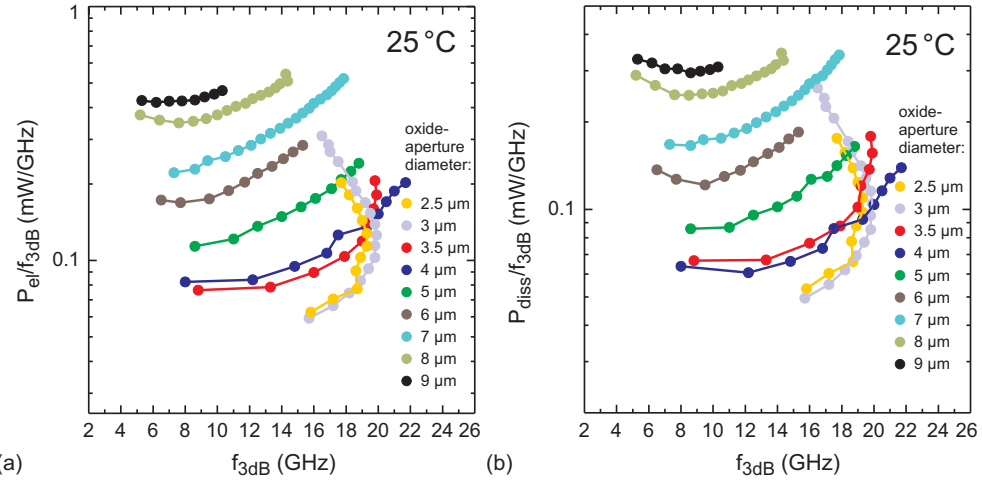

Figure 7.15.: Ratio of the electrical power P_{el} over f_{3dB} (a) and the ratio of P_{diss} over f_{3dB} versus the -3dB modulation bandwidth f_{3dB} for 850-nm VCSELs with oxide-aperture diameters ranging from 2.5 to 9 µm.

Energy efficiency versus current density

The bandwidth-to electrical power ratio can be used to calculate the energy per bit for a given M-factor value. Assuming that a certain f_{3dB} value results in an error-free bit rate that is double as large as the f_{3dB} value, e.g. $\mathrm{M} = 2.0\,(\mathrm{b/s})/\mathrm{Hz}$, a bandwidth-to electrical power ratio of 5 GHz/mW corresponds to an *EDR* value of 100 fJ/bit. The larger the bandwidth-to electrical power ratio the smaller is the energy per bit. Therefore the bandwidth-to

electrical power ratio is desired to be as large as possible. In addition the current density should be low for application in commercial and reliable systems. As can be seen in Figure 7.16 (a) and (b) the oxide-aperture diameter is very important. In Figure 7.16 (a) the bandwidth-to electrical power ratio at 10 kA/cm^2 is plotted versus the oxide-aperture diameter. A bandwidth-to electrical power ratio of 5 GHz/mW and larger, corresponding to an *EDR* of 100 fJ/bit or smaller, is achieved for VCSELs with oxide-aperture diameters of 5 µm or smaller. In the same plot the ratio of f_{3dB} over P_{diss} is shown. A value of 5 GHz/mW or larger corresponds to an *HBR* of 100 fJ/bit or lower dissipated energy per bit. At a larger current density of 15 kA/cm^2 all VCSELs get less energy-efficient and only the VCSELs with oxide-aperture diameters of 3.5 µm and smaller achieve a bandwidth-to electrical power ratio of 5 GHz/mW or larger. This shows that VCSELs with smaller oxide-aperture diameters are especially well-suited for application at low current densities, because they provide a large modulation bandwidth at a simultaneously low energy consumption and current density. The present drawback is the smaller optical output power compared to the VCSELs with larger oxide-aperture diameters. But in case data transmission is performed on-chip with link distances of millimeters to micrometers then the required optical power can be anticipated to be extremely low.

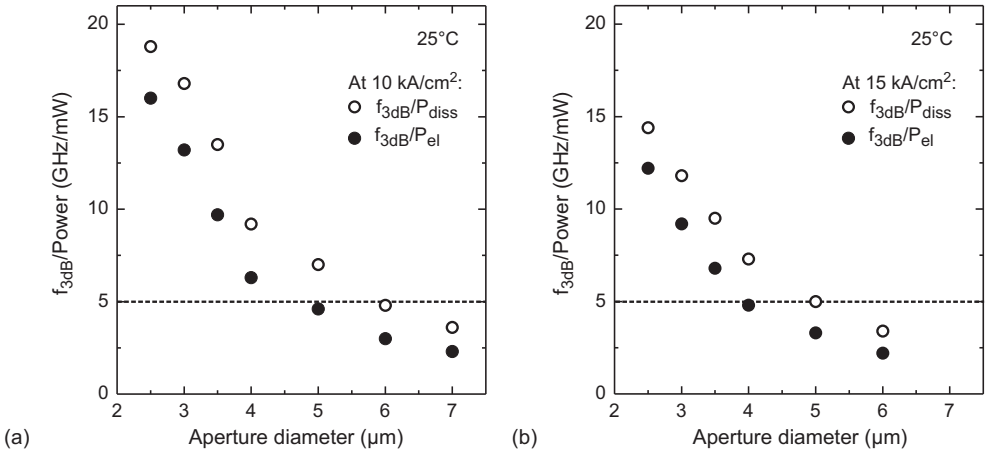

Figure 7.16.: Bandwidth-to-electrical-power ratio and bandwidth-to-dissipated-power ratio versus the oxide-aperture diameter at a current density of 10 kA/cm^2 (a) and at 15 kA/cm^2 for 850-nm VCSELs.

The ratio of f_{3dB} to P_{el} and to P_{diss} versus the current density for 850-nm VCSELs at 25°C with oxide-aperture diameters ranging from 2.5 to 9 µm is shown in Figure 7.17 (a) and (b), respectively. For all VCSELs the bandwidth-to electrical power ratio decreases with increasing current density. For a given current density both bandwidth-to-power ratios increase with decreasing oxide-aperture diameter. Only VCSELs with oxide-aperture diameters be-

tween 2.5 and 6 µm achieve bandwidth-to electrical power ratio values equal to or larger than 5 GHz/mW at a current density below 10 kA/cm^2 as marked with a light green box in Figure 7.17(a). For the smallest 2.5 µm oxide-aperture diameter VCSEL only the first data point lies at the border of this marked box, indicating that this VCSEL might be not suitable for practical applications given the stated performance attributes.

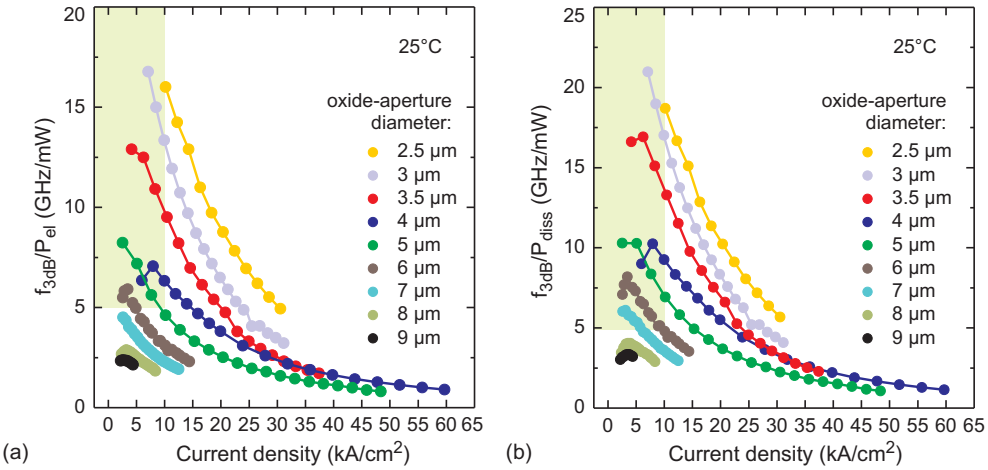

Figure 7.17.: Ratio of f_{3dB} over P_{el} (a) and the ratio of f_{3dB} over P_{diss} versus J for 850-nm VCSELs with oxide-aperture diameters ranging from 2.5 to 9 µm.

The *EDR* and *HBR* can be calculated from the plotted ratios of f_{3dB} over P_{el} and P_{diss} of Figure 7.17 (a) and (b). The *EDR* and *HBR* values calculated with M = 2.0 (b/s)/Hz are plotted versus the current density J for all 9 VCSELs in Figure 7.18. The light green box marks the region where the *EDR* and *HBR* is below 100 fJ/bit and J is simultaneously below 10 kA/cm^2. Only VCSELs with oxide-aperture diameters equal to or smaller than 6 µm achieve EDR values below 100 fJ/bit at a current density below 10 kA/cm^2. The largest oxide-aperture diameter that achieves an *HBR* below 100 fJ/bit is 7 µm. With increasing M-factor the *EDR* and *HBR* values at a given J decrease and vice versa. Since the *EDR* and *HBR* values are calculated by multiplying M with f_{3dB} the relative change of the *EDR* and *HBR* values is proportional for all VCSELs with different oxide-aperture diameters. Thus the absolute change of the *EDR* and *HBR* values is larger for the VCSELs with larger oxide-aperture diameters and a larger bandwidth-to electrical power ratio. The *EDR* and *HBR* values with M = 1.7 (b/s)/Hz versus J are shown for comparison in Figure 7.19 (a) and (b), respectively.

Energy efficiency and M-factor

As discussed in the previous Section the M-factor impacts the energy efficiency of the VCSEL at a given bias current or current density via the bit rate.

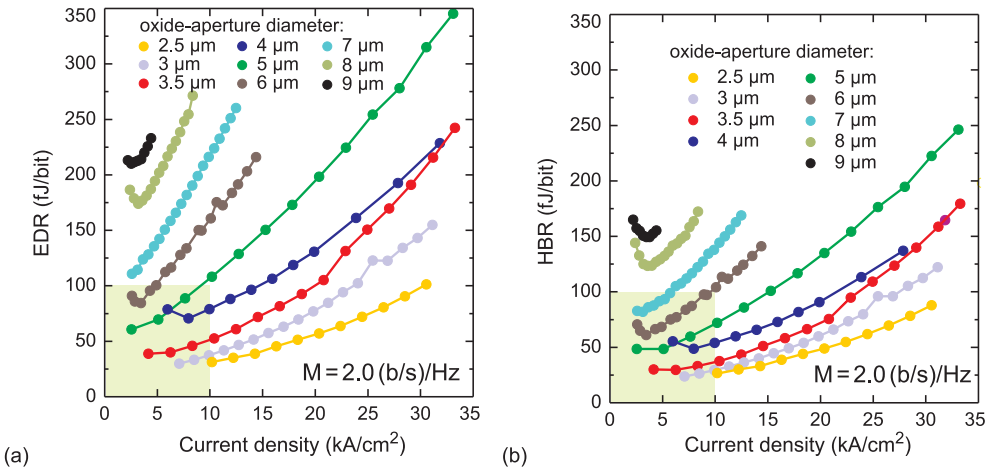

Figure 7.18.: Calculated *EDR* (a) and calculated *HBR* values versus J for 850-nm VCSELs with oxide-aperture diameters ranging from 2.5 to 9 µm assuming M = 2.0 (b/s)/Hz, based on measured f_{3dB}/P_{el} and f_{3dB}/P_{diss} values in Figure 7.17.

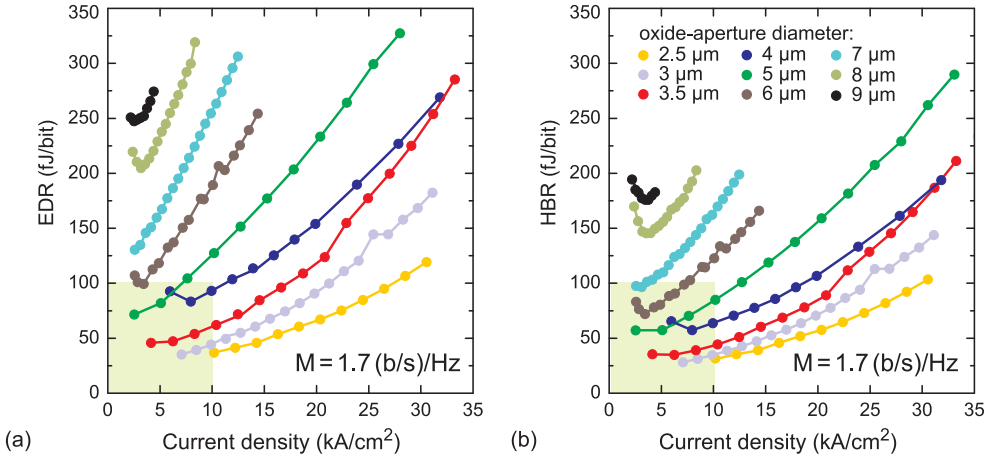

Figure 7.19.: Calculated *EDR* (a) and calculated *HBR* values versus J for 850-nm VCSELs with oxide-aperture diameters ranging from 2.5 to 9 µm with M = 1.7 (b/s)/Hz, based on measured f_{3dB}/P_{el} and f_{3dB}/P_{diss} values in Figure 7.17.

Therefore the optimal oxide-aperture diameter to achieve a certain required VCSEL performance will also depend on the M-factor.

In order to compare the VCSELs with 9 different oxide-aperture diameters with respect to their energy efficiency, the *EDR* versus the bit rate is calculated from the electrical power-to-bandwidth ratio for M-factors ranging from 1.7 to 2.46 (b/s)/Hz, as already demonstrated for the VCSELs with oxide-aperture diameters of 3 and 5 µm, respectively. Then the bit rate at an *EDR* = 100 fJ/bit is determined for each VCSEL and M-factor. The bit rate at an *EDR* of 100 fJ/bit versus the M-factor is plotted for the VCSELs 6 with dif-

ferent oxide-aperture diameters ranging from 2.5 to 7 µm in Figure 7.20 (a). The larger oxide-aperture diameter VCSELs do not achieve *EDR* values as low as 100 fJ/bit in the investigated M-factor range. The 4 µm oxide-aperture diameter VCSEL achieves the highest bit rate at an *EDR* of 100 fJ/bit, followed by the VCSELs with an oxide-aperture diameter of 3.5 and 3.0 µm, respectively. The slope of the linear fit for the bit rate versus the M-factor is smaller for the VCSELs with oxide-aperture diameters of 3.5 and 3.0 µm than for the VCSELs with larger oxide-aperture diameters, resulting in an intersection with the M-factor curve of VCSELs with a different oxide-aperture diameter. In Figure 7.20 (a) the curves of the 3 µm and 5 µm oxide-aperture diameter VCSELs have a intersection at M = 2.17 (b/s)/Hz as already shown in Figure 7.11 (c) and discussed on page 94. The bit rate at *EDR* = 100 fJ/bit with M = 2.0 (b/s)/Hz is plotted versus the oxide-aperture diameter in Figure 7.20 (b). The bit rates at a given *EDR* change with the M-factor as shown in Figure 7.21 (a), whereas the relative change of the bit rate increases with increasing oxide-aperture diameter as plotted in Figure 7.21 (b).

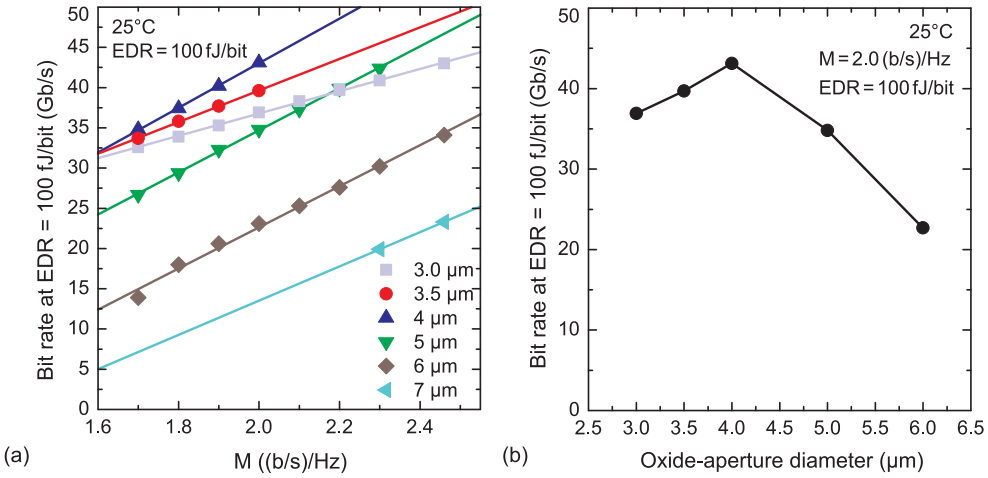

Figure 7.20.: (a) Bit rate at *EDR* = 100 fJ/bit versus the M-factor. (b) Bit rate at *EDR* = 100 fJ/bit versus the oxide-aperture diameter for M = 2.0 (b/s)/Hz.

Because VCSELs with different oxide-aperture diameters achieve their maximum f_{3dB} at different *EDR* values the bit rate changes differently for different oxide-aperture diameter VCSELs when the *EDR* is changed. An increase of the *EDR* can decrease the bit rate for smaller oxide-aperture diameter VCSELs when the maximum f_{3dB} is achieved at relatively small values of *EDR* whereas the same increase of the *EDR* can increase the bit rate for larger oxide-aperture diameter VCSELs. The bit rate at several different *EDR* values ranging from 60 to 150 fJ/bit is plotted for VCSELs with oxide-aperture diameters ranging from 2.5 to 7.0 µm in Figure 7.22 for M = 2.0 (b/s)/Hz. For oxide-aperture diameters smaller than 4.0 µm the bit rate decreases with increasing *EDR* whereas there is an increase in bit rate for the larger oxide-aperture diameter

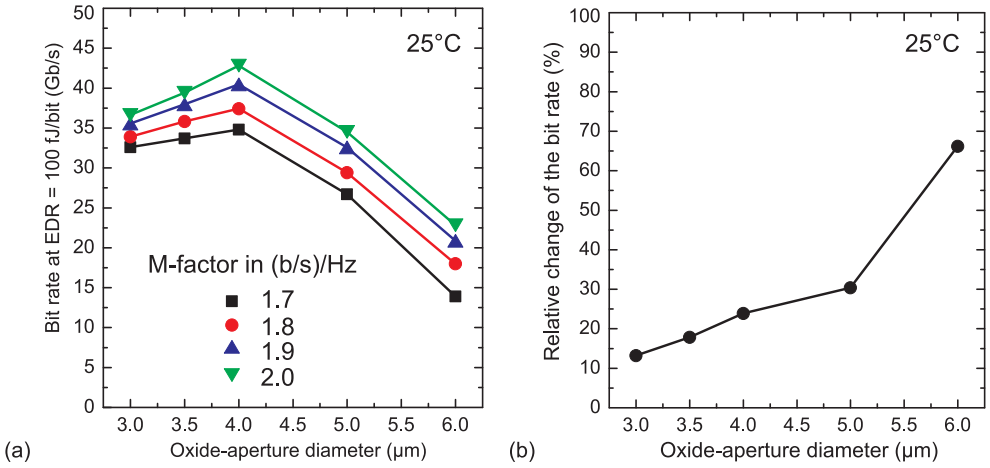

Figure 7.21.: (a) Bit rate at an $EDR = 100\,\mathrm{fJ/bit}$ versus the oxide-aperture diameter at M-factors of 1.7, 1.8, 1.9, and 2.0 (b/s)/Hz. (b) Relative change of the bit rate at $EDR = 100\,\mathrm{fJ/bit}$ when M is increased from 1.7 to 2.0 (b/s)/Hz versus the oxide-aperture diameter.

VCSELs when the *EDR* is increased. Thus the oxide-aperture diameter that yields the largest bit rate for a given allowed *EDR* increases with increasing *EDR*. For 60 and 70 fJ/bit the bit rate is maximum for the VCSEL with an oxide-aperture diameter of 3.0 µm for larger *EDR* values up to 100 fJ/bit the oxide-aperture diameter of 4.0 µm yields the maximum bit rate. At even larger *EDR* values the bit rate is not evaluated anymore for the 4 µm oxide-aperture diameter VCSEL, because these values are outside of the measurement range. However this observed change in the optimal oxide-aperture diameter, e.g. the oxide-aperture diameter yielding the largest bit rate at a given *EDR*, might be smaller than the inhomogeneity of the oxide-aperture diameter across a complete 3, 4, or even 6-inch wafer in commercial VCSEL production and might therefore be neglected here. Moreover when the required *EDR* needs to be reduced to well below 50 fJ/bit then a change of the oxide-aperture diameter by less than 0.5 µm might already be very difficult to control and to routinely achieve. The VCSELs with oxide-aperture diameters of 8 and 9 µm did not achieve *EDR* values in the range of 60 to 150 fJ/bit and are thus not included in this evaluation.

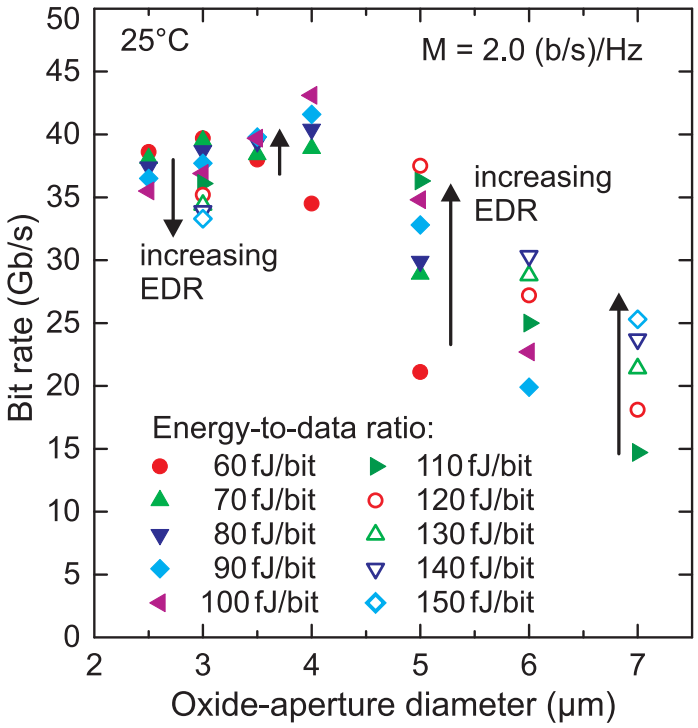

Figure 7.22.: Bit rates at different *EDR* values versus the oxide-aperture diameter for 850-nm VCSELs.

7.3. Energy-efficient data transmission

Large-signal modulation experiments are performed with a focus on the energy efficiency of the VCSELs. Thus in the following, the goal is not to achieve the maximum error-free bit rates that are possible with the VCSELs, but to achieve energy-efficient data transmission with *EDR* values close to or lower than 100 fJ/bit. In addition it is demonstrated that energy-efficient data transmission can also be realized across long distances of multimode optical fiber exceeding the 300 m of present 850-nm VCSEL-based optical interconnect standards. The bandwidth and sensitivity of the photodetectors or photoreceivers are found to be critical for achieving very energy-efficient data transmission.

Three different detectors or receivers are used for data transmission experiments with the 850-nm VCSELs. These detectors differ mostly in their sensitivity, bandwidth, and thus in the maximum possible bit rate they may detect. The California Scientific Inc. receiver CS-P101 has a high sensitivity and can be used for data transmission with very low received optical output power, but its maximum bit rate is limited to 17 Gb/s as discussed later in this Chapter. For larger bit rates a VIS D30-850M photodiode is used with a nominal bandwidth of 30 GHz. This detector is used for measurements at higher bit rates, but it requires much more received optical power for error-

free transmission than the California Scientific receiver. Even larger bit rates are measured using a VIS R40-850 prototype photoreceiver with an integrated limiting transimpedance amplifier (TIA) and a bandwidth of about 30 GHz. Having the same nominal bandwidth as the VIS D30-850M photodiode the R40-850 photoreceiver allows the measurement of larger bit rates, because the integrated limiting transimpedance amplifier creates larger eye-openings. For small oxide-aperture diameter VCSELs operated at very low bias currents and thus at low modulation bandwidth with low output power, the difference in using the photodiode or the photoreceiver is found to be very small. For bit rates of 30 Gb/s and larger the limiting TIA of the R40-850 prototype photoreceiver leads to significantly increased eye-openings that allow the measurement of larger error-free bit rates than with the detector without the TIA.

7.3.1. Impact of the oxide-aperture diameter on the energy efficiency of the data transmission

In order to validate the findings of the small-signal modulation experiments and the evaluation discussed in the previous Chapters, data transmission experiments are performed using the VCSELs with different oxide-aperture diameters from the investigated VCSEL array. Because the result of a data transmission experiment always reflects the combined performance of all components of the complete optical link, the VCSELs have to be measured with exactly the same setup in order to be able to directly compare the results. The dynamic and static properties of the VCSELs change significantly with changing oxide-aperture diameter. Thus only a few different oxide-aperture diameter VCSELs can be directly compared using the same measurement setup. For example VCSELs with larger oxide-aperture diameters typically require a larger modulation voltage for error-free transmission as compared to VCSELs with smaller oxide-aperture diameters. Therefore an electrical amplifier might be required if the amplitude of the electrical signal is too small to create an open optical eye for larger oxide-aperture diameter VCSELs. The additional amplifier introduces additional noise into the system and therefore also impacts the minimum achievable *EDR* and *HBR* values of the data transmission, and as a consequence the results achieved with and without an electrical amplifier can not be fairly compared to each other.

From the previous small-signal modulation analysis the most energy-efficient large-signal modulation of the VCSELs is expected to be achieved at bit rates ranging from roughly 20 to 25 Gb/s. Therefore the CS-P101 receiver cannot be used for this experiment. The following experiments are performed using the VIS D30-850M photo diode at a bit rate of 25 Gb/s which still is the maximum standard bit rate for present commercial 850-nm VCSELs although companies already are starting to report on their development of commercial 28 Gb/s VCSELs [7, 99]. Because the lowest possible *EDR* and *HBR* are of the greatest interest in this investigation, no additional electrical amplifier is used

between the electrical signal generator and the VCSEL. In tests without an amplifier and with an amplifier in combination with an electrical attenuator resulting in a 0 dB amplification, it is observed that error-free transmission at lower *EDR* and *HBR* values can be achieved in the case without an amplifier, although the effective modulation voltage was the same. In the case with an amplifier the VCSEL bias current had to be increased to enable error-free transmission, resulting in larger energy dissipation and consumption per bit. This is related to the additional noise introduced by the amplifier.

With our existing large-signal modulation setup error-free operation could not be achieved with the VCSELs having oxide-aperture diameters of 2.5 and 3.0 µm because of the sensitivity limitation of the detector. Due to low output power, coupling losses etc. no error-free and energy-efficient operation could be achieved with those VCSELs at bit rates exceeding 20 Gb/s. In Figure 7.23 error-free operation at 25 Gb/s is shown for three VCSELs with oxide-aperture diameters of 3.5, 4.0, and 5.0 µm, operated at low bias currents of 1.050, 1.165, and 1.410 mA, respectively. All three measurements are performed with the exact same experimental setup. The VCSELs are measured at the lowest bias current at which still error-free data transmission can be realized. The VCSELs with larger oxide-aperture diameters require a modulation voltage V_{PP} larger than the largest nominal V_{PP} provided by the bit pattern generator for error-free operation. Thus an electrical amplifier is required before the VCSEL to provide such large V_{PP} values, leading to a change of the measurement setup configuration. Therefore the VCSELs with larger oxide-aperture diameters cannot be directly compared to the smaller oxide-aperture diameter VCSELs presented in Figure 7.23. In addition these larger devices achieve *EDR* and *HBR* values larger than 100 fJ/bit and are therefore not investigated in greater detail here.

All three 850-nm VCSELs shown in Figure 7.23 achieve error-free operation at 25 Gb/s with record-low *EDR* and *HBR* values well below 100 fJ/bit [86]. The EDR is 77, 85, and 99 fJ/bit and the HBR is 56, 58, and 67 fJ/bit for the VCSELs with oxide-aperture diameters of 3.5, 4.0, and 5.0 µm, respectively. Both the *EDR* and *HBR* values increase with increasing oxide-aperture diameter [86], as shown in Figure 7.23 (b). The *EDR* and *HBR* values calculated from the ratio of f_{3dB} over P_{el} and over P_{diss} are also plotted in 7.23 (b). For these calculations an M-factor of 2.0 (b/s)/Hz is assumed. Thus these *EDR* and *HBR* are calculated for the maximum possible bit rate derived from the f_{3dB} at the respective bias current. At the bias currents of the 25 Gb/s data transmission the VCSELs with oxide-aperture diameters of 3.5, 4.0, and 5.0 µm have f_{3dB} values of 17.9, 17.3, and 15.2 GHz, respectively. Assuming $\mathrm{M} = 2.0\,(\mathrm{b/s})/\mathrm{Hz}$ for all three VCSELs, the maximum bit rates for the bias currents of 1.050, 1.165, and 1.410 mA are thus 35.8, 34.6, and 30.4 Gb/s, respectively. For the VCSELs with larger oxide-aperture diameters of 4.0 and 5.0 µm the calculated values of *EDR* and *HBR* match the values of the mea-

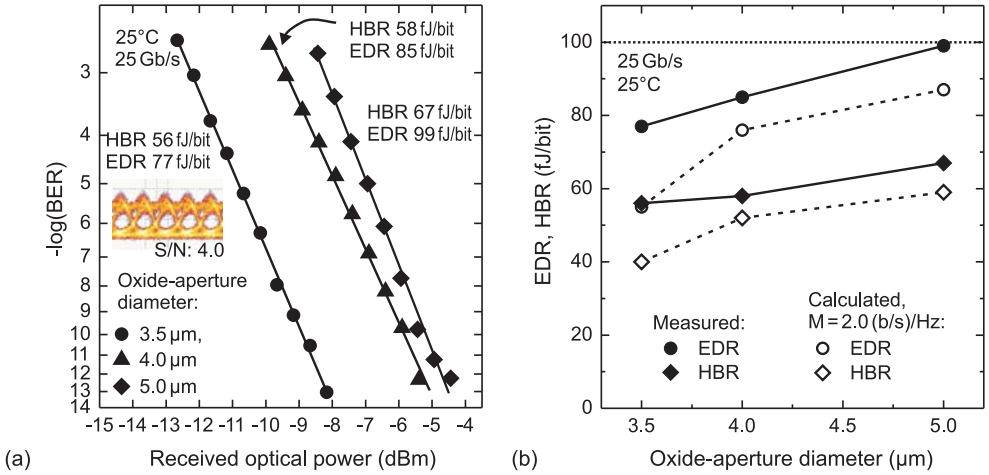

Figure 7.23.: (a) Bit error ratio (BER) versus received optical power for 850-nm VCSELs with oxide-aperture diameters of 3.5, 4.0, and 5.0 µm at 25 Gb/s at 25°C. The optical eye diagram at error-free transmission of the 3.5 µm oxide-aperture diameter VCSEL with a signal-to-noise ratio of 4.0 is shown as an inset. [86] © 2012 IET. (b) Measured *EDR* and *HBR* values at error-free operation at 25 Gb/s versus the oxide-aperture diameter for the data transmission results shown in (a). The calculated minimum *EDR* and *HBR* values are calculated with M = 2.0 (b/s)/Hz from the intrinsic electrical and dissipated power-to-bandwidth ratios and might therefore assume other bit rates than 25 Gb/s.

Table 7.3.: Data transmission at 25 Gb/s of VCSELs with three different oxide-aperture diameters. The parameters are at the bias currents of the data transmission.

Oxide-aperture diameter (µm)	3.5	4	5
Threshold power (mW)	0.24	0.31	0.38
Differential resistance (Ω)	220	190	140
Current density (kA/cm^2)	10.9	9.3	7.2
I/I_{th} (unitless)	7.0	6.1	5.9
Wallplug efficiency (%)	27.3	31.8	32.3
Optical output power (mW)	0.58	0.67	0.78
Side-mode suppression ratio (dB)	29	16	8
Spectral width (nm)	0.08	0.22	0.42
Modulation bandwidth (GHz)	17.9	17.3	15.2
M-factor (bit)	1.40	1.45	1.64
D-factor ($GHz/\sqrt{mA}$)	14.1	12.8	9.6
MCEF ($GHz/\sqrt{mA}$)	19.1	18.8	13.9
X = MCEF/D (unitless)	1.35	1.47	1.45
Received optical power (dBm)	-8.4	-5.3	-4.7
EDR (fJ/bit)	77	85	99
HBR (fJ/bit)	56	58	67

surements quite well. The calculated minimum *EDR* and *HBR* of the 3.5 µm oxide-aperture diameter VCSEL are much smaller than the values achieved at 25 Gb/s. The smallest VCSEL has to be operated at a larger current relative to the threshold current in order to provide enough optical output power for error-free transmission. The 3.5 µm oxide-aperture diameter single-mode VCSEL is operated at a bias current that is seven times the threshold current ($7\times I_{\mathrm{th}}$). The 4 and 5 µm oxide-aperture diameter VCSELs are both operated at bias currents of about $6\times I_{\mathrm{th}}$. Thus the sensitivity limitation of the measurement setup requires one to operate the single-mode VCSEL at a higher bias current relative to I_{th} as compared to the 4 and 5 µm oxide-aperture diameter VCSEL, despite its larger D-factor and MCEF value. As a consequence the current density at error-free operation is also larger for the 3.5 µm oxide-aperture diameter VCSEL than for the two VCSELs with larger oxide-aperture diameters. The current density at error-free 25 Gb/s operation is 10.9, 9.3, and 7.2 kA/cm^2 for the VCSELs with oxide-aperture diameters of 3.5, 4, and 5 µm, respectively. But still the smaller oxide-aperture diameter VCSEL operates more energy-efficiently at 25 Gb/s than the similar neighbor VCSELs with larger oxide-aperture diameters. Both the *EDR* and *HBR* values increase with increasing oxide-aperture diameter although the wallplug efficiency (WPE) is increasing with increasing oxide-aperture diameter as well. At the bias current of error-free transmission the WPE is 27.3, 31.8, and 32.3% for the VCSELs with oxide-aperture diameters of 3.5, 4, and 5 µm, respectively. As discussed in the previous Chapters the increase of the D-factor and the MCEF value with decreasing oxide-aperture diameter leads to the smaller *EDR* and *HBR* values of the smaller oxide-aperture diameter VCSELs. The most important static properties of the three VCSELs with different oxide-aperture diameters at the bias current of error-free operation such as the optical output power and side-mode suppression ratio as well as the most important dynamic properties including the f_{3dB}, D-factor, and MCEF are given in Table 7.3 for comparison. Not only the *EDR* and *HBR* values decrease with decreasing oxide-aperture diameter, but also the received optical power at error-free transmission decreases with decreasing oxide-aperture diameter. VCSELs with fewer modes have lower mode competition noise [100, 101] which can be one reason for the smaller required received optical power of the single- and quasi-singlemode VCSELs.

7.4. Energy-efficient data transmission up to 40 Gb/s and across up to 1 km of MMF

As discussed in the previous Chapters the oxide-aperture diameter determines the energy efficiencies and maximum bit rates as well as the CW properties of the VCSELs. Due to the intrinsic trade-off between the sensitivity and bandwidth of detectors with different active diameters, the CS-P101 receiver is used for the extremely energy-efficient data transmission of single-mode

lasers with low optical output power. Although the maximal nominal bit rate of this receiver is 12.5 Gb/s our particular CS-P101 receiver can be used to measure a maximum bit rate of 17 Gb/s. Already at slightly larger bit rates such as 18 Gb/s the measured optical eye diagram closes.

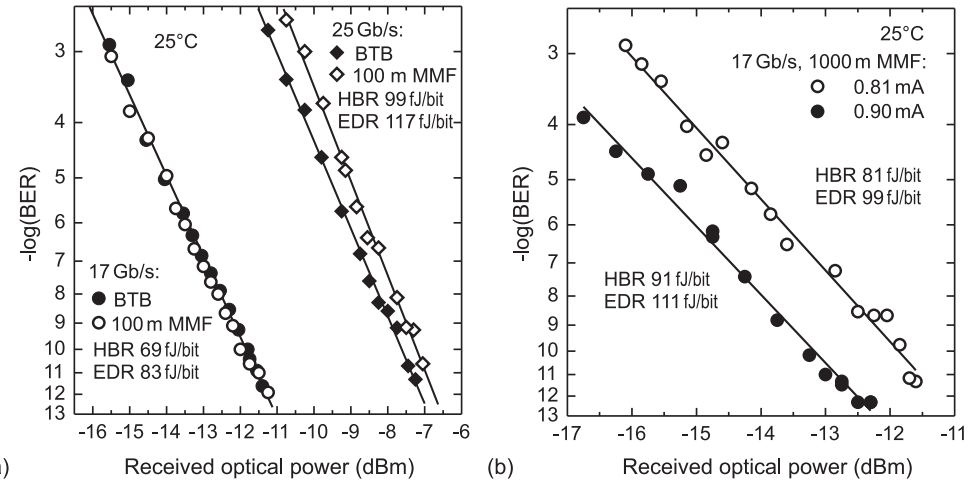

Figure 7.24.: (a) Bit error ratio (BER) versus received optical power for a single-mode 850-nm VCSEL with an oxide-aperture diameter of 2.0 µm at 17 and 25 Gb/s up to 100 m of MMF. (b) BER versus received optical power at 17 Gb/s across 1000 m of MMF. [74] © 2012 IEEE.

Due to the small spectral-width of the optical emission of such small oxide-aperture diameter VCSELs energy-efficient data transmission can also be performed across longer distances of multimode optical fiber. The following results are achieved using a single-mode VCSEL with an oxide-aperture diameter of 2 µm of the 850-nm VCSEL design A, thus not with the exact same VCSEL design of the 850-nm VCSELs presented in the previous Sections of this Chapter. Error-free operation at 17 Gb/s is achieved in a back-to-back configuration (BTB) configuration and across 100 m of MMF with *EDR* and *HBR* values of 83 and 69 fJ/bit [72], respectively. The VCSEL is operated at a low bias current of 0.66 mA, just 5.5 times the threshold current. There is no significant power penalty when 100 m of MMF are introduced demonstrating the potential to transmit error-free across even longer MMF distances at this bit rate. When the bias current is slightly increased to 0.81 mA error-free operation at 17 Gb/s is achieved up to 1000 m of MMF [74]. The *EDR* and *HBR* values then increase to 99 and 81 fJ/bit, respectively. Increasing the bias current to 0.90 mA reduces the received optical power by 1.3 dB and increases the *EDR* and *HBR* values to 111 and 91 fJ/bit, respectively. The BER curves at 17 Gb/s in a BTB configuration and across 100 m of MMF are shown in Figure 7.24 (a) and across 1000 m of MMF in Figure 7.24 (b), respectively. Using the same device and operating it at 25 Gb/s requires more energy per bit. The *EDR* and *HBR* are then 117 and 99 fJ/bit [72], respectively. The data can be

transmitted across 100 m of MMF without the need to change the bias current or modulation voltage V_{PP}. The optical eye-diagrams at error-free operation at 17 and 25 Gb/s for the data transmission experiments mentioned above are shown together with the signal-to-noise ratios (S/N) in Figure 7.25. Across 1000 m of MMF no bit rate larger than 17 Gb/s could be tested, because the California Scientific receiver CS-P101 is limited to this bit rate. At bit rates exceeding 17 Gb/s the detected optical eye closes due to the receiver's bandwidth limitation. The specified maximum bit rate of this receiver is 12.5 Gb/s, but as mentioned our detector operates well up to exactly 17 Gb/s.

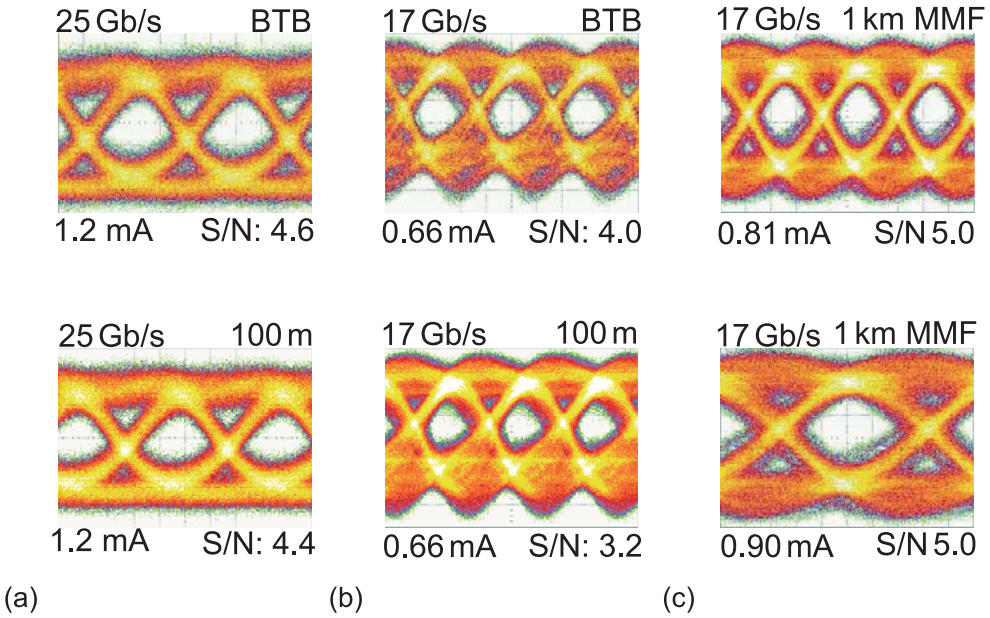

Figure 7.25.: Optical eye diagrams of a 2 µm oxide-aperture diameter 850-nm VCSEL at (a) 1.2 mA and 25 Gb/s in (top) a back-to-back configuration (BTB) and (bottom) across 100 m of multimode optical OM3 fiber (MMF). The optical eye diagrams are recorded at error-free operation with a VIS D30-850M photodiode. (b) Optical eye diagram at 17 Gb/s at 0.66 mA in a (top) BTB configuration and across (bottom) 100 m of MMF. (c) Same VCSEL as in (a) and (b) operated at 17 Gb/s at a larger bias current of 0.9 mA, increasing the signal-to-noise ratio in a (top) BTB configuration and enabling error-free operation up to (bottom) 1000 m of MMF. The optical eye diagrams in (b) and (c) are recorded using the CS-P101 photoreceiver.

To transmit data across long distances of multimode optical fiber, various approaches to reduce the spectral width of the optical emission of VCSELs are pursued. While the reduction of the spectral width can be achieved very successfully by introducing mode selective losses, this approach has severe drawbacks in terms of energy efficiency, but has led to long transmission distances across MMF at high bit rate and a record-low current density [12].

Using a VCSEL from the 850-nm design B (e.g. the same VCSELs that were used for the CW and the small-signal analysis) with a larger oxide-

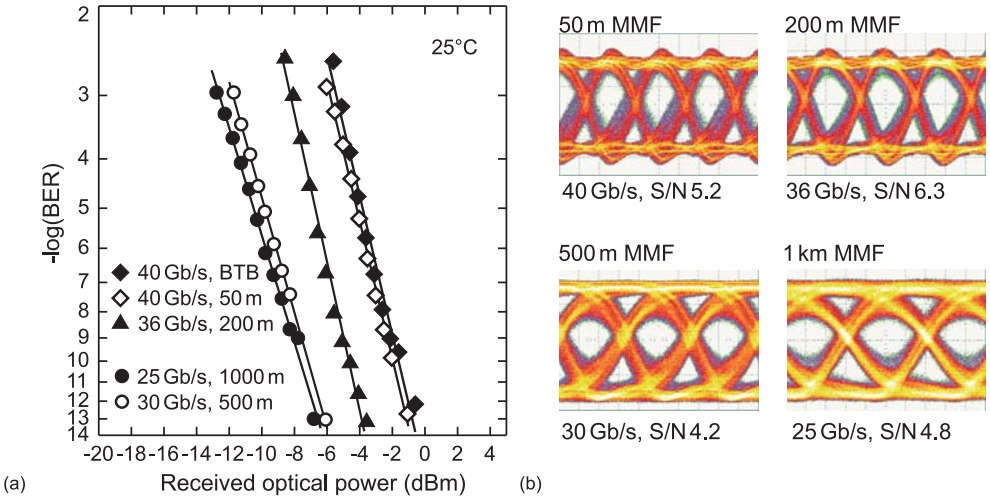

Figure 7.26.: (a) Bit error ratio (BER) versus received optical power for 850-nm VCSELs at bit rates ranging from 25 to 40 Gb/s and multimode fiber lengths up to 1000 m. (b) Optial eye-diagrams and signal-to-noise ratios (S/N) at error-free operation of the data transmission experiments shown in (a). [102] © 2013 IEEE.

aperture diameter of 3 µm and the photoreceiver with integrated TIA, the maximum error-free bit rate across 1000 m of MMF can be increased to 25 Gb/s at an *HBR* of 100 fJ/bit [65]. The VCSEL is operated at a current density of 20 kA/cm^2 at an *EDR* of 125 fJ/bit. With the same VCSEL operated at the same current density error-free operation at 30 Gb/s is also achieved across 500 m of MMF at *EDR* and *HBR* values of 105 and 85 fJ/bit [65], respectively. While the 1000 m MMF consists of a single OM4 MMF fiber spool, two spools of 200 m and one spool of 100 m of OM4 MMF are connected to achieve a total length of 500 m. For measuring the error-free data points across 500 and 1000 m the variable attenuator has to be removed, because it's minimum attenuation is too large for error-free operation. Without the variable attenuator no errors are detected at all up to the maximum number of bits the bit error analyzer can store and thus the BER is set to $< 1 \times 10^{-14}$. The S/N values are 4.2 and 4.8 across 500 and 1000 m of MMF, respectively. The BER versus the received optical power and the optical-eye diagrams recorded at error-free transmission as well as the respective S/N values are given in Figure 7.26 (a) and (b), respectively.

When the bit rate is reduced to 12.5 Gb/s the maximum transmission distance across MMF can be increased up to 2000 m. The CS-P101 photoreceiver can then be used for measuring the BER curve at very low received optical power. The bias current density can then be slightly reduced to 18 kA/cm^2 as compared to 20 kA/cm^2 across 1000 m of MMF resulting in low *EDR* and *HBR* values of 230 and 168 fJ/bit, respectively. The BER versus the received optical fiber at 12.5 Gb/s across 2000 m of OM4 MMF is shown in Figure

7.27. The BER curve starts to have a slight error floor approaching the BER of 1×10^{-12}. But by removing the optical attenuator, the BER for the last data point is 9×10^{-13} and thus error-free operation is achieved.

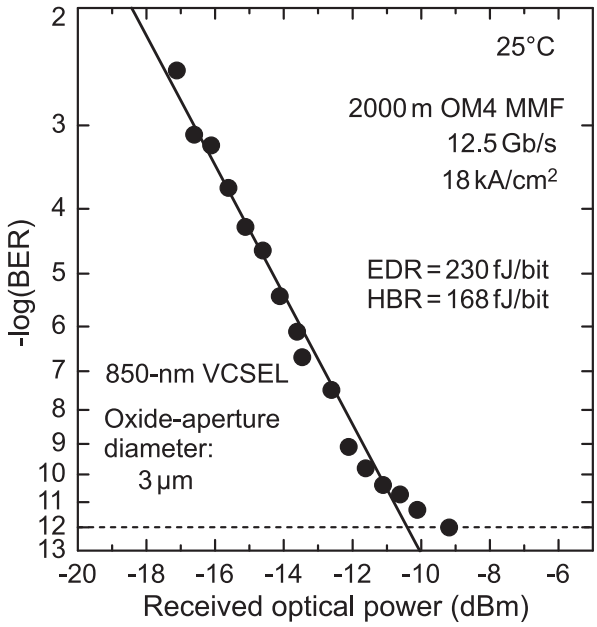

Figure 7.27.: Bit error ratio (BER) versus received optical power for a 3 µm oxide-aperture diameter 850-nm VCSEL at 12.5 Gb/s across 2000 m of OM4 multimode optical fiber.

At large bit rates of 36 and 40 Gb/s the maximum transmission distance reduces to 200 and 50 m of MMF [103], respectively. These results are achieved with VCSELs having a slightly larger oxide-aperture diameter of 4 µm and the photoreceiver with integrated TIA. At 36 Gb/s across 200 of MMF the bias current of the VCSEL is 3.1 mA and the *EDR* and *HBR* values are 182 and 127 fJ/bit, respectively. The optical eye-diagram shows a large S/N of 6.3. At 40 Gb/s and in a back-to-back configuration (BTB) the *EDR* and *HBR* values are 158 and 108 fJ/bit, respectively. The bias current is 3.0 mA corresponding to a current density of 24 kA/cm^2. When 50 m of OM3+ MMF are introduced the bias current needs to be increased to 3.17 mA to maintain error-free operation leading to a slightly larger current density of 25 kA/cm^2. The *EDR* and *HBR* then increase to 170 and 119 fJ/bit, respectively. Thus the *EDR* and *HBR* increase only by 12 and 11 fJ/bit when 50 m MMF are introduced at 40 Gb/s. The S/N is 5.2 in BTB configuration and across 50 m of MMF. The BER versus the received optical power at 40 Gb/s in a BTB configuration and across 50 m of MMF and at 36 Gb/s across 200 m of MMF are shown in Figure 7.26 (a) and the optical eye-diagrams together with the S/N values are given in Figure 7.26 (b), respectively.

In order to demonstrate the impact of the different MMF lengths on the data

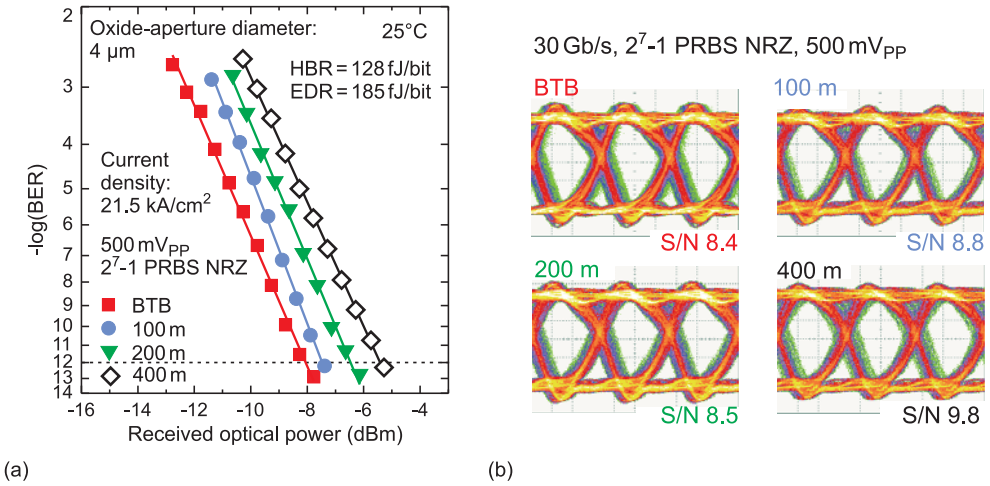

Figure 7.28.: (a) Bit error ratio (BER) versus received optical power for a 850-nm VCSEL with an oxide-aperture diameter of 4 µm at 30 Gb/s in back-to-back configuration (BTB) and across 100, 200, and 400 m of multimode optical fiber. (b) Optical eye-diagrams at error-free operation at 30 Gb/s of the data-transmission results shown in (a). The VCSEL is operated at an *EDR* and *HBR* of 185 and 128 fJ/bit, respectively. [65] © 2013 IEEE.

transmission at a constant bit rate, a 4 µm oxide-aperture diameter VCSEL is operated at a constant bias current of 2.7 mA, corresponding to a current density of 21.5 kA/cm^2, and a constant bit rate of 30 Gb/s. The modulation voltage V_{PP} is kept constant to 0.5 V for measurements across different lengths of MMF. The BER versus the received optical power is measured at 30 Gb/s in a BTB configuration and across 100, 200, and 400 m of OM3+ MMF. Because the bias current is kept constant for all measurements also the *EDR* and *HBR* values remain constant for all measurements and are 185 and 128 fJ/bit, respectively. The received optical power increases with the length of the MMF and is -8.0, -7.5, -6.5, and -5.4 dB in the BTB configuration and across 100, 200, and 400 m of OM3+ MMF, respectively. The S/N values are all well above 8 dB and are 8.4, 8.8, 8.5, and 9.8 dB for the BTB configuration and for 100, 200, and 400 m of MMF. The BER versus the received optical power and the optical eye-diagrams at error-free transmission are shown in Figure 7.28 (a) and (b), respectively. State-of-the art data transmission results with VCSELs across MMF distances of 500 m and more are compared in Tables 7.4 and 7.5.

Table 7.4.: State-of-the-art of energy-efficient 850-nm VCSELs across MMF

Affiliation	UIUC	CTH	CTH	TUB/ VIS	VIS/ TUB	TUB	TUB
Bit rate (Gb/s)	25	20	25	17	25	25	30
Fiber distance (m)	1000	1100	500	1000	603	1000	500
J (kA/cm^2)	5.4	38	18	26	20	20	20
$d_{aperture}$ (µm)	[1]11.8	3	5	2	4	3	3
EDR (fJ/bit)	-	-	-	-	-	125	105
HBR (fJ/bit)	620	280	>200	81	188	100	85
Fiber type	OM4	OM4	OM3+	OM4	OM3+	OM4	OM3+
$\Delta\lambda_{RMS}$ (nm)	-	0.29	0.27	0.17	-	0.11	0.11
ROP (dBm)	-11.5	-7.6	-2	-11	-5.4	-7	-6.5
Year of publication	2013	2012	2012	2011	2012	2013	2013
Reference	[12]	[104]	[44]	[74]	[92]	[65]	[65]

[1]: With a photonic crystal.

Table 7.5.: State-of-the-art of energy-efficient 850-nm VCSELs across MMF (continued)

Affiliation	TUB	CTH	CUT	NCU	BELL
Bit rate (Gb/s)	12.5	25	20	14	10
Fiber distance (m)	2000	1300	2000	2000	2820
J (kA/cm^2)	18	12	12	22	-
$d_{aperture}$ (µm)	3	[1]6	[1]6	[2]8.5	-
EDR (fJ/bit)	230	-	-	2382	720
HBR (fJ/bit)	168	323	258	-	650
Fiber type	OM4	OM4	OM4	OM4	-
$\Delta\lambda_{RMS}$ (nm)	-	0.25	0.25	-	[3]SM
ROP (dBm)	-10.4	-2.4	-3.3	0.5	-12
Year of publication	this	2014	2014	2011	2000
Reference	work	[11]	[11]	[15]	[62]

[1]: With 3 µm diameter surface relief.
[2]: With Zn diffusion.
[3]: single-mode.

Chapter 8.

980-nm VCSEL results

In addition to large modulation bandwidths and high energy efficiency, it is also important that the VCSELs can operate at various temperatures. Especially for short-distance optical interconnects the ambient temperature can be as high as 85°C. For those optical interconnects the performance and the properties of the VCSELs at high temperatures is even more important than at room temperature. Commonly VCSELs are referred to as being temperature-stable when they operate well at relatively high temperatures [19, 105, 106]. This may originate from the assumption that VCSELs operate better at room temperature than at elevated temperatures. If then the VCSEL still operates well at high temperatures it is called *temperature-stable*, because its performance did not degrade much due to an temperature increase. But it already has been demonstrated that the temperature at which the VCSEL performs best, e.g. has the lowest threshold current, the largest D-factor, and highest maximum f_{3dB}, can be much higher than room temperature, when a relatively large gain-to-cavity wavelength offset is used [105, 107, 108, 109]. In the following the change of the static and dynamic VCSEL characteristics due to a change of the ambient temperature is evaluated and quantified. The absolute and relative change of certain key parameters in a broader range of temperature (here 25 to 85°C) can then be used as a measure of the *temperature stability*. Thus a VCSEL is then very *temperature-stable* when the temperature-induced change of its static and dynamic properties is small.

In the following sections first the temperature-induced change of the static VCSEL properties is evaluated and discussed for a 4.5 µm oxide-aperture diameter 980-nm VCSEL for temperatures of 25 to 85°C. Then, in order to determine the impact of the oxide-aperture diameter on the static temperature stability, 980-nm VCSELs with 4 different oxide-aperture diameters of 4.5, 5, 6, and 7 µm are compared. In the next Section the temperature-induced change of the modulation bandwidth and the energy efficiency is evaluated and discussed for a VCSEL with an oxide-aperture diameter of 5 µm, followed by the evaluation of the impact of the oxide-aperture diameter on the temperature stability of f_{3dB} and the energy efficiency.

In this Chapter it is demonstrated that VCSELs with smaller oxide-aperture diameters are not only more energy-efficient at room temperature, but also at high temperatures. In addition VCSELs with smaller oxide-aperture diameters have also a more temperature-stable f_{3dB} and the energy efficiency is less sensitive to a change of the ambient temperature as well.

8.1. Static properties

In the following, first the change of the CW characteristics of a 4.5 µm oxide-aperture diameter 980-nm VCSEL are evaluated and discussed when the ambient temperature is increased from 25°C to 35, 45, 55, 65, 75, and 85°C. Then the impact of the oxide-aperture diameter on the CW temperature stability is demonstrated and discussed by comparing four 980-nm VCSELs with oxide-aperture diameters of 4.5, 5, 6, and 7 µm.

8.1.1. Temperature dependence of the LIV-characteristics of a 4.5 µm oxide-aperture diameter VCSEL

The *LI*- and *IV*-curves for a 980-nm VCSEL with an oxide-aperture diameter of 4.5 µm at heat-sink temperatures of 25, 35, 45, 55, 65, 75, and 85°C are shown in Figure 8.1 (a) and (b), respectively. The threshold current I_{th} and the threshold current density J_{th} are 0.29 mA and 1.82 kA/cm^2 at 25°C and increase with increasing temperature. At 85°C I_{th} and J_{th} are 0.41 mA and 2.58 kA/cm^2, respectively. The increase of I_{th} is 0.12 mA when the heat-sink temperature is increased from 25 to 85°C corresponding to a relative increase of 41%. As can be seen in Figure 8.1 (a) both the rollover current I_{RO} and the slope efficiency decrease with increasing temperature, leading also to a decrease of the maximum of the optical output power P_{opt}. The maximum of P_{opt} decreases from 1.8 mW at 25°C to 1.1 mW at 85°C corresponding to a decrease of -39%. The rollover current decreases from 5.3 mA at 25°C to 4.5 mA at 85°C which is a decrease of -15%. The *IV*-curve does not change significantly with temperature. The differential resistance values R_{d} are obtained by fitting the *IV*-curve from V_{th} to the maximum measured voltage with a linear fit. The R_{d} slightly increases by 20 Ω from 386 Ω at 25°C to 406 Ω at 85°C, respectively. This corresponds to an increase of R_{d} by 5%. The values of I_{th} and P_{th} versus the heat-sink temperature are shown in Figure 8.2 (a) top and bottom, respectively. The maximum output power and the rollover current versus the heat-sink temperature are plotted in Figure 8.2 (b) top and bottom, respectively.

Corresponding to the decrease of P_{opt}, the temperature increase leads to a decrease of the wall plug efficiency (WPE). The maximum WPE of the 4.5 µm oxide-aperture diameter VCSEL ranges from 20.3% at 1.32 mA at 25°C to 14.8% at 1.57 mA at 85°C. Due to the increase of I_{th} with increasing temperature the current at which the WPE is maximum also slightly increases with temperature, but this effect is rather small and can therefore be neglected. The WPE is plotted versus the bias current at 25, 35, 45, 55, 65, 75, and 85°C for the 4.5 µm oxide-aperture diameter VCSEL in Figure 8.3 (a).

Parameters such as the maximum P_{opt}, the P_{th}, or the I_{RO} describe VCSEL properties at one particular working point defined by an extremum in the output power or the laser threshold. In order to evaluate the temperature

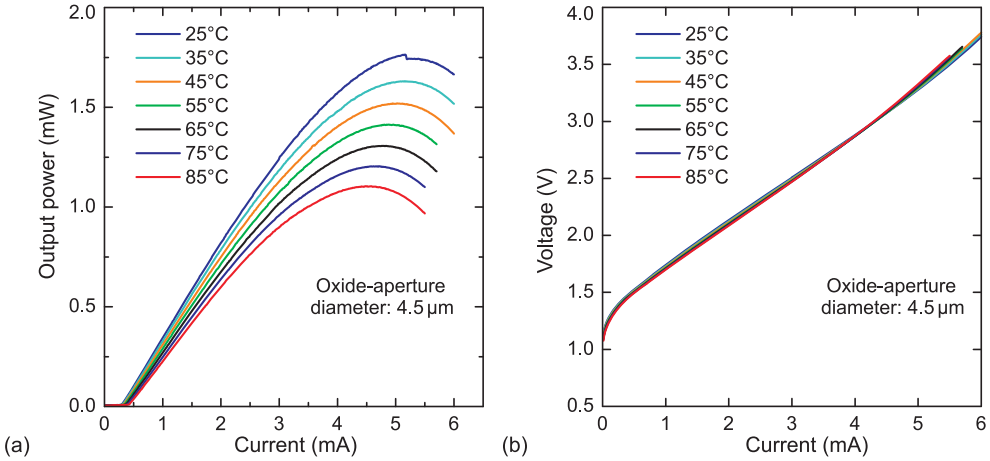

Figure 8.1.: Static LI-characteristics from 25 to 85°C (a) and IV-characteristics (b) of a 980-nm VCSEL with an oxide-aperture diameter of 4.5 µm.

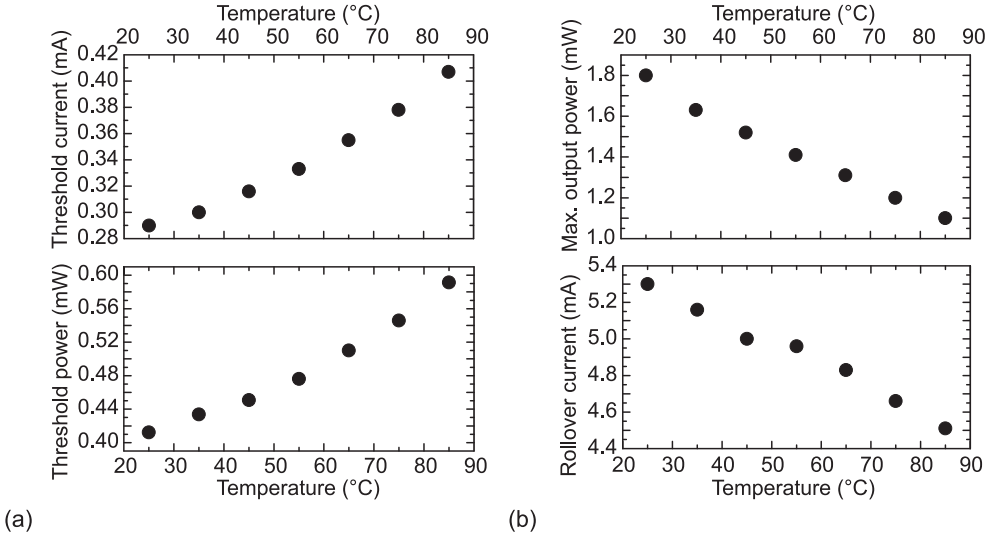

Figure 8.2.: (a) Threshold current I_{th} (top) and threshold power P_{th} (bottom), (b) maximum output power (top) and rollover current (bottom) versus ambient heat-sink temperature for a 980-nm VCSEL with an oxide-aperture diameter of 4.5 µm.

stability of the VCSEL over its complete bias current range from I_{th} to I_{RO} or even larger currents, the absolute change of P_{opt} is plotted versus the bias current in Figure 8.3 (b) for temperature increases from 25 to 35, 45, 55, 65, 75, and 85°C. Corresponding to the LI-curves shown in Figure 8.1 (a) the decrease of P_{opt} increases with increasing temperature and with increasing bias current. When the temperature is increased from 25 to 35°C the maximum decrease of P_{opt} is -0.126 mW at a current of 5.5 mA. This reduction increases further when the change of the ambient temperature gets larger and is -0.255,

-0.351, -0.511, -0.640, and -0.772 mW when the temperature is increased from 25 to 45, 55, 65, 75, and 85°C, respectively. At lower currents the reduction in P_{opt} is much lower, because the current-induced self-heating does not yet contribute much to the degradation of the VCSEL's CW performance. The absolute change of P_{opt} due to temperature increases from 25 to 35, 45, 55, 65, 75, and 85°C is shown versus the bias current for the 4.5 µm oxide-aperture diameter VCSEL in Figure 8.3 (b). The curve of the absolute P_{opt} change due to a temperature increase versus the bias current or current density J used for comparing the CW temperature stability of VCSELs with different oxide-aperture diameters.

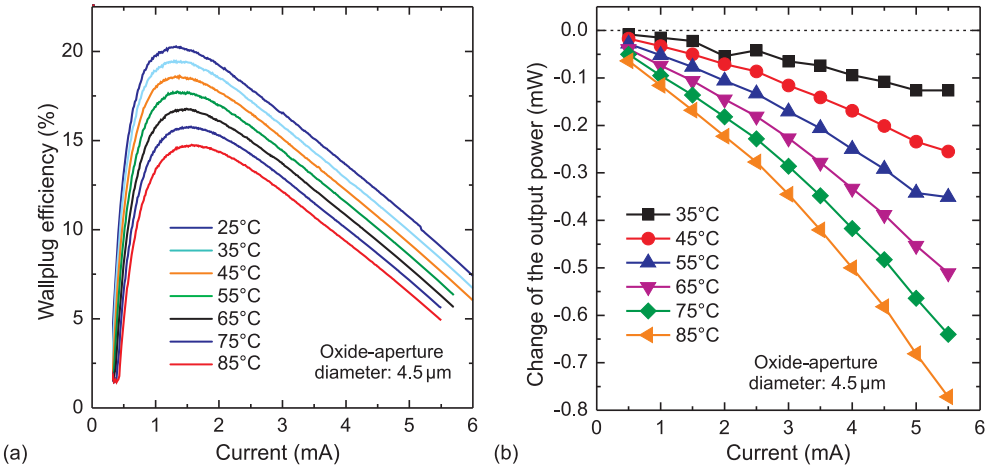

Figure 8.3.: (a) Wallplug efficiency (WPE) versus bias current for different heat-sink temperatures of 25, 35, 45, 55, 65, 75, and 85°C and (b) the absolute change of the output power P_{opt} due to a temperature increase from 25 to 35, 45, 55, 65, 75, and 85°C for a 4.5 µm oxide-aperture diameter 980-nm VCSEL.

Because all parameters change continuously with changing temperatures without reaching local maxima or minima the maximum change of all CW parameters occurs when the temperature is increased from 25 to 85°C. Thus in this case it is sufficient to only compare the CW parameter change for a temperature increase from the lowest to the highest temperature, e.g. from 25 to 85°C, when the temperature stability of VCSELs with different oxide-aperture diameters is compared, as is done in the following Section.

Due to the very temperature insensitive *IV*-characteristic of the VCSEL also the electrical power P_{el} does not change much with temperature. Thus the temperature stability of the *EDR* will be mainly determined by the temperature stability of the f_{3dB}. Due to the decrease of P_{opt} with increasing temperature the dissipated power at a given current increases with temperature. Thus the temperature stability of the *HBR* depends on how both P_{opt} and f_{3dB} change with changing temperature. Theoretically, an increase of f_{3dB} with temperature could compensate for the decreasing P_{opt} resulting in a very

temperature-stable *HBR*. In case the f_{3dB} of the VCSEL decreases with temperature like P_{opt}, then this would lead to a significantly lower temperature stability of the *HBR* compared to the *EDR*.

8.1.2. Impact of the oxide-aperture diameter on the static temperature-stability of the 980-nm VCSELs

In order to evaluate the impact of the oxide-aperture diameter on the CW temperature stability, the LI-characteristics of 3 additional 980-nm VCSELs with oxide-aperture diameters of 5, 6, and 7 µm are included in the evaluation. Because the mesa diameters of the first and second mesa impact the thermal resistance of the VCSELs, it is important to note here that with the oxide-aperture diameter also the diameter of the first and second mesa of these VCSELs differ. The three VCSELs with oxide-aperture diameters of 5, 6, and 7 µm are neighbor VCSELs from the same column of one unit-cell. Thus the distance from one VCSEL to the other is 600 µm and inhomogeneities due to growth and processing should be negligible. The first mesa diameter of the 5, 6, and 7 µm oxide-aperture diameter VCSELs are 26, 27, and 28 µm, respectively. For these three VCSELs the second mesa diameter is 20 µm larger than the first mesa diameter and thus 46, 47, and 48 µm for the VCSELs with oxide-aperture diameters of 5, 6, and 7 µm, respectively. The VCSEL with an oxide-aperture diameter of 4.5 µm is from a different unit-cell approximately 2 cm away from the three other VCSELs and has a different double-mesa design with a larger second mesa diameter. The first and second mesa diameter of this VCSEL is 25 and 85 µm, respectively. Tests with VCSELs having different oxide-aperture diameters and different double-mesa designs have shown that the impact of the oxide-aperture diameter on the CW temperature stability is much larger than the differences in the first and/or second mesa diameter. The diameter of the second mesa does not have a significant impact on the thermal resistance. Thus the difference in the mesa diameters of the VCSELs is neglected here.

For comparison the static *LIV*-characteristics of the 980-nm VCSELs with larger oxide-aperture diameters of 5, 6, and 7 µm are plotted together with that of the 4.5 µm oxide-aperture diameter in Figure 8.4 at (a) 25°C and (b) at 85°C, respectively. The threshold currents at 25°C are 0.31, 0.44, and 0.60 mA for the VCSELs with oxide-aperture diameters of 5, 6, and 7 µm, respectively. The maximum output power at 25°C is 2.6, 4.5, and 7.4 mW at rollover currents of 6.4, 10.4, and 15.8 mA for the 5, 6, and 7 µm oxide-aperture diameter VCSEL respectively. The maximum output power reduces to 1.7, 3.0, and 4.9 mW at currents of 5.3, 8.9, and 12.6 mA when the temperature is increased to 85°C corresponding to decreases of -35, -33, and -34% for the VCSELs with oxide-aperture diameters of 5, 6, and 7 µm, respectively. The threshold current increases to 0.40, 0.45, and 0.61 mA at 85°C for the 5, 6, and 7 µm oxide-aperture diameter VCSELs.

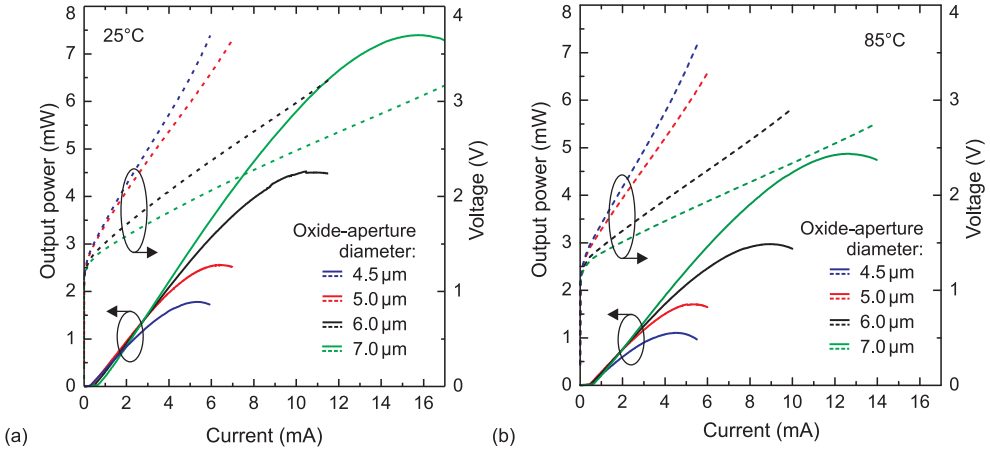

Figure 8.4.: Static *LIV*-characteristics for 980-nm VCSELs with oxide-aperture diameters of 4.5, 5, 6, and 7 µm at heat-sink temperatures of (a) 25°C [110] (© 2015 SPIE) and at (b) 85°C, respectively.

The absolute change of P_{opt} due to a temperature increase at a given bias current is the same for all four VCSELs in case the respective bias current is well below the thermal rollover current I_{RO}. When the bias current is close to I_{RO}, the drop of P_{opt} becomes larger. This can be clearly seen when the absolute change of P_{opt} due to a temperature increase from 25 to 85°C is plotted in Figure 8.5 (a) versus the bias current for the VCSELs with oxide-aperture diameters of 4.5, 5, 6, and 7 µm. Thus from the absolute change of P_{opt} versus the current one could conclude that VCSELs with larger oxide-aperture diameters are more temperature-stable than similar VCSELs with smaller oxide-aperture diameters, because they reach larger thermal rollover currents and thus P_{opt} changes less at higher currents as compared to smaller oxide-aperture diameter VCSELs. But as already shown on page 83 in Chapter 7.1.1 in Figure 7.3 (a), VCSELs with larger oxide-aperture diameters have lower rollover current *densities*. Thus the change of P_{opt} plotted against the current density increases at a given current density with increasing oxide-aperture diameter. The absolute change of P_{opt} due to a temperature increase from 25 to 85°C is plotted versus the current density for all four VCSELs with oxide-aperture diameters of 4.5, 5, 6, and 7 µm in Figure 8.5 (b). For low current densities up to approximately 5 kA/cm^2 the change of the VCSELs with the two smallest oxide-aperture diameters of 4.5 and 5 µm is nearly the same. For any larger given current densities the change of P_{opt} continuously increases with increasing oxide-aperture diameter.

This evaluation demonstrates that small oxide-aperture diameter VCSELs are advantageous for temperature-stable CW performance at low current densities and the advantage of using small oxide-aperture diameter VCSELs increases with increasing current density. The oxide-aperture diameter dependent evaluation of the energy efficiency of 850-nm VCSELs in the previous

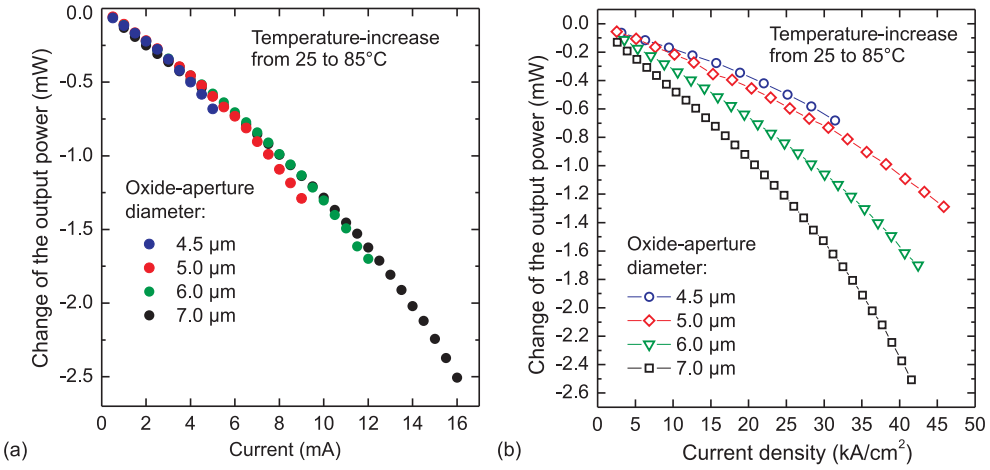

Figure 8.5.: Absolute change of the output power P_{opt} due to a temperature increase from 25 to 85°C for the 980-nm VCSELs with oxide-aperture diameters of 4.5, 5, 6, and 7 µm versus (a) the bias current and (b) the current density, respectively. [110] © 2015 SPIE.

Chapters demonstrates that small oxide-aperture diameter VCSELs operated at low current densities can achieve much higher energy-efficiencies, e.g. lower *EDR* and *HBR* values, than similar VCSELs with larger oxide-aperture diameters.

8.2. Small-signal modulation

In order to investigate the temperature stability of the modulation bandwidth of 980-nm VCSELs, S21-measurements are performed at different heat-sink temperatures for VCSELs with different oxide-aperture diameters. The $f_{3\mathrm{dB}}$ values are determined at 25 and 85°C.

8.2.1. Temperature stability of the modulation bandwidth of a 5 µm oxide-aperture diameter VCSEL

The $f_{3\mathrm{dB}}$ for a 980-nm VCSEL with an oxide-aperture diameter of 5 µm is shown versus the bias current at 25 and 85°C in Figure 8.6 (a). At very low currents up to approximately 0.75 mA the $f_{3\mathrm{dB}}$ is larger at 25 than at 85°C, because of the increase of threshold current with temperature. The device is operated much closer to threshold at 85 than at 25°C leading to the smaller $f_{3\mathrm{dB}}$. At larger currents $f_{3\mathrm{dB}}$ increases with temperature until approximately 2.6 mA where $f_{3\mathrm{dB}}$ remains unchanged when the temperature is increased from 25 to 85°C. At even larger currents $f_{3\mathrm{dB}}$ saturates at 85°C at 22.7 GHz whereas $f_{3\mathrm{dB}}$ still increases further at 25°C. The modulation bandwidth versus the square-root of the current above threshold at 25 and 85°C is

shown in Figure 8.6 (b) where the straight lines are the linear fits for obtaining the respective MCEF values. The MCEF is 14.8 GHz/$\sqrt{\text{mA}}$ at 25°C and increases to 17.6 GHz/$\sqrt{\text{mA}}$ at 85°C which is an increase of 19%.

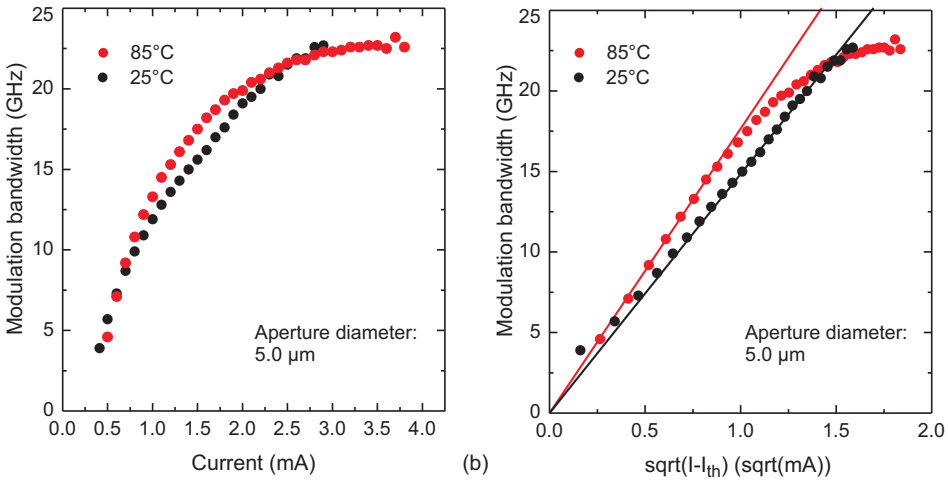

Figure 8.6.: Modulation bandwidth $f_{3\text{dB}}$ versus current for a 980-nm VCSEL with an oxide-aperture diameter of 5.0 µm at 25 and 85°C (a) and modulation bandwidth versus the square-root of the current above threshold current (b) of the same VCSEL as in (a). The straight lines are the linear fits for obtaining the modulation current efficiency factor (MCEF) values at 25 and 85°C, respectively.

In order to quantify the temperature stability of the $f_{3\text{dB}}$, both the absolute and the relative change of $f_{3\text{dB}}$ due to an increase of the temperature from 25 to 85°C are determined and plotted in Figure 8.7 (a) and (b), respectively. The first two data points show a decrease in $f_{3\text{dB}}$ which can be related to the temperature-induced increase in threshold current as already discussed earlier. Then the absolute change of $f_{3\text{dB}}$ ($\Delta f_{3\text{dB}}$) increases with increasing current. The maximum of $\Delta f_{3\text{dB}}$ is 2.0 GHz at 1.6 mA and then decreases until the bias current of maximum temperature stability, e.g. $\Delta f_{3\text{dB}}$ =0 GHz, is reached at 2.6 mA. At even larger currents $\Delta f_{3\text{dB}}$ becomes negative. At large currents where $f_{3\text{dB}}$ is saturated at both temperatures and thus does not vary with current anymore, $\Delta f_{3\text{dB}}$ is expected to be constant (not shown here) and will then simply be the difference of the maximum $f_{3\text{dB}}$ at both temperatures. The relative change of $f_{3\text{dB}}$ is nearly constant at 12.3% in the current range of 0.9 to 1.6 mA. At 0.5 mA close to the threshold current it is -20%.

8.2.2. Temperature stability of the energy efficiency of an 5 µm oxide-aperture diameter 980-nm VCSEL

The potential for energy-efficient data transmission of a VCSEL can be derived from the bandwidth-to electrical power ratio as already described in Section 7.2.2. Both electrical power consumption and $f_{3\text{dB}}$ versus current change

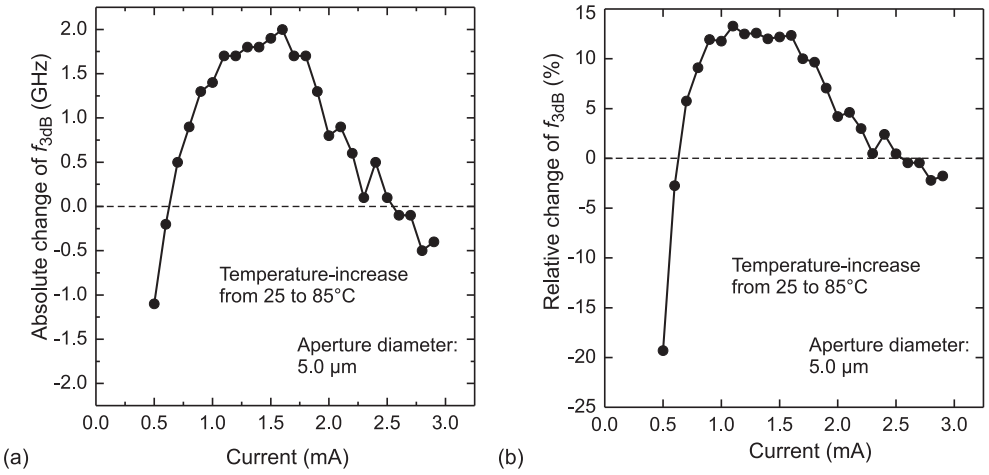

Figure 8.7.: (a) Absolute change of the modulation bandwidth f_{3dB} versus current for a 980-nm VCSEL with an oxide-aperture diameter of 5.0 µm when the temperature is increased from 25 to 85°C. (b) Relative change of f_{3dB} when the temperature is increased from 25 to 85°C.

with changing temperature. As already seen in Section 8.1.1 the VCSEL's IV-characteristic does not change significantly with temperature. Thus the temperature-induced change of f_{3dB} dominates the change of the bandwidth-to electrical power ratio with temperature. The bandwidth-to electrical power ratio for a 980-nm VCSEL with an oxide-aperture diameter of 5 µm is shown at 25 and 85°C in Figure 8.8 (a).

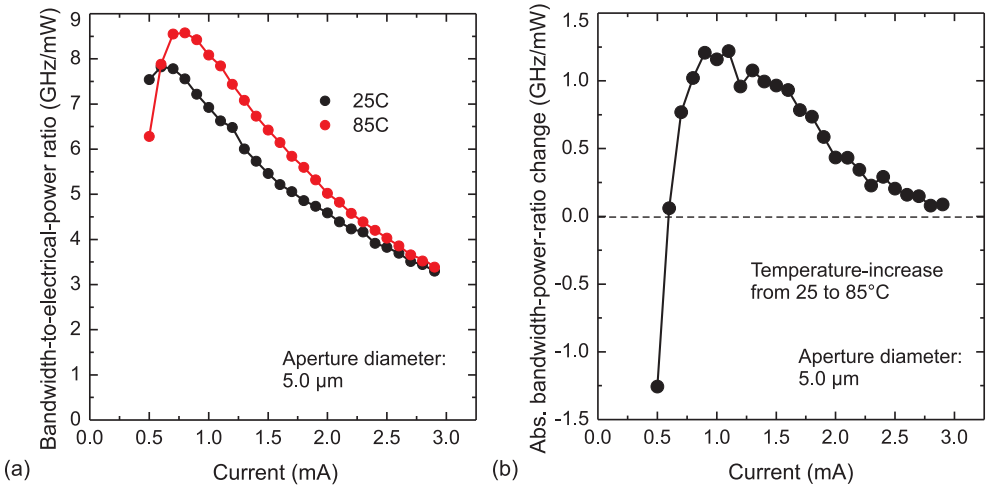

Figure 8.8.: (a) Bandwidth-to-electrical-power ratio versus current for a 980-nm VCSEL with an oxide-aperture diameter of 5.0 µm at 25 and 85°C. (a) Temperature-induced absolute change of the bandwidth-to electrical power ratio when the temperature is increased from 25 to 85°C.

At a low current of 0.5 mA the bandwidth-to electrical power ratio is smaller at 85 than at 25°C due to the smaller f_{3dB} which can be explained with the increased threshold current of the VCSEL at 85°C. At all larger currents the bandwidth-to electrical power ratio at 85°C exceeds the bandwidth-to electrical power ratio at 25°C. The absolute temperature-induced change of the bandwidth-to electrical power ratio versus the current is plotted in Figure 8.8 (b). The temperature-induced change of the bandwidth-to electrical power ratio looks similar to that of f_{3dB}. The maximum of the bandwidth-to electrical power ratio change of 1.2 GHz/mW is reached at 1.1 mA. At larger currents the change of bandwidth-to electrical power ratio decreases but remains larger than 0 in the measured current range.

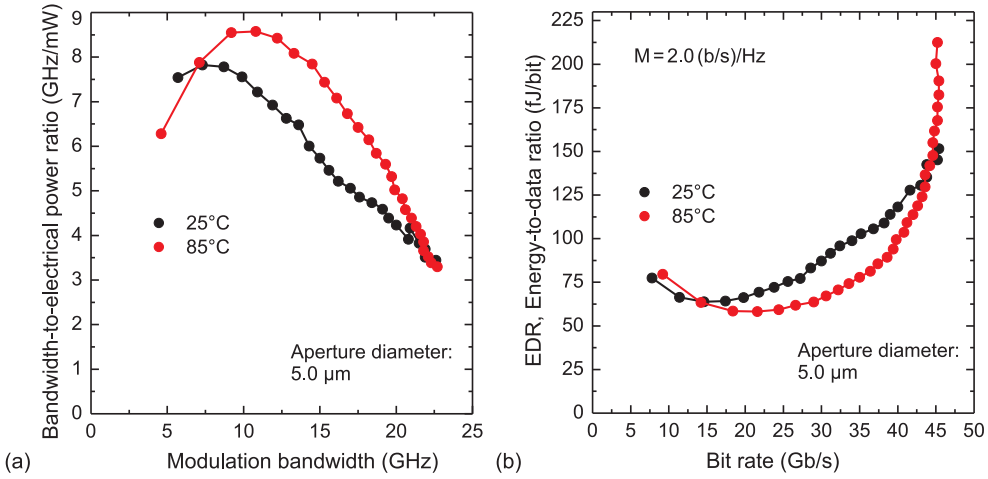

Figure 8.9.: (a) Bandwidth-to-electrical-power ratio versus the modulation bandwidth f_{3dB}, and (b) energy-to-data ratio *EDR* versus the bit rate for M = 2.0 (b/s)/Hz for a 5 µm oxide-aperture diameter 980-nm VCSEL at 25 and 85°C. [75] © 2014 IEEE

Since both the bandwidth-to electrical power ratio and f_{3dB} increase with temperature the impact on the temperature increase on the energy efficiency is even more pronounced when the bandwidth-to electrical power ratio is plotted against f_{3dB}. In a broad f_{3dB} range from ~6 to ~20 GHz the bandwidth-to electrical power ratio is much larger at 85 than at 25°C. The bandwidth-to electrical power ratio values at 25 and 85°C converge for f_{3dB} values larger than 20 GHz and are shown in Figure 8.9 (a). The energy-to-data ratio *EDR* can be calculated from the bandwidth-to-electrical-power ratios using Equation 4.7. With M = 2.0 (b/s)/Hz the *EDR* is smaller at 85°C than at 25°C for bit rates from approximately 15 to 45 Gb/s. The *EDR* versus the bit rate is shown at 25 and 85°C for M = 2.0 (b/s)/Hz in Figure 8.9 (b).

The *EDR* for M-factors of 1.7, 2.0, and 2.46 (b/s)/Hz is plotted versus the bit rate in Figure 8.10 at 25°C (a) and at 85°C (b). In order to compare the temperature stability of the energy efficiency the bit rates at the *EDR* values of 80, 100, and 120 fJ/bit are determined at 25 and 85°C and plotted versus the

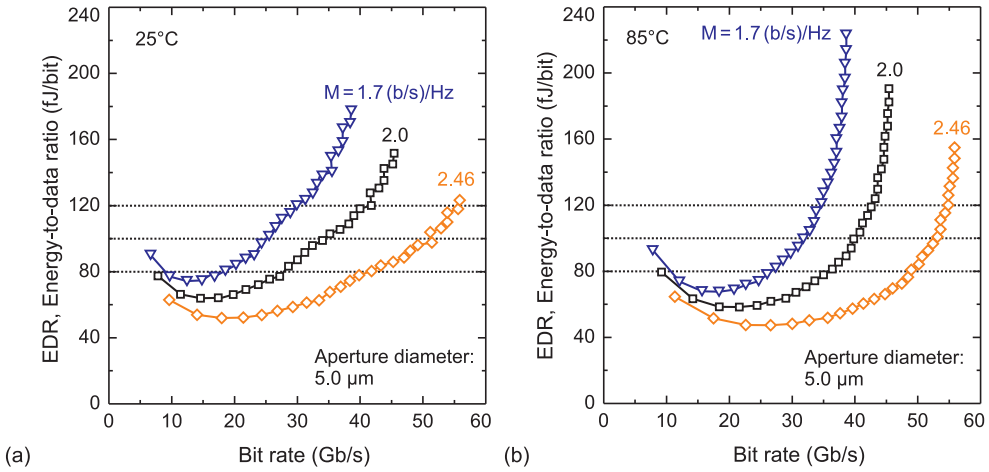

Figure 8.10.: Energy-to-data ratio *EDR* versus bit rate for a 5 µm oxide-aperture diameter 980-nm VCSEL at 25°C (a) and at 85°C (b) for M-factors of 1.7, 2.0, and 2.46 (b/s)/Hz. [75] © 2014 IEEE.

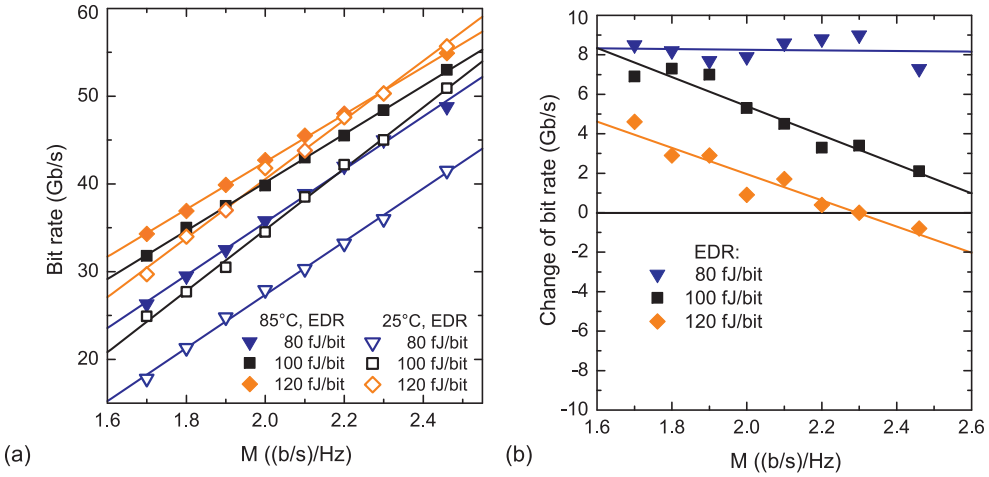

Figure 8.11.: Bit rates at energy-to-data ratios (*EDRs*) of 80, 100, and 120 fJ/bit versus the M-factor for a 5 µm oxide-aperture diameter 980-nm VCSEL at 25 and 85°C (a). Difference of the bit rate at an *EDR* of 80, 100, and 120 fJ/bit when the temperature is increased from 25 to 85°C versus the M-factor for a 980-nm VCSEL with an oxide-aperture diameter of 5 µm.

respective M-factors. At both temperatures the data can be fitted linearly with a very good accuracy as already shown in Section 7.2.2 for 850-nm VCSELs at 25°C. The temperature stability of the *EDR* can now be determined as the temperature-induced change of the bit rates at the given *EDR* values versus the M-factor, from the difference of the two respective M-factor curves at 25 and 85°C. Since the bit rates for the given *EDR* values plotted against the M-factor can be fitted linearly for both temperatures the temperature-induced

change of this bit rate will also depend linearly on the M-factor. The bit rates at *EDR* values of 80, 100, and 120 fJ/bit at 25 and 85°C for the 980-nm VCSEL with an oxide-aperture diameter of 5 µm are plotted versus the M-factor in Figure 8.11 (a). In the investigated range of M-factors from 1.7 to 2.46 (b/s)/Hz three different behaviors are observed for the bit rate change at *EDR* values of 80, 100, and 120 fJ/bit. At 80 fJ/bit the bit rate increases by nearly the same value at a given M-factor when T is increased from 25 to 85°C, resulting in a shift of the M-factor curve without any change of the slope. At an *EDR* of 100 fJ/bit the bit rate at 85°C is still larger than at 25°C, but the slope of the M-factor curve decreases. Thus the temperature-induced increase of the bit rate at 100 fJ/bit reduces with increasing M-factor but the bit rate is larger for all investigated M-factors at 85 than at 25°C. At an even larger *EDR* of 120 fJ/bit the temperature-induced change of the slope is larger leading to an intersection of the M-factor curves at 25 and 85°C at an M-factor of 2.3. At this M-factor where both lines cross each other the VCSEL achieves the same bit rate at the same *EDR* at both temperatures, e.g. at 25 and 85°C.

The change of the M-factor curve can be used as a measure of the *EDR* temperature stability of the VCSEL. The difference of the bit rates at *EDR* values of 80, 100, and 120 fJ/bit due to a temperature increase from 25 to 85°C is plotted for the 980-nm VCSEL with an oxide-aperture diameter of 5.0 µm in Figure 8.11 (b). The bit rate difference at 80 fJ/bit remains nearly constant at +8.2 Gb/s with changing M-factor. Thus for all M-factors in the investigated range the bit rate of the VCSEL increases by the same constant value. At 100 fJ/bit the increase of the bit rate determined from the linear fit ranges from +7.6 Gb/s at M = 1.7 (b/s)/Hz to +1.9 Gb/s at M = 2.46 (b/s)/Hz. Due to the differences in the slopes when *EDR* = 100 fJ/bit, the two M-factor curves will cross each other, but for these curves the intersection will occur at an M-factor that is larger than the maximum M-factor of 2.46 (b/s)/Hz in this analysis. For an *EDR* of 120 fJ/bit the maximum bit rate change of +4.0 Gb/s occurs at an M-factor of 1.7 (b/s)/Hz. At M = 2.3 (b/s)/Hz the bit rate does not change when the temperature is increased and reduces for larger M-factors. This temperature-stable bit rate at an *EDR* of 120 fJ/bit at 25 and 85°C at M = 2.3 (b/s)/Hz is 50.3 Gb/s. At M = 2.46 (b/s)/Hz the bit rate reduces by -1.1 Gb/s, which is still a very small bit rate change considering the large change in ambient temperature from 25 to 85°C.

As can be seen in Figure 8.11 (b) the temperature stability of the *EDR* increases at a given M-factor with increasing *EDR* values, e.g. the bit rate changes less with a temperature increase. This temperature stability phenomena can also be observed for M = 2.0 (b/s)/Hz in Figure 8.9 (b).

8.2.3. Impact of the oxide-aperture diameter on the temperature stability of the modulation bandwidth

In order to determine the impact of the oxide-aperture diameter on the temperature stability of the modulation bandwidth the two larger neighbor VCSELs of the already discussed 5 µm oxide-aperture diameter VCSEL are now included in the evaluation. These VCSELs have oxide-aperture diameters of 6 and 7 µm, respectively.

At 25°C the maximum f_{3dB} values are 24.7 and 25.6 GHz for the 6 and 7 µm oxide-aperture diameter VCSEL, respectively. The VCSEL with an oxide-aperture diameter of 5 µm was not measured until the saturation of f_{3dB}, but from large-signal modulation experiments it can be concluded that its maximum f_{3dB} is slightly lower than for the other two VCSELs. At 85°C the maximum f_{3dB} is approximately 23 GHz for all three VCSELs. The MCEF values are 14.8, 10.5, and 7.8 GHz/$\sqrt{\text{mA}}$ for the 5, 6, and 7 µm oxide-aperture diameter VCSELs at 25°C and increase to 17.6, 14.3, and 10.5 GHz/$\sqrt{\text{mA}}$ for the same devices at 85°C. The modulation bandwidth f_{3dB} of the three VCSELs is plotted versus the square-root of the current above threshold current at 25 and 85°C in Figure 8.12 (a) and (b), respectively. Thus the MCEF increases for all three oxide-aperture diameter VCSELs with increasing temperature. Because f_{3dB} increases faster with current at 85°C than at 25°C but saturates at lower currents and lower maximum f_{3dB} values, there exist a certain bias current at which the f_{3dB} is the same for 25 and 85°C. This current at which f_{3dB} is insensitive to a temperature increase from 25 to 85°C increases with increasing oxide-aperture diameter and is 2.6, 6.5, and 8.5 mA for the 5, 6, and 7 µm oxide-aperture diameter VCSEL, respectively. At larger currents f_{3dB} is larger at 25°C than at 85°C, because the saturation is not reached yet and the f_{3dB} continues to increase with current, whereas f_{3dB} does not change anymore with increasing bias current at 85°C or even starts to decrease. The relative temperature-induced change of the f_{3dB} increases with increasing oxide-aperture diameter. For the 5 µm oxide-aperture diameter VCSEL the current of $\mathrm{d}f_{3dB} = 0\%$ has a value of 41-48% of the thermal rollover current at 25 and 85°C, respectively. For the larger oxide-aperture diameter VCSELs the current of $\mathrm{d}f_{3dB} = 0\%$ occurs at currents that correspond to 54-73% of the rollover currents at 25 and 85°C. The relative change $\mathrm{d}f_{3dB}$ of f_{3dB} due to an increase of the temperature from 25 to 85°C is plotted versus the bias current for the 5, 6, and 7 µm oxide-aperture diameter VCSELs in Figure 8.13 (a).

The modulation bandwidth at $\mathrm{d}f_{3dB} = 0\%$ is 21.8, 22.1, and 21.9 GHz for the 5, 6, and 7 µm oxide-aperture diameter VCSELs and thus does not significantly vary with the oxide-aperture diameter. Assuming M = 2.0 (b/s)/Hz the *EDR* values at $\mathrm{d}f_{3dB} = 0\%$ are 129, 343, and 425 fJ/bit for the 5, 6, and 7 µm oxide-aperture diameter VCSELs, respectively. Thus VCSELs with smaller

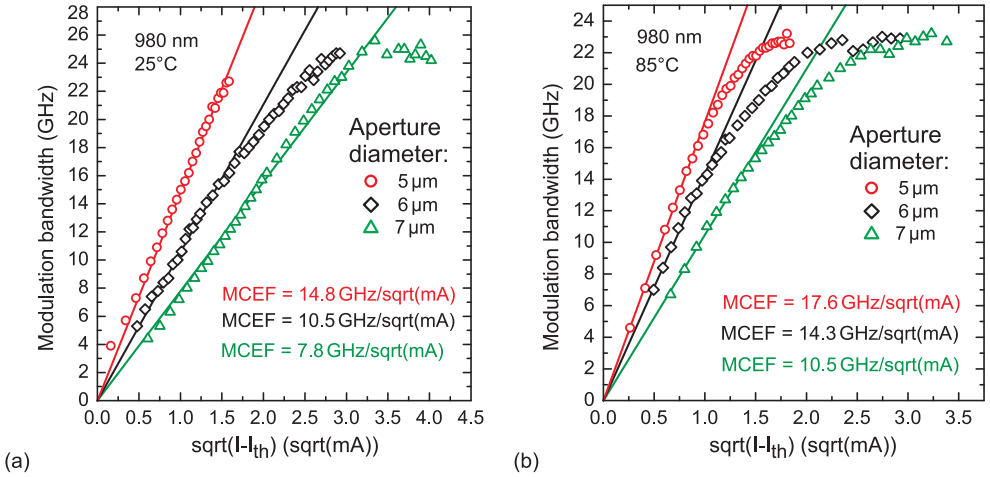

Figure 8.12.: Modulation bandwidth versus the square-root of the current above threshold current for the 5, 6, and 7 µm oxide-aperture diameter VCSELs at 25°C (a) and 85°C (b). The linear fits for obtaining the modulation-current efficiency factors (MCEFs) and the respective MCEF values are given. [75] © 2014 IEEE.

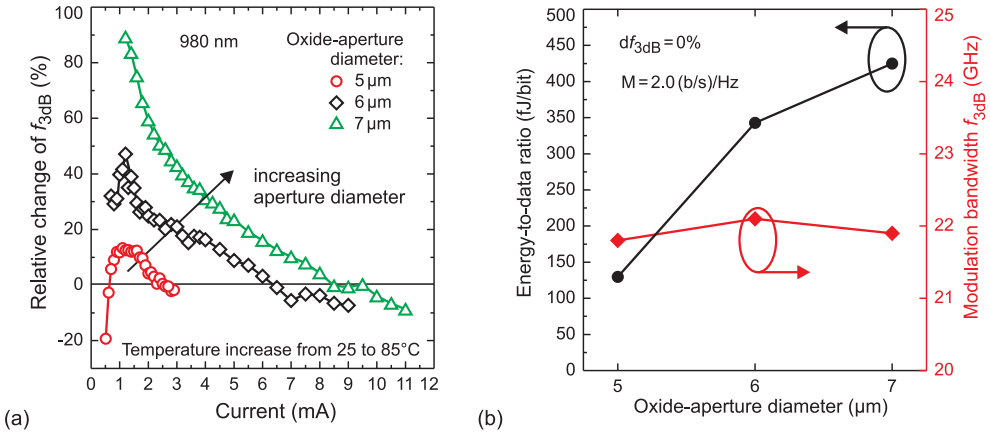

Figure 8.13.: (a) Relative change of $f_{3\mathrm{dB}}$ versus bias current for the 5, 6, and 7 µm oxide-aperture diameter VCSELs when the temperature is increased from 25 to 85°C, and (b) energy-to-data ratio EDR versus oxide-aperture diameter for $\mathrm{d}f_{3\mathrm{dB}} = 0\%$. [75] © 2014 IEEE.

oxide-aperture diameter are also more energy-efficient at the bias current of $\mathrm{d}f_{3\mathrm{dB}} = 0\%$. The $f_{3\mathrm{dB}}$ and EDR at the bias current of $\mathrm{d}f_{3\mathrm{dB}} = 0\%$ are plotted versus the oxide-aperture diameter in Figure 8.13 (b). The current density that yields the perfectly temperature-stable $f_{3\mathrm{dB}}$ is 13, 23, and 22 kA/cm^2 for the VCSELs with oxide-aperture diameters of 5, 6, and 7 µm. The current density is slightly smaller for the 7 µm oxide-aperture diameter VCSEL than for the VCSEL with an oxide-aperture diameter of 6 µm. From only three different oxide-aperture diameter VCSELs it is hard to conclude whether the

Table 8.1.: Static and dynamic VCSEL properties at the current of $\mathrm{d}f_{3\mathrm{dB}} = 0\%$ for a temperature increase from 25 to 85°C for 980-nm VCSELs with different oxide-aperture diameters.

Oxide-aperture diameter (µm)	5	6	7
Current (mA)	2.6	6.5	8.5
Current-density ($\mathrm{kA/cm^2}$)	13	23	22
P_{opt} at 25°C (mW)	1.29	3.37	5.01
P_{opt} at 85°C (mW)	1.01	2.61	4.00
ΔP_{opt} (mW)	-0.28	-0.76	-1.01
bandwidth-to electrical power ratio (GHz/mW)	3.74	1.52	1.03
$f_{3\mathrm{dB}}$ (GHz)	21.8	22.2	21.9

current density at $\mathrm{d}f_{3\mathrm{dB}} = 0\%$ monotonously increases with oxide-aperture diameter or whether the current density is constant once a certain oxide-aperture diameter is reached and does not increase further with oxide-aperture diameter. The temperature-induced reduction of the optical output power when the temperature is increased from 25 to 85°C increases with increasing oxide-aperture diameter. The absolute output power drop is -0.28, -0.76, and -1.01 mW for the VCSELs with oxide-aperture diameters of 5, 6, and 7 µm which corresponds to relative output power changes of -22, -23, and -20%, respectively. The most important static and dynamic device properties at $\mathrm{d}f_{3\mathrm{dB}} = 0\%$ are given for the 980-nm VCSELs with oxide-aperture diameters of 5, 6, and 7 µm in Table 8.1. Because the oxide-aperture diameter of the VCSEL impacts the temperature stability of both the static and dynamic properties, the temperature stability of the energy efficiency depends on the oxide-aperture diameter as well, as is demonstrated in the next Section.

8.2.4. Impact of the oxide-aperture diameter on the temperature stability of the energy efficiency

The temperature stability of the energy efficiency can be investigated from the measured bandwidth-to electrical power ratio at 25 and 85°C as already performed above for the 5 µm oxide-aperture diameter VCSEL. As discussed in Section 7.2.4 for 850-nm VCSELs at 25°C the bandwidth-to electrical power ratio is larger for VCSELs with smaller oxide-aperture diameters. The bandwidth-to electrical power ratio at 25°C is plotted versus $f_{3\mathrm{dB}}$ in Figure 8.14 (a). The 5 µm oxide-aperture diameter VCSEL achieves a clear maximum of the bandwidth-to electrical power ratio at approximately 8 GHz. For the two VCSELs with larger oxide-aperture diameter no distinct maximum of the bandwidth-to electrical power ratio can be observed. At 85°C the curvature and shape of the bandwidth-to electrical power ratio curve versus the $f_{3\mathrm{dB}}$ change. The maximum of the bandwidth-to electrical power ratio occurs at 11 GHz for the 5 µm oxide-aperture diameter VCSEL. For the 6 µm oxide-

aperture diameter VCSEL a maximum of the bandwidth-to electrical power ratio can now be observed at a slightly smaller f_{3dB} than for the smaller 5 µm oxide-aperture diameter VCSEL. The bandwidth-to electrical power ratio of the largest 7 µm oxide-aperture diameter VCSEL still does not show a distinct maximum value, but there is a plateau of the bandwidth-to electrical power ratio in the f_{3dB} range of approximately 6 to 9 GHz. The f_{3dB}/P_{el} ratios at 85°C of the 5, 6, and 7 µm oxide-aperture diameter VCSELs are plotted versus f_{3dB} in Figure 8.14 (b). Comparing the bandwidth-to electrical power ratio at 25 and 85°C in Figure 8.14 (a) and (b), respectively, one can clearly see that the change of the bandwidth-to electrical power ratio is significantly larger for the 6 and 7 µm oxide-aperture diameter VCSELs than for the 5 µm oxide-aperture diameter VCSEL. At 25°C the bandwidth-to-electrical power ratios differ more with changing oxide-aperture diameter than at 85°C.

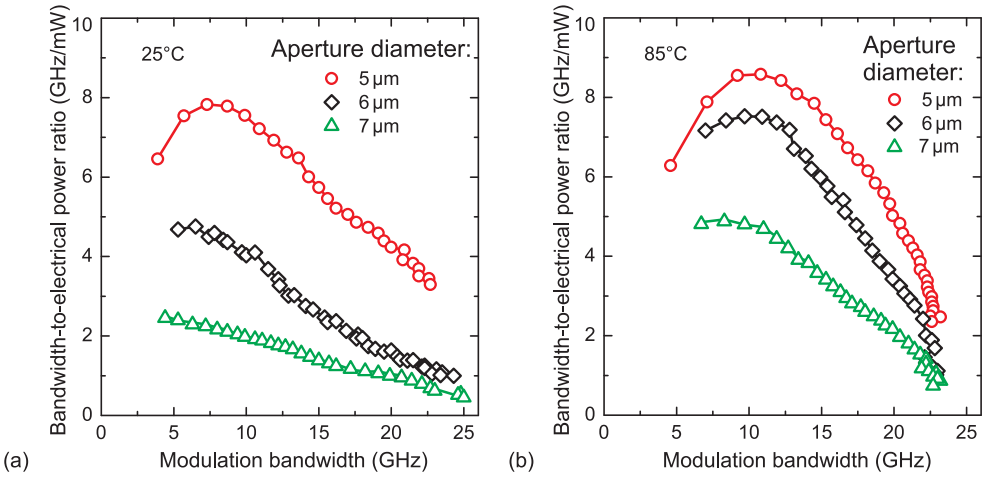

Figure 8.14.: Bandwidth-to-electrical power ratio versus the modulation bandwidth f_{3dB} for 980-nm VCSELs with oxide-aperture diameters of 5, 6, and 7 µm at (a) 25°C and (b) 85°C [75] © 2014 IEEE.

To illustrate the impact of the oxide-aperture diameter on the energy efficiency and its temperature stability the *EDR* values and bit rates are calculated assuming M = 2.0 (b/s)/Hz and plotted for 25°C and 85°C in Figure 8.15 (a) and (b), respectively. As discussed previously for 850-nm VCSELs at 25°C, the *EDR* increases with increasing oxide-aperture diameter for a given bit rate. For large bit rates approaching 50 Gb/s the *EDR* curves of the 6 and 7 µm oxide-aperture diameter VCSELs start to converge, similar to the bevahior of their f_{3dB}/P_{el} curves shown in Figure 8.14 (a). At 25°C the *EDR* of the 7 µm oxide-aperture diameter VCSEL achieves a minimum of 195 fJ/bit at 12.6 Gb/s and then increases up to more than 600 fJ/bit at 50 Gb/s. For low bit rates up to 16.8 Gb/s the *EDR* is below 100 fJ/bit for the 6 µm oxide-aperture diameter VCSEL. The change of the *EDR* with increasing bit rate is much smaller for the 5 µm oxide-aperture diameter VCSEL resulting in a

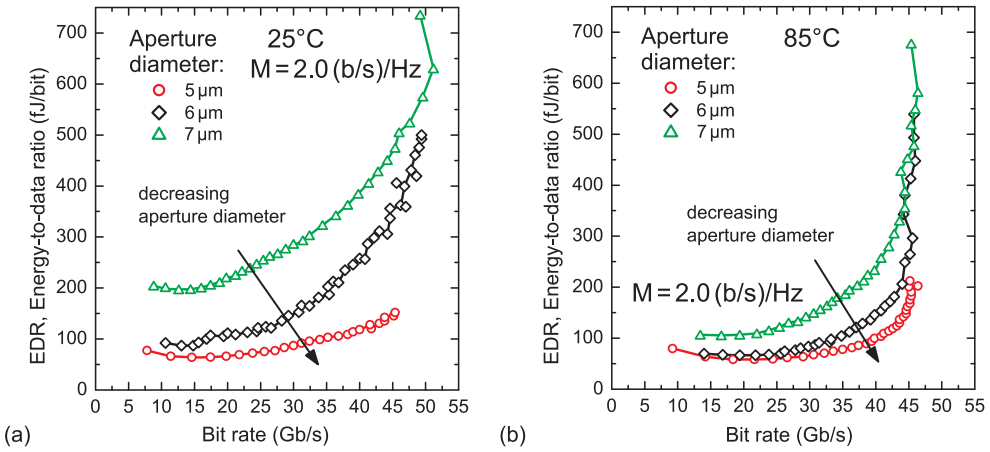

Figure 8.15.: Energy-to-data ratio *EDR* versus the bit rate for M = 2.0 (b/s)/Hz for 980-nm VCSELs with oxide-aperture diameters of 5, 6, and 7 µm at (a) 25°C and (b) at 85°C [75] © 2014 IEEE.

small *EDR* value even at high bit rates. The *EDR* is smaller than 100 fJ/bit up to 35 Gb/s and is still only 152 fJ/bit at 45 Gb/s.

All three 980-nm VCSELs become more energy-efficient when the temperature is increased from 25 to 85°C. For M = 2.0 (b/s)/Hz the *EDR* of the 7 µm oxide-aperture diameter VCSEL still remains larger than 100 fJ/bit in the complete investigated bit rate range, but the minimum value reduced to 103 fJ/bit at 16.6 Gb/s. Thus not only the minimum of the *EDR* reduced, also the bit rate at which the minimum *EDR* is achieved increased, in this case by 4 Gb/s which is an increase of nearly 32%. The minimum *EDR* of the 6 µm oxide-aperture diameter VCSEL is 67 fJ/bit at a bit rate of 20 Gb/s. For the smaller 5 µm oxide-aperture diameter VCSEL the minimum *EDR* reduces to 58 fJ/bit at 22 Gb/s. The difference of the *EDR* values for VCSELs with different oxide-aperture diameters at a given bit rate increases with bit rate. Thus at larger bit rates it is especially advantageous to use a small oxide-aperture diameter VCSEL.

The temperature stability for M = 2.0 (b/s)/Hz can simply be expressed as the absolute difference of the *EDR* at 85 and 25°C, where a negative value corresponds to a reduction of the *EDR*, thus an increase of the energy efficiency with temperature increase. The absolute change ΔEDR of the *EDR* versus the bit rate for the 5, 6, and 7 µm oxide-aperture diameter VCSELs when the temperature increases from 25 to 85°C is shown in Figure 8.16.

For all three oxide-aperture diameter VCSELs the temperature-induced reduction of the *EDR* increases with increasing bit rate, resulting in the already discussed increase of the bit rate at which the *EDR* is a minimum. The minimum of the ΔEDR is -25 fJ/bit at 32.5 Gb/s for the VCSEL with an oxide-aperture diameter of 5 µm. Then ΔEDR reduces and becomes positive for bit rates larger than approximately 43 Gb/s. At 45 Gb/s the *EDR* increases by

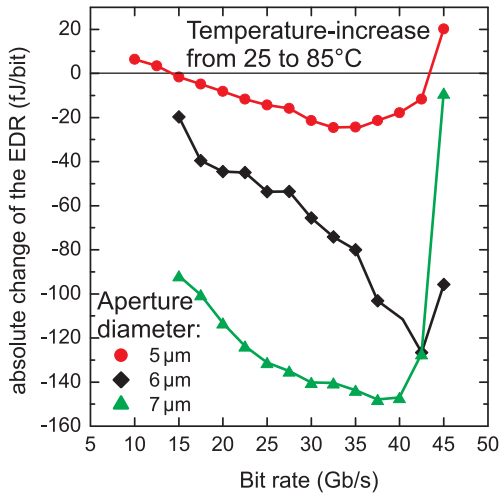

Figure 8.16.: Absolute change of the energy-to-data ratio *EDR* versus the bit rate for a temperature increase from 25 to 85°C for M = 2.0 (b/s)/Hz for 980-nm VCSELs with oxide-aperture diameters of 5, 6, and 7 µm, respectively.

20 fJ/bit when the temperature is increased from 25 to 85°C. In the investigated f_{3dB} and thus bit rate range the ΔEDR is negative for the 6 and 7 µm oxide-aperture diameter VCSELs, but the curves show a similar behavior as the curve of ΔEDR of the 5 µm oxide-aperture diameter VCSEL. The minimum of ΔEDR is -110 and -149 fJ/bit at 42.5 and 37.5 Gb/s for the 6 and 7 µm oxide-aperture diameter VCSELs, respectively. Thus maximum deviation of the *EDR* for M = 2.0 (b/s)/Hz and a temperature increase from 25 to 85°C is 25, 110, and 149 fJ/bit for the 5, 6, and 7 µm oxide-aperture diameter VCSELs, respectively. Thus the energy efficiency is more temperature-stable for VCSELs with smaller oxide-aperture diameters.

The bit rates at 25 and 85°C for *EDR* values of 100 fJ/bit and 120 fJ/bit of 980-nm VCSELs with oxide-aperture diameters of 5, 6, and 7 µm are plotted versus the M-factor in Figure 8.17 (a) and (b), respectively. As discussed previously the 7 µm oxide-aperture diameter VCSEL does not achieve *EDR* values as low as 100 fJ/bit. This VCSEL achieves an *EDR* of 120 fJ/bit but only at 85°C. Thus the temperature stability at *EDR* values of 100 and 120 fJ/bit can only be evaluated for the VCSELs with the smaller oxide-aperture diameters of 5 and 6 µm. Since the minimum *EDR* of the 7 µm oxide-aperture diameter VCSEL is 195 fJ/bit at 25°C, its *EDR* temperature stability can only be evaluated for *EDR* values of 195 fJ/bit or larger. Because the maximum *EDR* of the 5 µm oxide-aperture diameter VCSEL is well below 195 fJ/bit at 25°C, the *EDR* temperature stability of these two oxide-aperture diameter VCSELs can not be directly compared. Since the main focus of this work is on small *EDR* values, the temperature stability is compared for the two smallest and thus the two most energy-efficient VCSELs.

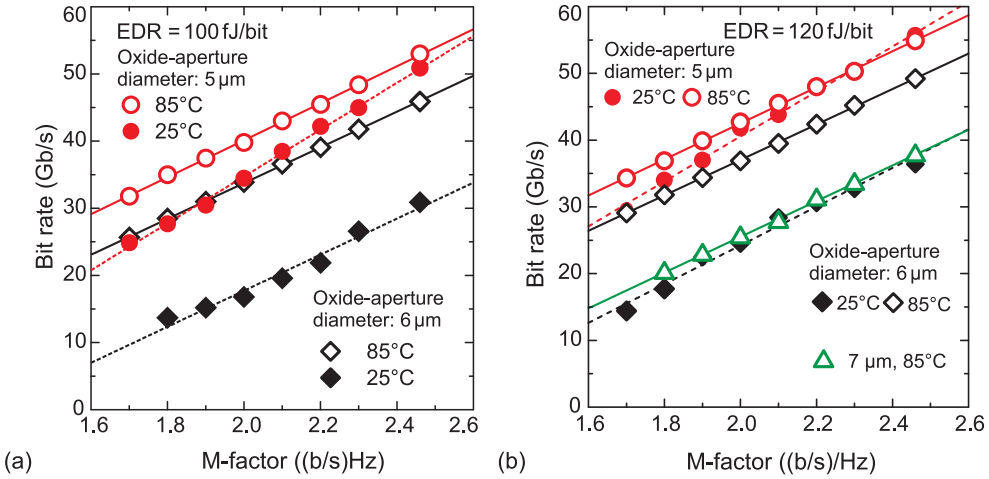

Figure 8.17.: Bit rate versus the M-factor at an *EDR* of (a) 100 fJ/bit [75] (© 2014 IEEE) and (b) 120 fJ/bit at 25 and 85°C for 980-nm VCSELs with oxide-aperture diameters of 5, 6, and 7 µm. In the investigated range of M-factors the 7 µm oxide-aperture diameter VCSEL does not achieve *EDR* values of 100 fJ/bit and an *EDR* of 120 fJ/bit can only be achieved at 85°C.

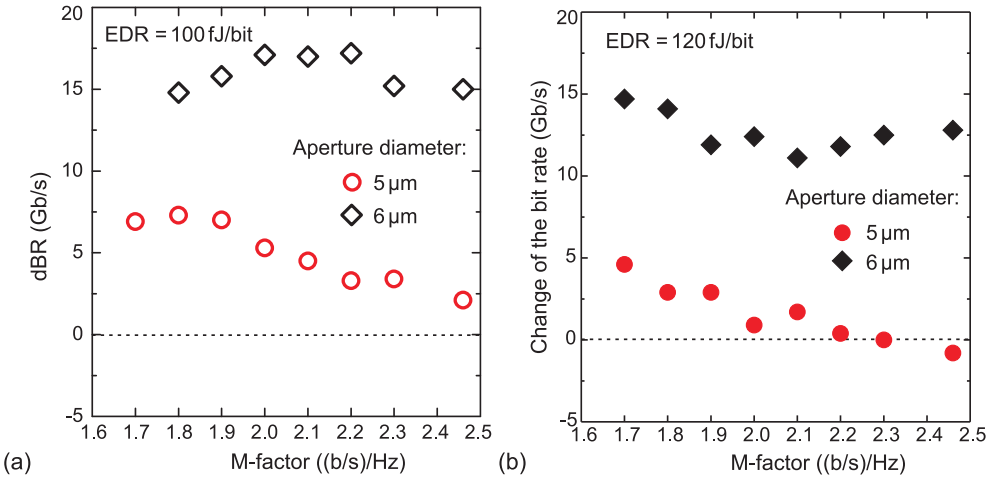

Figure 8.18.: Absolute change of the bit rate versus the M-factor at an *EDR* of (a) 100 fJ/bit and (b) 120 fJ/bit for a temperature increase from 25 to 85°C for 980-nm VCSELs with oxide-aperture diameters of 5 and 6 µm, respectively.

The temperature-induced bit rate change for a given M-factor is larger for the VCSEL with the larger oxide-aperture diameter. For the 5 µm oxide-aperture diameter VCSEL the maximum bit rate change is +7.3 Gb/s at an *EDR* of 100 fJ/bit and an M-factor of 1.8. This maximum bit rate change reduces to +4.6 Gb/s at M = 1.7 for a larger *EDR* of 120 fJ/bit. The 6 µm oxide-aperture diameter VCSEL has a much larger maximum bit range change of 17.2 Gb/s at an M-factor of 2.2 (b/s)/Hz for an *EDR* of 100 fJ/bit which

reduces to +14.7 Gb/s at M = 1.7 (b/s)/Hz for an *EDR* of 120 fJ/bit. The absolute temperature-induced bit rate changes for the 5 and 6 µm oxide-aperture diameter VCSELs are plotted versus the M-factor in Figure 8.18 (a) for an *EDR* of 100 fJ/bit and (b) for an *EDR* of 120 fJ/bit, respectively.

8.3. Impact of the photon lifetime on the temperature stability of the modulation bandwidth and energy efficiency

In the previous evaluations the oxide-aperture diameter was determined as the key-parameter for achieving energy-efficient data transmission. Varying the oxide-aperture diameter is possible for any given VCSEL design since it is only a change of the VCSEL geometry that is performed during processing via the mask set and the oxidation depth during the selective wet oxidation. By changing the oxide-aperture diameter the mode-volume of the VCSEL is changed and thus the static and dynamic properties of the VCSEL change as well.

Photon lifetime tuning is another method of simultaneously changing the static and dynamic properties of a given VCSEL epitaxial design. The photon lifetime can be changed by changing the reflectivity of the top DBR. This can be realized by removing semiconductor material from the topmost DBR layer by dry or wet etching [111, 112] or by adding material to the topmost DBR layer. Both methods change the optical thickness of the topmost DBR layer and thus impact the reflectivity phase and the power reflectance of the outcoupling mirror.

In order to investigate the impact of the photon lifetime on the temperature stability of the modulation bandwidth and the energy efficiency, the photon lifetime is reduced for the 980-nm VCSEL with an oxide-aperture diameter of 5 µm by adding 55 nm of Si_xN_y onto the topmost GaAs-layer of the top-DBR. This additional Si_xN_y-layer causes the photon lifetime to reduce from the initial value of the as-grown VCSEL of about 3.7 ps to a local minimum value of about 1.8 ps.

In the following paragraphs the impact of a photon lifetime change from 3.7 to 1.8 ps on the static properties at 25 and 85°C and the temperature stability of these properties is studied. Then the change and temperature stability of the modulation bandwidth are studied and finally the change of the energy efficiency and its temperature stability and potential trade-offs are discussed. The main focus of this evaluation is to demonstrate how the energy efficiency and simultaneously the temperature stability are affected by the change of the photon lifetime. Therefore most of the evaluation is performed qualitatively in order to simply present trade-offs. The focus is not on the actual photon lifetime tuning itself. For other VCSEL structures the change of the properties for a similar photon lifetime change can be different. Since all static and dynamic VCSEL properties change with the oxide-aperture diameter as well as the temperature stability of these properties, the oxide-aperture diameter also

has an impact on how and by how much a given change in the photon lifetime changes the static and dynamic VCSEL properties. The impact of the photon lifetime change on the energy efficiency and temperature stability as presented here is expected to increase with decreasing oxide-aperture diameters.

8.3.1. Impact of the photon lifetime on static properties and their temperature stability

By adding 55 nm of Si_xN_y to the topmost GaAs-layer of the top-DBR the photon lifetime τ_p is reduced from about 3.7 ps to about 1.8 ps. The reduction of τ_p leads to a slight increase of the threshold current from 0.31 mA to 0.35 mA at 25°C. At 85°C the threshold current increases from 0.40 to 0.43 mA for the VCSEL with a τ_p of 1.8 ps. Because the slope efficiency derived from the LI-slope simultaneously increases from 0.55 W/A to 0.56 W/A at 25°C and from 0.47 W/A to 0.48 W/A at 85°C, respectively, the optical output power P_{opt} increases with decreasing τ_p. The maximum P_{opt} increases by 25% to 3.19 mW at 25°C and by 28% to 2.18 mW at 85°C, respectively. There is no significant change of the temperature stability of the maximum P_{opt} and the rollover current when the photon lifetime is reduced from 3.7 to 1.8 s ps. For the VCSEL with a photon lifetime of 3.7 ps the maximum P_{opt} reduces by -34% and the rollover current reduces by -16% for an temperature increase from 25 to 85°C. For a lower τ_p of 1.8 ps the maximum of P_{opt} and the rollover current reduce by -32% and -17%, respectively, for the same temperature increase. The LI-curves at 25 and 85°C for the 5 µm oxide-aperture diameter 980-nm VCSEL with τ_p values of 3.7 and 1.8 ps are shown in Figure 8.19 (a).

In order to determine the impact of the τ_p change on the *temperature stability* of the output power versus the complete bias current range of interest the absolute change of P_{opt} due to an temperature increase from 25 to 85°C is evaluated versus the bias current from threshold current up to the rollover current at 85°C. In our case the photon lifetime reduction from 3.7 to 1.8 ps does not significantly affect the absolute temperature-induced output power change as depicted in Figure 8.19 (b).

8.3.2. Impact of the photon lifetime on the modulation bandwidth and its temperature stability

The method of photon lifetime tuning is typically used to increase the maximum f_{3dB} of VCSELs by reducing the damping [113, 111]. For the energy efficiency and its temperature stability the maximum value of f_{3dB} is of less interest than the f_{3dB} values at low currents and powers. Prior to this dissertation the impact of the photon lifetime tuning on the energy efficiency and the temperature stability of the modulation bandwidth f_{3dB} and the energy efficiency had not yet been investigated.

At 25°C the reduction of τ_p from 3.7 to 1.8 ps leads to an decrease of the

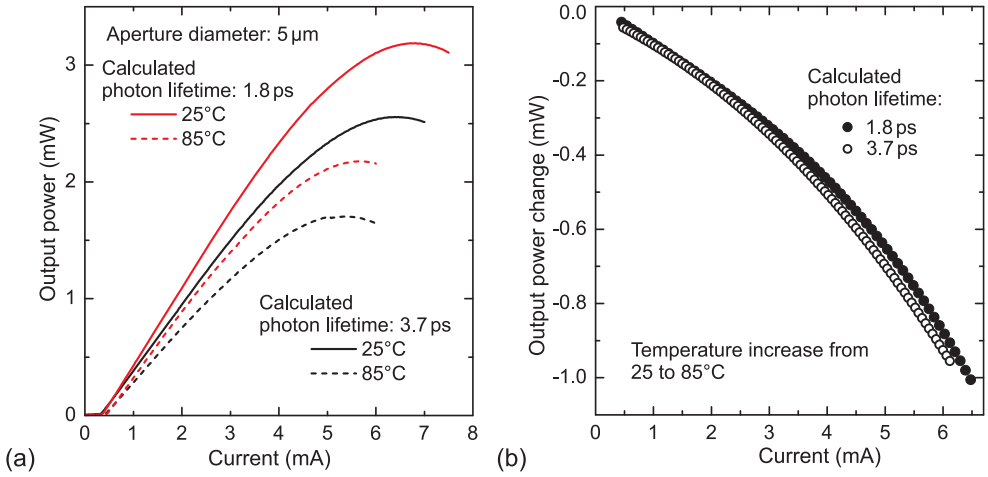

Figure 8.19.: (a) Optical output power P_{opt} versus current at 25 and 85°C for a 5 µm oxide-aperture diameter 980-nm VCSEL with calculated photon lifetimes of $\tau_{p1} = 3.7$ ps and $\tau_{p2} = 1.8$ ps, respectively. (b) Absolute change of P_{opt} versus the bias current for the 5 µm oxide-aperture diameter 980-nm VCSEL with photon lifetimes of $\tau_{p1} = 3.7$ ps and $\tau_{p2} = 1.8$ ps when the temperature is increased from 25 to 85°C. [110] © 2015 SPIE.

modulation bandwidth $f_{3\mathrm{dB}}$ for currents smaller than approximately 2.0 mA at 25°C [110]. At larger currents $f_{3\mathrm{dB}}$ becomes larger for the shorter photon lifetime VCSEL. At very low currents close to the threshold current the apparent decrease of $f_{3\mathrm{dB}}$ for the VCSEL with the smaller τ_{p} is due to the effect of the increased threshold current. At the given small currents around 0.5 mA the VCSEL with the shorter photon lifetime is operated much closer to the threshold current as the VCSEL with the higher photon lifetime and thus smaller threshold current value. At 85°C the decrease of $f_{3\mathrm{dB}}$ at a given low current is larger than at 25°C [110]. The current at which the shorter photon lifetime VCSEL becomes faster than the version with larger photon lifetime increases to approximately 3.0 mA. Therefore the decrease of the photon lifetime leads to an increase of the $f_{3\mathrm{dB}}$ at larger currents whereas the $f_{3\mathrm{dB}}$ is decreased at low currents and thus current densities that are desired for energy-efficient operation of the VCSELs. Thus the reduction of τ_{p} potentially leads to an increase of the *EDR* at low currents, because the electrical power P_{el} remains unchanged whereas $f_{3\mathrm{dB}}$ is decreased. The increase of the output power might partially compensate for the decrease of $f_{3\mathrm{dB}}$ or even lead to smaller *HBR* values for the VCSEL with a reduced τ_{p} of 1.8 ps. The $f_{3\mathrm{dB}}$ versus the bias current for the 5 µm oxide-aperture diameter 980-nm VCSEL with τ_{p} values of 3.7 and 1.8 ps given in Figure 8.20 at 25°C (a) and at 85°C (b), respectively.

The relative change of $f_{3\mathrm{dB}}$ due to the photon lifetime reduction to 1.8 ps is shown versus the bias current for 25°C and 85°C in Figure 8.21 (a).

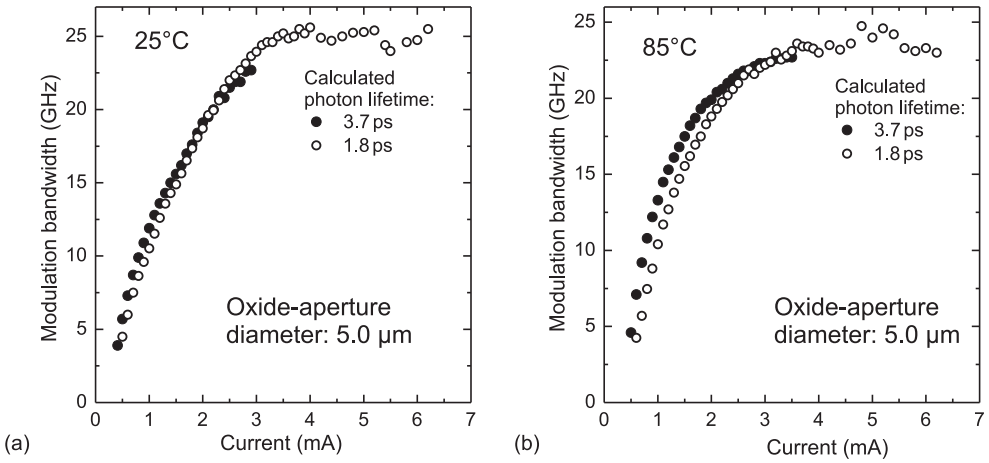

Figure 8.20.: Modulation bandwidth f_{3dB} versus the bias current for the 5 µm oxide-aperture diameter VCSEL with a calculated photon lifetime of 3.7 and 1.8 ps at (a) 25°C [110] (© 2015 SPIE) and (b) 85°C, respectively.

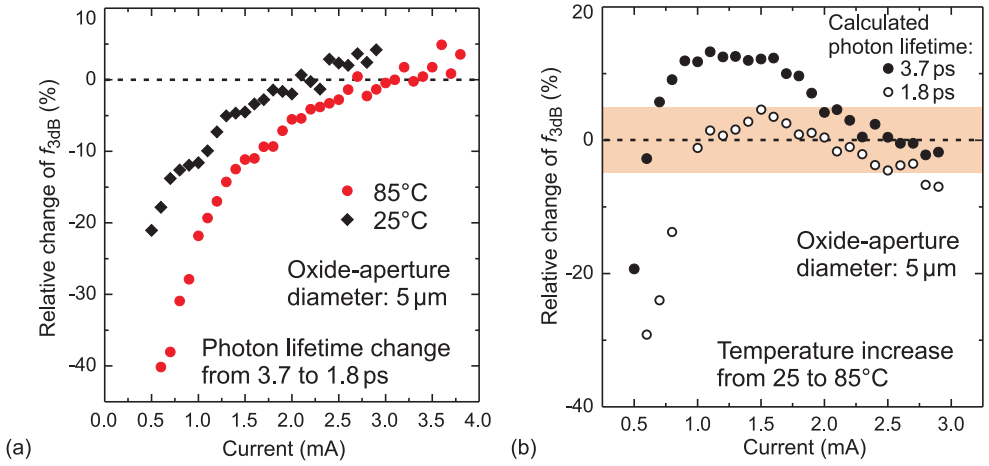

Figure 8.21.: (a) Relative change of the modulation bandwidth f_{3dB} due to the reduction of the photon lifetime from 3.7 to 1.8 ps versus the bias current for the 5 µm oxide-aperture diameter VCSEL at 25 and 85°C, respectively. (b) Relative change of f_{3dB} due to an increase of the temperature from 25 to 85°C for the 980-nm 5 µm oxide-aperture diameter VCSEL with photon lifetimes of 3.7 and 1.8 ps, respectively. For all data points that are in the red box the f_{3dB} change is within ±5%. [110] © 2015 SPIE.

Because the change of the photon lifetime leads to different changes of the f_{3dB} values at 25 and 85°C also the temperature stability of the f_{3dB} is changed. As for the VCSEL prior to the photon lifetime reduction with an inital τ_p of 3.7 ps the temperature stability of the f_{3dB} is evaluated by determining the temperature-induced relative change of f_{3dB} versus the bias current and plotted in Figure 8.21 (b) together with the temperature-induced

f_{3dB} change of the VCSEL with a τ_p of 3.7 ps that was already shown in Figure 8.7 (b).

At low currents close to the threshold currents f_{3dB} is smaller at 85°C than at 25°C and thus the relative change of f_{3dB} is negative. At about 0.6 mA Δf_{3dB} is negative for the 3.7 ps photon lifetime VCSEL and becomes positive for larger currents up to about 2.6 mA when df_{3dB} becomes negative again, as already discussed previously. The df_{3dB} for a τ_p of 1.8 ps shows a similar dependence on the current, but the bias current at which df_{3dB} becomes positive increases to about 1.0 mA. From 1.0 mA to approximately 2.0 mA df_{3dB} is positive with a maximum of +4.4% at 1.5 mA. For currents larger than approximately 2.0 mA df_{3dB} becomes negative again, because the saturation of the f_{3dB} sets in at 85°C whereas the f_{3dB} still increases with current at 25°C.

The behavior of df_{3dB} is impacted in several ways by the photon lifetime reduction from 3.7 to 1.8 ps. The temperature-induced increase of f_{3dB} is much smaller for the smaller photon lifetime corresponding to a more temperature-stable f_{3dB} in the respective current range. The maximum increase of f_{3dB} is +13.3% for a τ_p of 3.7 ps and only +4.4% for the 1.8 ps VCSEL as already mentioned above. For the VCSEL with $\tau_p = 1.8$ ps the df_{3dB} is within ±5% in a wide current range of 1.0 to 3.5 mA, corresponding to f_{3dB} values of 10.5 to 25.2 GHz at 25°C. For the larger τ_p of 3.7 ps this small change of the f_{3dB} is achieved at larger currents of 2.0 to 2.9 mA corresponding to f_{3dB} values of 19.1 to 22.7 GHz, respectively.

Table 8.2.: Impact of the photon lifetime on important VCSEL properties for a 5 µm oxide-aperture diameter 980-nm VCSEL with df_{3dB} =0% and M = 2.0 (b/s)/Hz.

Photon lifetime (ps)	3.7	1.8
Current density (kA/cm^2)	13	10
ΔP_{opt} (mW)	-2.8	-2.1
f_{3dB} (GHz)	21.8	18.7
EDR (fJ/bit)	129	105
Bit rate (Gb/s)	43.6	37.4

The reduction of the photon lifetime leads to a decrease of the current at which df_{3dB} is 0% from 2.6 to 2.0 mA for the VCSEL with photon lifetimes of 3.7 and 1.8 ps, respectively. As discussed previously the f_{3dB} at 2.6 mA is 21.8 GHz for the VCSEL with a photon lifetime of 3.7 ps. For a τ_p of 1.8 ps and 2.0 mA f_{3dB} is 18.7 GHz. Thus the perfectly *temperature-stable* modulation bandwidth has become smaller due to reduction of the photon lifetime. The current density at the zero-change of f_{3dB} is reduced from 13 to 10 kA/cm^2 for the photon lifetime reduction from 3.7 to 1.8 ps. Assuming

an M-factor of 2.0 (b/s)/Hz, the *EDR* and bit rate reduce from 129 fJ/bit and 43.6 Gb/s at a photon lifetime of 3.7 ps to 105 fJ/bit and 37.4 Gb/s at a smaller photon lifetime of of 1.8 ps. The absolute temperature-induced change of the output power P_{opt} at the respective currents for a perfectly temperature-stable $f_{3\mathrm{dB}}$ reduces from -2.8 mW for the VCSEL with a photon lifetime of 3.7 ps to -2.1 mW for the smaller τ_{p} of 1.8 ps. A selection of the most important parameters of the current at which $f_{3\mathrm{dB}}$ is insensitive to a temperature increase from 25 to 85°C is given for the two different photon lifetimes of 3.7 and 1.8 ps in Table 8.2 where M = 2.0 (b/s)/Hz is assumed for calculating the *EDR* and bit rate.

By reducing the photon lifetime the temperature stability of the $f_{3\mathrm{dB}}$ of the 5 µm oxide-aperture diameter VCSEL has been successfully improved. Due to the lower current at which $f_{3\mathrm{dB}}$ has the same value at 25 and 85°C for the VCSEL with the smaller photon lifetime, e.g. $\mathrm{d}f_{3\mathrm{dB}} = 0\%$, the temperature-stable $f_{3\mathrm{dB}}$ and the *EDR* at this current have become smaller as well. Thus there is a clear trade-off between a large temperature-stable $f_{3\mathrm{dB}}$ and a temperature-stable $f_{3\mathrm{dB}}$ at small current-densities and *EDR* values. Because the modulation bandwidth $f_{3\mathrm{dB}}$ and its temperature stability change with photon lifetime, the energy-effeciency and its temperature stability change as well as is analyzed in the following Section.

8.3.3. Impact of the photon lifetime on the energy efficiency and its temperature stability

The energy efficiency and its temperature stability is mainly affected by the $f_{3\mathrm{dB}}$ change with changing photon lifetime τ_{p}. For simplicity the energy efficiency in this work was mainly investigated in terms of the *EDR* and/or the bandwidth-to-electrical power ratio. A change of τ_{p} does not noticeably change the *IV*-characteristics of the VCSEL and thus the electrical power P_{el} remains unchanged when τ_{p} is modified. Etching away material from the highly doped topmost DBR layer of a VCSEL may lead to a small change of the resistance, but this effect is not included in the following analysis. In our case τ_{p} was changed by adding $\mathrm{Si_xN_y}$-layers to the conducting topmost GaAs-layer of our VCSEL.

As given in Equations (4.7) and (4.8) a change in τ_{p} affects the *EDR* only via a change of $f_{3\mathrm{dB}}$ whereas the *HBR* is changed by a change of P_{opt} and $f_{3\mathrm{dB}}$. Because a change of τ_{p} may change P_{opt} and $f_{3\mathrm{dB}}$ differently the impact of the photon lifetime change can be expected to be different for *EDR* and *HBR*. Because a smaller photon lifetime leads to an increase of the optical output power and thus a decrease of the dissipated heat power, in general the *HBR* may even decrease while the *EDR* decreases.

The already discussed decrease of $f_{3\mathrm{dB}}$ at low currents leads to a corresponding decrease of the bandwidth-to electrical power ratio. The maximum of the bandwidth-to electrical power ratio at 85°C decreases from 8.6 GHz/mW at

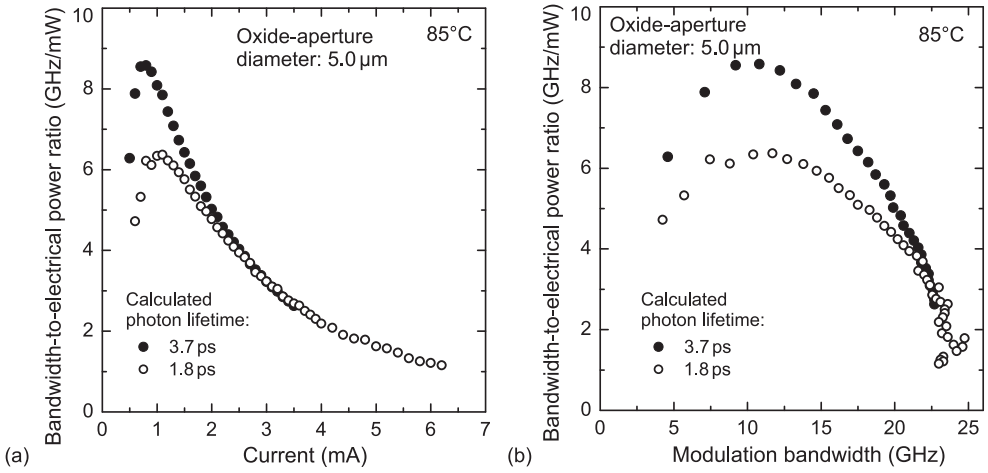

Figure 8.22.: Bandwidth-to-electrical power ratio at 85°C for the 980-nm 5 µm oxide-aperture diameter VCSEL with calculated photon lifetimes of 3.7 and 1.8 ps, respectively, versus (a) the bias current and (b) versus the modulation bandwidth.

0.8 mA for a τ_p of 3.7 ps to 6.4 GHz/mW at 1.1 mA for the VCSEL with a photon lifetime of 1.8 ps respectively. For currents of about 2.6 mA and larger the bandwidth-to electrical power ratio of the two different photon lifetimes converge. The bandwidth-to electrical power ratio at 85°C for the 5 µm oxide-aperture diameter 980-nm VCSEL with photon lifetimes of 3.7 and 1.8 ps is plotted versus the bias current in Figure 8.22 (a). Because the difference in the bandwidth-to electrical power ratio caused by the τ_p-change seems to only occur at a relative small bias current range, it might be considered to be only important for a rather restricted range of currents and thus f_{3dB} values. By plotting the bandwidth-to electrical power ratio versus f_{3dB} it becomes obvious that a change of the τ_p changes the bandwidth-to electrical power ratio in the complete f_{3dB} range that is practical and of interest for energy-efficient operation of the VCSELs. The bandwidth-to electrical power ratio values converge when the saturation of f_{3dB} sets in. But as already discussed several times in this work, the energy per bit is then very large and potentially impractial for future application. The bandwidth-to electrical power ratio is plotted versus the f_{3dB} at 85°C for the 5 µm oxide-aperture diameter VCSEL with photon lifetimes of 3.7 and 1.8 ps in Figure 8.22 (b).

The impact of the τ_p-change on the *EDR* is demonstrated by calculating the *EDR* versus the bit rate for an M-factor of 2.0 (b/s)/Hz. At 85°C and 25 Gb/s the *EDR* is 60 and 80 fJ/bit for the VCSEL with τ_p values of 3.7 and 1.8 ps, respectively. At 40 Gb/s, closer to the maximum bit rate, the *EDR* is 100 and 116 fJ/bit for the photon lifetimes of 3.7 and 1.8 ps, respectively. The *EDR* at 85°C versus the bit rate for M = 2.0 (b/s)/Hz is plotted for the 5 µm oxide-aperture diameter VCSEL in Figure 8.23 (b). The lower f_{3dB} caused by the reduction of τ_p leads to a corresponding increase of the *EDR*

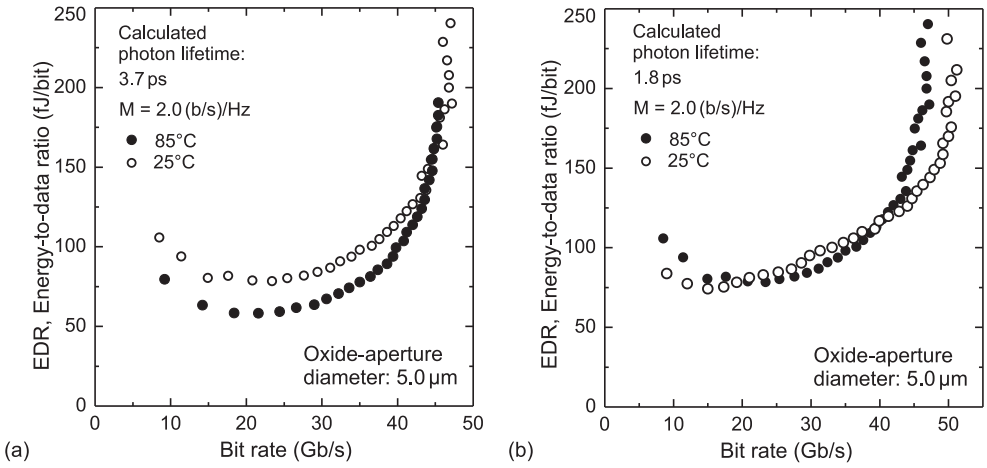

Figure 8.23.: Energy-to-data ratio *EDR* versus the bit rate at 25 and 85°C (with M = 2.0 (b/s)/Hz) for the 5 µm oxide-aperture diameter 980-nm VCSEL with calculated photon lifetimes of (a) 3.7 ps and (b) 1.8 ps.

[110]. In order to determine the impact of the τ_p-change on the temperature stability of the *EDR*, the *EDR* at 25 and 85°C is plotted versus the bit rate for M = 2.0 (b/s)/Hz and τ_p = 1.8 ps. Similar to the curves for a photon lifetime of 3.7 ps the *EDR* is smaller at 85°C than at 25°C for certain bit rates. With smaller τ_p the bit rate range in which the *EDR* is smaller at 85°C has become smaller and also the difference of the *EDR* values at both temperatures in this range is small. At low bit rates up to approximately 19 Gb/s the *EDR* is smaller at 25°C than at 85°C. For larger bit rates up to 40 Gb/s the *EDR* reduces with increasing temperature and at even larger bit rates the *EDR* is again smaller at 25°C, because the bit rate starts to saturate at 85°C. The absolute change of the *EDR* due to a temperature increase from 25 to 85°C is shown in Figure 8.24 versus the bit rate for the 5 µm oxide-aperture diameter 980-nm VCSEL with photon lifetimes of 1.8 and 3.7 ps, respectively. The direct comparison shows that the reduction of τ_p reduces the bit rate range in which the *EDR* reduces with increasing temperature and also the *EDR*-change within this bit rate range becomes significantly smaller than for a photon lifetime of 3.7 ps.

To compare the impact of the photon lifetime change on the energy efficiency and its temperature stability for different M-factors, the bit rate at an *EDR* of 100 fJ/bit is plotted versus the M-factor [110] at 25 and 85°C for photon lifetimes of 3.7 and 1.8 ps in Figure 8.25 (a) and (b), respectively. As already discussed previously, for τ_p = 3.7 ps the bit rate at 85°C is larger than at 25°C for all M-factors in the range of interest from 1.7 to 2.46 (b/s)/Hz. The slopes of the linear fits for the data points at 25 and 85°C differ, but the curves do not cross each other in the investigated M-factor range. For the smaller photon lifetime of 1.8 ps the difference of the bit rates for 25 and 85°C at a given M is

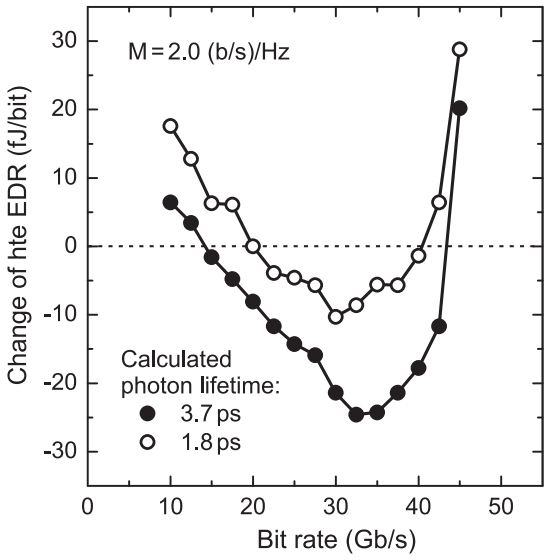

Figure 8.24.: Absolute change of the energy-to-data ratio *EDR* due to a temperature increase from 25 to 85°C versus the bit rate for M = 2.0 (b/s)/Hz for the 5 µm oxide-aperture diameter 980-nm VCSEL with photon lifetimes τ_p of 1.8 and 3.7 ps, respectively.

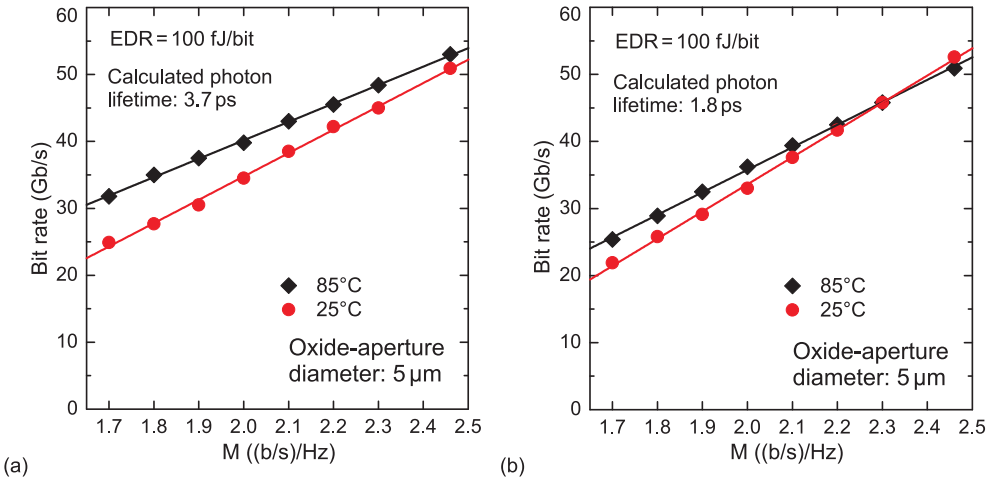

Figure 8.25.: Bit rate at an energy-to-data ratio of 100 fJ/bit versus the M-factor at 25 and 85°C for the 5 µm oxide-aperture diameter 980-nm VCSEL with photon lifetimes of (a) 3.7 ps and (b) 1.8 ps, respectively. [110] © 2015 SPIE.

smaller than for τ_p =3.7 ps. At an M of 2.3 (b/s)/Hz the bit rate at an *EDR* of 100 fJ/bit is the same for 25 and 85°C. At larger M-factors the bit rate at the same *EDR* is larger at 25°C than at 85°C. Thus at *EDR* = 100 fJ/bit the VCSEL with τ_p = 1.8 ps is for all M-factors less sensitive to a temperature increase from 25 to 85°C than with the larger photon lifetime of 3.7 ps.

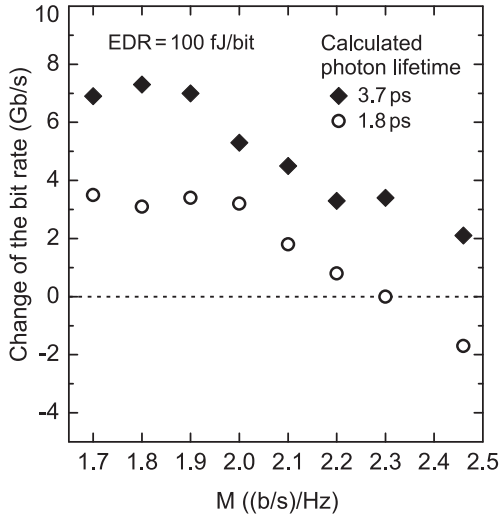

Figure 8.26.: Change of the bit rate due to a temperature increase from 25 to 85°C at an energy-to-data ratio *EDR* of 100 fJ/bit versus the M-factor for the 5 µm oxide-aperture diameter 980-nm VCSEL with photon lifetimes of 3.7 and 1.8 ps.

The difference of the bit rates at 25°C and 85°C for $EDR = 100\,\mathrm{fJ/bit}$ and for the two different τ_p-values are plotted versus the M-factor in Figure 8.26. For smaller M-factors up to approximately 1.9 the bit rate difference is nearly half as large for 1.8 ps as compared to the values with $\tau_p = 3.7\,\mathrm{ps}$.

8.3.4. Trade-offs between bit rate, energy efficiency, and current density at 85°C

The analysis of the impact of the oxide-aperture diameter on the static and dynamic performance of VCSELs presented in the previous Chapter and in this Chapter has shown that VCSELs with smaller oxide-aperture diameters operate more energy-efficiently and are more temperature-stable than similar VCSELs with larger oxide-aperture diameters. The analysis has shown that the most important performance goals such as high bit rates, low current density operation, and high ambient temperature operation can be achieved with low *EDR* and therefore also low *HBR* values when a small oxide-aperture diameter is used. For future ultrashort-reach (USR) optical interconnects all these performance goals have to be achieved simultaneously. For commercial application of oxide-confined VCSELs low current density operation with a maximum current density of $10\,\mathrm{kA/cm^2}$ is a prerequisite. In addition VCSELs for USR optical interconnects need to operate at high ambient temperatures up to 85°C. Therefore the bit rate, *EDR*, and *HBR* is compared for 980-nm VCSELs with different oxide-aperture diameters at 85°C, calculated from the measured intrinsic electrical power P_{el}, optical power P_{opt}, and the modulation bandwidth f_{3dB}.

As shown in the following Section for data transmission experiments with a 6 µm oxide-aperture diameter 980-nm VCSEL, M-factors of 2.1 and 2.0 (b/s)/Hz are achieved at 25 and 85°C, respectively. Therefore a value of 2.0 (b/s)/Hz is assumed for the M-factor in order to calculate the *EDR* and *HBR* values at 85°C. At a current density of 10 kA/cm^2 and at 85°C the bit rate decreases with increasing oxide-aperture diameter. The VCSELs with the two smallest oxide-aperture diameters of 4.5 and 5 µm achieve the same bit rate of 39.6 Gb/s and the bit rate reduces to 35.4 Gb/s for the VCSEL with the largest oxide-aperture diameter of 7 µm. The calculated *EDR* significantly increases with increasing oxide-aperture diameter from 78 to 184 fJ/bit for the 4.5 and 7 µm oxide-aperture diameter VCSELs, respectively. The *EDR* is 96 fJ/bit for the VCSEL with an oxide-aperture diameter of 5 µm. Thus in order to stay below an *EDR* of 100 fJ/bit at the given temperature and current density the maximum oxide-aperture diameter is 5 µm for the given VCSEL design and M-factor. Similar to the *EDR* the *HBR* increases with increasing oxide-aperture diameter as well and is 66 fJ/bit for the 4.5 µm oxide-aperture diameter VCSEL and 136 fJ/bit for the 7 µm oxide-aperture diameter VCSEL. The optical output power P_{opt} is an important VCSEL property as it limits the suitability for application to those detectors or receivers that have a large enough sensitivity. The optical output power increases with increasing oxide-aperture diameter. P_{opt} is 0.45 mW for the smallest VCSEL with an oxide-aperture diameter of 4.5 µm and increases to 1.78 mW for the largest 7 µm oxide-aperture diameter VCSEL. The output power is 0.74 and 1.18 mW for the 5 and 6 µm oxide-aperture diameter VCSELs, respectively. Thus if a minimum optical output power of 1 mW is required a minimum oxide-aperture diameter of ~6 µm has to be used. The calculated bit rate, *EDR* and *HBR* values, and the measured optical output power at 10 kA/cm^2 and at 85°C are shown versus the oxide-aperture diameter of the 980-nm VCSELs in Figure 8.27 (a) and (b), respectively. The exact values of the bit rate, *EDR*, *HBR*, and P_{opt} are given in Table 8.3.

The analysis of the intrinsic static and dynamic VCSEL properties of the given 980-nm VCSEL design at 85°C and for M = 2.0 (b/s)/Hz shows that 40 Gb/s operation at 85°C, 10 kA/cm^2 and an *EDR* of <100 fJ/bit is viable. In order to achieve this combination of performance goals an oxide-aperture diameter of 5 µm or smaller has to be used. The *HBR* is then 66 and 78 fJ/bit for oxide-aperture diameters of 4.5 an 5 µm, respectively. The low current density operation of small oxide-aperture diameter VCSELs leads to a small P_{opt} of 0.45 and 0.74 mW for these two oxide-aperture diameters. Although it can be anticipated that future USR optical interconnects will operate with very low values of P_{opt}, the development of simultaneously fast and sensitive detectors is a big challenge. In order to achieve more output power a larger oxide-aperture diameter can be used, leading to a reduction of the bit rate and an increase of both the *EDR* and *HBR*. As shown previously the output power for a given VCSEL and at a given bias current can be increased by lowering

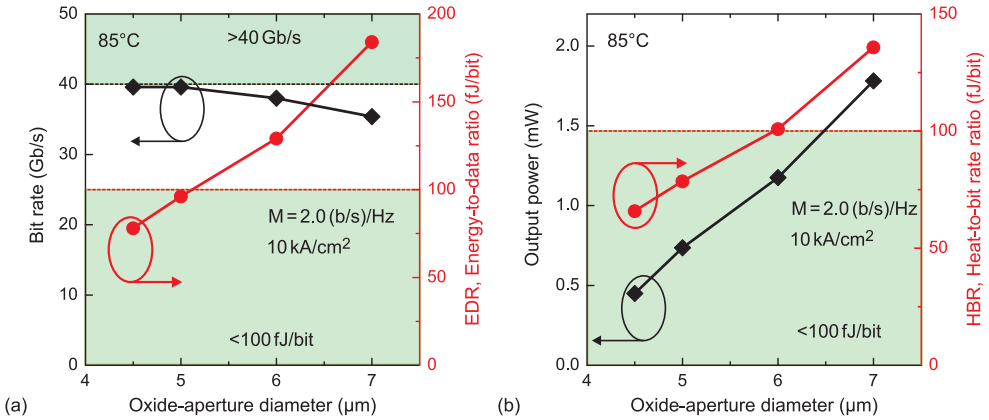

Figure 8.27.: Calculated (a) bit rate and energy-to-data ratio *EDR* and (b) measured optical output power P_{opt} and calculated heat-to-bit rate ratio *HBR* versus the oxide-aperture diameter at 10 kA/cm^2 at 85°C for M = 2.0 (b/s)/Hz.

the power reflectance of the out coupling DBR and thus the photon lifetime τ_{p} of the VCSEL cavity. In the demonstrated case of a photon lifetime reduction from 3.7 to 1.8 ps, the output power is successfully increased at 25 and 85°C without negatively impacting the temperature stability of the CW properties. For the 5 µm oxide-aperture diameter VCSEL operated at 85°C at 10 kA/cm^2, the output power increases from 0.74 to 0.86 mW when τ_{p} is decreased from 3.7 to 1.8 ps which is an increase of 16%. Because the modulation bandwidth $f_{3\mathrm{dB}}$ reduces the calculated bit rate (with M = 2.0 (b/s)/Hz) reduces from 39.6 Gb/s for 3.7 ps to 37.1 Gb/s at 1.8 ps which corresponds to a decrease of -6%. Due to the increase of the output power P_{opt} at a given current density, the dissipated power P_{diss} decreases as well. Thus $f_{3\mathrm{dB}}$ decreases and P_{diss} as well. In the case of the 5 µm oxide-aperture diameter VCSEL operated at the given condition the calculated *HBR* stays constant at 79 fJ/bit when the photon lifetime is changed from 3.7 to 1.8 ps. This means that the reduction of $f_{3\mathrm{dB}}$ is compensated by the increase of the wallplug efficiency, leading to a constant ratio of the dissipated power P_{diss}. The electrical power consumption is not affected by a change of the photon lifetime, thus the *EDR* change is given by the change of the $f_{3\mathrm{dB}}$. The *EDR* increases from 96 to 103 fJ/bit for a photon lifetime reduction from 3.7 to 1.8 ps which is an increase of 7%. The calculated bit rate, *EDR* and *HBR* values, and the measured optical output power at 10 kA/cm^2 and at 85°C are shown for a 5 µm oxide-aperture diameter 980-nm VCSEL with photon lifetimes of 1.8 and 3.7 ps in Figure 8.28 (a) and (b), respectively.

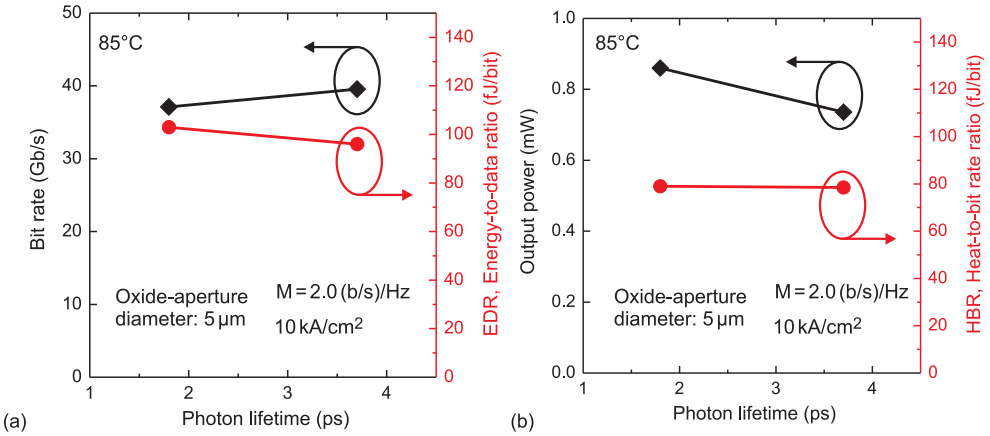

Figure 8.28.: Calculated (a) bit rate and energy-to-data ratio *EDR* and (b) measured optical output power P_{opt} and calculated heat-to-bit rate ratio *HBR* versus the photon lifetime of a 5 µm oxide-aperture diameter 980-nm VCSEL at 10 kA/cm^2 at 85°C for M = 2.0 (b/s)/Hz.

Table 8.3.: Static and dynamic VCSEL properties at 10 kA/cm^2 and 85°C for M = 2.0 (b/s)/Hz.

Oxide-aperture diameter (µm)	4.5	5	6	7
P_{opt} (mW)	0.45	0.74	1.18	1.78
Bit rate (Gb/s)	39.6	39.6	38	35.4
EDR (fJ/bit)	78	96	129	184
HBR (fJ/bit)	66	78	101	136

8.4. Data transmission

Data transmission experiments at 25°C and 85°C are performed with the 980-nm VCSELs using a photoreceiver module from u^{2}t (now part of Finisar Inc.) with a 30 GHz bandwidth and a integrated limiting transimpedance amplifier. Since the receiver module is based on a relatively small 22 µm diameter InGaAsP-detector and thus optimized for highest speed and not highest sensitivity at 980 nm, the main focus of the following data transmission experiments is to achieve record-high bit rates, and not extremely energy-efficient operation at comparably low bias currents and thus low output power.

The maximum error-free bit rates of the 980-nm VCSELs are tested at 25°C and 85°C. Error-free data transmission is achieved up to 50 Gb/s at 25°C with a 6 µm oxide-aperture diameter VCSEL at a bias current of 8.0 mA with a $f_{3\mathrm{dB}}$ of 23.9 GHz, thus the M-factor is here 2.1 (b/s)/Hz. The maximum error-free bit rate reduces only slightly to a record-large 46 Gb/s at 85°C at a $f_{3\mathrm{dB}}$ of 22.8 GHz and thus M = 2.0 (b/s)/Hz. Thus for the the 6 µm oxide-aperture diameter VCSEL the maximum bit rate reduces by only -8% when the heat-

sink temperature is increased from 25 to 85°C which is similar to the decrease of the maximum f_{3dB} of the 6 µm oxide-aperture diameter VCSEL of -7%. The received optical power at error-free operation with a bit error ratio (BER) of $< 1 \cdot 10^{12}$ is +2.9 dBm at 25°C at 50 Gb/s and is +1.9 dBm at 85°C and 46 Gb/s. The BER curves versus the received optical power at 50 and 46 Gb/s at 25 and 85°C are shown together with the optical eye diagrams at error-free transmission in Figure 8.29.

Error-free 50 Gb/s is the largest reported bit rate for 980-nm VCSELs at any temperature or for any optical interconnect configuration. At 85°C 46 Gb/s is the highest reported bit rate for any VCSEL at any wavelength without a special driver or modulation scheme such as predistortion. Recently error-free record-high bit rate operation at 50 Gb/s at 90°C could be demonstrated [77] with 850-nm VCSELs using a driver circuit with feed forward equalization. The employed VCSELs have a maximum f_{3dB} of 21.0 GHz at 85°C [9]. Assuming the VCSELs are operated at their maximum f_{3dB} this corresponds to a M-factor of 2.38 (b/s)/Hz at 85°C. The 980-nm VCSELs presented here achieve larger maximum f_{3dB} values of 23.0 GHz at 85°C. Assuming M = 2.38 (b/s)/Hz, error-free operation at ~55 Gb/s at 85°C can be expected from our 980-nm VCSELs with a f_{3dB} of 23.0 GHz.

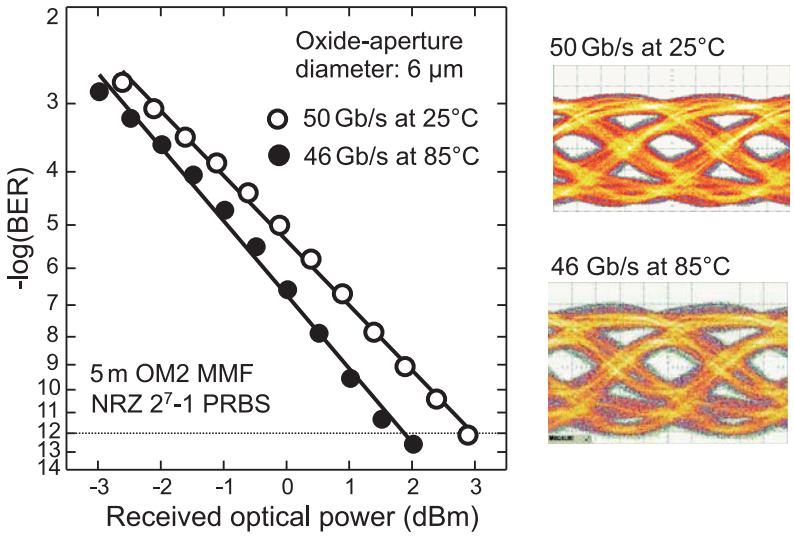

Figure 8.29.: Bit error ratio versus received optical power for a 6 µm oxide-aperture diameter 980-nm VCSEL with error-free operation at 50 Gb/s at 25°C and at 46 Gb/s at 85°C. M-factors of 2.1 and 2.0 are realized at 25°C and 85°C, respectively. Optical eye diagrams recorded at error-free operation at 50 Gb/s at 25°C and at 46 Gb/s at 85°C are shown on the right hand side. [58] © 2014 IET.

Chapter 9.

Conclusions and Outlook

The final Chapter of this dissertation summarizes the main achievements and conclusions of this work. In addition to performance records such as large bit rates and record energy efficiency values, the focus is on the general principles of the dynamic energy efficiency that apply to all oxide-confined VCSELs. These principles will most probably lead to an improvement of the record performance presented in this work, in the not-too-distant future. The dissertation closes with an outlook on suggested future work based on the work in this dissertation. Additionally, I briefly outline suggested future work that substantially extends the work I present in this dissertation.

9.1. Summary and Conclusions

This dissertation provides the first systematic evaluation of the impact of the oxide-aperture diameter on the dynamic energy efficiency in terms of the consumed and dissipated energy per bit of VCSELs that apply for all oxide-confined VCSELs. General principles on how to achieve low energy per bit operation with VCSELs are developed and verified in this dissertation by performing small- and large-signal modulation experiments with oxide-confined 850-nm and 980-nm VCSELs. In addition the temperature stability of the dynamic energy efficiency and the modulation bandwidth of VCSELs is investigated and important intrinsic trade-offs between different performance goals of VCSELs are revealed.

The energy-to-data ratio *EDR* and the heat-to-bit rate ratio *HBR* are defined as useful figures-of-merit for comparing the dynamic energy efficiency of VCSELs and their suitability for application in energy-efficient optical interconnects. The modulation factor M is introduced for optical interconnects as equivalent to the spectral efficiency η in the Information Theory. The M-factor is used as a technology-based variable representing the optical interconnect in which the VCSEL is used. By separating the intrinsic VCSEL properties from the influence of the optical interconnect system represented by the modulation factor M, the VCSEL performance in different optical interconnect systems is compared with respect to bit rate, energy efficiency, and temperature stability by varying the M-factor. The main conclusion of this dissertation is that VCSELs with small oxide-aperture diameters of 3-5 µm must be used if low energy consumption and dissipation become as or even more important than the error-free bit rate alone. Such small oxide-aperture diameter VCSELs

also show a significantly more temperature-stable modulation bandwidth and *EDR*. The new proposed evaluation method based on the use of the *EDR* and the *HBR* as comparative figures-of-merit allows one to determine the optimal oxide-aperture diameter for a given VCSEL technology and optical interconnect technology, represented by the respective M-factor, that achieves the largest bit rate at a given *EDR*. This work demonstrates that by using small 3-5 μm oxide-aperture diameter VCSELs and operating them at low current densities one may achieve data transmission at high bit rates, across long multimode optical fiber distances, and at high ambient temperatures, all with record-low consumed and dissipated energy per bit.

The following key achievements have been demonstrated in this dissertation:

1. General conclusions
    - VCSELs with smaller oxide-aperture diameters operate more energy-efficiently than similar VCSELs with larger oxide-aperture diameters.
    - VCSELs must be operated at moderate bit rates below the maximum bit rate to achieve low energy dissipation per bit.
    - The modulation bandwidth f_{3dB} is more temperature-stable for VCSELs with smaller oxide-aperture diameters than for similar VCSELs with larger oxide-aperture diameters.
    - The energy-to-data ratio *EDR* is more temperature-stable for VCSELs with smaller oxide-aperture diameters than for similar VCSELs with larger oxide-aperture diameters.
    - VCSELs with smaller oxide-aperture diameters require less received optical power for energy-efficient error-free data transmission as compared to similar VCSELs with larger oxide-aperture diameters.
    - The temperature stability of the modulation bandwidth f_{3dB} and the energy-to-data ratio *EDR* can be increased via a photon lifetime change which is traded-off with a smaller bandwidth-to electrical power ratio, e.g. larger *EDR* values.
    - Increasing the maximum modulation bandwidth f_{3dB} via a photon lifetime change, reduces the f_{3dB} at lower currents leading to larger *EDR* values.

2. Data transmission records
    - Error-free operation with 56 and 108 fJ/bit energy-dissipation at 25 and 40 Gb/s with 850 nm VCSELs
    - Error-free operation at 25 Gb/s across 1000 m of multimode fiber and at 30 Gb/s across 500 m of multimode fiber with 100 and 85 fJ/bit of dissipated energy per bit with 850-nm VCSELs.
    - Error-free operation at 46 Gb/s at 85°C with a record large modulation bandwidth of 23 GHz with 980-nm VCSELs.
    - Error-free operation at 50 Gb/s at 25°C with 980-nm VCSELs.

9.2. Outlook

Large potential exists for the systematic evaluation of the impact of the photon lifetime on the dynamic energy efficiency and temperature stability of VCSELs. So far the method of photon lifetime tuning is mostly used to overcome limitations of the maximum modulation bandwidth caused by damping. As demonstrated in this work, low energy per bit operation of VCSELs is achieved at low currents and at modulation bandwidths below the maximum bandwidth. Thus the damping limit should not be as important here as for work aiming at record-large bit rates. In fact it has been demonstrated in this dissertation that a lower photon lifetime that increased the maximum modulation bandwidth led to a decrease of the energy-to-data ratio *EDR* at low currents. Thus the optimal photon lifetime for energy-efficient operation is different than that for a large maximum modulation bandwidth.

The impact of the photon lifetime on the static and dynamic properties and their temperature stability should be studied in dependence of the oxide-aperture diameter. The optimal photon lifetime can be expected to be different for different oxide-aperture diameters. Also the sensitivity to a photon lifetime change will most likely be different for different oxide-aperture diameters. Thus the absolute and relative improvements of the energy efficiency, modulation bandwidth, and the temperature stability of the energy efficiency and modulation bandwidth will depend on the oxide-aperture diameter.

As shown in this dissertation a photon lifetime reduction can reduce the modulation bandwidth at low currents but simultaneously lead to an increase of the modulation bandwidth at large currents. Thus the impact of the photon lifetime differs for different currents and current densities. Because this affects the static and dynamic VCSEL properties at different bias current values and therefore the potential of VCSELs to achieve certain performance goals at given required low current densities, the impact of the photon lifetime on the static and dynamic properties should be evaluated across the complete current range from threshold to rollover as a function of oxide-aperture diameter.

More research work should be performed on VCSELs with even smaller current-confining aperture diameters of 1-2 µm. While oxide-apertures add increasing scattering-losses with decreasing oxide-aperture diameter, recent work on lithographic oxide-free VCSELs demonstrated very high output powers in excess of 10 mW for small-aperture diameter single-mode VCSELs. The aperture diameter dependent small-signal modulation analysis performed in this dissertation should be repeated with such lithographic oxide-free VCSELs to verify whether the significantly improved static properties also translate into similar improvements of the dynamic performance.

Appendix A.

Process flow

The processing flow presented below is used to process quarter-pieces of a 3-inch wafer. The main limiting process steps inhibiting the processing of complete 3-inch wafers are homogeneity of the dry-etch steps for mesa-definition and the homogeneity of the home-built oxidation furnace.

1. Cleaving and Cleaning of Wafer

The waver is cleaved with a diamond scriber into quarter waferpieces.

Acetone	5 min at 70°C
Isopropanol	5 min at room temperature
	N_2 dry blow

2. Lithography for Alignment Markers and Top Metal Contacts

Negative photo-resist process. The alignment markers for all following processing steps and the top contacts are defined.

Acetone	5 min at 70°C
Isopropanol	5 min at room temperature
	N_2 dry blow
Spin MaN 1420 resist	30 s at 3000 rpm
Softbake on a Hotplate	120 s at 100°C
Exposure	20 s in Hard-Contact mode
Development	70 s in MaD 533s
	H_2O rinse
Plasma oxidation descum	3 min at 150 W, O_2 plasma

3. Evaporation of Alignment Markers and Top Metal Contacts

The alignment markers and the Ti/Pt/Au top metal contacts are evaporated using an electron beam deposition system.

Remove surface oxides	15 s in HCl:H_2O (1:5)
Ti deposition	20 nm
Pt deposition	50 nm
Au deposition	300 nm
Lift-off,	
N-Methyl-2-pyrrolidon (NMP)	~20 min at 70°C
remove NMP with Isopropanol	15 min at 70°C, 15 min at 25°C
Plasma oxidation descum	5 min at 600 W, O_2 plasma

4. Lithography for the first mesa definition

The photoresist mask for the first mesa etch is defined using a positive photoresist.

Acetone	5 min at 70°C
Isopropanol	5 min at room temperature
	N_2 dry blow
Spin AZ 701 resist	40 s at 3000 rpm
Softbake on a Hotplate	120 s at 90°C
Exposure	35 s in Hard-Contact mode
Development	~35 s in AZ351B:H_2O (1:5)
	H_2O rinse
Plasma oxidation descum	3 min at 150 W, O_2 plasma

5. Dry etch of first mesa, ICP-RIE

The first mesa is etched using a Sentech ICP-RIE (SI 500) and an *in situ*-controlled Cl+BCl_3 process.

Cl_2	2.5 sscm
BCl_3	12.5 sscm
pressure	0.33 Pa
RF power	15 W
ICP power	500 W
AlOx-Chuck and Santovac oil	for good thermal contact
	stop 4 DBR pairs after the active region
Remove resist and Santovac oil	20 min in NMP at 70°C
remove NMP with Isopropanol	15 min at 70°C, 15 min at 25°C
Plasma oxidation descum	5 min at 600 W, O_2 plasma

6. Selective Wet Oxidation, Formation of Oxide Apertures

The oxide apertures are formed by the selective wet oxidation using the *in situ*-controlled oxidation furnace.

Remove surface oxides	5 in 726 MIF developer
	H_2O rinse
chamber pressure	50 mbar
H_2O flow	0.8 l/min
N_2 flow	0.8 l/min
CEM temperature	200°C
temperature ramp up	3 min at 80°C, 3 min at 100°C, 3 min at 120°C
process temperature	420°C
illumination wavelength	850 nm for 980 nm and 940 nm for 850 nm VCSELs
oxidation depth	8-9 µm

7. Lithography for the second mesa definition

The photoresist mask for the first mesa etch is defined using a positive photoresist.

Acetone	5 min at 70°C
Isopropanol	5 min at room temperature
	N_2 dry blow
Spin AZ 4562 resist	30 s at 4000 rpm
Softbake on a Hotplate	420 s at 100°C
Exposure	150 s in Hard-Contact mode
Development	~140 s in AZ351B:H_2O (1:5)
	H_2O rinse
Plasma oxidation descum	3 min at 150 W, O_2 plasma

8. Dry etch of the second mesa, ICP-RIE

The second mesa is etched using a Sentech ICP-RIE (SI 500) and an *in situ*-controlled Cl+BCl_3 process.

Cl_2	2.5 sscm
BCl_3	12.5 sscm
pressure	0.33 Pa
RF power	15 W
ICP power	500 W
AlOx-Chuck and Santovac oil	for good thermal contact
	stop in the contact layer
Remove resist and Santovac oil	20 min in NMP at 70°C
remove NMP with Isopropanol	15 min at 70°C, 15 min at 25°C
Plasma oxidation descum	5 min at 600 W, O_2 plasma

9. Lithography for the Bottom Metal Contacts

Negative photo-resist process. The bottom contacts are defined.

Acetone	5 min at room temperature
Isopropanol	5 min at room temperature
	N_2 dry blow
Spin MaN 490 resist	30 s at 3000 rpm
Softbake on a Hotplate	14 min at 100°C
Exposure	150 s in Hard-Contact mode
Development	240 s in MaD 532s
	H_2O rinse
Plasma oxidation descum	3 min at 150 W, O_2 plasma

10. Evaporation of the Bottom Metal Contacts

The alignment markers and the Ti/Pt/Au top metal contacts are evaporated using an electron beam deposition system.

Remove surface oxides	15 s in HCl:H_2O (1:5)
Ni deposition	20 nm
Au:Ge deposition	88:12 nm
Au deposition	300 nm
Lift-off, NMP	~20 min at 70°C
remove NMP with Isopropanol	15 min at 70°C, 15 min at 25°C
Plasma oxidation descum	5 min at 600 W, O_2 plasma

Optionial: Si_xN_y deposition as optical etch-stop layer

The complete waferpiece is covered with a Si_xN_y-layer that serves as optical etch-stop layer during the dry etch of the BCB. A Sentech ICP-PECVD (SI 500) is used for this step.

Chamber pressure	8 Pa
Chuck temperature	300°C
ICP power	400 W
deposition rate	15.88 nm/min

12. Planarization with Photo-BCB

The structure is planarized using photosensitive BCB to enable coplanar ground-signal-ground contact pads.

Acetone	5 min at room temperature
Isopropanol	5 min at room temperature
Spin dry	90 s at 4000 rpm
Spin adhesion promoter AP 3000	20 s at 3000 rpm
Spin BCB 4026-46	10/40 s at 700/3000 rpm
Edge bead removal, EBR	remove ~2 mm from the edge
Spin dry	10 s at 3000 rpm
Backside cleaning, T1100	remove any residual BCB
Softbake on Hotplate	90 s at 80°C
Exposure	50 s in Hard-Contact mode
Development, DS3000	10 min at 35°C
Stop development and clean sample, DS3000	90 s at room temperature
Dry blow	N_2
Spin dry	90 s at 3000 rpm
Post development bake on hotplate	60 s at 90°C
Hard cure BCB in N_2 atmosphere	400 mbar
Temperature ramp	in 15 min up to 150°C
Hold temperature	15 min at 150°C
Temperature ramp	in 15 min up to 250°C
Hold temperature	1 h at 250°C
	cool down to <100°C

13. Dry Etch BCB, open Top Mesa and Bottom contacts, RIE

Residual hard cured BCB on the outcoupling facet, the top contact rings, and the bottom contacts is etched away using an O_2+CF_4 RIE-process.

O_2	20 sscm
CF_4	5 sscm
pressure	40 Pa
RF power	50 W
Optical Microscope control	repeat etch until top contact is free
	If SiN was deposited as optical etch stop
	layer, etch until apparent color change appears.

14. Lithography for the GSG Contacts

Negative photo-resist process. The high-frequency GSG-pads are defined.

Acetone	5 min at room temperature
Isopropanol	5 min at room temperature
	N_2 dry blow
Spin MaN 1440 resist	30 s at 3000 rpm
Softbake on a Hotplate	5 min at 90°C
Exposure	24 s in Hard-Contact mode
Development	105 s in MaD 533s
	H_2O rinse
Plasma oxidation descum	3 min at 150 W, O_2 plasma

15. Evaporation of the GSG Contacts

The GSG contact pads are evaporated using an electron beam metal deposition system.

Cr deposition	50 nm
Pt deposition	50 nm
Au deposition	300 nm
Lift-off, NMP	~20 min at 70°C
remove NMP with Isopropanol	15 min at 70°C, 15 min at 25°C

Bibliography

[1] R. S. Tucker, "Green Optical Communications Part I: Energy Limitations in Transport," *IEEE Journal of Selected Topics in Quantum Electronics*, vol. 17, no. 2, pp. 245–260, Mar./Apr. 2011.

[2] ——, "Green Optical Communications PartII: Energy Limitations in Networks," *IEEE Journal of Selected Topics in Quantum Electronics*, vol. 17, no. 2, pp. 261–274, Mar./Apr. 2011.

[3] CISCO VNI, "Cisco Visual Networking Index: Forecast and Methodology, 20132018: Visual networking index (vni)," June 2014. [Online]. Available: http://www.cisco.com/c/en/us/solutions/collateral/service-provider/ip-ngn-ip-next-generation-network/white_paper_c11-481360.html

[4] Green Mountain Data Centers, Stavanger and Telemark, Norway, "Green Mountain Data Centers, Stavanger and Telemark, Norway." [Online]. Available: http://www.greenmountain.no

[5] M. Grabherr, "New applications boost VCSEL quantities: recent developments at Philips," in *Vertical-Cavity Surface-Emitting Lasers XVIV*, SPIE, Ed., 7-12 Feb. 2015, San Francisco, CA, USA, pp. 9381–1.

[6] P. Westbergh, J. Gustavsson, and A. Larsson, "VCSEL Arrays for Multicore Fiber Interconnects with an Aggregate Capacity of 240 Gbit/s," *IEEE Photonics Technology Letters*, p. 1, 2014 (early access). doi: 10.1109/LPT.2014.2369827.

[7] J. Tatum, D. Gazula, L. Graham, J. Guenter, R. Johnson, J. King, C. Kocot, G. Landry, I. Lyubomirsky, A. MacInnes, E. Shaw, K. Balemarthy, R. Shubochkin, D. Vaidya, M. Yan, and F. Tang, "VCSEL Based Interconnects for Current and Future Data Centers," *Journal of Lightwave Technology*, p. 1, 2014, DOI: 10.1109/JLT.2014.2370633.

[8] P. Westbergh, R. Safaisini, E. Haglund, B. Kögel, J. S. Gustavsson, A. Larsson, M. Geen, R. Lawrence, and A. Joel, "High-speed 850 nm VCSELs with 28 GHz modulation bandwidth operating error-free up to 44 Gbit/s," *Electronics Letters*, vol. 48, no. 18, pp. 1145–1147, Aug. 2012.

[9] P. Westbergh, R. Safaisini, E. Haglund, J. Gustavsson, A. Larsson, M. Geen, R. Lawrence, and A. Joel, "High-Speed Oxide Confined 850-

nm VCSELs Operating Error Free at 40 Gbit/s up to 85°C," *Photonics Technology Letters, IEEE*, vol. 25, no. 8, pp. 768–771, Mar. 2013.

[10] P. Westbergh, E. P. Haglund, E. Haglund, R. Safaisini, J. Gustavsson, and A. Larsson, "High-speed 850 nm VCSELs operating error free up to 57 Gbit/s," *Electronics Letters*, vol. 49, no. 16, pp. 1021–1023, Aug. 2013.

[11] R. Safaisini, E. Haglund, P. Westbergh, J. S. Gustavsson, and A. Larsson, "20 Gbit/s data transmission over 2 km multimode fibre using 850 nm mode filter VCSEL," *Electronics Letters*, vol. 50, no. 1, pp. 40–42, Jan. 2014.

[12] M. P. Tan, S. T. M. Fryslie, J. A. Lott, N. N. Ledentsov, D. Bimberg, and K. D. Choquette, "Error-Free Transmission Over 1-km OM4 Multimode Fiber at 25 Gb/s Using a Single Mode Photonic Crystal Vertical-Cavity Surface-Emitting Laser," *IEEE Photonics Technology Letters*, vol. 25, no. 18, pp. 1823–1825, Sep. 2013.

[13] S. T. M. Fryslie, M. P. Tan, D. F. Siriani, M. T. Johnson, and K. D. Choquette, "37-GHz Modulation via Resonance Tuning in Single-Mode Coherent Vertical-Cavity Laser Arrays," *IEEE Photonics Technology Letters*, vol. 27, no. 4, pp. 415–418, Feb. 2015.

[14] F. Koyama and H. Dalir, "Highly stable operations of transverse-coupled cavity vcsels with enhanced modulation bandwidth," *Electronics Letters*, vol. 50, no. 11, pp. 823–824, 2014.

[15] J.-W. Shi, Z.-R. Wei, K.-L. Chi, J.-W. Jiang, J.-M. Wun, I.-C. Lu, J. Chen, and Y.-J. Yang, "Single-Mode, High-Speed, and High-Power Vertical-Cavity Surface-Emitting Lasers at 850 nm for Short to Medium Reach (2 km) Optical Interconnects," *Journal of Lightwave Technology*, vol. 31, no. 24, pp. 4037–4044, Dec. 2013.

[16] Y.-C. Chang, C. S. Wang, and L. A. Coldren, "High-efficiency, high-speed VCSELs with 35 Gbit/s error-free operation," *Electronics Letters*, vol. 43, no. 19, pp. 1022–1023, Sep. 2007.

[17] Y.-C. Chang and L. A. Coldren, "Efficient, High-Data-Rate, Tapered Oxide-Aperture Vertical-Cavity Surface-Emitting Lasers," *IEEE Journal of Selected Topics in Quantum Electronics*, vol. 15, no. 3, pp. 704–715, Jun. 2009.

[18] ——, "High-efficiency, high-speed VCSELs for optical interconnects," *Applied Physics A*, vol. 95, no. 4, pp. 1033–1037, Feb. 2009.

[19] A. Mutig, G. Fiol, P. Moser, D. Arsenijevic, V. A. Shchukin, N. N. Ledentsov, S. S. Mikhrin, I. L. Krestnikov, D. A. Livshits, A. R. Kovsh,

F. Hopfer, and D. Bimberg, "120°C 20 Gbit/s operation of 980 nm VCSEL," *Electronics Letters*, vol. 44, no. 22, pp. 1305–1306, Oct. 2008.

[20] A. Mutig, J. A. Lott, S. A. Blokhin, P. Moser, P. Wolf, W. Hofmann, A. M. Nadtochiy, A. S. Payusov, and D. Bimberg, "Highly temperature-stable modulation characteristics of multioxide-aperture high-speed 980 nm vertical cavity surface emitting lasers," *Applied Physics Letters*, vol. 97, no. 15, pp. 151 101–1–3, Oct. 2010.

[21] A. Mutig and D. Bimberg, "Progress on High-Speed 980nm VCSELs for Short-Reach Optical Interconnects," *Advances in Optical Technologies*, vol. 2011, pp. 1–15, Jun. 2011.

[22] P. Moser, P. Wolf, A. Mutig, G. Larisch, W. Unrau, W. Hofmann, and D. Bimberg, "85°C error-free operation at 38 Gb/s of oxide-confined 980-nm vertical-cavity surface-emitting lasers," *Applied Physics Letters*, vol. 100, no. 8, pp. 081 103–1–3, Feb. 2012.

[23] N. Suzuki, T. Anan, H. Hatakeyama, K. Fukatsu, K. Yashiki, K. Tokutome, T. Akagawa, and M. Tsuji, "High Speed 1.1- μm-Range InGaAs-Based VCSELs," *IEICE Transactions on Electronics*, vol. E92-C, no. 7, pp. 942–950, Jul. 2009.

[24] H. Hatakeyama, T. Akagawa, K. Fukatsu, N. Suzuki, K. Tokutome, K. Yashiki, T. Anan, and M. Tsuji, "25 Gbit/s 100°C operation of highly reliable InGaAs/GaAsP-VCSELs," *Electronics Letters*, vol. 45, no. 1, pp. 45–46, Jan. 2009.

[25] H. Hatakeyama, T. Anan, T. Akagawa, K. Fukatsu, N. Suzuki, K. Tokutome, and M. Tsuji, "Highly Reliable High-Speed 1.1- μm-Range VCSELs With InGaAs/GaAsP-MQWs," *IEEE Journal of Quantum Electronics*, vol. 46, no. 6, pp. 890–897, Mar. 2010.

[26] S. Imai, K. Takaki, S. Kamiya, J. Yoshida, Y. Kawakita, T. Takagi, K. Hiraiwa, H. Shimizu, T. Suzuki, N. Iwai, T. Ishikawa, N. Tsukiji, and A. Kasukawa, "Recorded low power dissipation in highly reliable 1060-nm VCSELs for "Green" Optical Interconnection," *IEEE Journal of Selected Topics in Quantum Electronics*, vol. 17, no. 6, pp. 1614–1620, Jan. 2011.

[27] A. Kasukawa, "VCSEL Technology for Green Optical Interconnects: VCSEL for Green Optical Interconnects," *IEEE Photonics Journal*, vol. 4, no. 2, pp. 642–464, Apr. 2012.

[28] J. B. Heroux, T. Kise, M. Funabashi, T. Aoki, C. Schow, A. Rylyakov, and S. Nakagawa, "Energy-efficient 1060 nm optical link operating up to 28 Gb/s," *Journal of Lightwave Technology*, vol. 33, no. 4, pp. 733–740, Feb. 2015.

[29] D. Kuchta, A. Rylyakov, F. E. Doany, C. Schow, J. Proesel, C. Baks, P. Westbergh, J. Gustavsson, and A. Larsson, "A 71 Gb/s NRZ Modulated 850 nm VCSEL-based Optical Link," *IEEE Photonics Technology Letters*, vol. 27, no. 6, pp. 577–580, Mar. 2015.

[30] J. E. Proesel, B. G. Lee, C. W. Baks, and C. L. Schow, "35-Gb/s VCSEL-Based optical link using 32-nm SOI CMOS circuits," in *Optical Fiber Communication Conference (OFC/NFOEC), 2013*, Los Angeles, CA, USA, 4-8 March 2013, pp. 1–3.

[31] B. M. Hawkins, R. A. Hawthorne, J. K. Guenter, J. A. Tatum, and J. R. Biard, "Reliability of various size oxide aperture VCSELs," in *52nd Electronic Components and Technology Conference*. IEEE, 28-31 May 2002, San Diego, CA, USA, pp. 540–550.

[32] D. A. B. Miller, "Device Requirements for Optical Interconnects to Silicon Chips," *Proceedings of the IEEE*, vol. 97, no. 7, pp. 1166–1185, Jul. 2009.

[33] A. Larsson, "Advances in VCSELs for Communication and Sensing," *IEEE Journal of Selected Topics in Quantum Electronics*, vol. 17, no. 6, pp. 1552–1567, Nov./Dec. 2011.

[34] C. F. Lam, Hong Liu, B. Koley, X. Zhao, V. Kamalov, and V. Gill, "Fiber optic communication technologies: What's needed for datacenter network operations," *IEEE Communications Magazine*, vol. 48, no. 7, pp. 32–39, Jul. 2010.

[35] H. Liu, C. F. Lam, and C. Johnson, "Scaling Optical Interconnects in Datacenter Networks Opportunities and Challenges for WDM," in *2010 IEEE 18th Annual Symposium on High-Performance Interconnects (HOTI)*. IEEE, 18-20 Aug. 2010, Mountain View, CA, USA, pp. 113–116.

[36] Albert Einstein, "Strahlungs-Emission und -Absorption nach der Quantentheorie," *Verhandlungen der Deutschen Physikalischen Gesellschaft*, vol. 18, pp. 318–323, 1916.

[37] S. M. Sze and K. K. Ng, *Physics of semiconductor devices*, 3rd ed. Hoboken, N.J.: Wiley-Interscience, Oct. 2006, \C 2007.

[38] D. Bimberg, "From Ugly Duckling to Radiant Swan: Half a Century After the Discovery of the Semiconductor Laser," *IEEE Photonics Society News*, vol. 27, no. 3, pp. 4–9, Jun. 2013.

[39] L. A. Coldren and S. W. Corzine, *Diode lasers and photonic integrated circuits*, ser. Wiley series in microwave & optical engineering. New York, NY, USA: Wiley, 1995.

[40] K. F. Brennan, *Introduction to Semiconductor Devices: For computing and telecommunications applications*. Cambridge: Cambridge University Press, 2005.

[41] H. Martinsson, J. A. Vukusic, M. Grabberr, R. Michalzik, R. Jager, K. J. Ebeling, and A. Larsson, "Transverse mode selection in large-area oxide-confined vertical-cavity surface-emitting lasers using a shallow surface relief," *IEEE Photonics Technology Letters*, vol. 11, no. 12, pp. 1536–1538, Dec. 1999.

[42] J. S. Gustavsson, Å. Haglund, J. Bengtsson, P. Modh, and A. Larsson, "Dynamic behavior of fundamental-mode stabilized VCSELs using a shallow surface relief," *IEEE Journal of Quantum Electronics*, vol. 40, no. 6, pp. 607–619, Jun. 2004.

[43] Å. Haglund, J. S. Gustavsson, J. Vukusic, P. Modh, and A. Larsson, "Single Fundamental-Mode Output Power Exceeding 6 mW From VCSELs With a Shallow Surface Relief," *IEEE Photonics Technology Letters*, vol. 16, no. 2, pp. 368–370, Feb. 2004.

[44] E. Haglund, Å. Haglund, P. Westbergh, J. S. Gustavsson, B. Kögel, and A. Larsson, "25 Gbit/s transmission over 500 m multimode fibre using 850 nm VCSEL with integrated mode filter," *Electronics Letters*, vol. 48, no. 9, pp. 517–519, Apr. 2012.

[45] Y. Zhou, M. Huang, and C. J. Chang-Hasnain, "Large Fabrication Tolerance for VCSELs Using High-Contrast Grating," *IEEE Photonics Technology Letters*, vol. 20, no. 6, pp. 434–436, Mar. 2008.

[46] Ye Zhou, M. Huang, C. Chase, V. Karagodsky, M. Moewe, B. Pesala, F. G. Sedgwick, and C. J. Chang-Hasnain, "High-Index-Contrast Grating (HCG) and Its Applications in Optoelectronic Devices," *IEEE Journal of Selected Topics in Quantum Electronics*, vol. 15, no. 5, pp. 1485–1499, Sep./Oct. 2009.

[47] M. Gebski, M. Dems, J. Chen, Q. J. Wang, D. H. Zhang, and T. Czyszanowski, "The influence of imperfections and absorption on the Performance of a GaAs/AlO High-Contrast Grating for Monolithic Integration With 980 nm GaAs-Based VCSELs," *Journal of Lightwave Technology*, vol. 31, no. 23, pp. 3853–3858, Dec. 2013.

[48] J. A. Lott, "Polymorph," computer modeling software (unpublished), private communication, 2015.

[49] S. L. Chuang, *Physics of photonic devices*, 2nd ed., ser. Wiley series in pure and applied optics. Hoboken, N.J.: John Wiley & Sons, ©2009.

[50] J. M. Dallesasse, N. Holonyak, A. R. Sugg, T. A. Richard, and N. El-Zein, "Hydrolyzation oxidation of $Al_xGa_{1-x}As$-GaAs quantum well heterostructures and superlattices," *Applied Physics Letters*, vol. 57, no. 26, p. 2844, Dec. 1990.

[51] J. M. Dallesasse and N. Holonyak, "Oxidation of Al-bearing III-V materials: A review of key progress," *Journal of Applied Physics*, vol. 113, no. 5, p. 051101, Feb. 2013.

[52] D. L. Huffaker, D. G. Deppe, K. Kumar, and T. J. Rogers, "Native-oxide defined ring contact for low threshold vertical-cavity lasers," *Applied Physics Letters*, vol. 65, no. 1, pp. 97–99, Apr. 1994.

[53] K. D. Choquette, R. P. Schneider, K. L. Lear, and K. M. Geib, "Low threshold voltage vertical-cavity lasers fabricated by selective oxidation," *Electronics Letters*, vol. 30, no. 24, pp. 2043–2044, Oct. 1994.

[54] K. L. Lear, K. D. Choquette, R. P. Schneider, S. P. Kilcoyne, and K. M. Geib, "Selectively oxidised vertical cavity surface emitting lasers with 50% power conversion efficiency," *Electronics Letters*, vol. 31, no. 3, pp. 208–209, Feb. 1995.

[55] J. M. Dallesasse and D. G. Deppe, "III-V Oxidation: Discoveries and Applications in Vertical-Cavity Surface-Emitting Lasers," *Proceedings of the IEEE*, vol. 101, no. 10, pp. 2234–2242, Aug. 2013.

[56] K. D. Choquette, K. M. Geib, C. Ashby, R. D. Twesten, O. Blum, H. Q. Hou, D. M. Follstaedt, B. E. Hammons, D. Mathes, and R. Hull, "Advances in selective wet oxidation of AlGaAs alloys," *IEEE Journal of Selected Topics in Quantum Electronics*, vol. 3, no. 3, pp. 916–926, Jun. 1997.

[57] P. Westbergh, J. S. Gustavsson, B. Kögel, Å. Haglund, A. Larsson, A. Mutig, A. M. Nadtochiy, D. Bimberg, and A. Joel, "40 Gbit/s error-free operation of oxide-confined 850 nm VCSEL," *Electronics Letters*, vol. 46, no. 14, pp. 1014–1015, Jul. 2010.

[58] P. Moser, J. A. Lott, P. Wolf, G. Larisch, H. Li, and D. Bimberg, "Error-free 46 Gbit/s operation of oxide-confined 980 nm VCSELs at 85°C," *Electronics Letters*, vol. 50, no. 19, pp. 1369–1371, Sep. 2014.

[59] R. L. Naone and L. A. Coldren, "Tapered air apertures for thermally robust VCL structures," *IEEE Photonics Technology Letters*, vol. 11, no. 11, pp. 1339–1341, Nov. 1999.

[60] D. Cunningham and P. Dawe, "Review of the 10Gigabit Ethernet Link Model: White paper: Onids 2002." [Online]. Available: http://www.avagotech.com/docs/AV02-2485EN

[61] ——, "IEEE Spreadsheet model," 2001. [Online]. Available: http://www.ieee802.org/3/ae/public/email_attach/10GEPBud2_4_1.xls

[62] G. Giaretta, R. Michalzik, and A. J. Ritger, "Long distance (2.8 km), short wavelength (0.85 µm) data transmission at 10Gb/sec over new generation high bandwidth multimode fiber," in *Lasers and Electro-Optics (CLEO) and the International Quantum Electronics Conference (IQEC)*, 7-12 May 2000, San Francisco, CA, USA, pp. 678–679.

[63] N. Yokouchi, A. J. Danner, and K. D. Choquette, "Two-dimensional photonic crystal confined vertical-cavity surface-emitting lasers," *IEEE Journal of Selected Topics in Quantum Electronics*, vol. 9, no. 5, pp. 1439–1445, Sep. 2003.

[64] J. A. Vukusic, H. Martinsson, J. S. Gustavsson, and A. Larsson, "Numerical optimization of the single fundamental mode output from a surface modified vertical-cavity surface-emitting laser," *IEEE Journal of Quantum Electronics*, vol. 37, no. 1, pp. 108–117, Jan. 2001.

[65] P. Moser, J. A. Lott, P. Wolf, G. Larisch, H. Li, and D. Bimberg, "85-fJ Dissipated Energy Per Bit at 30 Gb/s Across 500-m Multimode Fiber Using 850-nm VCSELs," *IEEE Photonics Technology Letters*, vol. 25, no. 16, pp. 1638–1641, Aug. 2013.

[66] Y. C. Chang, C. S. Wang, L. A. Johansson, and L. A. Coldren, "High-efficiency, high-speed VCSELs with deep oxidation layers," *Electronics Letters*, vol. 42, no. 22, p. 1281, Oct. 2006.

[67] B. J. Thibeault, E. R. Hegblom, P. D. Floyd, R. Naone, Y. Akulova, and L. A. Coldren, "Reduced optical scattering loss in vertical-cavity lasers using a thin (300 Angstrom) oxide aperture," *IEEE Photonics Technology Letters*, vol. 8, no. 5, pp. 593–595, May 1996.

[68] X. Yang, M. Li, G. Zhao, Y. Zhang, S. Freisem, and D. G. Deppe, "Oxide-free vertical-cavity surface-emitting lasers with low junction temperature and high drive level," *Electronics Letters*, vol. 50, no. 20, pp. 1474–1475, Jul. 2014.

[69] X. Yang, M. X. Li, D. G. Deppe, G. Zhao, and S. Freisem, "Small oxide-free vertical-cavity surface-emitting lasers with high efficiency and high power," *Electronics Letters*, vol. 50, no. 24, pp. 1864–1866, Nov. 2014.

[70] X. Yang, M. X. Li, G. Zhao, Y. Zhang, S. Freisem, and D. G. Deppe, "Small-sized lithographic single-mode vcsels with high-power conversion efficiency," in *Vertical-Cavity Surface-Emitting Lasers XVIV*, SPIE, Ed., 7-12 Feb. 2015, San Francisco, CA, USA, pp. 9381–25.

[71] T. R. Chen, B. Zhao, L. Eng, Y. H. Zhuang, J. O'brien, and A. Yariv, "Very high modulation efficiency of ultralow threshold current single quantum well InGaAs lasers," *Electronics Letters*, vol. 29, no. 17, pp. 1525–1526, Aug. 1993.

[72] P. Moser, W. Hofmann, P. Wolf, J. A. Lott, G. Larisch, A. S. Payusov, N. N. Ledentsov, and D. Bimberg, "81 fJ/bit energy-to-data ratio of 850 nm vertical-cavity surface-emitting lasers for optical interconnects," *Applied Physics Letters*, vol. 98, no. 23, pp. 231 106–1–3, Jun. 2011.

[73] P. Moser, J. A. Lott, and D. Bimberg, "Energy Efficiency of Directly Modulated Oxide-Confined High Bit Rate 850-nm VCSELs for Optical Interconnects," *IEEE Journal of Selected Topics in Quantum Electronics*, vol. 19, no. 4, pp. 1 702 212–1–12, Jul./Aug. 2013.

[74] P. Moser, J. A. Lott, P. Wolf, G. Larisch, A. S. Payusov, N. N. Ledentsov, W. Hofmann, and D. Bimberg, "99 fJ/(bit · km) Energy to Data-Distance Ratio at 17 Gb/s Across 1 km of Multimode Optical Fiber With 850-nm Single-Mode VCSELs," *IEEE Photonics Technology Letters*, vol. 24, no. 1, pp. 19–21, Jan. 2012.

[75] P. Moser, J. A. Lott, G. Larisch, and D. Bimberg, "Impact of the Oxide-Aperture Diameter on the Energy-Efficiency, Bandwidth, and Temperature Stability of 980 nm VCSELs," *Journal of Lightwave Technology*, vol. 33, no. 4, pp. 825–831, Feb. 2015.

[76] D. Kuchta, A. V. Rylyakov, C. L. Schow, J. Proesel, C. Baks, P. Westbergh, J. S. Gustavsson, and A. Larsson, "64 Gb/s Transmission over 57 m MMF using an NRZ Modulated 850 nm VCSEL," in *Optical Fiber Communication Conference (OFC)*, 9-13 Mar. 2014, San Francisco, CA, USA, p. Th3C.2.

[77] D. M. Kuchta, A. V. Rylyakov, C. L. Schow, J. E. Proesel, C. W. Baks, P. Westbergh, J. S. Gustavsson, and A. Larsson, "A 50 Gb/s NRZ Modulated 850 nm VCSEL Transmitter Operating Error Free to 90°C," *Journal of Lightwave Technology*, vol. 33, no. 4, pp. 802–810, Feb. 2015.

[78] E. P. Haglund, P. Westbergh, J. S. Gustavsson, and A. Larsson, "Impact of Damping on High-Speed Large Signal VCSEL Dynamics," *Journal of Lightwave Technology*, pp. 1–8, Oct. 2014 (early access). doi: 10.1109/JLT.2014.2364455.

[79] C. E. Shannon, "Communication in the Presence of Noise," *Proceedings of the IRE*, vol. 37, no. 1, pp. 10–21, Jan. 1949.

[80] ——, "Communication in the Presence of Noise: Classic paper," *Proceedings of the IEEE*, vol. 86, no. 2, pp. 447–457, Feb. 1998 (reprint).

[81] F. R. Yu, X. Zhang, and V. Leung, *Green communications and networking*. Florida, USA: CRC Press, 2012.

[82] J. E. Proesel, C. L. Schow, and A. V. Rylyakov, "Ultra Low Power 10- to 25-Gb/s CMOS-Driven VCSEL Links: Optical fiber communication conference 2012," in *Optical Fiber Communication Conference and Exposition (OFC)*, 4-8 Mar. 2012, Los Angeles, CA, USA, pp. 1–3.

[83] K. D. Choquette, W. W. Chow, G. R. Hadley, H. Q. Hou, and K. M. Geib, "Scalability of small-aperture selectively oxidized vertical cavity lasers," *Applied Physics Letters*, vol. 70, no. 7, pp. 823–825, Feb. 1997.

[84] M. Jungo, F. M. Di Sopra, D. Erni, and W. Baechtold, "Scaling effects on vertical-cavity surface-emitting lasers static and dynamic behavior," *Journal of Applied Physics*, vol. 91, no. 9, pp. 5550–5557, May 2002.

[85] P. Moser, J. A. Lott, P. Wolf, G. Larisch, A. S. Payusov, G. Fiol, N. N. Ledentsov, W. Hofmann, and D. Bimberg, "Energy-efficient vertical-cavity surface-emitting lasers (VCSELs) for "green" data and computer communication," in *Proc. of SPIE 8276, Vertical-Cavity Surface-Emitting Lasers XVI*, 21-26 Jan. 2012, San Francisco, CA, USA., pp. 82 760J–1–8.

[86] P. Moser, J. A. Lott, P. Wolf, G. Larisch, H. Li, N. N. Ledentsov, and D. Bimberg, "56 fJ dissipated energy per bit of oxide-confined 850 nm VCSELs operating at 25 Gbit/s," *Electronics Letters*, vol. 48, no. 20, pp. 1292–1294, Sep. 2012.

[87] ——, "Impact of the aperture diameter on the energy efficiency of oxide-confined 850 nm high speed VCSELs," in *SPIE OPTO, Vertical-Cavity Surface-Emitting Lasers XVII*, ser. SPIE Proceedings. SPIE, 2-7 Feb. 2013, San Francisco, CA, USA, p. 86390V.

[88] P. Moser, J. A. Lott, P. Wolf, G. Larisch, N. N. Ledentsov, and D. Bimberg, "25 Gb/s operation of oxide-confined 850-nm VCSELs with ultralow 56 fJ dissipated power per bit," in *IEEE 23rd International Semiconductor Laser Conference*. IEEE, 7-10 Oct. 2012, San Diego, CA, USA, pp. 157–158.

[89] J. A. Lott, A. S. Payusov, S. A. Blokhin, P. Moser, N. N. Ledentsov, and D. Bimberg, "Arrays of 850 nm photodiodes and vertical cavity surface emitting lasers for 25 to 40 Gbit/s optical interconnects," *physica status solidi (c)*, vol. 9, no. 2, pp. 290–293, Nov. 2011.

[90] J. A. Lott, P. Moser, A. Payusov, S. Blokhin, P. Wolf, G. Larisch, N. N. Ledentsov, and D. Bimberg, "Energy efficient 850 nm VCSELs operating error-free at 25 Gb/s over multimode optical fiber up to 600 m," in *2012*

IEEE Optical Interconnects Conference, 20-23 May 2012, Santa Fe, NM, USA, pp. 42–43.

[91] P. Moser, J. A. Lott, P. Wolf, G. Larisch, A. Payusov, G. Fiol, N. N. Ledentsov, W. Hofmann, and D. Bimberg, "Energy-efficient vertical-cavity surface-emitting lasers (VCSELs) for green data and computer communication," in *SPIE OPTO, Vertical-Cavity Surface-Emitting Lasers XVI*, ser. SPIE Proceedings. SPIE, 21-26 Jan. 2012, San Francisco, CA, USA, p. 82760J.

[92] P. Moser, J. A. Lott, P. Wolf, G. Larisch, A. S. Payusov, N. N. Ledentsov, and D. Bimberg, "Energy-Efficient Oxide-Confined 850 nm VCSELs for Long Distance Multimode Fiber Optical Interconnects," *IEEE Journal of Selected Topics in Quantum Electronics*, vol. 19, no. 2, pp. 7 900 406–1–8, Sep. 2012.

[93] P. Moser, P. Wolf, J. A. Lott, G. Larisch, A. Payusov, A. Mutig, W. Unrau, N. N. Ledentsov, W. Hofmann, and D. Bimberg, "High-speed VCSELs for energy efficient computer Interconnects," in *SPIE Photonics Europe, Semiconductor Lasers and Laser Dynamics V*, ser. SPIE Proceedings. SPIE, 16-19 Apr. 2012, Brussels, Belgium, pp. 843 202–1–8.

[94] M. A. Afromowitz, "Thermal conductivity of GaAlAs alloys," *Journal of Applied Physics*, vol. 44, no. 3, pp. 1292–1294, Mar. 1973.

[95] D. H. Lim, G. M. Yang, J.-H. Kim, K. Y. Lim, and H. J. Lee, "Sealing of AlAs against wet oxidation and its use in the fabrication of vertical-cavity surface-emitting lasers," *Applied Physics Letters*, vol. 71, no. 14, p. 1915, Oct. 1997.

[96] J. L. Jewell, Y. H. Lee, S. L. McCall, J. P. Harbison, and L. T. Florez, "High-finesse (Al,Ga)As interference filters grown by molecular beam epitaxy," *Applied Physics Letters*, vol. 53, no. 8, p. 640, Aug. 1988.

[97] M. Volwahsen, "The Influence of the Mirror Reflectivity on the Temperature Performance of High Speed VCSELs," *Bachelor Thesis*, Technische Universität Berlin, Berlin, Germany, Aug. 2014.

[98] P. Moser, P. Wolf, G. Larisch, H. Li, J. A. Lott, and D. Bimberg, "Energy-efficient oxide-confined high-speed VCSELs for optical interconnects," in *Proc. SPIE 9001, Vertical-Cavity Surface-Emitting Lasers XVIII*, ser. SPIE Proceedings. SPIE, 7-12 Feb. 2014, San Francisco, CA, USA, p. 900103.

[99] T. R. Fanning, J. Wang, Z.-W. Feng, M. Keever, C. Chu, A. Sridhara, C. Rigo, H. Yaun, T. Sale, G.-H. Koh, R. Murty, S. Aboulhouda, and L. Giovane, "28-Gbps 850-nm oxide VCSEL development and

manufacturing progress at Avago," in *Proc. SPIE 9001, Vertical-Cavity Surface-Emitting Lasers XVIII*, ser. SPIE Proceedings, vol. 9001. SPIE, 7-12 Feb. 2014, San Francisco, CA, USA. [Online]. Available: http://dx.doi.org/10.1117/12.2039499

[100] F. Tan, M. K. Wu, M. Liu, M. Feng, and N. Holonyak, "Relative intensity noise in high speed microcavity laser," *Applied Physics Letters*, vol. 103, no. 14, p. 141116, Sep. 2013.

[101] F. Tan, M.-K. Wu, M. Liu, M. Feng, and N. Holonyak, "850 nm Oxide-VCSEL With Low Relative Intensity Noise and 40 Gb/s Error Free Data Transmission," *IEEE Photonics Technology Letters*, vol. 26, no. 3, pp. 289–292, Feb. 2014.

[102] P. Moser, G. Larisch, P. Wolf, H. Li, J. A. Lott, and D. Bimberg, "Green photonics for data and computer communication," in *2013 IEEE Photonics Society Summer Topical Meeting Series*, 8-10 Jul. 2013, Waikoloa, HI, USA., pp. 5–6.

[103] P. Wolf, P. Moser, G. Larisch, H. Li, J. A. Lott, and D. Bimberg, "Energy efficient 40 Gbit/s transmission with 850 nm VCSELs at 108 fJ/bit dissipated heat," *Electronics Letters*, vol. 49, no. 10, pp. 666–667, May 2013.

[104] R. Safaisini, K. Szczerba, E. Haglund, P. Westbergh, J. S. Gustavsson, A. Larsson, and P. A. Andrekson, "20 Gbit/s error-free operation of 850 nm oxide-confined VCSELs beyond 1 km of multimode fibre," *Electronics Letters*, vol. 48, no. 19, pp. 1225–1227, Sep. 2012.

[105] A. Mutig, G. Fiol, K. Pötschke, P. Moser, V. A. Shchukin, N. N. Ledentsov, S. S. Mikhrin, I. L. Krestnikov, D. A. Livshits, A. R. Kovsh, F. Hopfer, and D. Bimberg, "Temperature-Dependent Small-Signal Analysis of High-Speed High-Temperature Stable 980-nm VCSELs," *IEEE Journal of Selected Topics in Quantum Electronics*, vol. 15, no. 3, pp. 679–686, May/Jun. 2009.

[106] H. Hatakeyama, T. Akagawa, K. Fukatsu, N. Suzuki, K. Yashiki, K. Tokutome, T. Anan, and M. Tsuji, "25 Gbit/s 100°C operation and high reliability of 1.1- μm-range VCSELs with InGaAs/GaAsP strain-compensated MQWs," in *Conference on Lasers and Electro-Optics (CLEO/QELS) 2008*, 4-9 May 2008, San Jose, CA, USA, p. CMW3.

[107] D. Young, J. Scott, F. Peters, M. Peters, M. Majewski, B. Thibeault, S. Corzine, and L. A. Coldren, "Enhanced performance of offset-gain high-barrier vertical-cavity surface-emitting lasers," *IEEE Journal of Quantum Electronics*, vol. 29, no. 6, pp. 2013–2022, Jun. 1993.

[108] S. Mogg, N. Chitica, U. Christiansson, R. Schatz, P. Sundgren, C. Asplund, and M. Hammar, "Temperature sensitivity of the threshold current of long-wavelength InGaAs-GaAs VCSELs with large gain-cavity detuning," *IEEE Journal of Quantum Electronics*, vol. 40, no. 5, pp. 453–462, May 2004.

[109] H. Li, P. Wolf, P. Moser, G. Larisch, A. Mutig, J. A. Lott, and D. H. Bimberg, "Impact of the Quantum Well Gain-to-Cavity Etalon Wavelength Offset on the High Temperature Performance of High Bit Rate 980-nm VCSELs," *IEEE Journal of Quantum Electronics*, vol. 50, no. 8, pp. 613–621, Aug. 2014.

[110] P. Moser, M. Volwahsen, G. Larisch, J. A. Lott, and D. H. Bimberg, "Maximizing the temperature insensitivity, energy efficiency, and bit rate of 980-nm VCSELs via small oxide-aperture diameters and photon lifetime tuning," in *Vertical-Cavity Surface-Emitting Lasers XVIV*, SPIE, Ed., 7-12 Feb. 2015, San Francisco, CA, USA, pp. 9381–28.

[111] P. Westbergh, J. S. Gustavsson, B. Kögel, Å. Haglund, and A. Larsson, "Impact of Photon Lifetime on High-Speed VCSEL Performance," *IEEE Journal of Selected Topics in Quantum Electronics*, vol. 17, no. 6, pp. 1603–1613, Nov./Dec. 2011.

[112] D. Ellafi, V. Iakovlev, A. Sirbu, G. Suruceanu, Z. Mickovic, A. Caliman, A. Mereuta, and E. Kapon, "Control of cavity lifetime of 1.5 µm wafer-fused VCSELs by digital mirror trimming," *Optics Express*, vol. 22, no. 26, p. 32180, Dec. 2014.

[113] P. Westbergh, J. S. Gustavsson, B. Kögel, Å. Haglund, A. Larsson, and A. Joel, "Speed enhancement of VCSELs by photon lifetime reduction," *Electronics Letters*, vol. 46, no. 13, pp. 938–939, Jun. 2010.

Index

$\lambda/2$-cavity, 32
$\lambda/2$-layer, 25
-3dB bandwidth, f_{3dB}, 43
L_{eff}, 70
bandwidth-to electrical power ratio, 93, 129
f_{3dB}, 43, 127
$\lambda/2$-cavity, 30
$\lambda/2$-layer, 21, 23, 25, 32, 71
$\lambda/4$-layer, 19
850-nm VCSEL design, 68
850-nm data transmission, 105, 108
980-nm VCSEL design, 69

absentee layer, 21, 23, 25, 71
absorption, 11

BCB planarization, 58

cavity, 15, 30
constructive interference, 19
current density, 82, 83, 92, 98, 143
current spreading region, 71
current-confinement, 34
CW temperature stability, 116

D-factor, 41, 42, 84
data transmission, 105, 108
DBR, 17
deep oxidation layers, 38
destructive interference, 19
distributed Bragg reflector, DBR, 17
double mesa design, 63
dynamic temperature stability, 121

EDR, 46, 88, 124
effective cavity length, L_{eff}, 70
electron photon interaction, 11
energy consumption, 46
energy dissipation, 46
energy-efficient data transmission, 105, 108
energy-to-data ratio, 46

HBR, 46, 88
heat-to-bit rate ratio, 46

impedance mismatch, 47

K-factor, 41, 42

large-signal modulation, 105
laser cavity, 15
long MMF data transmission, 108, 113

M-factor, 48, 100, 124, 132
mask layout, 63
mask set, 63
MCEF, 43, 84
modulation bandwidth, 43, 127
modulation energy, 47
modulation factor M, 48, 100, 124, 132
modulation-current efficiency factor, MCEF, 43, 84

number of DBR pairs, 28

oxidation, 60
oxide-aperture, 34

phase change, $\Delta\varphi$, 19
photon lifetime, 135
photon lifetime τ_p, 134
photon lifetime, τ_p, 75
photonic crystal, 38
population inversion, 12

population inversion in semiconductors, 13
power reflectance, R, 18
power-to-bandwidth ratio, 86, 88

rate equations, 40
refractive index contrast, Δn, 28
relaxation resonance frequency, f_{r}, 41

selective wet oxidation, 60
small-signal modulation, 42
spectral efficiency, η, 51
spontaneous emission, 11
stimulated emission, 11
surface relief, 38

temperature stability, 116, 121, 129, 134
temperature stability $f_{3\mathrm{dB}}$, 127, 134
threshold gain, $\mathrm{g_{th}}$, 16
threshold power, 79
trade-offs, 143
transmittance, T, 18

Acknowledgement

First of all I would like to thank Prof. Dr. Dieter Bimberg for allowing me to pursue my studies with such great degree of freedom, although it might not have been clear at the beginning how far these might lead. The unique environment he created consisting of the clean room and the measurement lab made this work possible. I am grateful to Prof. Dr. Anders Larsson for spending his time to review my dissertation thesis and for agreeing to be part of the dissertation committee. Many thanks also to Prof. Dr. Janina Maultzsch for serving as the presider of the dissertation committee.

I can not thank Prof. Dr. James A. Lott enough for his support, patience, advice, and help with this dissertation work throughout the past years. We have spent countless hours making plans, discussing results, exchanging ideas, and preparing presentations and papers. Throughout the years he has been a great mentor and has become a true friend. *Many mahalo kahuna kimo!*

I would like to thank many VCSEL group members, especially Dr. Friedhelm Hopfer and Dr. Alex Mutig for creating such a friendly working atmosphere that made it easy for me to learn the basics of the VCSEL work, Gunter Larisch for great help with various technical and organizational issues and the support in the second half of my dissertation work, and Waldemar Unrau for great teamwork in reparing clean room equipment and for being a patient listener.

A large amount of my time was spent on process development and processing of VCSELs. Therefore I thank everyone who keeps the cleanroom running and makes processing possible, above all our engineers and technicians Stefan Bock, Ronny Schmidt, René Linke, Kathrin Schatke, and Bernhard Tierock. I thank Dejan Arsejinević and Kristijan Posilovic for advice with some machines and processes in the clean room. I am thankful to Klaus-Jürgen Hensel and Tom Gaertner from the TZL of the Fraunhofer Heinrich-Hertz Institut.

I would like to thank our secretaries and administrative staff members Roswitha Koskinas, Ines Rudolph, Doreen Nitzsche, Thu Hoang, Ulrike Grupe, and Hella Farell who have always been very helpful, friendly, and competent in solving smaller or larger problems. I am also grateful to Bernd Schöler.

I am deeply thankful to my wife Prof. Dr. Yongling Bao for her incredible patience, her love and for caring for our baby without much help from me in the last months and for never losing her optimism. I am proud of our son Jan who has been as patient as a baby can be, when I needed to work on this dissertation instead of playing with him. I am also thankful for each of his smiles. I am truly grateful to my brother Kilian and my mother Jutta for all the good times and support during my life.